A TISSUE ENGINEERING PLATFORM TO INVESTIGATE EFFECTS OF FINITE DEFORMATION ON EXTRACELLULAR MATRIX PRODUCTION AND MECHANICAL PROPERTIES

by

John Ashley Stella

Bachelor of Science, Mechanical Engineering, Pennsylvania State University, 2003

Submitted to the Graduate Faculty of

The Swanson School of Engineering in partial fulfillment

of the requirements for the degree of

Doctor of Philosophy

University of Pittsburgh

2011

UNIVERSITY OF PITTSBURGH

SWANSON SCHOOL OF ENGINEERING

This dissertation was presented

by

John Ashley Stella

It was defended on

September 9, 2011

and approved by

Sanjeev G. Shroff, PhD, Professor of Bioengineering and Medicine, University of Pittsburgh

William R. Wagner, PhD, Department of Surgery, Bioengineering, Chemical and Petroleum Engineering, University of Pittsburgh

Ann M. Robertson, PhD, Departmental of Mechanical Engineering and Materials Science, University of Pittsburgh

Bradley B. Keller, MD, Cardiovascular Innovation Institute, University of Louisville

Dissertation Director: Michael S. Sacks, PhD, Professor, Department of Bioengineering, University of Pittsburgh

A TISSUE ENGINEERING PLATFORM TO INVESTIGATE EFFECTS OF FINITE DEFORMATION ON EXTRACELLULAR MATRIX PRODUCTION AND MECHANICAL PROPERTIES

John Ashley Stella, PhD

University of Pittsburgh, 2011

It is estimated that more than 85,000 prosthetic heart valves are implanted annually in the US and ~275,000 worldwide. Although current heart valve replacements have extended the lives of many patients, there is to date still no ideal alternative. Pediatric applications, in particular, pose unique problems because current valve replacement options are unable to accommodate somatic growth of the patient. Since its inception, the tissue engineering paradigm has garnered widespread attention as a means to recapitulate native tissue structure, composition, and mechanical function in a controlled and reproducible manner by combining engineering and life science principles. Before fully functioning tissue surrogates can be developed for clinical use, many complex biological, chemical and mechanical aspects of native tissues must be addressed. Furthermore, contemporary literature lacks a consolidated approach, instead, presenting a wide variety of scaffold materials, cell sources, and mechanical conditioning regimes in efforts to restore native tissue function. These challenges coupled with the paucity of structurally based, finite deformation framework constitutive models hinders our understanding of engineered tissues and their ability to perform as tissue surrogates.

The focus of this dissertation is to elucidate the effects of large deformation mechanical stimuli on the development of engineered leaflet tissues. With our ability to incorporate viable cells distributed throughout the scaffold via concurrent electrospraying and electrospinning of

poly (ester urethane) urea (PEUU) fiber scaffolds, we are provided a unique, controllable platform to: (1) characterize the mechanical behavior of electrospun PEUU and cellular response to global deformation, (2) assess our ability to create functional cell integrated surrogates via dynamic culture, and (3) develop a generalized finite deformation framework than can be used to gain an understanding of how the evolving extracellular matrix phase contributes to the construct gross mechanical behavior. We contend that much can be learned about the mechanical modulation of functional tissue from electrospun PEUU scaffolds since they capture aspects of native tissue microstructure and exhibit the ability to endure large deformations while recovering completely. It is our hope that these studies will guide the emergence of new materials and processing methods to develop functional pulmonary valve (PV) tissue surrogates which serve a predominantly biomechanical function.

TABLE OF CONTENTS

LIST OF TABLES

LIST OF FIGURES

ACRONYMS

APS	Ammonium persulfate
AV	Aortic valve
CAR	Cell aspect ratio
DNA	Deoxyribonucleic acid
ECM	Extracellular matrix
EDTA	Ethylenediaminetetraacetic acid
GAG	Glycosaminoglycan
GMA	Glycomethacrylate
H&E	Hematoxylin and eosin
HV	Heart valve
LSCM	Laser scanning confocal microscope
MMP	Matrix metalloproteinases
MV	Mitral valve
MVAL	Mitral valve anterior leaflet
NAR	Nuclear aspect ratio
PAM	Polyacrylamide
PBE	Phosphate buffered EDTA
PBS	Phosphate buffered saline
PD	Preferred fiber direction

PCL	Polycaprolactone
PEUU	Poly (ester urethane) urea
PGA	Polyglycolic acid
PLLA	Poly l-lactic acid
PMSF	Phenylmethylsulfonyl fluoride
PSR	Picrosirius red
PV	Pulmonary valve
RP	Rapid prototyping
RVOT	Right ventricular outflow track
SDS	Sodium dodecyl sulfate
SEM	Scanning electron microscope
SIS	Small intestinal submucosa
SMC	Smooth muscle cell
TIPS	Thermally induced phase separation
TEPV	Tissue engineered pulmonary valve
UBM	Urinary bladder matrix
VEC	Valvular endothelial cells
VIC	Valvular insterstitial cell
VSMC	Vascular smooth muscle cell
QLV	Quasi-linear viscoelastic
XD	Cross preferred fiber direction

NOMENCLATURE

Symbols	Definition
C	Right Cauchy-Green strain tensor
E	Green's strain tensor
P, **P**	1st Piola-Kirchhoff stress (tensor)
S, **S**	2nd Piola-Kirchhoff stress (tensor)
ε	Strain
λ	Stretch
σ	Stress
Ψ	Strain energy

PREFACE

Looking back, it is hard to believe how quickly time has passed and even more difficult putting my graduate career into perspective. However, I can pinpoint the genesis of my interest in tissue engineering and biomechanics to an undergraduate course taught by Dr. Peter Butler. From there, I had the opportunity to participate in a NIH/NSF funded summer research program at Clemson University. It was this experience, working under the direction of Dr. Naren Vyavahare and Dr. Joshua Lovekamp (who was then completing his own doctoral research), which lead me to pursue an advanced degree of my own. Since then, I have been both challenged and rewarded in ways beyond what I would have ever expected.

I would like to extend sincere gratitude to my advisor, Dr. Michael Sacks, for his guidance and the opportunity to work on such an interesting and fruitful research project. In the time I've spent here at the University of Pittsburgh, I have had the opportunity to develop some of the most important relationships of my life, both personally and professionally. For the sake of brevity, I am not going to list all of the names. However, I can say with confidence that these relationships will continue for a long time to come.

I would also like to thank the boundless love and support of my family. My parents have raised my sister and I to be very hardworking and determined individuals and I feel safe knowing that through their life lessons, we have been given the tools to handle anything the future brings us. Moreover, in the face of adversity, my mother has blessed us through her strength,

determination, and courage. To say that it is inspiring is a gross understatement and it brings me great pleasure knowing that I am returning the favor of being someone to turn to in difficult times. It is for these reasons that I would like to dedicate this body of work to her.

1.0 INTRODUCTION

1.1 MAMMALIAN HEART AND ITS VALVES

The four-chamber heart, a common anatomical feature of humans and other mammals (Figure 1-1), functions to pump blood to the lungs (deoxygenated; right ventricle) and the systemic circulation (oxygenated; left ventricle) via heart valves. In the most general terms, heart valves (HVs) are thin, planar membranes that are positioned in the mammalian heart such that blood flow progresses in the forward direction only. During the cardiac cycle, blood depleted of oxygen by the metabolic demands of the body is returned to the right atrium of the heart via the inferior and superior Vena Cava. Deoxygenated blood is then pushed into the right ventricle

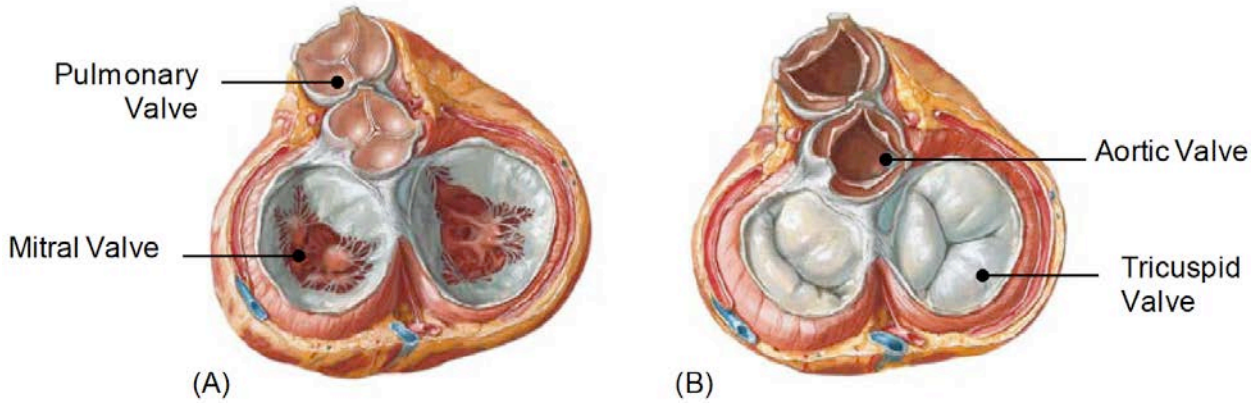

Figure 1-1. Mammalian heart gross anatomy.

through the tricuspid valve, and subsequently pumped to the lungs via the pulmonary valve and pulmonary artery. Blood replenished with oxygen in the lungs returns to the left atrium of the heart via the pulmonary veins. Completing the cycle, oxygenated blood is pumped into the left ventricle through the mitral valve, and subsequently pumped back to the systemic circulation and organs via the aortic valve and aorta. While healthy heart function is critically dependent on the efficient performance of each of the valves, the structures and functions of the semilunar valves (i.e., aortic, pulmonary) are both more simple, and more frequently subject to disease, than those of the muscularly-anchored atrio-ventricular valves (i.e, tricuspid and mitral valves). Thus, in the following sections the semilunar valves will be primarily considered.

1.1.1 Organ Level

The aortic and pulmonary valves are comprised of a unique tri-leaflet structure, with each of the individual leaflets exhibiting a semilunar (i.e., half-moon) shape (Figure 1-2) and the surrounding root. While there are subtle variations in the fiber architecture of the AV and PV, their gross structures are very similar. These valves are demarcated on the ventricular side by a semilunar line of attachment named the annulus fibrosis, and on the outflow side by a circular ridge of thickened tissue circumscribing the apices (i.e., commissures) of the semilunar leaflets referred to as the sinotubular junction [1]. The body of each leaflet spans from the annulus fibrosis to the free edge, forming a pocket-like cavity between the leaflet and its associated root wall. When open, the valve allows for unobstructed outflow of blood from the ventricle during systole; with flow deceleration, it closes via Bernoulli effects, and the leaflet provides a complete closure to prevent valve regurgitation. When closed, the leaflet tissue that forms a seal against retrograde blood flow is called the coapting surfaces or lunulas. At the center of each lunula is a

small nodule of thickened tissue called the nodulus Arantii that supposedly reduces regurgitation. Because each of the leaflets is roughly equal in size, the circumferential angular distance from commissure to commissure is approximately 120 degrees.

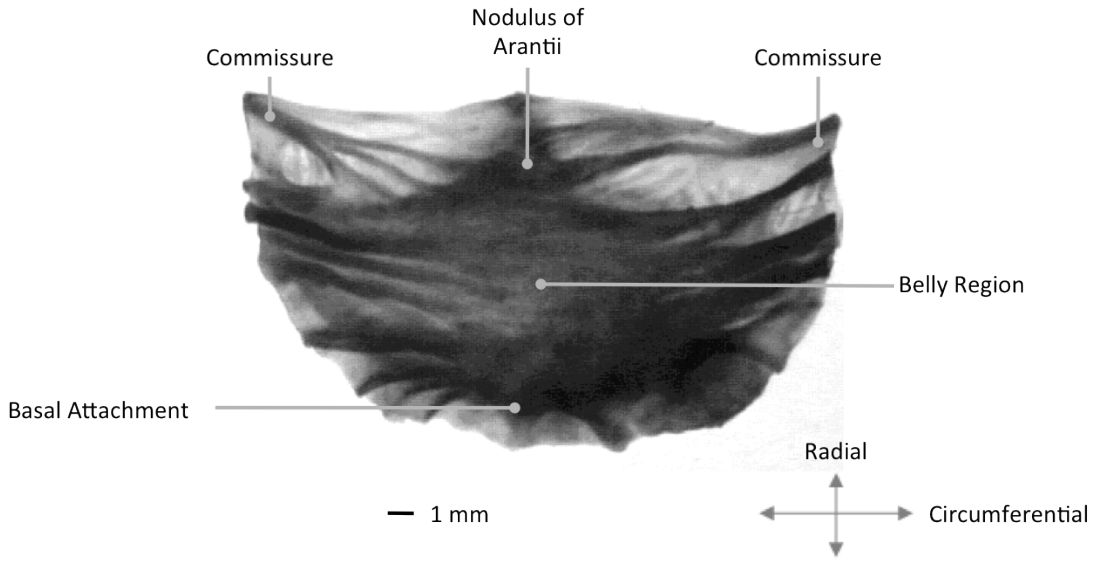

Figure 1-2. A partially polarized image of a semilunar valve leaflet highlighting the heterogeneous fibrous structure and main anatomical regions.

1.1.2 Valve leaflet structure and function

Soft biological tissue is composed of cellular and non-cellular entities. Included among its many roles, the latter serves a complex structural function by surrounding and supporting the cells. Referred to as the extracellur matrix (ECM), this structural entity is also adaptive to the functional requirements of the tissue and is a defining contributor to physical properties. Specifically in heart valve tissue, the ECM is composed of proteoglycans and structural proteins. Characterized as a binding agent, proteoglycans are an ECM constituent associated with tissue regulation, maintenance and hydration. T he structural proteins, collagen and elastin, are

attributed to the transmission of mechanical loads and tissue elasticity. As compared to elastin, valvular collagen is relatively stiff in a tensile environment and is considered the primary load-bearing constituent. It has been speculated that the elastin component observed in valvular tissues serves as a restoring feature once the load is removed [2]. Collagen and elastin are the primary constituents of semi-lunar ECM accounting for approximately 50% and 13% of the composition respectively [3].

The leaflet consists of three distinct layers: the fibrosa, spongiosa, and ventricularis (Figure 1-3) [2]. Each layer is composed of varied amounts structural proteins, collagen and elastin, as well as glycosaminoglyans (GAG's) and valve interstitial cells. The structure and composition of each layer is distinctly different. A highly organized collagen fiber network characterizes the fibrosa layer. Elastin and unorganized collagen fibers dominate the ventricularis composition. Consisting mainly of GAGs, the spongiosa layer separates the fibrosa and ventricularis. Investigators believe that spongiosa serves to dampen leaflet vibration. Total leaflet thickness is approximately 100 to 300 μm with 45% of the thickness stemming from the fibrosa layer. The spongiosa and ventricularis comprise 35% and 25% of the thickness respectively.

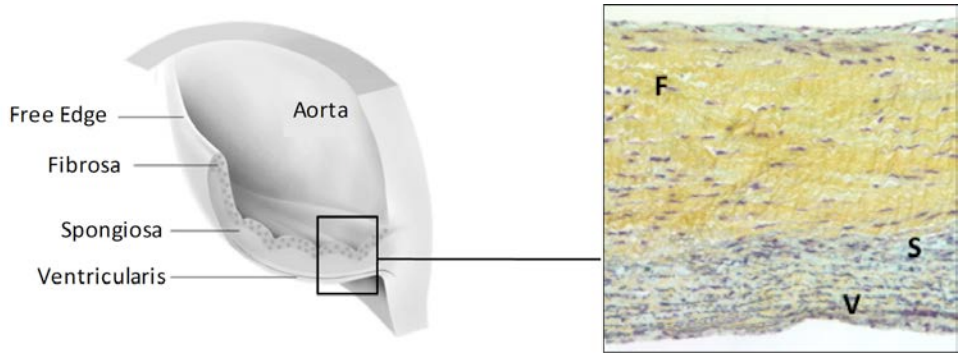

Figure 1-3. Layers of the aortic valve leaflet. Movat stained specimens highlight the ventricularis, spongiosa and fibrosa layers.

In the context of gross mechanical response, the structure of the fibrillar collagen network defines leaflet mechanical behavior. The arrangement and density of collagen fibers is the primary mechanism responsible for leaflet mechanical strength. Properties of this fiber structure are directly correlated with tissue function and response to mechanical stimuli. The highly aligned and organized fibers of the fibrosa layer are the dominant contributor to mechanical character. C ollagen fiber bundles of the fibrosa layer are predominantly aligned in the circumferential direction spanning between the commissures. Regional differences in fiber structure combined with directional alignment preferences create a n on-homogeneous anisotropic material character. This fiber alignment accommodates the radial expansion required for effective leaflet coaptation or valve closure.

1.1.3 Micro-structure of the semilunar valve leaflet tissue

Building from a fundamental triple helix unit, fibrillar collagen is a "bundled" structure consisting of tropocollagen, microfibrils and fibrils (Figure 1-4). The triple helical structure of the collagen molecule consists of three polypeptide strands and has a length of approximately 300 nm. These coiled units are organized into overlapping bundles to form microfibrils and fibrils. At a larger scale, fibers are developed from a collection of bundled fibrils. In the context of leaflet biomechanical descriptors, the term collagen fiber refers to a fibril collection. The complex architecture of the collagen fiber network, as visualized by multi-photon microscopy (highlighted in red, Figure 1-5), develops numerous overlapping and cross-linking conditions.

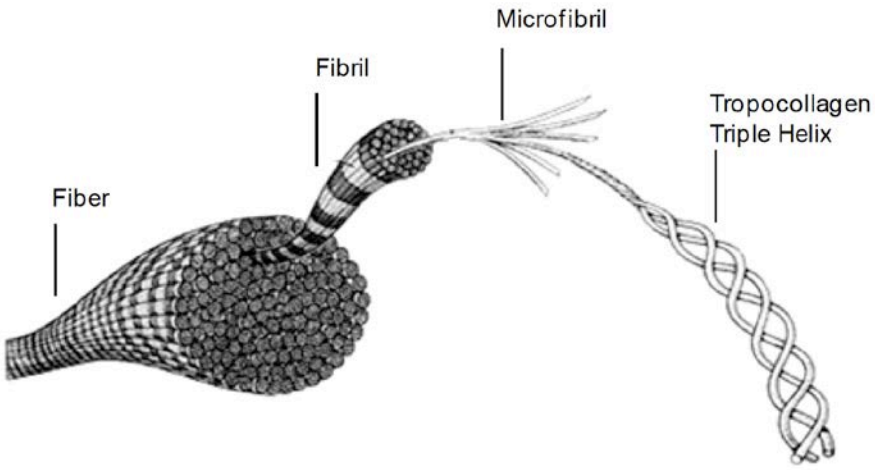

Figure 1-4. Collagen fiber structure. Based on a fundamental triple helix unit, collagen fibers consist of bundled fibril and microfibril collections.

Semilunar valve leaflets are populated by a mixed population of cells that are generally referred to as valvular interstitial cells (VIC). These cells can be readily observed in various imaging modalities such as Movat's pentachrome stained histological sections (black, Figure 1-5 left) or DAPI stained section view with multiphoton confocal microscopy (yellow, Figure 1-5b). These VIC express a p henotype intermediate between smooth muscle cells (SMC) and fibroblasts, and have been characterized as VA-type myofibroblasts due to their dual expression of fibroblast markers such as vimentin and SMC markers such as alpha smooth muscle actin (α-SMA) [4-6]. While the quiescent state of the VIC appears to be more fibroblastic, under conditions of fetal development and/or active remodeling, the VIC expresses a more SMC-like (i.e., α-SMA+) phenotype [7, 8]. Interestingly, recent studies have linked expression of the SMC-like phenotype to the contractile properties, leaflet stiffness, and mechanical environment of the valve [9, 10]. At the blood-leaflet interface, the leaflets are covered with a confluent lining of valvular endothelial cells (VEC). VEC, while similar in many respects to other vascular

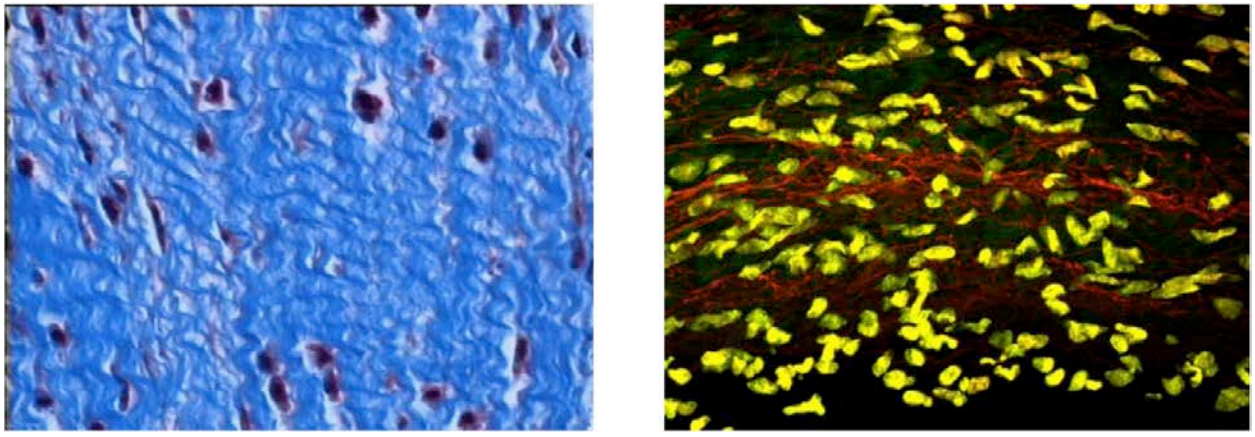

Figure 1-5. Fibrillar architecture of native porcine aortic valve.

endothelial cells, the VEC express certain unique phenotypic and morphologic attributes [11, 12].

While the structural components linking interstitial cells to their adjacent fibrous environment is reasonably well know, a functional understanding of how cells sense and respond to their local environment remains poorly elucidated [13]. VICs, on the scale of 13 nm, populate the tissue and are interwoven within the collagen fiber network. The crimped form and highly aligned nature of the fiber architecture can be observed via histological preparations (Figure 1-5). These characteristics have been shown to be significantly different in the fibrosa and ventricularis layer. Furthermore, the form of the fiber architecture changes under mechanical strain as fibers straighten and rotate providing the load bearing properties required to resist transvalvular pressure.

1.2 ESSENTIAL VALVE FUNCTION BELIES COMPLEX UNDERLYING MECHANISMS

1.2.1 Valve function and development

During the cardiac cycle valve leaflets experience a multi-modal mechanical environment. They experience planar tension (diastole, ~60%), bending (opening and closing, ~10%) and shear (systole, ~30%) as the heart transitions between systole and diastole. The membrane tension state developed by the coapted leaflets is considered to be a dominant mechanical deformation mode. In this mode, deformation stems from transvalvular pressure and develops a relatively high membrane tension of 25 and 70 N/m for pulmonary and aortic valves respectively. The planar biaxial response is highly anisotropic with directional strain magnitudes of approximately 15 and 60%. Corresponding directional strain rates have been estimated at 440 and 1240 s^{-1}. However, valve opening and closure mechanisms are controlled by hemodynamic characteristics. Peaking at 1.35 ± 0.35 m/s [14], variations in blood flow acceleration influence flow inertia and initiate valve movement. This dynamic behavior creates pressure differences and flow vortices in the sinus region which are believed to cycle the valve over a period of 20-25 ms. Although several mechanisms have been attributed to valve closure, the axial pressure difference alone is sufficient to close the valve [15]. Under these conditions, the leaflet response is characterized by a bending mode of deformation and leaflet boundaries are exposed to shear forces.

1.2.2 Subtleties of valve tissue tensile behavior

Despite available biaxial mechanical experimental studies on the mechanical behavior of the intact leaflet [16-19], there have been limited studies that characterize the mechanical properties of the individual leaflet layers. Knowledge of these subtle but important layer properties and interactions is vital to our understanding native valve function, and will lay the basis for rational replacement heart valves. In addition, all previous heart valve tissue constitutive models either assume uniform transmural wall stress or utilize a membrane tension formulation [17, 20-22]. Development of true 3D stress-based constitutive models requires knowledge of the individual layer responses. To this end, Stella et al. [23] recently investigated the role of each leaflet layer in the mechanical function of the native aortic valve leaflet. In order to obtain layer specific mechanical properties, a micro-dissection protocol was developed so that the leaflet could be separated into two distinct layers without damage. The intact leaflet and separated layers were then subjected to mechanical testing, histological evaluations, and detailed thickness measurements to determine how the layers interact and contribute to the function of the intact leaflet.

The biaxial mechanical behavior of native intact and manually separated leaflet layers was measured. Due to differences in their respective morphologies, each leaflet layer exhibited distinct mechanical behaviors. We were able to show that stress varies through the thickness of the leaflet while the strain experienced is homogeneous. Our experimental results also indicate that the fibrous layers of the leaflet are inherently anisotropic from the onset of loading. We concluded that histology based thickness measurements are the most appropriate since they enable us to determine layer specific thicknesses. Accordingly, the ratio of the fibrosa and ventricularis thicknesses is critical in modeling the stress-strain behavior of each layer and their

contribution to intact tissue function. A more detailed explanation of these subtle but important functional characteristics, please refer to Appendix a.

Valve leaflet gross anatomical structure, ECM microstructure, and concomitant mechanical properties appear to parallel physiological functional requirements (e.g., they exhibit a dense network of circumferentially oriented collagen fibers to support diastolic transvalvular pressure). Traditionally, soft collagenous tissues such as the AV leaflet have been characterized as anisotropic non-linear viscoelastic materials. Modeling and simulation of their time-dependent responses has most often utilized the quasi-linear viscoelastic (QLV) approach [24]. As with most classic viscoelastic theories, the QLV approach assumes that the tissues time dependent mechanical properties are all manifestations of the same mechanism, represented as a continuous spectrum. The underlying physical basis for the observed viscoelastic behavior may include collagen fibril-fibril interactions [25] or intrinsic collagen viscoelasticity. If these assumptions hold, then both creep and relaxation behaviors would be derivable from each other [26].

However, Thornton et al. observed a disparity between the rate of relaxation and creep at low stress level and further demonstrated that ligament creep could not be predicted from relaxation data utilizing QLV theory. Mechanistically, it was shown that collagen fiber crimp was reduced during ligament creep, indicating a fiber recruitment mediated behavior [27, 20]. Mechanistically, it was shown that collagen fiber crimp was reduced during ligament creep, indicating a fiber recruitment mediated behavior In a related study, Provenzano et al. [28] suggested a more general approach than QLV theory is required to describe the nonlinear viscoelastic behavior of rat medial collateral ligament. During this study the author's observed the rate of creep and relaxation to be dependent upon initial stress and strain levels respectively.

It was also observed that the rate of relaxation proceeded faster than the rate of creep in contra-lateral ligaments.

However, recent studies by Stella et al. clearly indicate that the mechanisms responsible for creep and relaxation in the AV leaflet are functionally independent and the fiber-recruitment model of Thornton cannot account for the observations of the current study [29]. Thus, in agreement with recent MV anterior leaflet studies [30-32], the AV leaflet does not conform to viscoelastic material definitions when exposed to planar biaxial loading states. Instead, it is more appropriate to describe these tissues as quasi-elastic as they resemble elastic materials when subjected to physiological loading states. That is to say, AV and MV leaflets both exhibit the following unique mechanical properties:

1. Are capable of undergoing large, rapid strains during valve closure in response to the trans-valvular pressure gradients and returning to their original configuration when unloaded.
2. Exhibit no measurable creep under physiologically relevant loading conditions (e.g. when the valve is closed and loaded).
3. Exhibit very small viscous dissipative effects (hysteresis)
4. Exhibit substantial, directionally dependent stress relaxation.

Taken as a whole, our results suggest that it is probably not necessary to develop models of valve tissue time dependent behavior since, under physiologic loading states the valvular tissues appear to exhibit elastic-like behavior. We feel that it is perhaps more relevant to focus on how the valvular tissue achieves this amazing feat and how it may be altered in diseased states. For a more detailed explanation of these subtle but important functional characteristics, please refer to Appendix B.

Although the structural mechanisms underlying the time dependent mechanical behavior of the AV leaflet has been shown to be rather complex, its functional basis is straightforward and intuitive. Na mely, the ability of the tissue to primarily exhibit an elastic behavior while exhibiting the capability to locking up at physiologic loading conditions is highly desirable. It is interesting to note that valvular tissues are comprised of typical soft tissue constituents but exhibit functionally unique behaviors. The exact structural mechanisms underlying this unique behavior remain uncertain and warrant further investigation as they may have important implications related to degenerative valve disease [33] as well as developing engineered valvular tissues in-vivo [34].

Proper function of valve leaflet tissues rely heavily on the complex, coordinated function of its constituents spanning multiple length scales from the system, organ, tissue, and cellular scales. In healthy native tissues, structures constituting the semilunar valves perform remarkably well, typically withstanding 3×10^9 cycles during an average human lifespan. Conversely, disruption of the complex arrangement of these tissue and organ-level structures, either by congenital malformation or acquired by disease, can lead to clinical symptoms mandating valve replacement.

1.3 DISEASE STATES AND CURRENT THERAPIES

Heart valve disease represents a l eading cause of mortality and morbidity in today's world. Nearly 300,000 va lve replacement surgeries are performed each year, and this number is expected to triple as the aging population increases over the next 30 years [35]. While there are several valve replacement options available commercially, the currently available prostheses are

not appropriate for pediatric patients due to size limitations and the need for reoperations as the patients grow [36]. Nearly 20,000 children worldwide are born each year with congenital heart defects, many of which require a heart valve replacement [37, 38].

Conditions warranting replacement of either the semilunar (i.e., aortic or pulmonary) or atrio-ventricular (i.e., mitral or tricuspid) valves can be generally characterized as either congenital or acquired. Congenital lesions in pediatric patients (e.g., pulmonary atresia, tetralogy of Fallot) often require complete reconstruction of the valvular outflow tract [39-41]. In older patients (i.e., 8th decade), senile degeneration of the valve leaflets is common, clinically manifesting as either stenosis (decreased valvular orifice area), insufficiency (regurgitant blood flow), or a combination thereof [42]. While mechanical, bioprosthetic, and homograft valve replacements have significantly improved the quality of life of many patients since their inception in the 1960's (Figure 1-6), currently available valve replacements continue to suffer from serious limitations [43].

Mechanical valves offer superior long-term durability; essentially lasting the lifetime of the recipient; however they require chronic anticoagulation therapy to reduce the potential for thromboembolism and are susceptible to infection [44]. These drawbacks are of particular concern in women of child-bearing age, who carry an elevated risk of valve-related thrombosis and anticoagulant-related embryopathy during pregnancy [45, 46].

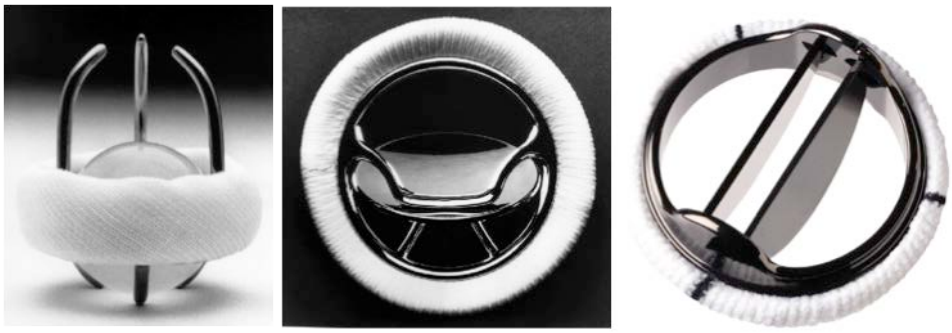

Figure 1-6. Mechanical valve replacements.

Bioprosthetic heart valves, fabricated from chemically treated porcine valves or bovine pericardium, provide excellent hemodynamics, thereby avoiding the requirement of anticoagulation (Figure 1-7). Unfortunately BHV incur calcific and fatigue-related damage over a relatively short time frame of 10 to 15 years, resulting either in surgical intervention or mortality [43, 47, 48]. Homograft valves from human cadavers represent the gold standard in terms of hemodynamics and functionality; however their use is restricted by donor scarcity. Efforts to improve the biocompatibility and durability of mechanical valves and BHV, respectively, will likely yield some degree of success in the future. Traditional valve designs,

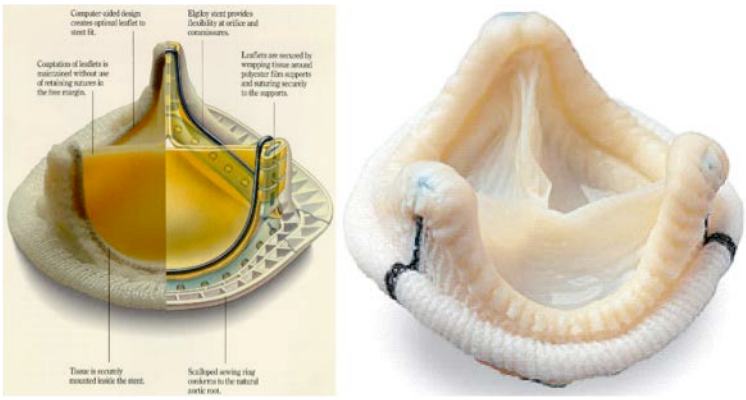

Figure 1-7. Bioprosthetic valve replacements. Bovine pericardium (left) and porcine aortic valve (right).

however, all lack living cells and thus do not possess the capacity for growth that is conceptually appealing in reconstructing pediatric valvular lesions.

Physicians and scientists alike have proposed tissue-engineered heart valves to be the ultimate solution for treating valvular heart disease. Rather than replacing a diseased or defective native valve with a mechanical or animal tissue–derived artificial valve, a tissue-engineered valve would be living tissue, able to respond to growth and physiological forces in the same way that the native valve tissue does. This potential of growth, repair, and remodeling is most exciting for pediatric applications eliminating the need for repetitive surgeries typically necessitated by the inability of a valve substitute to enlarge as an individual grows. Other advantages of an engineered tissue heart valve would likely include nonthrombogenicity, infection resistance, and cellular viability. Currently, the goal to engineer functional heart valve tissue presents a unique combination of challenges yet to be met by current regenerative or tissue engineering approaches.

1.4 TREATMENT TRENDS FOR CONGENITAL HEART DEFECTS

As of July 2011, the National Heart Lung and Blood Institute reports that about 0.8% of all births or about 35,000 newborns are afflicted with some type of heart defect each year. This makes congenital defects of the heart the leading type of birth defect. Many of these defects are simple conditions that require no intervention but some newborns present with complex congenital heart defects necessitating urgent interventional measures soon after birth. Complex congenital heart defects encompass a broad spectrum of issues and can involve one or more of the following tissues: (i) myocardium, (ii) valves, and (iii) arteries and veins.

While defects can be isolated to valvular malformations (i.e. stenosis), patients typically present with complex malformations involving multiple tissue types. It is for this reason that clinicians seek valved conduits, which provide the necessary material for full outflow tract reconstruction. Since the application of this dissertation is focused primarily on e ngineered pulmonary valves, the following review of clinical interventions is specific to right ventricular outflow tract (RVOT) reconstruction. Conduit repair of RVOT discontinuity began in the early 1960s and various efforts utilizing many conduit types have been employed [49, 50]. These conduits can be subdivided into the following three categories: homografts, stented xenografts, and stentless xenograft conduits.

RVOT reconstruction typically occurs in very young patients ranging from newborns and infants to teenagers [51, 52]. As a result, graft sizing is a critical issue in clinical practice with a slightly oversided grafts being preferred. M oreover, when these devices are employed for RVOT reconstruction in very young patients, the rate of reoperation is significant (Table 1). A majority of which are due to conduit obstructions resulting

Table 1. Feature comparison of valved conduits for RVOT reconstruction. Adapted from [53].

	Homografts	Stented Xenografts	Stentless Xenografts
% conduit failure at ~2 yr.	9-55	35	25
Reoperation rate	8-31	12.2-25	1.8-14.1
% freedom from reoperation (5yr.)	22 (infant), 87-98.2	79.5	82.95-93.9
Complications	Stenosis/obstruction Endocarditis Aneurysmal formation Calcification Outgrowth Sternal compression	Mild insufficiency Conduit obstruction Leaflet dysfunction Calcification Conduit kinking	Stenosis Aneurysmal formation Endocarditis Regurgitation Thrombosis
Site of obstruction	Proximal	Proximal	Throughout length
Biological characteristics			
Low thrombogenicity	Yes	Yes	Yes
Freedom from anticoagulation	Yes	Yes	Yes
Durability	Yes	No	Unknown
Full size availability	No	Yes	Yes
Resistence to infection	Yes	Yes	Yes
Easy implantability	Yes	Yes	Yes
Low price	No	Yes	Yes

from valvular stenosis, distal anastomotic stenosis, conduit kinking, and somatic outgrowth [54]. The pulmonary homograft is still the most commonly used RVOT conduit, particularly in small children, but suffers from limited availability and high cost. X enograft conduits, while exhibiting inferior long-term durability, are more readily available and at more manageable costs. The ideal valved conduit should possess low thrombogenicity, freedom from anticoagulation, durability, availability, resistance to infections, good handling characteristics

and ease of implantation, and low cost. Unfortunately, the ideal valved conduit is beyond our current capabilities and conduit failure and explant is inevitable necessitating the need for multiple surgical interventions throughout the life of the patient. The mechanisms responsible for this lack of success are poorly elucidated. None of the currently employed methods of RVOT reconstruction involve the use of materials that exhibit the capacity to grow and remodel with the patient. Since its inception, the tissue engineering paradigm has garnered widespread attention as a means to recapitulate native tissue structure, composition, and mechanical function eliminating the chronic surgical burden placed on patients and poor long-term outcomes.

1.5 TISSUE ENGINEERED VALVULAR THERAPIES

Replacement or regeneration of load bearing soft tissues has long been the impetus for the development of bioactive materials. While maturing, current efforts continue to be confounded by our lack of understanding of the intricate multi-scale hierarchical arrangements and interactions typically found in native tissues. The current state of the art in biomaterial processing enables a degree of controllable microstructure that can be used for the development of model systems to deduce fundamental biological implications of matrix morphologies on cell function. Furthermore, the development of computational frameworks, which allow for the simulation of experimentally derived observations, represents a positive departure from what has mostly been an empirically driven field, enabling a deeper understanding of the highly complex biological mechanisms we wish to ultimately emulate. Ongoing research is actively pursuing new materials and processing methods to control material structure down to the micro-scale to

sustain or improve cell viability, guide tissue growth, and provide mechanical integrity all while exhibiting the capacity to degrade in a controlled manner.

Advances in regenerative medicine continue in response to the ever-growing need for tissue replacement options. It is estimated that $400 billion is spent each year in the United States on patients suffering from organ failure or tissue loss [55]. To meet this need, a multidisciplinary approach combining biology, medicine, and engineering is required to overcome the significant challenges preventing the successful repair or replacement of biomechanically functioning tissues. Many of the reasons for poor implant performance or failure remain ill defined. Often they are a combination of inadequate or miss-matched mechanical properties and biological complexities. As such, a great deal of effort focuses on gaining a deeper insight into the structural and behavioral characteristics of native tissues to guide design criteria for the development of tissue surrogates.

Despite the multitude of challenges, many early approaches and technologies have shown promising results. For example, heart valve prostheses derived from bovine pericardium or porcine aortic valves have long been used to enhance survival and improve the quality of life of patients presenting with a variety of valvular maladies. Similarly, engineered dermal grafts have successfully been used clinically to treat severe burns or wounds that would otherwise be unable to close and heal properly. Pioneering work by Badylak et al. in applying decellularized extracellular matrix scaffolds has also shown successes in regenerating organized tissue after severe tissue loss or injury [56]. In addition to providing invaluable educational experience to guide future efforts, this incremental progress moves the field ever closer towards the ultimate goal of developing technologies for safer and more efficacious tissue repairs and replacements.

In order for an engineered tissue to perform a predominantly load bearing function and sufficiently recapitulate the mechanical behavior of native tissues, advancements in the current technologies are necessary to attain more complex biological functionality as well as biomechanical stability. It is generally accepted that both chemical and mechanical factors modulate cell biosynthesis when producing extracellular matrix [57-60]. Healthy native tissues undergo intricate, multi-scale modes of deformation, which work synergistically with biochemical stimuli to determine physiologic responses. In order to mimic native tissue structure and organization it is first necessary to develop techniques to produce scaffolds in a controlled manner with characteristic lengths on a scale comparable to those observed in nature (Figure 1-8).

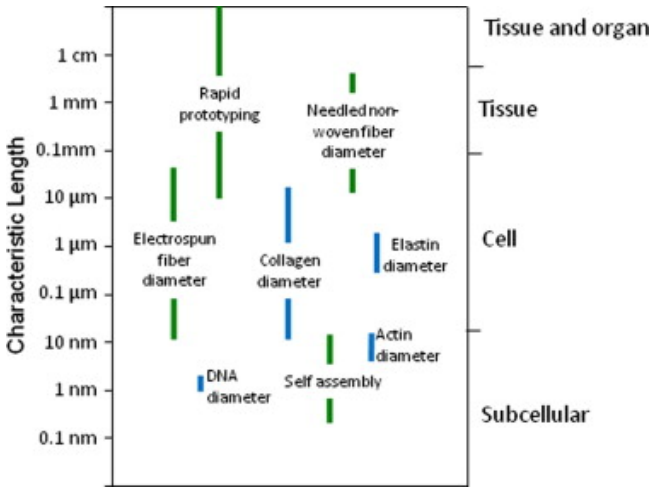

Figure 1-8. Characteristic length scales of native and artificial scaffolds.

The ability to create engineered tissue replacements would be enhanced by a detailed command of the complex, dynamic, and reciprocal interactions that occur at the cell-matrix interface. This includes how mechanical cues from the tissue or organ level are transmitted to the cell or cellular components and elucidation of the signaling pathways responsible for the

cellular processes observed experimentally. Furthermore, the use of new technologies in the production of engineered scaffolds necessitates a detailed understanding of the structure-function relationships unique to these materials. Currently, the exact microstructural characteristics of engineered scaffolds (that induce deformations experienced by the cellular inclusions) often remain ill defined and presumably will have a profound influence on cellular function. Long-term efficacy of tissue replacements or regenerative therapies will rely on the critical processes of cell proliferation and differentiation, the production of organized matrix, and concurrent tissue remodeling or growth.

1.6 EMULATING NATIVE TISSUE MECHANICAL BEHAVIOR

All of the scaffold manufacturing methods cited above can be employed to produce a 3D scaffold appropriate for cell culture and will likely foster the production of new tissue. However, the fields of tissue engineering and regenerative medicine continue to struggle to adequately match the mechanical behavior of native tissues. Collagenous soft tissues and tissue surrogates exhibit a wide array of unique mechanical behaviors that can be probed in a variety of testing modes (tension, shear, bending, torsion, etc). Unfortunately, traditional engineering indices of material behavior can fall short in describing the complete response of highly nonlinear and anisotropic materials and often require more sophisticated or extensive characterization approaches. Load bearing soft collagenous tissues are typically characterized by a bimodal stress-strain response with a compliant response or “toe region” at low strains which then transitions to a stiff response at large strain. While matching metrics related to tensile strength or tensile modulus has merit when applied appropriately, this approach gives little indication of the

Table 2. Structural scaffold design criteria and corresponding function for engineered tissues.

Scaffold design criteria	Resulting function in engineered tissue
Biologic compatibility Non-thrombogenic Non immunogenic Low or zero toxicity (degredation products)	Non-toxic and minimal inflamatory response
3D matrix architecture	Physiologicly relevant environment for cell function Known multi-scale architectural features mediating macro-micro transmission of force
Void space	Highly porous and interconnected pores allow cell infiltraction, transport of nutrients, humoral factors, and waste products
Surface chemistry and topography	Cell attachment and cell-matrix interactions
Degredation rate	Scaffold gives way to functional matrix formation
Fiber orientation	Anisotropic mechanical behavior Influence orientation of cells and ECM deposition
Sound mechanical behavior	Seamless integration with surrounding tissue(s), able to withstand in-vivo forces and avoid stress shielding

full material response during loading potentially leading to insufficient implant performance, undesirable tissue formation, or a lack of viable tissue production.

Practically speaking, the application of traditional engineering metrics of material behavior to soft biological materials cannot only be difficult but potentially unsuitable. When characterizing material performance, it is important to consider the functional relevance of a chosen method of mechanical testing and its interpretation relating to tissue function. For instance, valvular tissue stiffness with their highly anisotropic and highly nonlinear behavior cannot be adequately described by singular indices of material behavior. T his is apparent in the circumferential response of valvular tissues under biaxial loading where specimen contraction is observed at high stress states rendering the calculation of a maximum tangent modulus erroneous (Figure 1-9). The transition from low to high stiffness is attributed to a coupled fiber recruitment process capable of exhibiting lateral contraction at high stress levels (circumferential shortening). As a

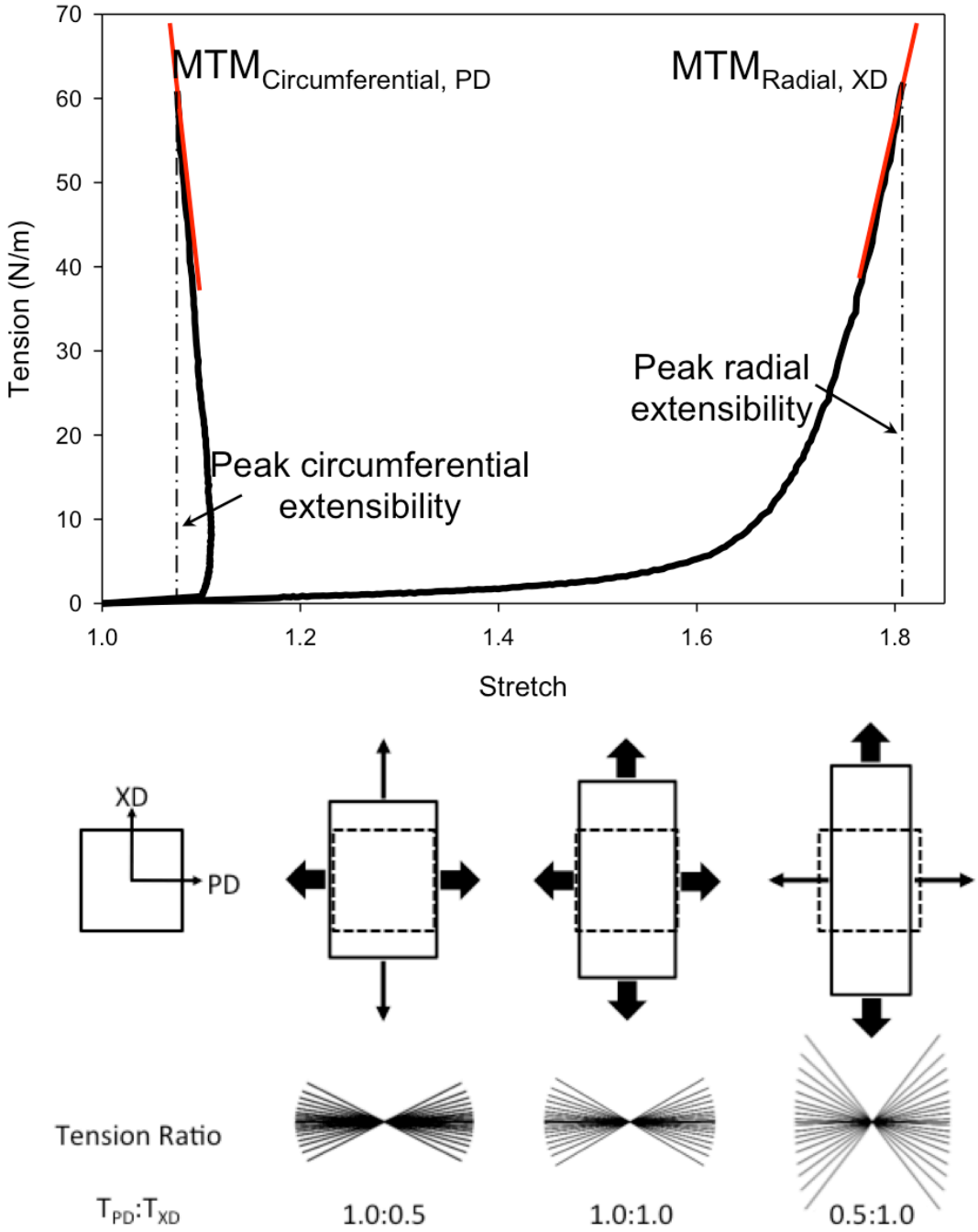

Figure 1-9. Application of traditional engineering metrics of material behavior are often inadequate descriptors of the complex behaviors observed in biological materials.

consequence, the determination of traditional engineering indices of material behavior, such as tensile modulus has little meaning (i.e. negative modulus). While helpful in providing potentially comparable metrics of tissue behavior, tabulated values that appear in contemporary literature can be misleading and belie the complex mechanical responses characteristically observed in soft load bearing tissues. While matching metrics related to tensile strength (i.e. ultimate tensile stress and ultimate percent elongation) or tensile modulus has merit when applied appropriately, this approach gives little indication of the full material response during loading. Again, in the case of valvular tissues, if one was to simply match peak stress-strain values without regard to the native material loading response, it would likely lead to inadequate coaptation or closing of the heart valve and result in poor function. Native tissues often exhibit highly specific, complex mechanical behaviors necessitating more sophisticated and thorough methods of characterization.

Elastomeric scaffolds fabricated by electrospinning natural polymers, synthetic polymers or polymer blends have received widespread attention that is largely due to the ability to produce biocompatible polymer constructs, which exhibit many soft tissue-like mechanical behaviors [61-63]. Electrospinning is a highly versatile process capable of creating a wide array of material behaviors through the alteration of production parameters or polymer choice. As such, it is necessary to assess these mechanical behaviors in a systematic manner. For practicality reasons, uniaxial tensile testing is often employed to obtain basic material properties such as the elastic modulus, strain at the onset of yielding, and ultimate tensile strength [64-70]. From the systematic mechanical evaluation conducted by Courtney et al., several scaffolds were manufactured with varying degrees of structural anisotropy or fiber alignment that was controlled by altering the rotational velocity of the collection mandrel. Increasing rotational

velocity results in an increase in fiber alignment [62, 71-73] and was experimentally measured from SEM micrographs via an image analysis algorithm. The controlled structural anisotropy produced during manufacturing directly led to more non-linear, anisotropic material responses. These structural properties form a complex 3D scaffold with tunable tissue-level mechanical behavior that can be remarkably similar to the gross biaxial mechanical response of the native pulmonary valve leaflet [61]. It has also been shown that the tensile response of some musculoskeletal tissues can be emulate well by electrospun scaffolds, namely, knee meniscus and annulus fibrosis tissues [62, 74].

Much of the work found in recent literature has focused on structural and mechanical characterization of electrospun materials with limited effort in the development of modeling frameworks to further assess our understanding of electrospun material behavior. Nerurkar et al. have adapted a homogenization modeling approach originally presented by Yin and Elliot to compare predicted mechanical behaviors of electrospun poly-ε-caprolatone and the inner and outer lamella of native annulus fibrosus tissue. Structural based modeling attempts originally developed for dense collagenous planar tissues have proven quite successful in capturing the mechanical behavior of electrospun scaffolds under biaxial modes of deformation [61]. It was noted that the model predicted a higher degree of fiber orientation than measured experimentally. This is attributed to structural characteristics of the polymer fibers measured in the image analysis algorithm but are not accounted for in the model formulation.

In order to improve upon these initial modeling efforts and gain a better appreciation of how these materials function across multiple length scales, recent work by Stella et al. was conducted to quantify additional structural characteristics. The electrospun scaffolds investigated in this study, exhibited complex, hierarchical architectures spanning multiple length

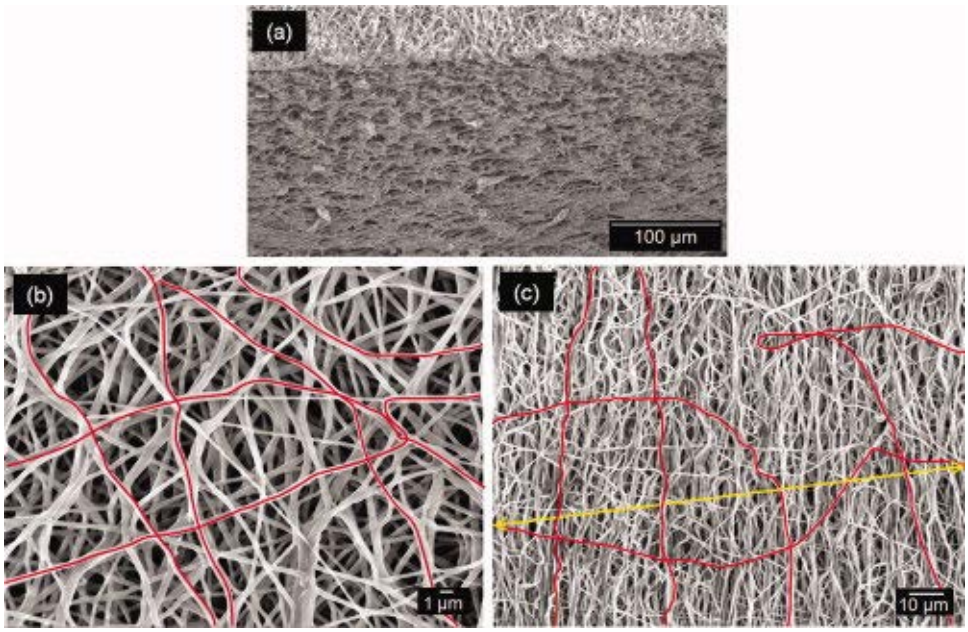

Figure 1-10. Complex, hierarchical architectures observed in electrospun PEUU.

scales (Figure 1-10b-c). For instance, PEUU fibers are seen to exhibit significant tortuosity, as highlighted in red, with this structural characteristic becoming much more prominent with increasing scale (Figure 1-10c). Tortuosity is defined as the ratio of a given fiber's actual length (perimeter) to its end-to-end length.

As a result, understanding the mechanisms by which these materials deform and behave under various loading conditions is not an elementary task. Fiber tortuosity, diameter, and fiber orientation distributions were all quantified as the electrospun specimen underwent planar biaxial modes of deformation. In addition, the deformation behavior of the scaffold was investigated across multiple scales by defining three characteristic lengths (micro (1-2 µm), meso (40-50 µm), and macro (1-3 mm)). Fiber tortuosity, a measure of how much a fiber deviated from being straight, in the unloaded scaffold, was observed to be dependent on both mandrel velocity during production and fiber orientation. A s the scaffold underwent planar biaxial modes of deformation, fiber tortuosity is extinguished and substantial fiber rotational kinematics was

observed contributing to an intricate fiber recruitment process [75]. Electrospun constructs were observed to follow gross affine fiber transformations and can be described in a manner similar to collagenous scaffolds [76]. Interestingly, some fibers were observed to rotate or change their direction of orientation during deformation while as a population, no net change was measured. This is likely an additional manifestation of the local heterogeneity that exists at the micro scale. With increased specimen deformation, a monotonic decrease in PEUU fiber diameter was measured for all specimens. Furthermore, it was observed that neighboring the fibers were well attached where they overlapped or intersected impeding translation of fibers with respect to one another but does not appear to inhibit rotational fiber kinamatics about these points of intersection. Johnson et al. presented a similar hypothesis for reduced fiber mobility in electrospun polymers exhibiting "point bonding" [77]. In short, polymer sintering was utilized on electrospun poly (ε-caprolatone) scaffold to invoke definite point bonds between fibers. Scale-dependent variations in deformation were observed and were attributed to the complex, spatially variant structure which results from the electrospinning process. These heterogeneous variations occur at the micro-scale which a cell might experience. The overall strain behavior tends to become increasingly more homogenous as the scale of interest approaches the tissue level.

The unique coupled matrix-cell deformation response of electrospun scaffold integrated with cells was also recently investigated [75]. The scaffolds exhibited micro-fiber morphologies and kinematics that were shown to directly influence local cellular deformations. For instance, in the unstrained configuration the electrospun fibers exhibited a tortuous architecture that transitioned to a web-like network of straight, interconnected fibers at high levels of strain. The deformations of the micro-integrated cells were found to be primarily mediated by this

phenomenon. The cell integrated constructs underwent fully recoverable large deformations akin to many native tissues. Initially, the integrated cells exhibited a rapid increase in NAR as fibers straightened and tortuosity was reduced. Once the PEUU fibers became straightened and the architecture transitioned to an interconnected web like structure, changes in NAR were observed to remain constant. Microintegrated cell deformation was mediated by the local reduction of tortuosity or straightening of the PEUU fibers. Thus, cell-scaffold interactions can be subtle and can bring about unique deformation behaviors. These results indicate that it may be possible to successfully emulate gross native tissue behavior without exactly replicating their highly complex micro-architectures. Attempting to delineate the individual contributions of structural fiber characteristics such as tortuosity and fiber kinematics to the constructs mechanical behavior would be quite cumbersome and better lends itself to the development of a numerical framework to explore this unique, interrelated phenomenon.

1.7 SCAFFOLDS FOR ENGINEERING LOAD-BEARING SOFT TISSUES

One of the earliest implemented approaches for tissue replacement was the use of processed or preserved allograft and homograft tissues. These tissues are typically obtained from cadaveric sources and cryopreserved without chemical cross-linking to control biological function for transplantation into another individual. Cryopreserved allograft heart valves exhibit good hemodynamic profiles and require little or no chronic anticoagulation therapy but are plagued by progressive degradation characterized by leaflet distention, fibrosis, possible leaflet calcification or even valve stenosis attributed to somatic growth of the surrounding tissues. Similarly, xenograft tissues are used with proper tissue processing to overcome immunogenetic responses

and stabilize the extracellular matrix. Chemical processing (i.e. cross-linking) of xenograft tissues has long been used in therapeutic applications to stabilize collagen architecture while significantly reducing the risks of an immunogenic response.

The mechanical response of native and glutaraldehyde treated porcine aortic valve leaflets and bovine pericardium has been systematically evaluated in their application to valve replacement therapies [16, 23, 29, 78-80]. After chemical cross-linking, the highly mobile fiber kinematics typical of native valvular tissues is altered significantly owing to disparate mechanical behavior such as becoming less extensible [16]. Furthermore, it has been shown that cross-linked tissues for valve replacement are susceptible to fatigue induced changes that lead to compromised mechanical behavior. These injuries can present in both locations of calcific nucleation and without calcification [48, 81, 82]. Lastly, aldehyde cross-linking of tissues with glutaraldehyde, which is known to exhibit cytotoxic properties, is associated with poor host cell infiltration. This lack of viable cells precludes growth and remodeling, resulting in an inability to maintain tissue homeostasis and repair structural insults [83]. Unfortunately, the processing techniques required for storage (cryopreservation) or matrix stabilization (cross-linking) of valvular tissue replacements significantly alters tissue mechanical behavior resulting in a continuing risk for morbidity and mortality [84].

More recently, non-crosslinked terminally sterilized biologic scaffolds of naturally occurring extracellular matrix have shown promise as a therapeutic option. For example, porcine small intestinal submucosa (SIS) has been successfully used in multiple applications to treat damaged or diseased tissue in human patients (i.e. musculotendinous, dermal, cardiovascular, gastrointestinal, lower urinary tract). This approach represents a “top down” method to obtain materials for therapeutic purposes whereby undesirable constituents such as cellular materials are

stripped away leaving potentially bioactive ECM. DNA and membrane proteins have been implicated in the immune response typical of transplanted tissues and must be removed while organized ECM proteins are relatively well conserved across species causing lower rates of rejection [85]. Though there are many variables affecting the viability of these materials, such as tissue source (presence of antigens), rate of scaffold degradation, and manufacturing methods, they have been shown to exhibit adequate mechanical function in many load bearing applications.

The mechanical response of these materials is dictated by their fibrous constituent arrangements and kinematics. Systematic evaluations of decellularized tissues are currently limited with the exception of small intestinal submucosa (SIS), urinary bladder matrix (UBM), and aortic valve leaflets. SIS and valvular tissue sources exhibit anisotropic mechanical behaviors owing to a preferred fiber alignment while UBM (submucosa and tunica propria) has a more isotropic fiber orientation and mechanical behavior [76]. The mechanical resiliency of an individual SIS layer is typically inadequate but the material mechanical response can be tailored to particular applications by the use of multiple layers [86]. Gilbert et al. used a multi-layer SIS device in the repair of canine Achilles tendon. The implant showed the ability to support the remodeling response of host cell infiltration and tissue ingrowth, leading to an organized, dense collagenous SIS-ECM similar to normal tendon tissue without catastrophic loss of function [56].

Despite these intriguing in-vivo remodeling events, the processing techniques required to eliminate cellular debris from these tissues can cause profound alterations in mechanical behavior. Chemical cross-linking, as mentioned above, alters the collagen fiber architecture resulting in a change in mechanical behavior. In a recent study by Liao et al., the effects of chemical decellularization on the mechanical and structural properties of the porcine aortic valve

leaflet were investigated [87]. In short, an anionic detergent, enzymatic agent, and a non-ionic detergent (sodium dodecyl sulfate, Typsin, Triton X-100 respectively) were used to process porcine aortic valve leaflets prior to mechanical testing or structural examination [87]. It was determined that the processing chemicals were responsible for profound increases in tissue extensibility and reductions in flexural rigidity all while no measureable change in gross fiber orientation was observed. Other common methods for terminal sterilization of biological materials include ethylene oxide, gamma radiation, and electron beam irradiation and each have unique effects on material behavior. When SIS is terminally sterilized, each of the above sterilization methods has been shown to reduce maximum material stiffness. Both methods of irradiation have been shown to reduce maximum force at failure and maximum tangential stiffness while ethylene oxide treatment induced marked increases in extensibility without significant alterations to force at failure [88]. The specific mechanisms by which the matrix architecture is altered during manufacturing are currently ill defined and require further investigation to improve the effectiveness of these technologies.

1.7.1 Synthetic ECM and processing methods for synthetic scaffolds

Though native tissues represent ideal scaffolds in their in-vivo form and function, the use of native ECM based scaffolds can have significant drawbacks. As mentioned above, host recognition of antigens can induce an acute or chronic immunogenic host response compromising implant function. In addition, the processing methods required for the production of these materials can be a source of inconsistencies between specimens resulting in varied degradation behaviors and mechanical responses. The use of biodegradable synthetic scaffolds can circumvent the pathogen transmission and immune recognition concerns associated with

collagen based tissues from animal or cadaver sources, albeit with local inflammation characteristics of such implants.

Designing scaffolds for tissue repair represents a "bottom up" approach whereby scaffolds are produced with desired chemical, physical, and mechanical characteristics in a controlled and reproducible manner to recapitulate native ECM structure and function. Common physical characteristics of interest include: surface texture to promote cell attachment, highly porous microstructure to allow tissue ingrowth, and an interconnected porous network to allow adequate nutrient transport all while maintaining a desired mechanical behavior (Table 1). As such, material processing techniques are implemented to produce 3D scaffolds with desired material behaviors which encourage desirable cellular responses. For the purposes of this article, scaffold morphologies will be segregated into two types: non-fibrous and fibrous. Both scaffold types have unique manufacturing processes and characteristics allowing them to function in a wide range of mechanical environments. Obtaining tissue-like tensile mechanical behaviors can be challenging with non-fibrous scaffolds as it is difficult to match the highly anisotropic and highly non-linear response characteristic of soft collagenous tissues. Fibrous scaffolds on the other hand, have the ability to bear significant tensile loads while maintained relatively low bending rigidities and can be manufactured to exhibit varying mechanical behaviors. Furthermore, long fiber composites better mimic natively observed matrix architectures with the potential to direct 3D tissue formation and organization [89].

1.7.2 Non-fibrous synthetic scaffolds

Polymer scaffold processing techniques such as phase separation, particle leaching, and high pressure gas foaming can all produce highly porous morphologies and provide a 3D environment

to support a viable cell population (Figure 1-11). Each of these processes allows a degree of control over pore size and pore structure; both of which are critical during culture to facilitate cellular ingrowth [90]. Emulsification/freeze-drying and thermally induced phase separation (TIPS) are two commonly employed phase separation approaches used in the production of non-fibrous scaffolds [91-95]. The porous media produced by phase separation techniques are capable of attaining porosities greater than 96% [96]. Moreover, TIPS is a versatile processing method allowing considerable control over scaffold morphology [97] with phase separation thermodynamics playing a crucial role in determining structure (Figure 1-11a,d) [98, 99]. The process of solvent casting and particulate leaching allows the preparation of regularly porous structures and can produce scaffolds with ~87% porosity and pore sizes greater than 100 μm. In this system, compressing beads (porogen) in a mold prior to injecting melted polycaprolactone can attain increased porosity (Figure 1-11b,e). However, the reliance on cytotoxic solvents for these techniques means that special care must be taken to remove such hazardous chemicals to ensure cell viability. Gas foaming represents a processing technique which circumvents the use of cytotoxic organic solvents [100, 101]. The cell nucleation process during expansion is important as it dictates scaffold microstructure and in turn, material properties (Figure 1-11 c,f). Manufacturing parameters affecting scaffold morphology include: processing temperatures, degree of saturation, hydrostatic pressure, interfacial energy, and visco-elastic properties of gas/polymer mixture [101]. Some drawbacks of this process include excessive heat during compression molding, which limits the incorporation of thermo-labile materials, and difficulties obtaining highly interconnected pore structures.

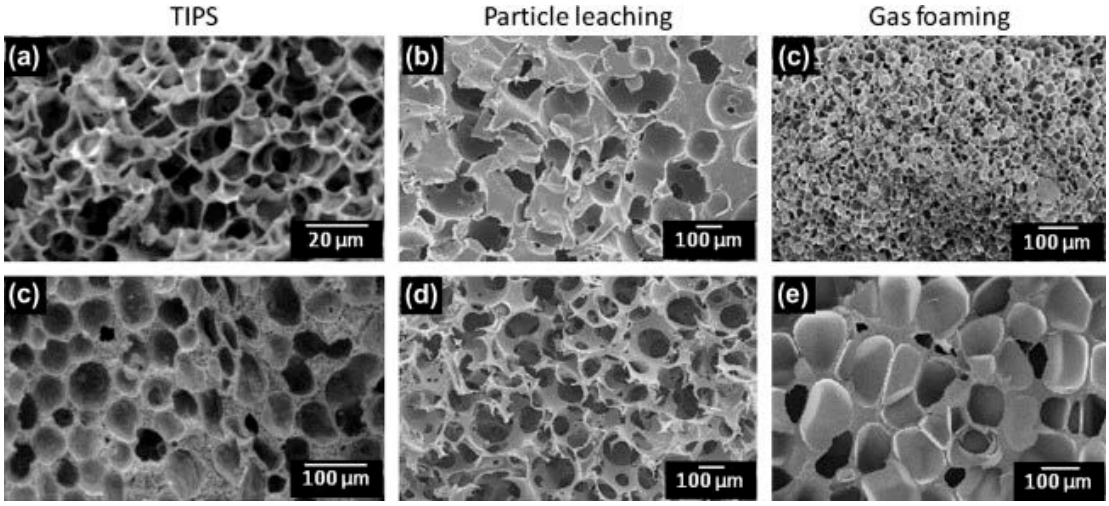

Figure 1-11. Cross-sectional scanning EM micrographs of non-fibrous methods to manipulate micro-morphology.

From a mechanical design perspective, using these techniques must strike a balance between porosity and mechanical integrity to withstand the dynamic environment of a load bearing tissue. Increased porosity necessitates a reduction of scaffold material per unit volume, reducing mechanical strength. Furthermore, tailoring mechanical behavior to emulate tissue mechanical behavior such as anisotropy is difficult and requires an ability to controllably induce structural anisotropy. The thermally induced phase separation technique can be modified by applying thermal gradients during the separation process to induce oriented pore formation resulting in an anisotropic material response with the preferred material direction being approximately 6 fold stiffer (Figure 1-12 a,d) [102, 103]. Also, supercritical gas foaming has been

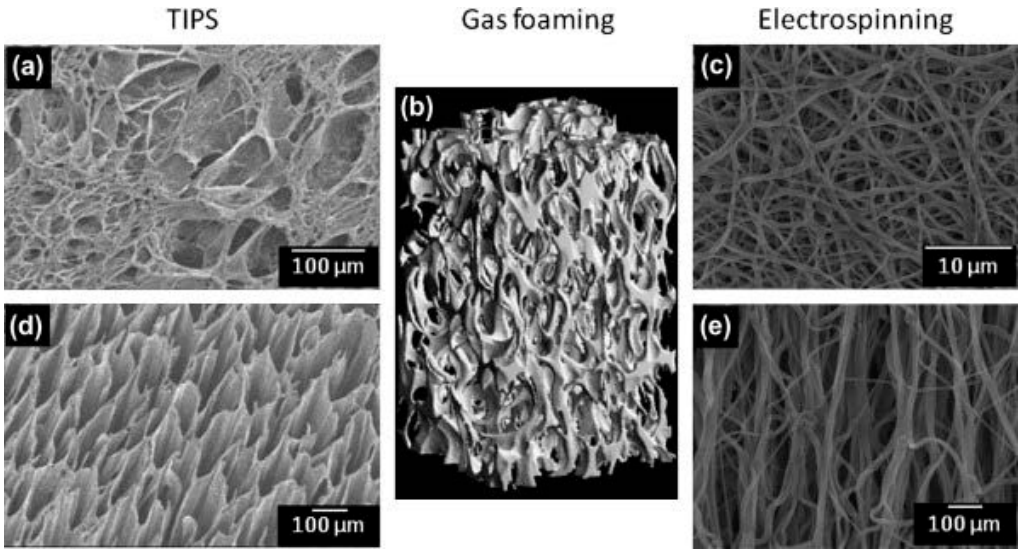

Figure 1-12. Attaining structural anisotropy through material processing.

used to create open cell composite foams for bone tissue engineering which exhibit morphologic and mechanical anisotropy with pores oriented in the foaming direction (Figure 1-12c). Moreover, the oriented pores could potentially induce a cell micro-patterning effect to orient the cells and the matrix that they produce.

1.7.3 Fibrous synthetic scaffolds

Synthetic scaffolds comprised of fibrous micro or nano-architectures present many advantages for tissue engineering applications. Namely, long continuous structures with diameters on the order of native ECM (50 – 500 nm) grossly approximate the local cellular environment (Figure 1-13). A population of fibrous structures makes them appropriate for handling tensile loads while maintaining relatively low bending rigidities.

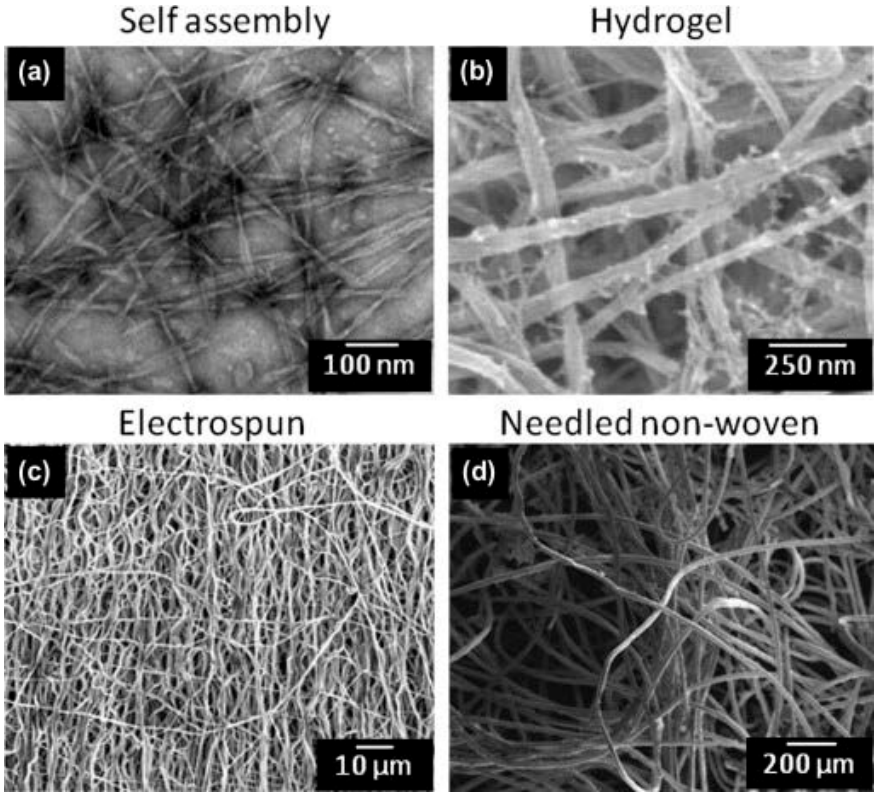

Figure 1-13. Scanning electron micrographs of methods commonly employed to create 3D scaffolds exhibiting fibrous structures with diameters on the order of native ECM.

Control of the distribution of fibers during manufacturing enables the production of scaffolds exhibiting a wide array of mechanical behaviors. Furthermore, scaffolds comprised predominantly of fibrous structures provide high surface area to volume ratios and high porosity. These characteristics encourage cell contact and transport of nutrients or removal of waste products respectively.

1.7.4 Self-assembly

Self-assembling materials are a relatively new technology capable of producing nano-scale fibers. The process of self-assembly can be observed throughout the natural world (nucleic acid

synthesis, protein synthesis, etc.) and is mediated by weak non-covalent bonds, ionic bonds, hydrophobic interactions, van der Waals interactions, and water mediated hydrogen bonds [104, 105]. Self-assembly or self-organization is a spontaneous event where individual components combine to form an ordered structure with preprogrammed non-covalent bonds within and between molecules. This process can be used to produce a range of structures that can themselves self-organize into superstructures [104].

Controlling the self-assembly process is a complex procedure and fabricating 3D scaffolds with reproducible microstructure and satisfactory mechanical properties poses significant challenges. Self-assembled materials typically exhibit morphological characteristics on a sub-cellular scale. For instance, fiber dimensions are on the order of 5-10 nm in diameter and 1 μm in length with pore diameters ranging from 5-200 nm. These materials have many relevant applications such as the investigation of molecular interactions [106], environmental sensors, use as a delivery vehicle for drugs or cells [107], and the development of 3D tissue engineering scaffolds [108, 109]. Bioactive molecularly engineered nanofibers have also shown promising results in guiding de novo tissue regeneration processes such as angiogenesis [110, 111]. As the production methods mature, this technology may prove viable in the production of organized structures up to the macroscopic scale comparable to native tissues. Furthermore, understanding mechanisms of the self-assembly process may prove valuable in attempts to guide in-vivo or in-vitro self-assembly to regenerate viable tissues or organs.

1.7.5 Hydrogels

Hydrogels represent a state of material and are comprised of cross-linked, hydrophilic polymers allowing them to maintain large fractions of interstitial fluid (water) [112]. The properties of

these materials can be designed for various applications by specifying material characteristics such as biocompatibility, permeability, mechanical and chemical stability, as well as easily controlling gross scaffold geometry and cellular distribution. Cellularized hydrogel constructs can be produced by three main methods; adhesion, matrix entrapment, and mico-encapsulation [113, 114]. Hydrogels can be rather weak, exhibiting only marginal mechanical strength. However, their mechanical properties can often be tailored to a reasonable degree by controlled alterations of their microstructure. The density of cross-links (chemical bonds, ionic interactions, hydrogen bonds, physical bonds) directly influences mechanical strength both in shear and tension [115]. Polymerization conditions can also dramatically alter the material behavior of the hydrogel produced. Alterations in reaction time, temperature, and the amount of solvent used can influence polymer structure, number of cross-links, and type of cross-linking bonds formed.

In tension, hydrogels typically do not exhibit material strengths observed in dense collagenous tissues. Instead, these materials exhibit ultimate stress levels on the order of tens to several hundred kPa. Due to their hydrogel characteristics, significant amounts of fluid (incompressible) can be retained, producing a high compressive modulus comparable with native articular cartilage. As a result, hydrogel materials are often investigated in orthopedic applications for the treatment or repair of articular cartilage displaying loss of function due to arthritis or acquired via severe trauma to the joint. Retention of their aqueous component during loading is important since fluid loss often results in reduced mechanical integrity, visco-elastic like behavior, and can even produce anisotropic material behaviors. These phenomena, though interesting and important to global mechanical function of these materials, can obscure true polymer material behaviors under loading. Since polymer chain architecture will dictate gross

mechanical behavior it is important to understand how the polymer chains behave individually and how they interact with one another during loading. Currently, the understanding of hydrogel lattice microstructure during deformation is limited and requires further investigation.

A subclass of hydrogels utilizes biomacromolecules (collagen, glycosaminoglycans, fibrin, etc.) to create artificial scaffolds for tissue engineering applications (Figure 1-13b) [116-120]. For example, Tranquillo et al. has extensively investigated the use of fibrin gels as a base scaffold for seeding cells in attempts to develop engineered constructs for cardiovascular applications such as heart valve tissues and vascular grafts and the study of Schwann cell mechanobiology [118-123]. C ollagen gels have seen similar use to characterize mechanical behavior as well as to study a variety of cell-matrix interactions and their resulting phenomena such as the effects of matrix stiffness on cellular contraction or the ability of cells to remodel the collagen matrix [124]. The naturally occurring polymers chitosan and alginate have both seen widespread use in tissue engineering applications for cartilage, liver, nerve, cardiac tissue [125-130]. T hough they both exhibit minimal foreign body reactions, can be readily processed without harsh chemicals, and can be designed to exhibit controllable mechanical and degradation properties, these materials often lack mechanical integrity without additional processing to manipulate polymer crosslinks or being augmented with other materials [131, 132].

Biopolymer gels inherently exhibit good cytocompatibility, are easily formed into physiologically relevant geometries, and can be manipulated to produce constructs that exhibit a relatively large range of mechanical behaviors. Currently, it is not clear whether these scaffolds exhibit a structure-function relationship comparable to native collagenous tissues nor has there been substantial evidence demonstrating the characteristic length of these polymerized biopolymers. In a recent study by Thomopoulous et al.[133], the authors attempted to apply a

structural continuum model [134-136] but found it to underestimate the level of mechanical anisotropy in aligned gels. This may be indicative that these gels do not functionally behave as long fiber composite materials. This may also lend insight to the shortcoming of these biopolymer gels of lacking mechanical integrity, rendering them unable to adequately mimic native tissues in a functional manner. Native valvular tissues on the other hand exhibit collagen fibers or fiber bundles spanning the leaflet that measure on the order of tens of mm.

1.7.6 Needled non-woven

Polymer processing techniques originating in the textile industry have proven valuable in producing synthetic fiber meshes which are capable of stimulating isolated cells to regenerate tissue (Figure 1-13d) [137, 138]. Needled non-woven scaffolds can be manufactured quickly, at relatively low cost, and withstand sterilization processes necessary for in-vivo use. Isolated cells of a desired lineage can then be seeded and cultured in static or dynamic conditions. Since these highly porous scaffolds exhibit an open pore structure, the seeded cells can quickly and easily infiltrate the scaffold producing a construct populated with cells throughout.

Flat sheets of PGA/PLLA non-woven textile have recently been employed to recapitulate the geometry of the native pulmonary valve and trunk by Sutherland et al [34]. After seeding and culturing ovine endothelial progenitor cells on the non-woven scaffold, the constructs were implanted into the pulmonary valve position of a juvenile ovine model. After 16- to 20-weeks, the engineered valve constructs were explanted for histological evaluation. Interestingly, histological preparations of the ECM architecture resembled that of native valves remarkably well with a tri-layered structure of organized tissue. To investigate more fundamental mechanisms of tissue evolution in response to mechanical cues and their resulting effects on

mechanical behavior, Engelmayr et al. developed a modeling framework for the flexural properties of these needled non-woven scaffolds [138, 139]. In short, the structural model accounts for unique fiber morphologies which arise from the fabric manufacturing process and the production of new ECM to predict the scaffold's effective stiffness during bending which was in agreement with experimental values. Furthermore, it was determined that matrix deposition during culture resulted in increased scaffold stiffness and can be attributed to an increased number of fiber-fiber bonds. For additional information regarding the utility of these materials in elucidating aspects of tissue development see section titled "Engineered tissues as model systems".

1.7.7 Electrospinning

The final fibrous scaffold production technique covered in this review is electrospinning (Figure 1-13c). J.F. Cooley and W.J. Morton first patented this technology at the turn of the twentieth century but the theoretical foundation of this phenomenon was not determined until Sir Geoffrey Ingram Taylor published three seminal papers dating from 1964 to 1969 [140-142]. Scaffolds fabricated by electrospinning natural polymers, synthetic polymers or polymer blends have received widespread attention. Beyond its relative affordability and simplicity, this popularity is largely a result of a versatile manufacturing process where slight alterations during fabrication enable the production of scaffolds with a wide array of fiber morphologies (i.e. fiber diameter, porosity, packing density, orientation, etc) directly influencing bulk mechanical properties [143, 144]. Controlled structural and mechanical anisotropy are highly desirable material properties in mimicking native tissue architecture and has even been shown to approximate the highly nonlinear biaxial mechanical response of collagenous soft tissues, such

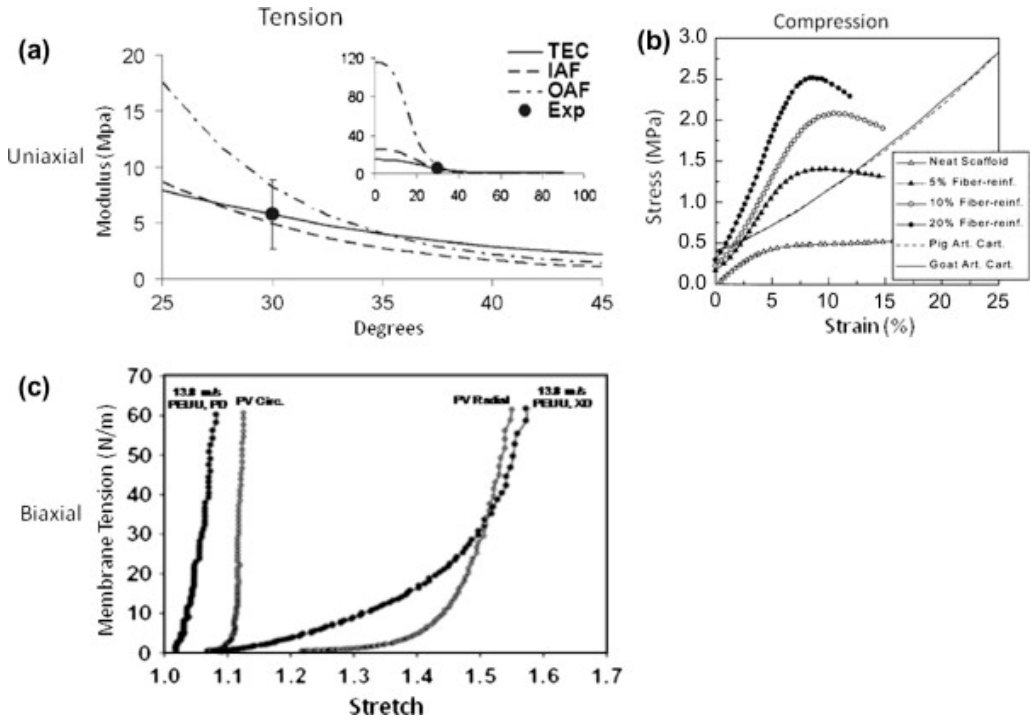

Figure 1-14. Synthetic scaffold production to recapitulate native tissue mechanical behavior.

as the native porcine pulmonary valve leaflet [61]. This has been accomplished for some non-fibrous constructs and one commonly employed method for controlled mechanical anisotropy during electrospinning is attained by using a rotating collection surface which induces a preferred fiber direction as the rotational speed of the collector increases (Figure 1-12c,e and 1-14c) [61, 71, 72]. S imilarly, the electrospinning process has shown the ability to produce biocompatible polymer constructs that exhibit tissue-like mechanical behaviors comparable with nucleus fibrosis tissues (Figure 1-14a) and articular cartilage (Figure 1-14b) [61, 62]. Electrospinning produces continuous fiber scaffolds exhibiting a wide range of mechanical properties, while also providing suitable surfaces for cell proliferation and growth [62, 63, 73, 145-147]. A substantial amount of work can be found in recent literature concerning the mechanical and structural characterization of electrospun scaffolds [61, 62, 75, 148, 149]. Initial

attempts to produce electrospun scaffolds for tissue engineering were concerned with the production and characterization of the materials including uniaxial tensile properties, measurements of porosity, and fiber diameter. Courtney et al. were the first to characterize multiaxial mechanical behavior of electrospun fabrics via planar biaxial testing and found their behavior remarkably comparable to the gross biaxial mechanical response of the native pulmonary valve leaflet (Figure 1-14c) [61].

The production of continuous fibers using this process has the added benefit of creating multiple interrelated functional length scales, a characteristic observed in biological materials. However, while electrospinning can fabricate scaffolds that possess ECM-like structures, this morphology also results in pore sizes that are generally smaller (<5 μm) and more irregular than those produced by some of the non-fibrous production methods introduced above [150, 151]. While it may be possible that cells seeded on the surfaces of electrospun matrices can migrate into the interior by displacing or enzymatically degrading individual fibers, an extended culture period and appropriate signals for cell migration into thick construct interiors might also be required. Thus, while electrospinning permits fabrication of biodegradable matrices that resemble the scale, architecture, and mechanical behavior of the native ECM [65], achieving high cellular density and infiltration remains challenging. To overcome this limitation numerous potential approaches have been proposed in recent literature. These approaches range from controlling microstructure through the alteration of production parameters (e.g. fiber diameter and packing) [152, 153], inclusion of native ECM proteins [154], or the inclusion of labile porogens or fiber families [155-158]. Cell populations can also be dispersed throughout an electrospun scaffold directly as initially shown by Stankus et al. [145]. This process that

employs a technique to concurrently deposit electrospun polymer and electrosprayed cells suspended in culture media is the subject of active work.

1.7.8 Rapid prototyping

Though not strictly fibrous in nature, rapid prototyping (RP) allows for the production of scaffolds with precise control over matrix architecture with a freedom of design unattainable in conventional processing techniques. RP, an additive process, starts from a computer aided design and is built up layer by layer to create 3D scaffolds with designed porosity, channel interconnections, pore distribution, and mechanical strength [159, 160]. There are numerous manufacturing techniques for RP materials that are classified into two categories. Direct fabrication, as the name implies, involves the successive build of the scaffold by melt-dissolution deposition or particle bonding techniques [160]. In contrast, indirect RP fabrication aims to create a sacrificial mold, which is then used to cast the actual engineered scaffold. Efforts are currently underway to expand the repertoire of RP materials for tissue engineering to match desirable degradation rates and products, mechanical strength, and biocompatibility. As new RP materials are developed (i.e. segmented polyurethanes, PLLA, PCL) it is possible to develop soft tissue like materials from this technology [161]. RP technologies have also served as inspiration for other automated fabrication approaches to build cell integrated constructs such as organ printing [162], cell laser printing [163], and photopatterning of hydrogels [164]. These approaches overcome limitations of cell infiltration and can likely be manipulated to incorporate some degree of control over material behavior. A thorough exploration of the mechanical behavior of these constructs and their fundamental effects on cell function (cell-matrix

interactions, biosynthetic activity, proliferation/apoptosis, etc.) would be a valuable addition to the field of tissue engineering.

1.8 OVERCOMING COMLICATIONS OF ENGINEERED VALVULAR TISSUES

Since its inception, tissue engineering has been touted as the definitive solution for treating valvular heart disease. Implantation of a living organ with the ability to grow and remodel is particularly appealing in pediatric applications where the current state of the art necessitates multiple reoperations through the life of the patient. To date, progress toward this ultimate solution has been limited by deficits in our understanding of the complex chemo-mechanical underpinnings that define tissue homeostasis and gross biological function. However, advances in the production and processing of new materials present us with novel platforms conducive to the systematic investigation of complex biological phenomena. For example, biocompatible material production with controllable structure and mechanical behavior can be used to mimic gross native tissue function while systematically investigating cellular responses to finite mechanical stimuli. While the current body of work is specific to future valve tissue therapies, the overarching goal of the current body of work aims to exploit such an advanced technology in hopes of informing the rational design of future engineered tissues that perform load-bearing functions.

1.9 SPECIFIC CONTRIBUTIONS

Heart valve leaflets are continuously exposed to large cyclical deformations and stresses. In addition, heart valve leaflets function in a demanding, highly dynamic environment where they exhibit unique, "quasi-elastic" mechanical behavior [29, 30, 165]. Due to the demanding environment and specialized nature of these tissues, contemporary efforts lack appropriate materials to recapitulate native tissue function. Tissue engineering represents a conceptually appealing alternative to current non-viable prosthetic valves as they have a capacity for growth, self-repair, and resistance to infection. However, the development of tissue engineered surrogates is hampered by numerous, unanswered fundamental questions. For example, it is unclear how a resident cell population maintains tissue homeostasis in response to exogenous cues in-vivo. On the other hand, with the ability to create scaffolds capable of fully recoverable large deformations and controllable anisotropy, electrospun PEUU constructs provide a unique platform to examine the effects of known local micro-architecture and its unique kinematics on cellular processes in response to tissue level deformation. We hypothesize that mechanical cues unique to heart valves (i.e. cyclic stretch, flexure, and flow) can be determined that optimize ECM synthesis within electrospun scaffolds in-vitro necessary to foster in-vivo ECM accretion and remodeling to produce a TEPV leaflet tissue**.** Furthermore, we also hypothesize that finite deformation within an elastomeric scaffold will promote improved matrix organization and mechanical integrity. It is our goal to develop a rigorous, quantitative understanding of the biomechanical events that occur during in-vitro tissue formation and remodeling within PEUU scaffolds and how they translate to native tissue homeostasis.

We will investigate our hypothesis through the following specific aims:

1. **Characterize the scale dependent fiber kinematics and mechanical behavior of electrospun PEUU scaffolds and the coupled cell-scaffold deformation behavior.** In engineered tissues, it is pertinent to understand how global deformations alter the fiber network as this dictates what the cell experiences and its response. To elucidate these unique mechanisms, micro-structural characteristics such as fiber splay, tortuosity, and diameter will be quantified in unstrained and deformed configurations. Furthermore, cell microintegrated polymer scaffolds provide a novel system to investigate cellular deformations within a three dimensional elastomeric fibrous scaffold. Specimens will be subjected to controlled biaxial stretch with 3D cellular deformations and local fiber micro-architecture simultaneously quantified, relating cellular deformation with global construct strain.

2. **Quantify the effects of controlled finite deformation mechanical stimuli on ECM accretion.** Mechanical stimulation is known to alter many cellular processes including biopolymer synthesis. Building on our understanding of the scaffold microstructure and kinematic properties defined in Aim1, it is our assertion that it is possible to induce robust matrix accretion through controlled global mechanical cues. By experimentally estimating physiologically relevant PEUU leaflet deformations, it is possible to rationally inform in vitro assessment of the mechano-depended matrix accretion behavior of rat VSMC. Specifically, electrospun PEUU will be constructed into a tri-leaflet valve, mimicking native ovine geometry, and subjected to physiologically relevant hemodynamic conditions to quantify global deformation at

the organ level. From this, finite strain mechanical conditioning regimes will be chosen to investigate ECM biosynthesis in vitro.

3. **Quantify the mechanical contribution of de-novo matrix.** In this aim, we will test our hypothesis that controlled finite deformation can be used to improve matrix mechanical integrity. Focusing on cell integrated electrospun constructs exhibiting significant matrix production; thorough planar tensile characterization will be conducted to assess evolving mechanical behavior. From these experimental observations, estimates of de novo matrix mechanical behavior can be directly obtained and compared with more detailed theoretical strain energy based theoretical examination will be employed to delineate phase specific mechanical contributions.

2.0 SCALE DEPENDENT FIBER KINEMATICS OF ELASTOMERIC ELECTROSPUN SCAFFOLDS

It is axiomatic that structural-mechanical interactions of matrix or scaffold components are critical to understand the mechanical behavior of native and engineered biological tissues. Yet, for native soft tissues, which are comprised of dense fibrous networks with complex multi-scale hierarchical structures, it remains a substantial task to relate all structural features to resultant mechanical responses. Moreover, in engineered tissues the mechanisms by which cells embedded within scaffolds perceive and respond to their local environment is critical to develop clinically successful tissue engineered replacements [75]. It is also well accepted that mechanical stimulation has a profound impact on cellular processes and regulation [13, 166, 167]. For example, cellular differentiation of mesenchymal cells can be guided through the application of compressive forces [168, 169]. Song et al. have shown that cyclic strain promotes proliferation of rat bone marrow mesenchymal stem cells [170]. Similarly, both static and cyclic modes of mechanical stimulation have been shown to alter protein synthesis and the amount and integrity of extracellular matrix (ECM) proteins. Engelmayr et al. [139] demonstrated that cyclic flexural deformation not only increased ECM mass in nonwoven scaffold-ECM composites, but also the effective ECM stiffness. Yet, despite our growing understanding of the cause-effect relationship of mechanical stimulation on cellular processes, the specific mechanisms responsible for these phenomenona continue to be poorly understood, especially for cells embedded within three

dimensional synthetic scaffolds [75, 171]. Ultimately, development of engineered tissue or organ replacements must rest on a strong fundamental knowledge of cellular interactions with the local environment and how these interactions span multiple length scales to contribute to the overall function [172-174].

Elastomeric scaffolds fabricated by electrospinning natural polymers, synthetic polymers or polymer blends have received widespread attention, which is largely due to the ability to produce biocompatible polymer constructs which exhibit many soft tissue-like mechanical behaviors [61-63]. Beyond basic characterization of the mechanical behavior of electrospun scaffolds, little has been done to gain a deeper understanding of how these scaffolds deform across multiple length scales. Moreover, this lack of knowledge underscores the need for an experimental and mathematical framework beyond phenomenological modeling approaches to elucidate the functional performance of these scaffolds. Though they may be able to recapitulate the mechanical behavior of native collagenous tissues at the tissue level, it is unclear how their microstructure deforms at the cellular level. This has further reaching implications when cells are introduced into the scaffold and how they would respond to their local environment when exposed to dynamic deformation.

While we have studied both the gross fibrous structure [61] and induced cellular deformations [75] in electrospun elastomeric poly (ester urethane) urea (PEUU) [65] scaffolds, the current study was undertaken to elucidate micro-structural characteristics and mechanical behavior and its relation to scaffold function across multiple length scales. Specifically, the fiber orientation distributions, tortuosity, and diameter were all quantified as the electrospun specimen underwent controlled planar biaxial modes of deformation. In addition, the deformation behavior of the scaffold was investigated across multiple scales by defining three characteristic

lengths. The characteristic lengths were defined as micro (1-2 μm), meso (40-50 μm), and macro (1-3 mm).

2.1 PROTOCOLS

2.1.1 Scaffold fabrication and imaging

PEUU was synthesized and electrospun as presented previously by Stankus et al. [65]. Briefly, solubilized PEUU polymer (5-wt%) was fed through a stainless steel capillary suspended 13 cm over a 4.5 inch diameter aluminum mandrel at a rate of 1.0 mL/h. By applying a large voltage gradient across the delivery capillary and the rotating collection mandrel, continuous electrospun polymer fibers were created. By altering the rotational velocity of the collection mandrel, PEUU fiber alignment could be controlled resulting in a preferred fiber and cross-preferred fiber direction (PD and XD respectively). In the current study, mandrel, tangential velocities ranging from 1.5 m/s to 13.8 m/s were utilized to create PEUU fiber mats with increasing levels of fiber alignment. Furthermore, 1.5 m/s, 4.5 m/s, and 9.0 m/s scaffold micro-structures were analyzed in unstrained and deformed states. These tangential velocities were chosen as they produce fiber networks exhibiting random fiber orientation (1.5 m/s), a marginal level of alignment (4.5 m/s) and a high degree of fiber alignment (9.0 m/s)

2.1.2 Image acquisition and structural characterization

Electrospun PEUU constructs measuring approximately 1 cm^2 were first placed onto a custom biaxial stretching device and sputter coated with a thin layer of gold measuring only 0.3 nm in thickness. The specimens were mounted in the stretching device by four stainless steel tethers on each of the specimen sides. The stretching device was designed so that it could be placed into the scanning electron microscope (SEM) enabling simultaneous specimen deformation and imaging. The gold sputter coat was not observed to exhibit any measurable necking even at high levels of strain (>100%). Moreover, sputter coating did not appear to alter fiber kinematic behavior during deformation in any appreciable manner as we have previously shown comparable morphologies between laser scanning confocal microscopy and SEM imaging modalities during deformation [75]. To characterize the construct fiber morphologies and the effects of deformation, scanning election microscope (SEM, JEOL JSM6330F) images were obtained (grayscale, 8-bit) at the unstained state and deformed configurations for comparison. Specimens were imaged at 3500X magnification with each image measuring 1280 x 1024 pixels and an average image area of approximately 1000 μm^2.

2.1.3 Bulk electrospun PEUU mechanical property characterization

Development of engineered tissue or organ replacements must rest on a strong fundamental knowledge of cellular interactions with its local environment and how these interactions span multiple length scales to contribute to the overall function [172-174]. Beyond initial attempts to produce and characterize the mechanical behavior of electrospun scaffolds, little has been done to gain a deeper understanding of how these scaffolds behave. This underscores the need for a

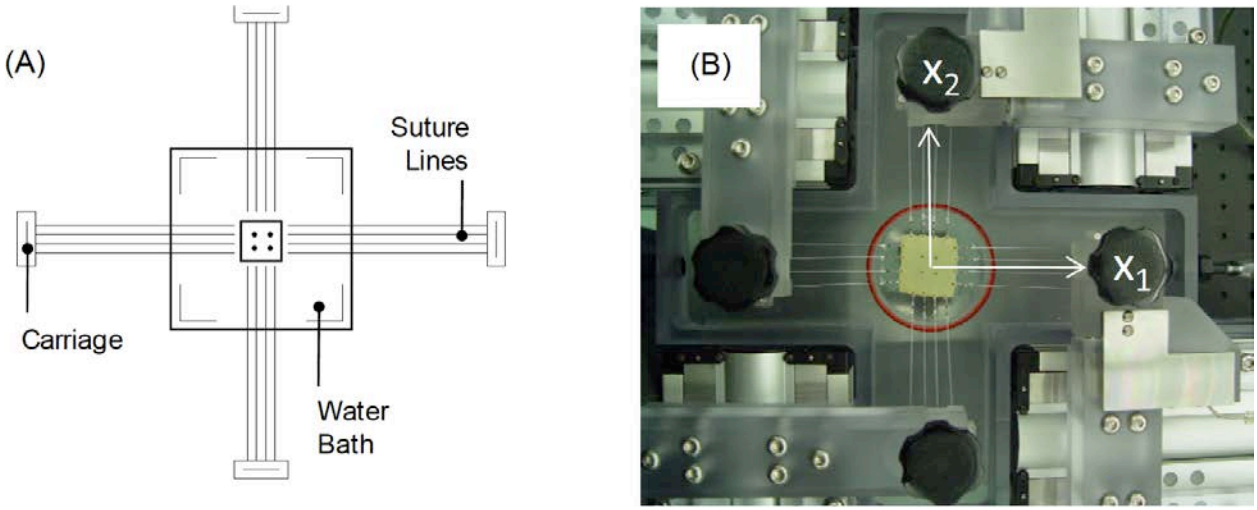

Figure 2-1. Schematic of the biaxial mechanical experimental setup (a) and corresponding photo of biaxial testing device (b).

deeper understanding of the micro-structural characteristics and mechanical behavior of the electrospun PEUU and how it translates to scaffold mechanical function.

The biaxial testing procedure has previously been described [175]. Briefly, A finite-element based surface interpolation technique using a four-node linear Lagrangian element was employed to determine the two-dimensional in-surface Eulerian strain tensor at each time point. In order to reference the deformed state configuration and calculate the strain tensor, a convective, in-surface coordinate system was used in which the axes were aligned to the local longitudinal and circumferential directions of the conduit. In this analysis, an Eulerian strain tensor component was computed for each load iteration. Additionally, the first and second Piola-Kirchhoff stresses were computed using the deformation gradient tensor. In all analyses, the post-preconditioned 0.5 gram tare configuration was used as the reference state.

In the present study 20 x 20mm specimens were used, with the specimen edges aligned to the longitudinal (x_1) and circumferential (x_2) axes of the mandrel (Figure 2-1b). A tissue marking

dye (Cancer Diagnostics) was used to form four small markers (~1mm diameter) in the central 4 x 4mm region of the specimen used to compute local strains using established method. The resulting deformation gradient tensor **F** was computed, from which the axial stretches $\lambda_{PD} = F_{11}$ and $\lambda_{XD} = F_{22}$ were determined, where PD and XD refer to the preferred and cross-preferred fiber directions, respectively. All testing was performed in water at room temperature. During all tests the maximum Lagrangian membrane tension tensor T (force/original unit length) level was chosen as 90 N/m. Membrane tension was chosen for run-time control to facilitate comparisons to our previous studies on valvular tissues [17, 165]. All test protocols maintained a constant ratio of membrane tension (T_{PD}:T_{XD}) throughout cycling. Testing began with two equi-biaxial protocols of T_{PD}:T_{XD} equal to 90:90 N/m. The next 7 consecutive tests were performed with T_{PD}:T_{XD} equal to 9:90, 45:90, 67.5:90, 90:90, 90:67.5, 90:45, and 90:9, respectively (Figure 2-1). These ratios were chosen to cover a wide range of stress states. A final equi-biaxial test was performed to determine if mechanical behavior changed during the experiment. Total testing time was approximately 2 h per specimen.

2.1.4 Effect of macro-level deformation on fiber micromechanics

Construct deformation was quantified at several characteristic length scales for evaluation (Figure 2-2). First, specimens were prepared for imaging by placing a 2x2 array of fiducial markers on the specimen surface with tissue marking dye (Cancer Diagnostics Inc., Birmingham, MI, USA). The markers were used to calculate the "macro" scale scale deformation gradient tensor F experienced by each specimen using standard methods [175]. Specimens were imaged in the unstrained reference configuration. As in our studies of native tissues, equibiaxial strain

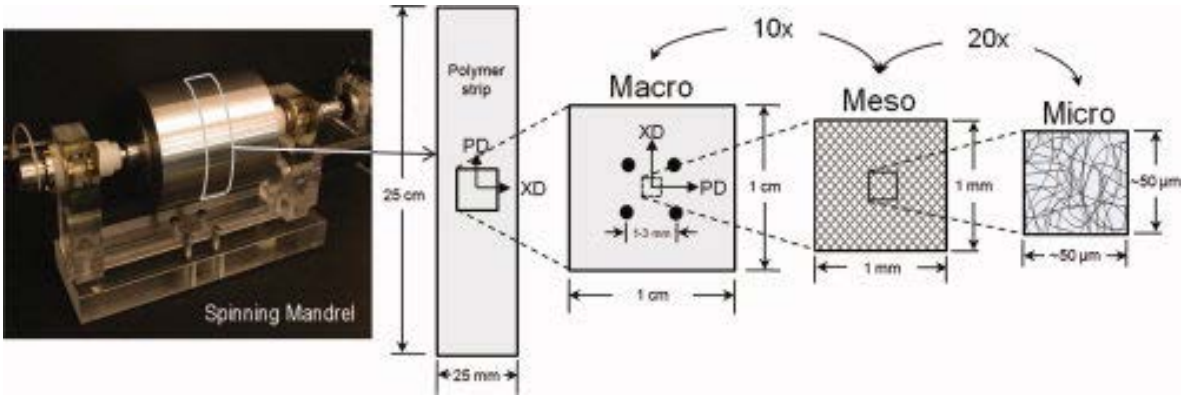

Figure 2-2. Electrospun PEUU scaffolds exhibit complex multi-scale hierarchical structures.

levels were chosen for the current study to examine the effects of fiber stretch without fiber rotations [76, 176]. It should be noted that the measured deformations obtained at run time represented only the macro-level deformation behavior of the scaffold. To allow a more detailed analysis, a more comprehensive method to quantify deformations at each scale was employed. Scaffold deformation was measured at three scales defined as micro, meso, and macro. At the micro and meso scales, the structural characteristics of fiber orientation, tortuosity, and diameter were quantified. This allowed for ranges in specimen deformation at the macro, meso, and micro scales were obtained in both the preferred and cross- preferred fiber directions (PD and XD respectively), as detailed in the following.

2.1.5 Quantifying scale dependent deformation

Rather than appearing as long, fully independently acting fibers, all fiber intersections were observed to be well adhered; allowing for rotation yet no slip. This allowed the bond points to act as natural material fiducial points, so that intersection displacements were quantified during deformation to a consistent metric to calculate scaffold micro-scale deformation behavior. The

displacements of fiber intersection points (n>60) were tracked between the reference and deformed configurations, allowed the use of a single Lagrangian 9 node element to interpolate the 2D strain field [16, 177]. In the case of the macro and meso scale strains, the deformation gradient was determined via bilinear interpolation [178]. The meso scale measurements had a characteristic length approximately 20 times larger than the micro scale. Finally, macro scale strains (1mm or larger) were dictated by the displacements of four fiducial markers on the specimen surface.

2.1.6 Fiber diameter, tortuosity, and orientation

SEM micrographs of the PEUU construct cross section appear to be visually consistent in architecture through the thickness of the specimen (Figure 1-10a). As such it is reasonable to conclude that measurements such as fiber diameter, orientation, and tortuosity obtained from the specimen surface represent the entire fiber population reasonably well. Several image analysis techniques were employed to quantify fiber diameter, orientation, and tortuosity. Fiber diameter, determined from the distance between fiber edges perpendicular to the fiber axial direction, was measured from 50 arbitrarily chosen fibers throughout the image via a custom, semi-automated image analysis algorithm implemented in MATLAB (The MathWorks, Inc., Natick MA, United States). We also noted that increasing the sampling frequency greater than 50 fibers was not observed to significantly alter the population mean or variance.

PEUU fiber alignment was ascertained by an image analysis algorithm as presented in detail by Courtney et al. [61]. Briefly, a 7 x 7 pixel array or mask was applied to image subregions which were defined by the mean fiber diameter of 6 fibers throughout the image. Within each subregion, the gradient-weighted contribution of each pixel of the mask was

calculated for each angle (-90-90) to determine the dominant orientation. The orientation information from each subregion of the image was then compiled into a histogram representing the splay of the entire fiber population with 1 degree increments.

Lastly, fiber tortuosity, as defined as the ratio of the total fiber length (or perimeter) to the fiber end-to-end length, was quantified for approximately 150 fibers across a mosaic image created from a 3 x 3 array of SEM micrographs. The 150 fibers represented the upper limit of fibers which could be consistently visualized on the specimen surface spanning the mosaic image which spatially measured approximately 150 μm wide by 120 μm high for each spin speed in the unstrained configuration. Incorporating nearly all visible fibers was also beneficial since it prevented the observer from inadvertently skewing the population by selection error. This process was accomplished via custom software which tracked fibers along their length in a semi-automated manner. First, the user arbitrarily defined fibers of interest, which visually spanned the image to quantify fiber tortuosity, and was assigned values in increments of 0.01. It should also be noted that from preliminary data (not shown), and as in our previous study [61], no observable change in fiber splay was measured between the specimen surface facing the mandrel and the exterior specimen surface. Moreover, SEM micrographs of the specimen surface were previously observed to show close agreement with subsurface images obtained via laser scanning confocal microscopy [75].

2.1.7 Measured relation between fiber angle and tortuosity

Raw tortuosity data, which was originally measured over $\theta \in (-90°, 90°]$ was reflected to $\theta \in [0°, 90°]$, as justified by the observed symmetry about the preferred fiber direction (i.e. $\theta = 0°$).

To visualize the results, a 2D histogram of all data was created from the occurrences of fibers located at a particular angle (θ) and given tortuosity (T) which could then be transformed into a probability distribution $P(\theta,T)$. This approach enables us to further investigate correlations between fiber tortuosity and orientation and describe the unique recruitment behavior of the scaffolds under large deformations. Due to the cumbersome nature of obtaining additional experimental data (see above for tortuosity measurement methods) to further populate a complete probability distribution, a continuous approximation was necessary. From preliminary inspections of the experimental 2D histogram data from each scaffold, large gradients were observed between neighboring points prohibiting the use of conventional surface fitting techniques. An interpolation approach was formulated through the use of an unstructured grid which could be tailored to sufficiently capture the features of the discrete tortuosity distribution while eliminating the need for higher order element equations. As such, the data was binned into angle increments of 15 degrees such that one-dimensional tortuosity distributions for constant θ could be fit in a piecewise manner. Each interval of discrete data was fit by a finite element based numerical approximation using multiple 1D quadratic elements. It was determined that a minimum of three 1D elements were necessary to adequately capture the T distributions for each value of constant θ. A resulting continuous surface, $P(\theta,T)$, was then created by linearly interpolating probability values between each of the 15 degree increments. Lastly, the volume bound by the created surface from each mandrel speed scaffold was normalized to have a unit volume.

2.2 RESULTS

2.2.1 Biaxial mechanical properties of electrospun PEUU

Electrospinning is a versatile process and slight alterations in the manufacturing process enable the production of scaffolds with a wide array of fiber morphologies (i.e. fiber diameter, porosity, packing density, orientation, etc), which directly influence bulk mechanical properties [144, 179]. Electrospinning, which produces continuous fiber scaffolds, can also provide suitable surfaces for cell proliferation and growth [62, 63, 73, 145, 146, 180]. The electrospinning process produces scaffold sheets of PEUU fibers (~0.8 μm in diameter) of a desired thickness to approximate the scale and mechanical behavior of native extracellular matrix, including the ability to undergo large deformations and fully recover when unloaded (i.e. nearly elastic gross behavior). The mechanical behavior of electrospun scaffolds can be controlled in a reproducible manner by altering the geometry or orientation of the collector.

For our purposes, a rotating cylindrical mandrel was used to induce structural and mechanical anisotropy (Figure 2-3) with the preferred fiber direction (PD) occurring in the direction of rotation and the cross-preferred fiber direction (XD) occurring in the orthogonal direction. For random (i.e. flat sheet) specimens and those electrospun onto a mandrel with low tangential velocities (in the range of 0.3–1.5 m/s) an isotropic network was observed with no discernible difference between the flat sheet and the 1.5 m/s scaffolds. Aligned fiber networks were produced when the mandrel velocity equaled 3.0 m/s or greater with a noticeable increase in alignment as the mandrel velocity was further increased. Further investigation via a custom image analysis algorithm showed that the scaffolds exhibited a high degree of structural uniformity as measured by fiber splay.

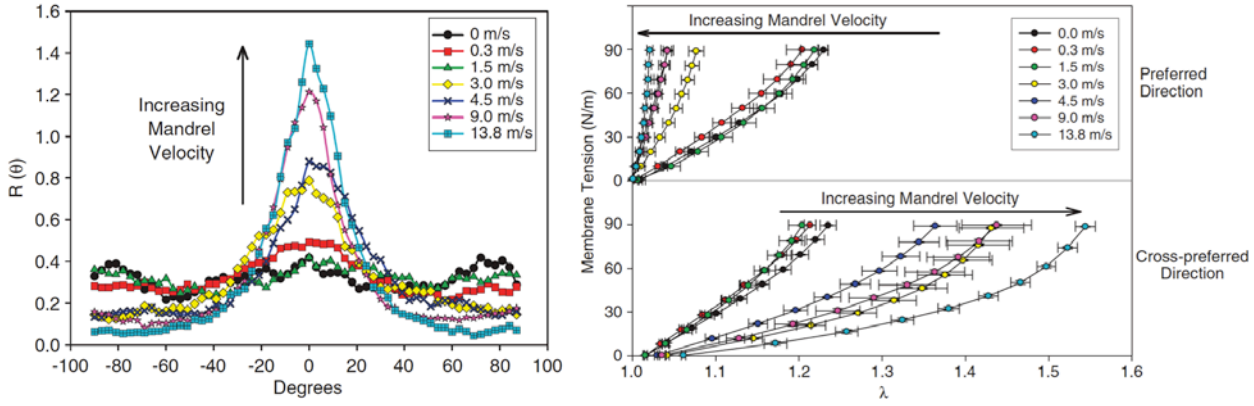

Figure 2-3. Scaffold structural and mechanical changes due to increased mandrel rotational velocity.

Under planar equi-biaxial mechanical stress states (i.e. where the two axial stress components are equal and the shear stress is zero); random and low mandrel velocity specimens exhibit an isotropic mechanical response. Above mandrel tangential velocities of 1.5 m/s, the mechanical response became substantially anisotropic, with increasing mandrel velocity (Figure 2-3b). Interestingly, all scaffolds exhibited a non-linear stress-strain behavior similar to collagenous soft tissues. It should be noted that the highest velocity group (13.8 m/s) exhibited planar biaxial mechanical response very similar to the highly non-linear and highly anisotopic behavior exhibited by the native porcine pulmonary valve leaflet (Figure 2-33) [61]. This demonstrates the ability of electrospun PEUU scaffolds to recapitulate the long, independently acting fiber response exhibited by the dense collagen network of the native PV (Figure 2-3, right panel).

2.2.2 P(θ,T)

The surface fitting method outlined above was capable of capturing the behavior of the raw data well (r^2 = 0.967 or greater) for all mandrel velocity constructs. Although changes in the surface created by the P(θ,T) data for each spin speed were subtle, several interesting trends were observed (Figure 2-4). For all scaffolds a primary probability peak was observed about the origin or preferred fiber direction. As construct fiber alignment increased, the breadth of this peak increased and the height of the peak decreased accordingly. This indicated a shift in the population from fibers with relatively low tortuosity levels at low spin speeds to increased tortuosity levels at all angles. In particular, the probability of observing a fiber of very high tortuosity increased with mandrel velocity. For the 1.5 m/s and 3.0 m/s constructs, which are known to exhibit minor differences in fiber splay [61], very similar P(θ,T) were observed. This result was also indicative of our ability to consistently and repeatedly produce PEUU constructs of similar architecture. Interestingly, secondary probability peaks were always observed in the XD (see the * in Figure 2-4) while in the PD a peak was seen to evolve with increasing mandrel velocity.

Though counterintuitive, increased levels of tortuosity were observed in the specimens produced at higher spin speeds. For instance, the fiber tortuosity distribution across all angles in the highly aligned 9.0 m/s specimen peaked at a tortuosity value of approximately 1.3 and was centered about the preferred fiber direction. Conversely, 1.5 m/s mandrel velocity specimens produced with no measurable fiber alignment exhibited a rather constant tortuosity distribution with no discernable peaks and an average tortuosity value of 1.08. It should also be noted that a higher density of fibers was observed in the PD with increasing alignment as anticipated.

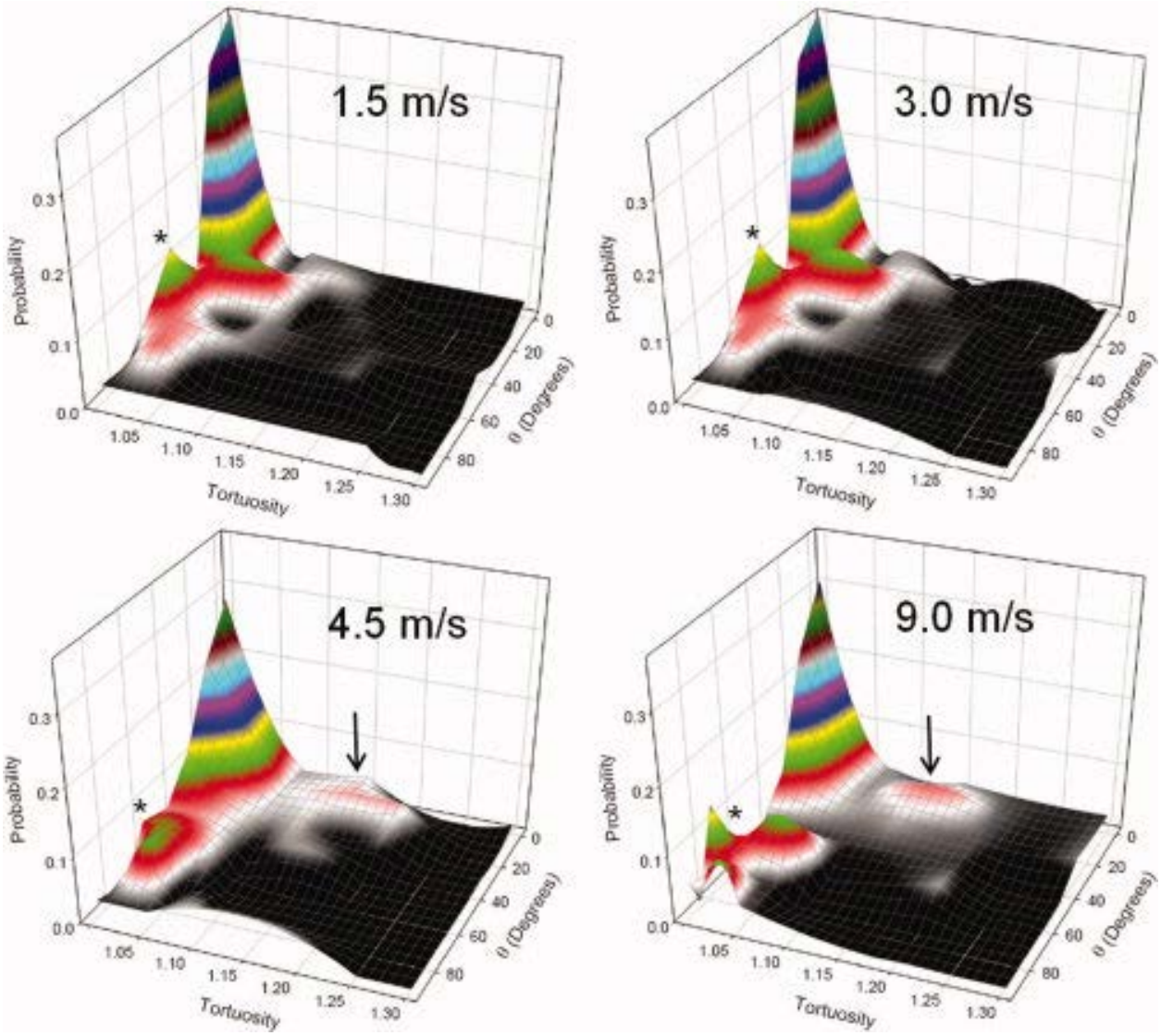

Figure 2-4. The complex relation between fiber tortuosity and its angle of orientation was observed to be a function of increased mandrel velocity.

2.2.3 Micro-structural response to biaxial deformation

As expected, the equibiaxial deformation states utilized in the current study resulted in no change in the orientation of the fiber population. A number of individual fibers were observed to rotate or change their direction of orientation, however, as a population these effects canceled such that no net change was observed. While the effects of equibiaxial deformation on fiber orientation were not surprising, the fiber tortuosity response proved to be rather interesting and complex. As equibiaxial deformation increased, fiber tortuosity was reduced in both the PD and XD but not extinguished completely (Figure 2-5). The PEUU fiber intersections appear to be quite secure and while allowing relatively free rotation about the point of intersection, fiber slippage or translation was inhibited, limiting fiber straightening and resulting in a residual level of tortuosity. The multi-scale deformation behavior for each specimen spin demonstrated that, as the scaffold was stretched to increasing levels, the computed stretch value ranges increased accordingly at each scale.

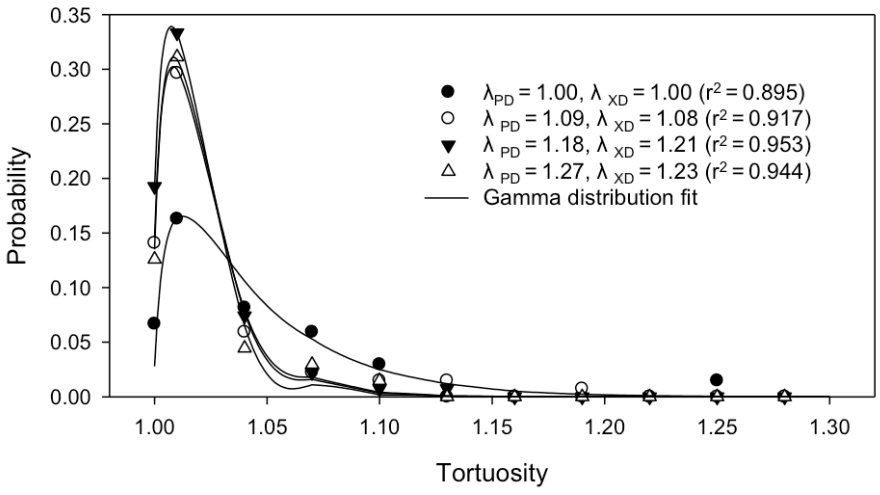

Figure 2-5. Tortuosity probability distribution of a representative specimen (9.0 m/s) shifts towards the left with scaffold deformation, indicating fiber straightening.

Presented is the mean and standard error (meso) or standard deviation (micro) values as a function of mean macro scale deformation for comparison (Figure 2-6). Raw values (open symbols) are also plotted to depict the true span of the observed deformation. When electrospun PEUU scaffolds are deformed, some discrepancies do arise between the defined scales as seen by data which diverges from unity (grey line). This is attributed to the complex, spatially variant structure which results from the electrospinning process at the micro scale. As the characteristic length is increased the measured deformation field becomes increasingly homogeneous such that a reasonably uniform response is observed at the macro scale (1-3 mm). As shown below, the superimposed line represents unity at the macro scale and data that falls along this line shows agreement between its respective scale and the macro deformation observed. The XD results show good agreement while the macro scale deformation in the PD underestimates the deformations seen at the meso and micro scales. Raw measured values are also presented to show the actual distribution of the data, so as to avoid any assumptions of their actual distribution.

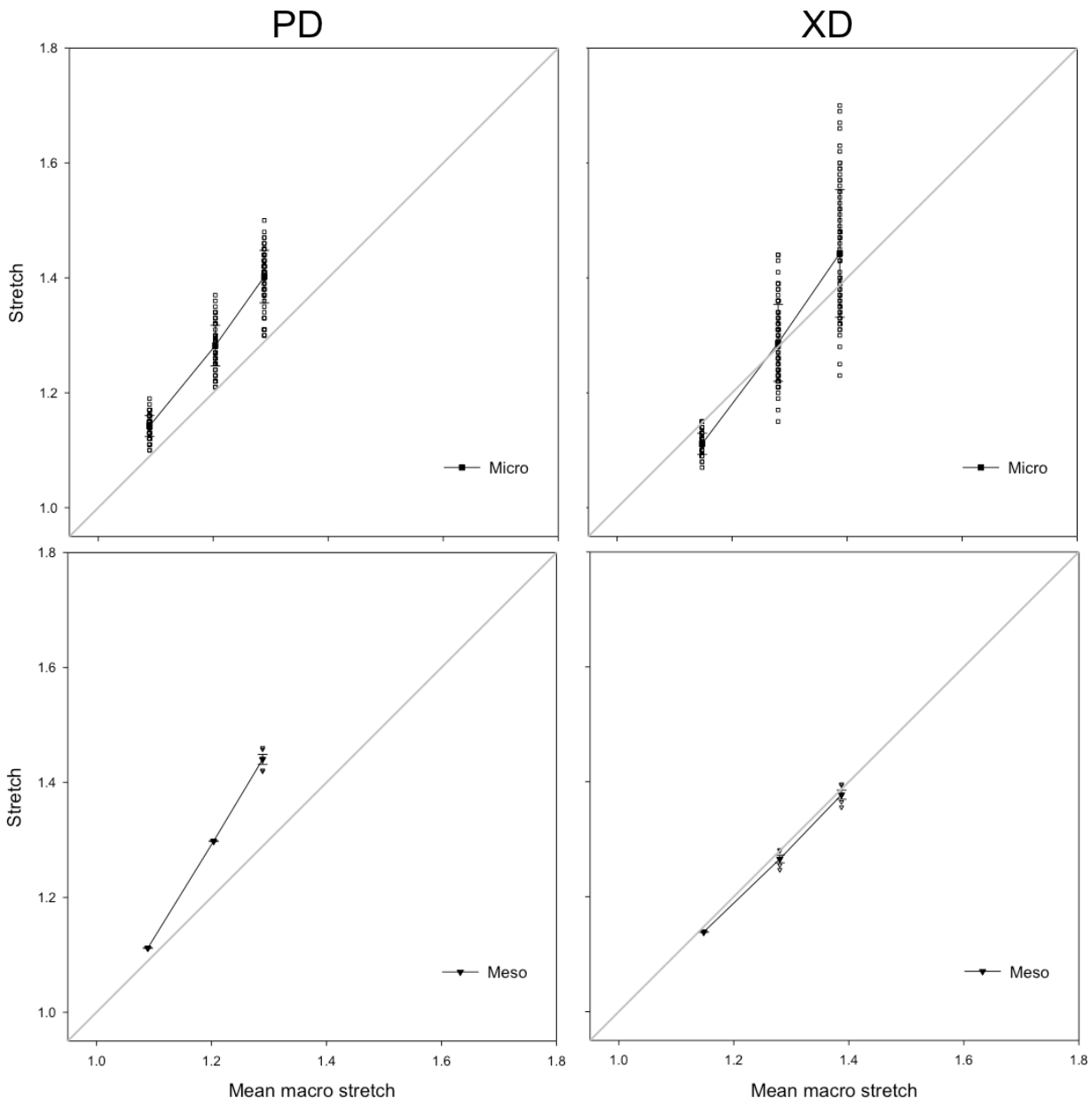

Figure 2-6. Observed multi-scale deformation behavior.

At the micro scale a very heterogeneous deformation response is observed throughout the image plane (Figure 2-7) with large changes in deformation. The firmly adhered fiber intersection points provide an ideal measure of micro-scale deformation. By tracking the displacement of these intersections between the reference and deformed configurations, the stretch in both the PD and XD were calculated via a single Lagrangian 9 node element (Figure 2-7, right panel). In short, the stretch values in each material axis (PD and XD respectively) are simply defined as the displacement gradient or strain plus 1. Note the heterogeneous deformation behavior exhibited at the micro scale. Warm colors denote large stretch values while cool colors denote regions of low stretch.

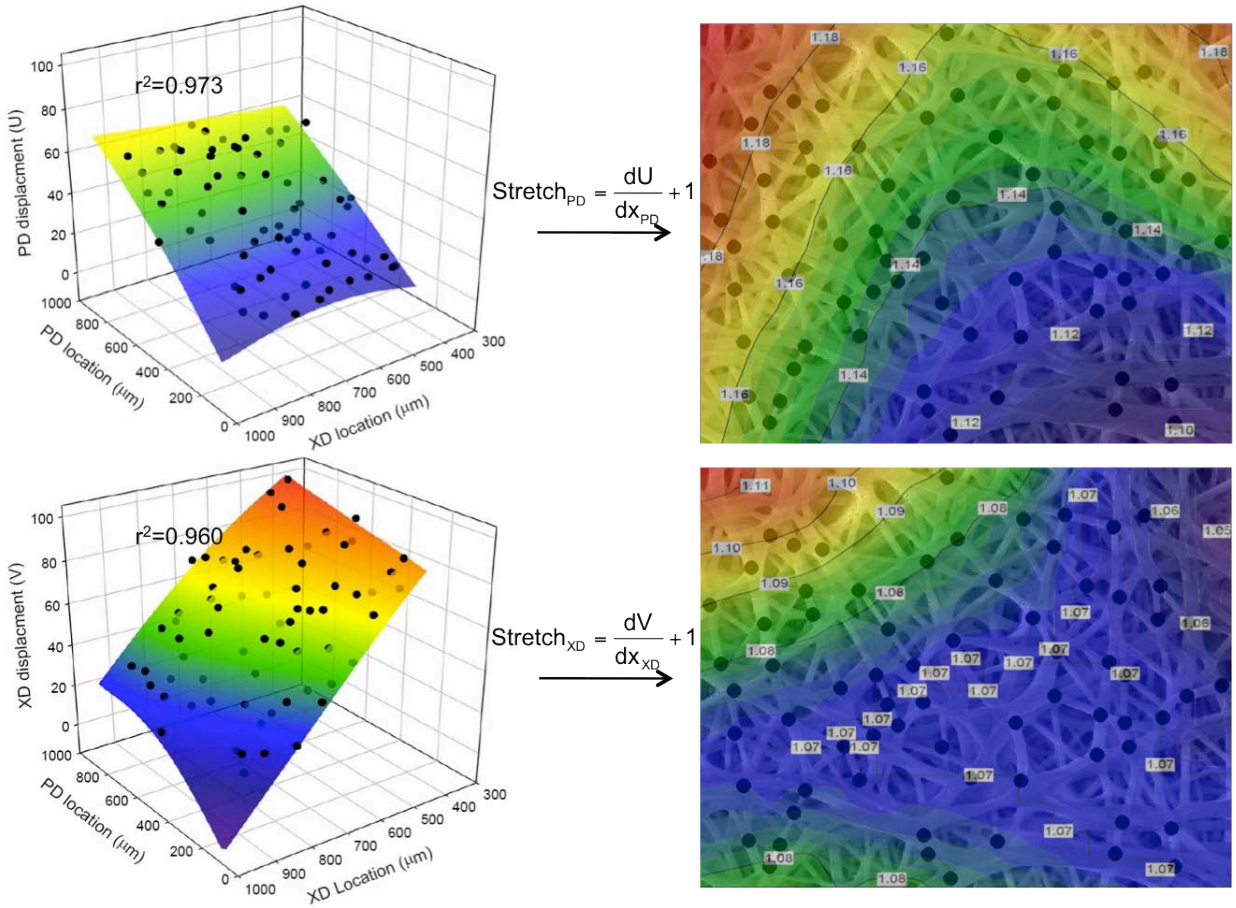

Figure 2-7. Heterogeneous deformation behavior exhibited at the micro scale in electrospun PEUU scaffolds.

At the meso scale, substantially less variation is observed in the deformation response but the interpolated ranges in deformation remain relatively large. It is not until the macro scale, on the order of 1000-3000 μm, that homogeneous deformation behavior was observed.

At the micro scale a very heterogeneous deformation response is observed throughout the image plane (Figure 2-5) with large changes in deformation. At the meso scale, substantially less variation is observed in the deformation response but the interpolated ranges in deformation remain relatively large. It is not until the macro scale, on the order of 1000-3000 μm, that homogeneous deformation behavior was observed.

In the unstrained state, a trend was observed wherein the PEUU fiber diameter decreased with increasing mandrel velocity during production. Furthermore, with increased deformation a monotonic decrease in PEUU fiber diameter was measured for all specimens indicating an incompressible (or nearly incompressible) material behavior. The fiber diameter underwent statistically significant decreases in diameter at each strain level for the specimens produced with 1.5 m/s and 4.5 m/s mandrel velocities.

2.3 DISCUSSION

2.3.1 Relevance to tissue engineering

Ideally, it would be possible to manufacture tissue surrogates from a scaffold precisely mimicking tissue mechanical function, containing viable cells or encourages cell migration from the host, and also serves to guide cellular processes and the arrangement of newly produced extracellular matrix. While this technology does not currently exist, electrospun PEUU scaffolds

provide a logical "next-step" from current fibrous scaffold technologies for tissue engineering such as needled non-woven biodegradable polymers [137, 181] or biopolymer scaffolds [116, 117, 123]. Needled non-woven scaffolds are limited in their abilities to emulate soft tissue tensile deformation behaviors since they cannot undergo fully recoverable large deformations. Biopolymer gels, while inherently exhibiting good cytocompatibility, may not functionally behave as long fiber composite materials as indicated in a recent study by Thomopoulous et al. [133] where they were unable to satisfactorily apply a structural continuum model [135, 136, 182]. This may also lend insight to their general lack of mechanical integrity rendering them unable to adequately mimic native tissues in a functional manner. Native valvular tissues on the other hand exhibit collagen fibers or fiber bundles spanning the leaflet which measure on the order of tens of mm. Electrospun scaffolds better emulate this hierarchical structural organization since the manufacturing process is basically a continuous extrusion of polymer.

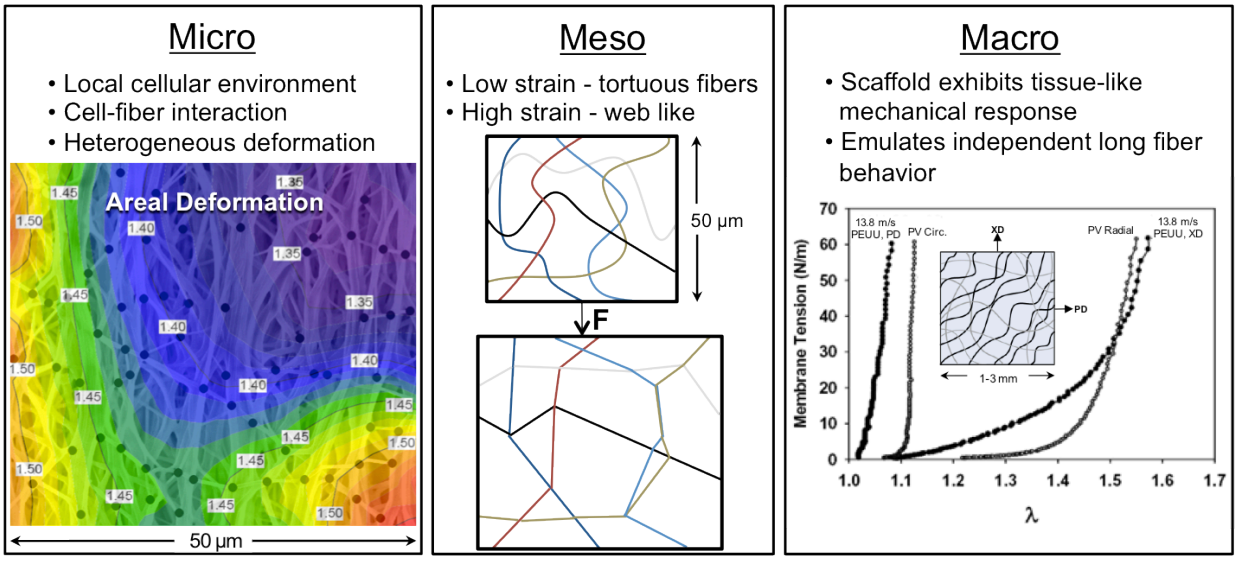

Figure 2-8. Despite exhibiting a tissue-like mechanical response at the macro scale, scaffold exhibits vastly different micro and meso mechanical behaviors.

The electrospun PEUU scaffolds investigated in this study exhibit complex, hierarchical architectures spanning multiple length scales (Figure 2-8). For instance, at the micro-scale a heterogeneous deformation response is observed. In addition, fibers in the unstrained configuration exhibit an undulated or tortuous morphology which transitions to a highly interconnected web-like architecture at finite strains. These structures combine to form a complex 3D scaffold with tunable tissue-level mechanical behavior that can be remarkably similar to the biaxial mechanical response of the native PV leaflet [61]. However, understanding the mechanisms by which these materials deform and behave under various loading conditions is not an elementary task. At the macro scale, the electrospun PEUU scaffold is capable of recapitulating the long, independently acting fiber response exhibited by the dense collagen network of the native PV (Figure 2-8 right panel). Moreover, recent modeling attempts originally developed for dense collagenous planar tissues proved quite successful in capturing the mechanical behavior of electrospun scaffolds under biaxial modes of deformation [61].

Yet, despite the success of these initial attempts, some of the assumptions made during the formulation of the model preclude it from accurately capturing the effects of microstructural characteristics [17, 61, 134, 135]. Namely, it was assumed that the scaffold could be idealized as a planar network of independently acting fibers with the fiber strain being computed from the tensorial transformation of the global strain tensor (the affine assumption). In the current and previous study [61], at the macro-scale the electrospun PEUU scaffolds deformed as long-fibrous networks. More importantly, the current study has shown that both fiber tortuosity and fiber orientation are dependent upon mandrel velocity. This result clearly indicates that fiber recruitment with strain would proceed in an angle associated manor necessitating model modifications to account for these structures related behaviors. This finding exemplifies the need

to elucidate micro-structural characteristics and their functional role at the macro scale in both native and synthetically derived matrices.

2.3.2 Multi-scale deformation behavior

Scale-dependent variations in deformation levels were observed (Figure 2-8). We attributed this behavior to the complex, spatially variant structure that results from the electrospinning process (Figures 2-6 and 2-8). It is anticipated that other regions throughout the specimen would behave in a unique manner dependent upon its local architecture at the micro scale. However, as the characteristic length is increased from the heterogeneous micro-structural scale to the macro scale, the scaffold deformation behavior becomes increasingly more homogeneous. Interestingly, it is at the macro scale (~1-3 mm) that the highly aligned electrospun PEUU behaves remarkably similar to native pulmonary valve tissue under biaxial testing regimes. This indicates that it may be possible to successfully emulate gross native tissue behavior without exactly replicating their highly complex micro-architectures.

2.3.3 Micro-scale fiber kinematics of electrospun PEUU and native collagenous tissues

In the present study, we have shown that the PEUU fibers undergo a recruitment process with deformation wherein the unstrained configuration, characterized by a population of tortuous fibers, transitions into a highly interconnected web-like architecture at finite deformation levels (Figure 2-8 center panel). Despite recapitulating the gross mechanical response, electrospun PEUU micro-structure and its resulting behaviors are different than the bi-modal crimp reduction and fiber compaction mechanisms observed in the native valve leaflet in response to increasing

transvalvular pressure [183]. Instead, the microstructure of the PEUU scaffold is largely mediated by firmly adhered fiber intersections and fiber straightening effects which can induce a different deformation response for encapsulated cells during scaffold deformation [75].

2.3.4 Effects of fiber morphology and kinematics on scaffold mechanical behavior

With increased mandrel velocity, increased levels of fiber alignment are obtained along with increased tortuosity. Increased mandrel velocity would be expected to shift the fibers towards the preferred direction, as observed. However, it was also observed that fibers oriented in the preferred direction exhibited increased tortuosity. Hypothetically, the spinning mandrel would pull on the newly polymerized fibers as they are deposited. This is a counterintuitive phenomenon as one might anticipate tortuosity to be decreased in the preferred direction as a result of the potential for increased fiber tension as the mandrel spins.

From a functional standpoint, this phenomenon may contribute to the highly non-linear anisotropic behavior exhibited during biaxial deformation. Specifically, the presence of fibers with varying tortuosity indicates an intricate directionally dependent fiber recruitment process during deformation. When the biaxial mechanical response (equi-tension, previously presented by Courtney et al. [61]) in the PD and XD are normalized we see little difference in the shapes of the PD behavior with increased spin speed while the XD shows a trend to become more concave or non-linear (Figure 2-9). With increased mandrel velocity we see an increased density of fibers about the PD with a range of tortuosity levels that results in little change in the PD response. Fiber tortuosity, though not ubiquitous in electrospinning literature, can visually be observed when segmented polyurethane materials are used [184, 185]. The true mechanism for the production of tortuous fibers, though interesting, is beyond the scope of the current study but

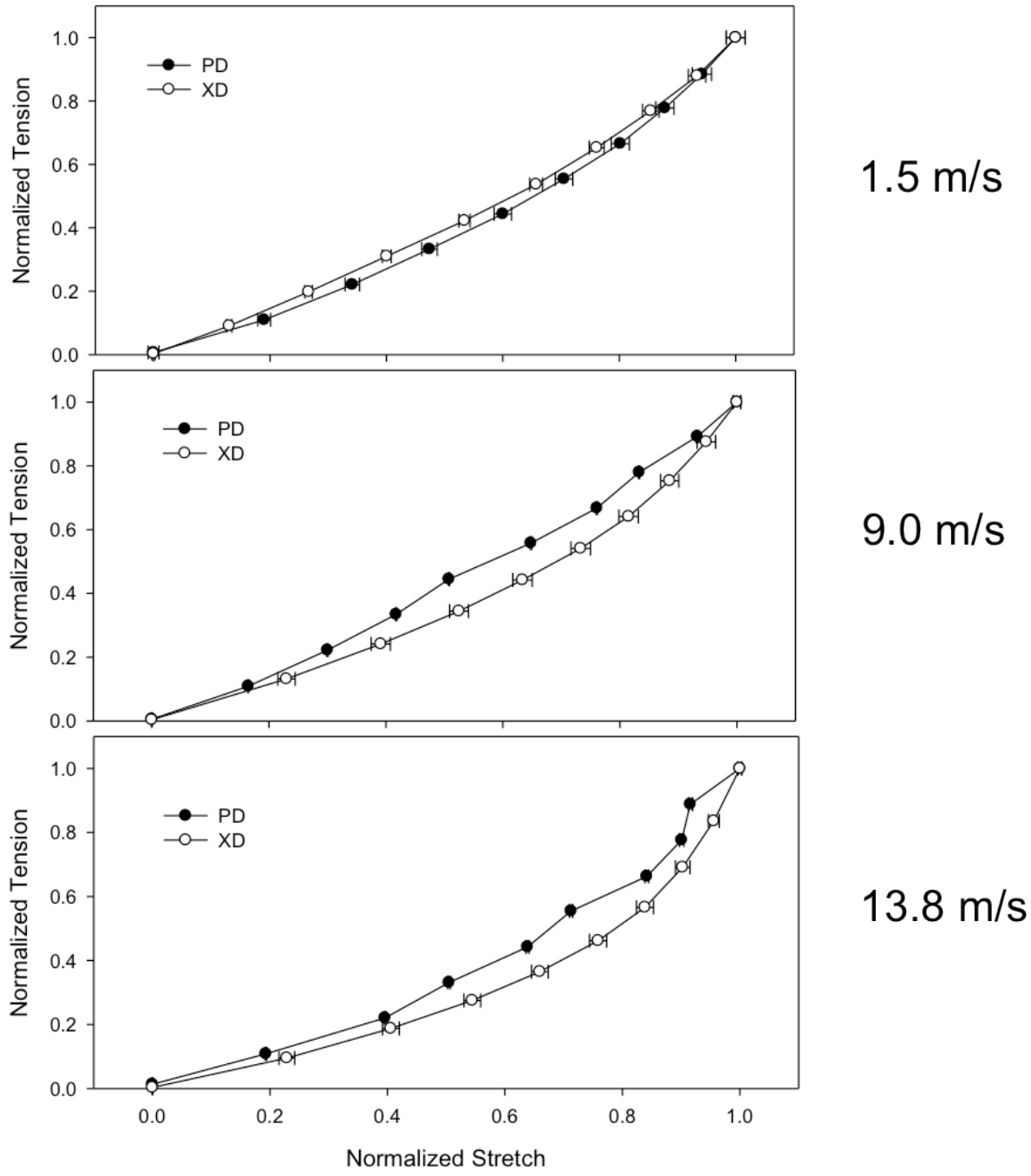

Figure 2-9. By normalizing the PD and XD equi-biaxial tension behavior (adapted from Courtney et al. [61]), the characteristic shape of the curves can be directly compared.

may be a result of a "whipping" instability in the polymer jet during deposition causing the jet to bend and stretch [186-188].

The anisotropic behavior of native valve leaflets has been shown to be a result of rotational fiber kinematics under biaxial modes of deformation [16, 17]. In addition, electrospun PEUU constructs have been shown to follow affine fiber transformations from a global perspective and can be described in a manner similar to collagenous scaffolds[76]. Interestingly, some fibers were observed to rotate or change their direction of orientation during deformation while as a population, no net change was measured. This is likely an additional manifestation of the local heterogeneity that exists at the micro scale. Though the affine transformation was valid in at the macro scale, it is likely that PEUU fiber translation is limited by the presence of secure interconnections between fibers. Johnson et al. presented a similar hypothesis for reduced fiber mobility in electrospun polymers exhibiting "point bonding" [77]. In short, polymer sintering was utilized on electrospun poly (ε-caprolatone) scaffold to invoke definite point bonds between fibers. Therefore, the presence of increasingly tortuous fibers in the XD and their recruitment with scaffold strain many work in conjunction with fiber kinematics to produce the anisotropic biaxial mechanical behavior that so closely mimics native leaflet tissue. Attempting to delineate the individual contributions of fiber tortuosity and kinematics to the constructs mechanical behavior would be quite cumbersome and better lends itself to the development of a numerical framework to explore this unique, interrelated phenomenon.

2.4 LIMITATIONS

It should be noted that the current study was limited to the investigation of one specimen per spin speed. However, we have shown that scaffold structure is well preserved across the entire specimen or from multiple specimens produced from a single production batch. For example, Courtney et al. [61] showed that fiber splay quantified from several regions across the specimen show very close agreement. Furthermore, there is close agreement between structural characterization (fiber splay) of both the specimen surface facing the mandrel and the exposed surface. Biaxial mechanical characterization of multiple constructs at each of the mandrel velocities investigated here showed close agreement owing to consistent architectures.

In the current study, it has been shown that the measured θ-T-P(θ,T) profiles for the 1.5 m/s and 3.0 m/s constructs, which exhibit comparable effective fiber properties, were very similar upon visual inspection. As such, we are confident that any inter-specimen variation that may exist is beyond our ability to measure and thus would have inconsequential effects on scaffold kinematics and mechanical behavior. In a similar light, it is difficult to speculate what affects the inclusion of specimens from successive batches of scaffolds produced under the same or similar manufacturing conditions may have on our results. Although the electrospinning process is done in a controlled manner, it is not an exact process but relies heavily on a multitude of manufacturing parameters working in unison to produce a given scaffold.

3.0 TISSUE TO CELLULAR LEVEL DEFORMATION COUPLING

In engineered tissues we are challenged to reproduce extracellular matrix and cellular deformation coupling that occurs within native tissues, which is a meso-micro scale phenomenon that profoundly affects tissue growth and remodeling. With our ability to electrospin polymer fiber scaffolds while simultaneously electrospraying viable cells, we are provided with a unique platform to investigate cellular deformations within a three dimensional elastomeric fibrous scaffold. In this chapter, we will investigate the response of scaffold specimens micro-integrated with vascular smooth muscle cells (VSMC) and subjected to controlled biaxial stretch with 3D cellular deformations and local fiber micro-architecture simultaneously quantified. Obtaining a baseline for how rat VSMC cells experience and response to their environment has fundamental implications when attempting to elucidate the events of de-novo tissue development and remodeling in engineered tissues.

3.1 METHODS

3.1.1 Specimen fabrication and preparation

For a detailed account of the concurrent electrospraying and electrospinning process, the interested reader is referred to the previous work of Stankus et al.[65, 145, 189]. Briefly, the electrospinning process produces continuous fiber scaffolds exhibiting a wide range of mechanical properties while providing a suitable environment for cell proliferation and growth [62, 63, 73, 145-147]. Electrospinning involves the deposition of a solubilized polymer across a large voltage gradient onto a collection surface, with the polymer solution delivered via a small capillary tube where the applied electric potential induces a charge accumulation on the surface of the expelled polymer (Figure. 3-1a). O nce electrostatic forces exceed viscoelastic forces within the polymer solution and surface tension, a fine jet is ejected towards the collection surface while being accompanied by rapid solvent evaporation. The result is a mat of continuous polymer fibers that, depending upon the processing parameters and polymer utilized, can exhibit mechanical behavior very similar to native soft collagenous tissues [61, 62].

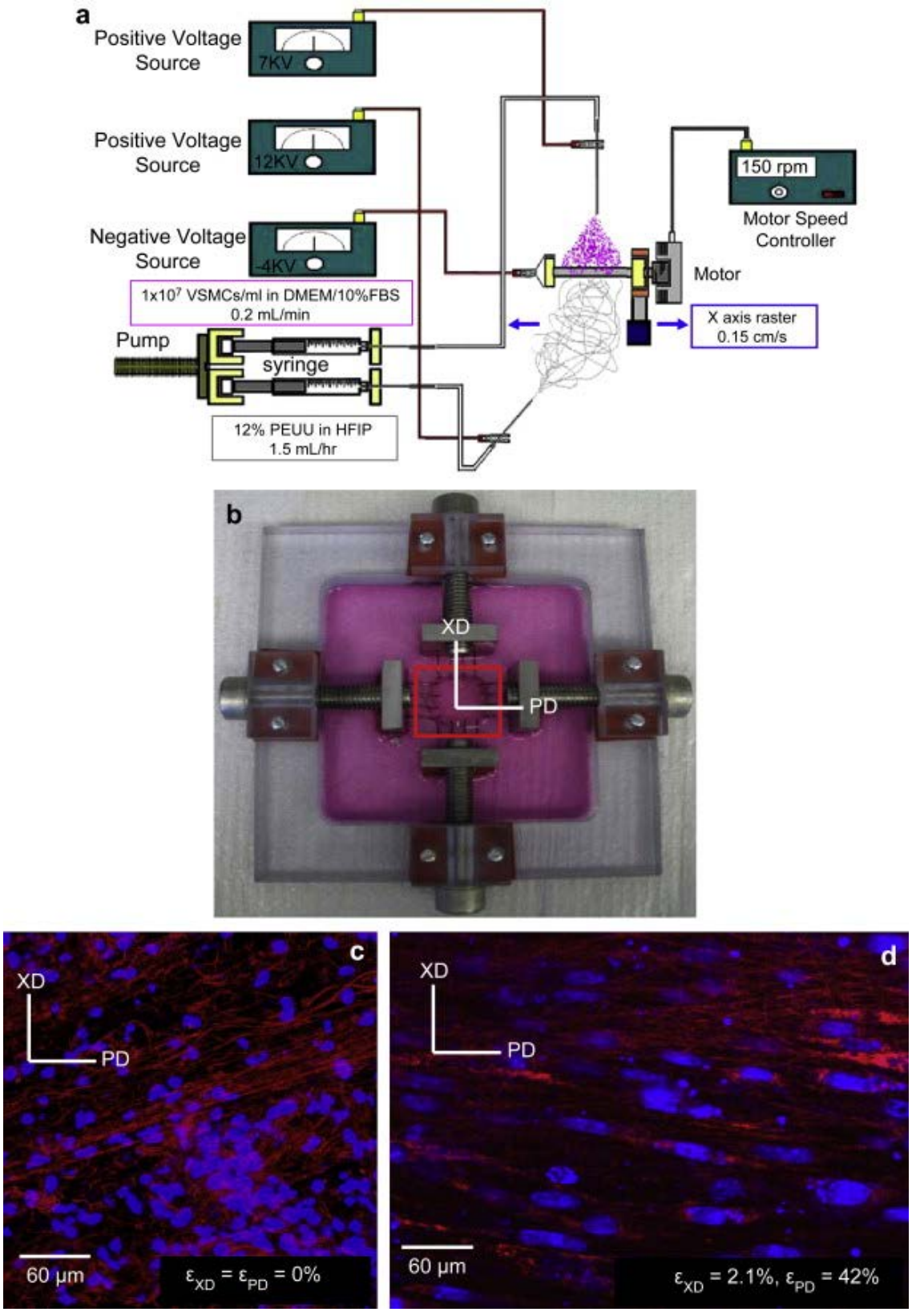

Figure 3-1. Fabrication and imaging under biaxial stretch of cell integrated elastomeric scaffolds.

For the current study, electrospraying of rat VSMCs was accomplished by feeding $1x10^7$ cells/ml into a sterilized capillary charged at 7 kV and located 4 cm from the target mandrel (4.7 mm diameter) concurrent with PEUU/1,1,1,3,3,3-hexafluoroisopropanol solution (12 wt%) deposition from a capillary charged at 12 kV and located 20 cm from the target mandrel (Figure. 3-1a). The mandrel was charged at -4 kV and was rotated at 150 rpm while translating 8 cm along the z-axis at 0.15 c m/s. A fter 30 m in of electrospinning and electrospraying, the microintegrated tube was removed from the mandrel and cultured in a spinner flask at a rotation rate of 15 rpm for 24-48 h prior to imaging. With the capability of simultaneously distinguishing living VSMC nuclei stained with DRAQ5 and PEUU fibers below the specimen surface, an inverted Laser Scanning Confocal Microscope (LSCM, Olympus Fluoview 1000) was chosen (Figure 3-1c-d).

3.1.2 Biaxial stretch device and testing

Biaxial modes of deformation are well known to better approximate physiological deformations of planar anisotropic tissues [175]. Moreover, we were interested how the scaffold fibers stretch under biaxial deformations without the confounding effects of simultaneous fiber rotations [76]. A biaxial stretcher was thus custom designed for use with an inverted laser scanning confocal microscope (LSCM, Olympus Fluoview 1000). The biaxial stretcher consisted of a polycarbonate specimen chamber with two pairs of orthogonally positioned lead screws (Figure. 3-1b). Two loops of 5-0 polyester suture of equal length were attached from the lead screws to each side of the specimens with four custom-made stainless steel hooks. Subsurface specimen imaging was facilitated by a glass cover slip (Electron Microscopy Sciences Hatfield, PA, USA) mounted to the stretching device spanning a 30 mm diameter opening in the chamber beneath the

specimen. This system was capable of applying both strip biaxial and equibiaxial stretch regimes. Strip biaxial stretch refers to a special loading regime wherein the stretch along one axis is increased while the orthogonal axis is constrained such that no deformation occurs. Conversely, equibiaxial deformation is defined as an equal level of stretch in the two orthogonal specimen directions.

3.1.3 Confocal imaging

An inverted Laser Scanning Confocal Microscope (LSCM) was chosen to observe living cells and scaffold in situ, with images taken via a coverslip window below the specimen. Just prior to imaging, specimens measuring 12 mm square were stained with DRAQ5 for 30 minutes, a far red-fluorescing DNA probe for viable cells. DRAQ5 has been demonstrated not to be toxic to cells with nuclear DNA staining being stable up to 4 h [190]. Moreover, DRAQ5 proved to be DNA staining specific in our experiments allowing us to image live cells concurrently with the auto-fluorescing PEUU fibers. Cell nuclear images were taken under CY5 channel and the scaffold was imaged under CY3 channel via polymer autofluorescence. For each strain level, randomly selected regions were imaged at a subsurface depth ranging from approximately 15-75 μm. For three specimens, 25-86 image stacks were obtained with section thicknesses of 0.972 μm - 2.831 μm with image intervals ranging from 0.6 μm - 0.8 μm, producing a net thickness of 17.4 to 68.0 μm. This imaging approach produced good quality representations of both the nuclei and fibers under stretch (Figures. 3-1c,d).

3.1.4 Cellular deformations and scaffold stretch protocols

Nuclear aspect ratio (NAR) has been used as a measure of overall cellular deformation in native tissues (see discussion) [183, 191-193]. For example, aortic heart valve tissues are populated with valvular interstitial myofibroblast cells (AVIC) that serve to maintain the valve leaflet extracellular matrix (ECM) [9, 194]. We have shown [183] that AVICs undergo very large deformations with changes in NAR from 1.8 in the unloaded state to 5.0 under full transvalvular pressure, which is likely related to their biosynthetic function (Figure. 3-2a). Thus, to quantify the 3D geometry of the living micro-integrated cell nuclei within the scaffolds, complete LSCM image stacks spanning 15-75 μm were obtained for specimens in the reference and deformed configurations (n=3). From the image stacks we reconstructed the complete 3D VSMC nuclear surface and observed the cell nuclei consistently exhibited a s calene ellipsoidal geometry (Figure. 3-2b). Amira (Mercury Computer Systems, Inc., Carlsbad, CA, USA) was used to stack the registered images and segment cell nuclei manually. Next, MATLAB (The MathWorks, Inc., Natick, MA, USA) was employed to perform principle component analysis (PCA) on t he segmented cell nuclei. The full 3D nuclear orientation was computed using principle component analysis of the reconstructed nuclear surface by determining the angles of the three principle nuclear directions with respect to the specimen coordinate axes (α, β, and γ respectively (Figure. 3-2c). Cell nuclei aspect ratios of 2D images were quantified using the commercial software Sigma Scan Pro (SPSS Inc., Chicago, IL, USA). For each strain state, the NAR for 80 cells were analyzed with data being presented as AVG ± SEM.

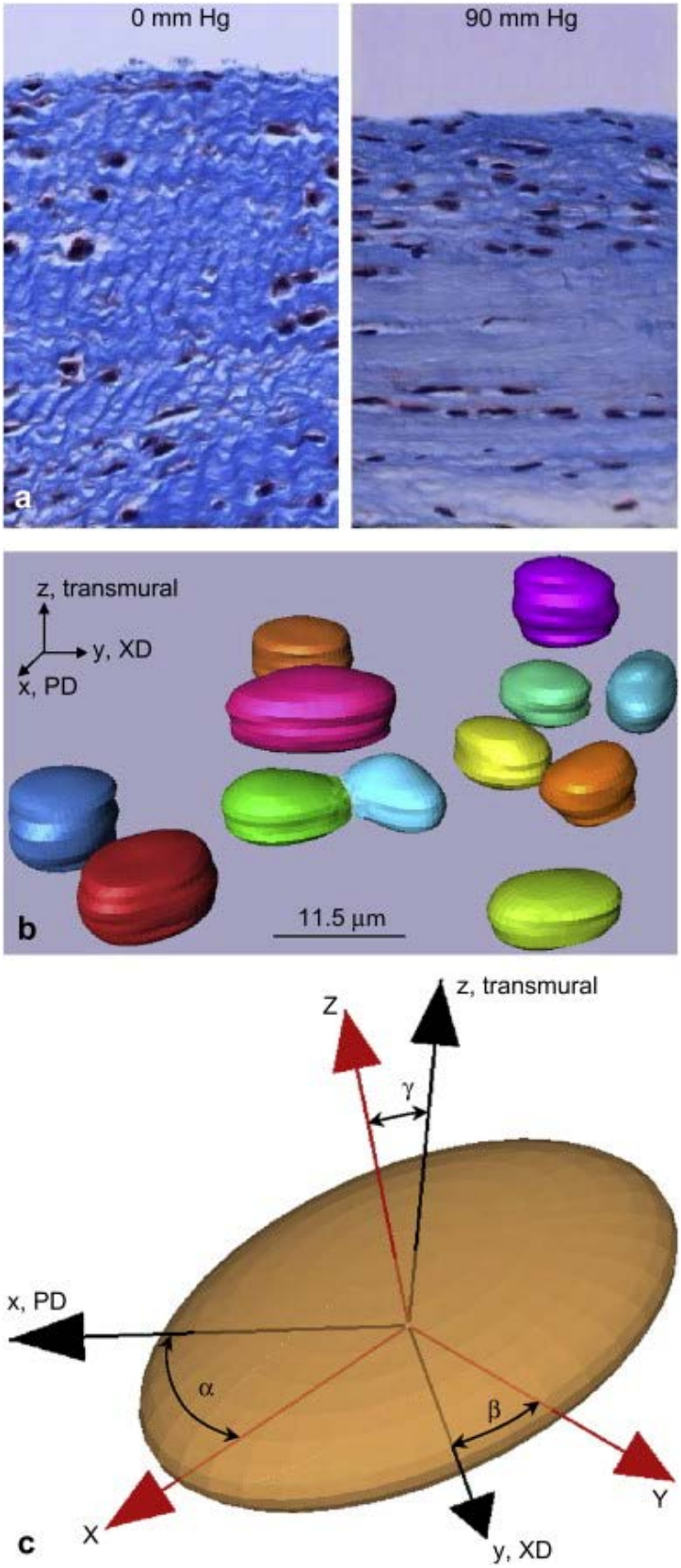

Figure 3-2. Nuclear aspect ratio deformation and orientation.

As in our previous work with soft tissues [76, 176], we utilized equi-biaxial deformation states (i.e. were the specimen is loaded such that the axial strains, ε_{PD} and ε_{XD}, remain equal), to allow extensional strains without fiber rotations. This was accomplished with both the scaffold fibers imaged by LSCM and also by scanning electron microscopy (SEM) to provide additional detail. Next, in order to induce the largest changes in fiber stretch and rotation, as well as cellular deformations, "strip" biaxial strain states were chosen wherein extensional strain is applied in one direction while the strain the other direction is held at zero. Specific deformation levels utilized included the unloaded configuration followed by states of increasing strip biaxial strain ranging from 5% to 102%, and equi-biaxial strain states of 10% to 50% in 10% increments (n=15 total).

3.1.5 TEM cellular imaging

To verify that NAR could be used as an index of cellular deformations using micro-integrated VSMCs, transmission electron microscopy (TEM) was used to compare and quantify the geometries of the VSMC membrane and nucleus. Due to the polymeric nature of the cell integrated scaffolds it was not possible to fix specimens in their deformed states. As a result, it was only possible to image cells in a free floating configuration. Cell-scaffold construct sections were cut parallel to the preferred and cross-preferred fiber directions for imaging. In total, 22 cells were imaged in the preferred direction while 10 were imaged in the cross-preferred direction. The major and minor axis lengths were then measured manually with the image analysis software Sigma Scan Pro (Systat Software, Inc., San Jose, CA USA). NAR and cell

membrane aspect ratios of cells in unstrained PEUU scaffolds were not observed to be significantly different in either the PD or XD directions ($p_{PD} = 0.745$ and $p_{XD} = 0.213$).

3.1.6 Scaffold fiber kinematical analysis

Fiber orientation was also quantified from the LSCM images (Figure. 3-1c,d) using custom image analysis software in the unstrained and deformed configurations. Methods for this custom image analysis software have been previously presented in detail [61, 195, 196]. Essentially, the software directly produces statistical distributions of fiber orientation probability, R(θ), from all measured fibers over the range of all possible orientations, $-90° \leq \theta \leq 90°$. Next, to gain a better understanding of how the electrospun PEUU fibers deform as a function of macroscopic scaffold strain, we utilized an affine fiber deformation transformation model to evaluate if the electrospun PEUU followed this model, as we have done for collagenous scaffolds [76].

Key to the assumption of affine deformations is the relation $d\mathbf{x} = \mathbf{F}(\mathbf{X},t)d\mathbf{X}$, where **F** is the deformation gradient tensor mapping the undeformed material line element d**X** to the corresponding deformed configuration d**x** at time t. To determine how an orientation deformation function (ODF) transforms under the affine transformation, we follow Dalafias [197] by considering a spherical region of constant radius $|d\mathbf{X}| = 1$. Such a sphere will transform to the Eulerian Stretch Ellipsoid (ESE) of variable radius $|d\mathbf{x}| =$, with semi-axes equal to the principal stretches. We assume that the deformation within the ESE is homogenous so that $d\mathbf{x} = \mathbf{F}\,d\mathbf{X}$. Next, consider a material stereo angle element, $d\Delta_0$, in the reference configuration with its apex at **X** and axis d**X**. It will be transformed to apex at x and axis dx after the deformation with stereo angle $d\Delta_t$. As in our previous studies [76, 176], we will assume that the

number of fibers is conserved. If ξ represents the total number of fibers and R_0 and R_t are the ODF before and after deformation, then $\xi\, R_0\, d\Delta_0 = \xi\, R_t\, d\Delta_t$. Thus, $R_t/R_0 = d\Delta_t/d\Delta_0$ and we have to thus determine the expression for $d\Delta_t/d\Delta_0$. We note that $\xi = \int_{\Delta_0} \xi R_0 d\Delta_0 = \int_{\Delta_1} \xi R_1 d\Delta_1$, so that $\int_{\Delta_0} R_0 d\Delta_0 = \int_{\Delta_1} R_1 d\Delta_1 = 1$, and if R_0 is constant (i.e. an isotropic ODF) then $R_0 = 1/4\pi$. Next, note that the measure of the stereo angle element $d\Delta_0$ in spherical radians is given by obtained by an area vector element $d\mathbf{A}$ capping $d\Delta_0$ onto dX divided by $|dX|^2$. This projection is obtained using $\frac{d\mathbf{A}\, d\mathbf{X}}{|d\mathbf{X}|}$. Thus,

$$d\Delta_0 = \frac{d\mathbf{A}\, d\mathbf{X}}{|d\mathbf{X}|^3},\ d\Delta_t = \frac{d\mathbf{a}\, d\mathbf{x}}{|d\mathbf{x}|^3} \qquad \text{EQ. 3-1}$$

Next, according to Nanson's relation $d\mathbf{a} = J\mathbf{F}^{-T} d\mathbf{A}$ with J = det(**F**), it can be shown that $d\mathbf{a} \cdot d\mathbf{x} = J\mathbf{F}^{-T} d\mathbf{A} = J\, d\mathbf{A}\, d\mathbf{X}$. Thus, the final relation is

$$\frac{R_t}{R_0} = \frac{\lambda^3}{J} \qquad \text{EQ. 3-2}$$

where λ is the fiber stretch along d**X** and J accounts for volumetric changes. Similarly, if we consider a two-dimensional (i.e. planar) problem, we have

$$\frac{R_t}{R_0} = \frac{\lambda_{2d}^2}{J_{2d}} \qquad \text{EQ. 3-3}$$

Noting that $\lambda_{2d}^2 = \mathbf{N} \cdot \mathbf{C}_{2d} \cdot \mathbf{N}$, we have

$$\frac{R_t}{R_0} = \frac{\mathbf{N} \cdot \mathbf{C}_{2d} \cdot \mathbf{N}}{J_{2d}} \qquad \text{EQ. 3-4}$$

3.2 RESULTS

3.2.1 Fiber kinematics

Comparison of both the LSCM and SEM imaging modes demonstrated the LSCM provided comparable levels of detail, and at least sufficient fiber density to obtain accurate orientation information (Figures. 3-3a,b). Upon stretch, a substantial increase in fiber local straightening was observed with increased equi-biaxial stretch (Figures. 3-3c,d). Interestingly, at high strain levels there was an upper bound of fiber alignment observed, corresponding to a transition from an ensemble of tortuous fibers seen in the non-deformed specimen to a web-like architecture as manifested by a scaffold with straight, interconnected fibers. Thus, electrospun PEUU fibers do not completely loose their tortuosity with strain, and appear to be bonded together. Next, fiber orientation distributions indicated that when unloaded, the fiber network returned immediately back to its original orientation (Figure. 3-4a), clearly indicating the elastic nature of the scaffold. Moreover, when strained equi-biaxially by various levels, no detectable change in orientation occurred, as predicted by affine fiber kinematics. (Figure 3-4b).

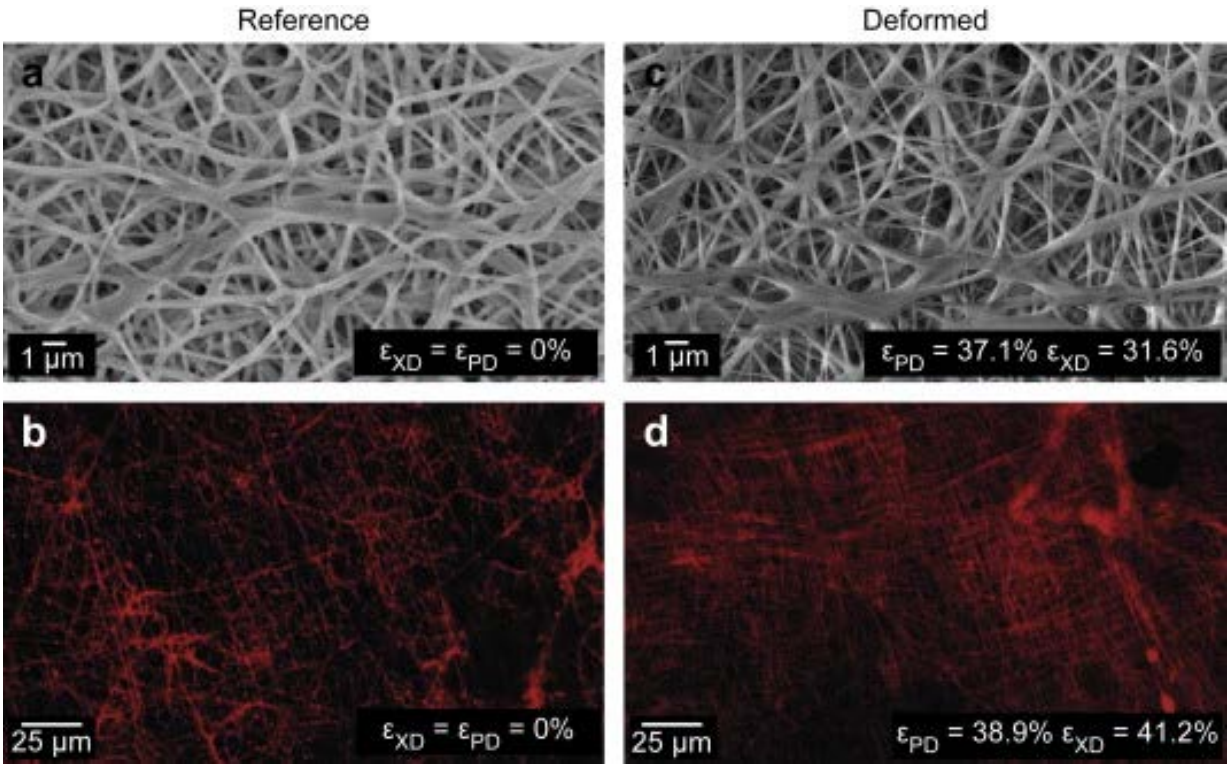

Figure 3-3. Changes in electrospun PEUU fiber microarchitecture under biaxial stretch.

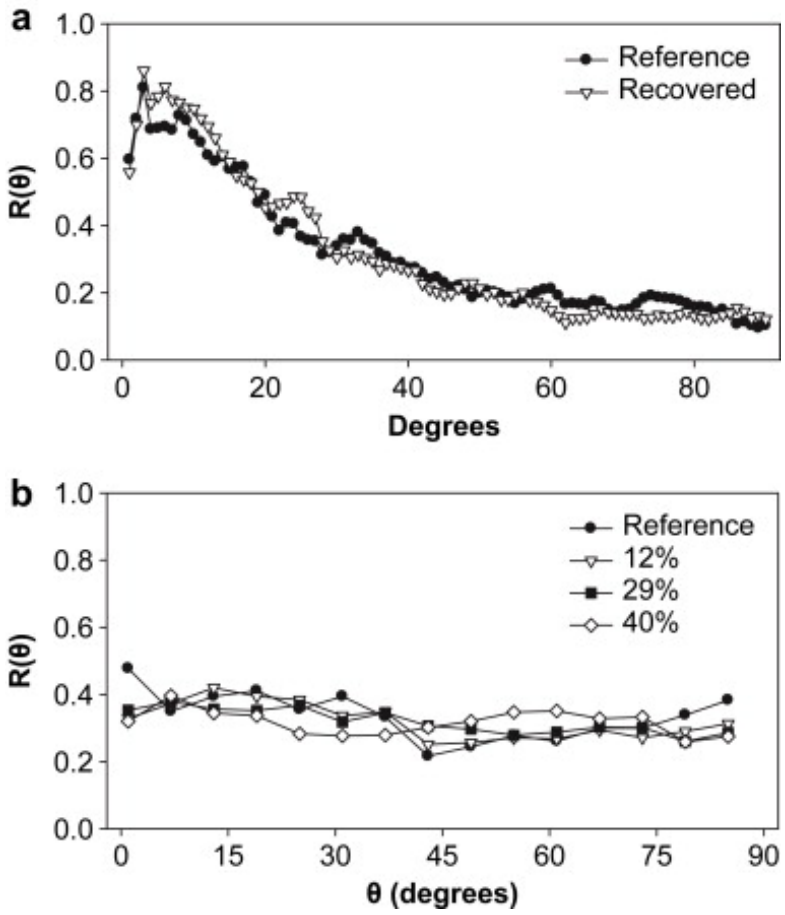

Figure 3-4. Observed affine fiber kinematics.

In further exploration of the changes in fiber orientation in the strip biaxial strain tests, the fiber orientation distribution R(θ) was observed to become more random with increasing strain (Figure 3-5a). This result was consistent with the fiber network deforming orthogonally from its preferred direction. Next, we assessed whether the electrospun PEUU fibers deform according to an affine rules (EQ 1-1 to 1-3) in non-equibiaxial strain states. Interestingly, at both low (Figure. 3-5b) and high (Figure. 3-5c) strain levels the affine rule predicted good agreement with the experimental data. Thus, due to their high inter-connectivity (e.g. Figure. 3-3) the fibers in an average sense deform in accordance to the bulk strain field.

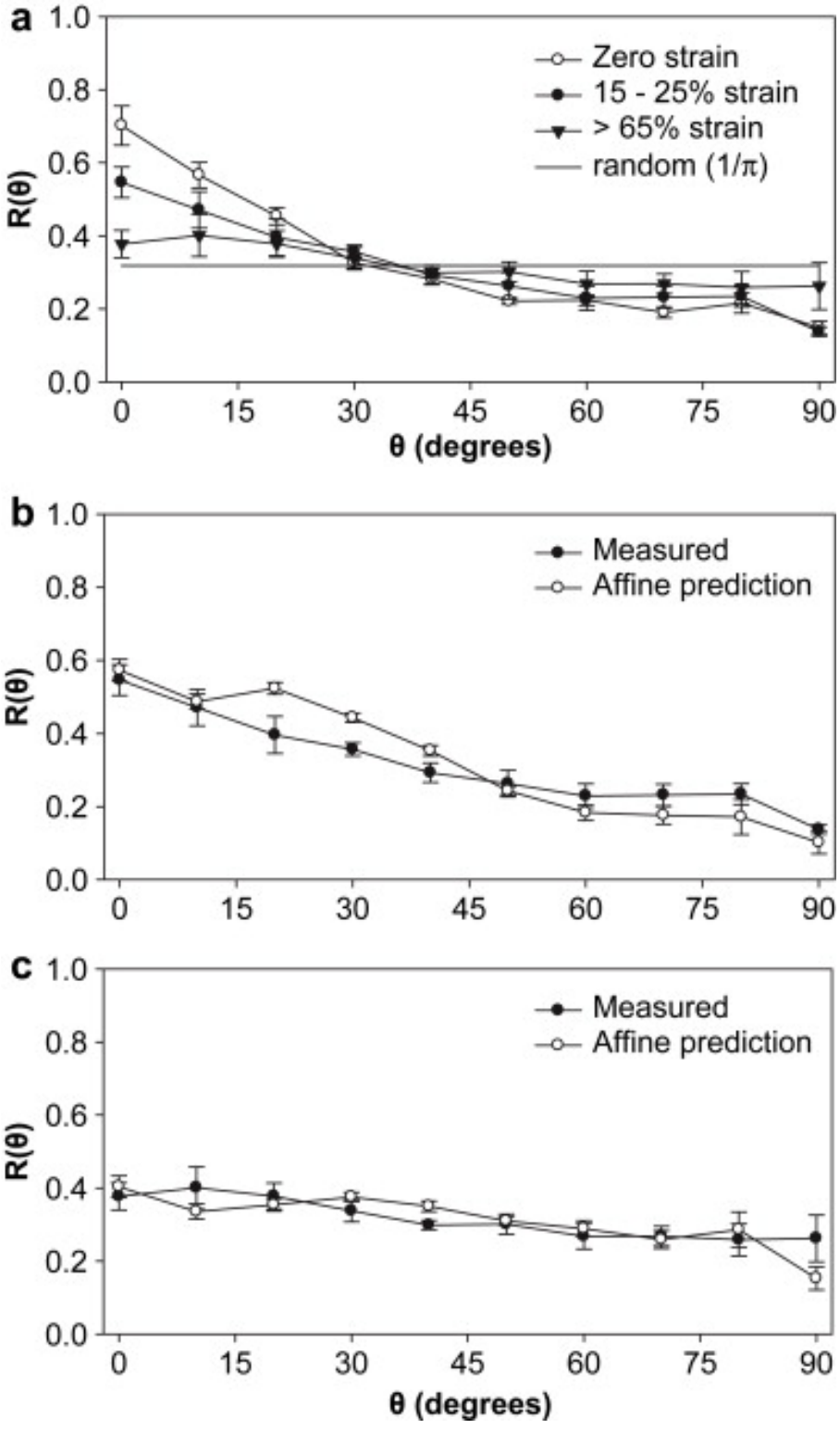

Figure 3-5. Electrospun PEUU fiber architecture responds to strain in an affine sense.

3.2.2 3D cellular deformations and the relation to local fiber kinematics

From the 3D cellular nuclei reconstructions, we noted that for all measured cells (n = 20) the angle γ, which defined the out-of-plane orientation of the nucleus (Figure 3-2c), was 5.92 ± 1.57° in the unloaded configuration. This indicated that the micro-integrated cells were aligned mainly in the plane of the scaffold. Moreover, under increasing strip biaxial deformation the major principle direction rotated in the direction of deformation (Figure 3-6), suggesting substantial mobility with strain.

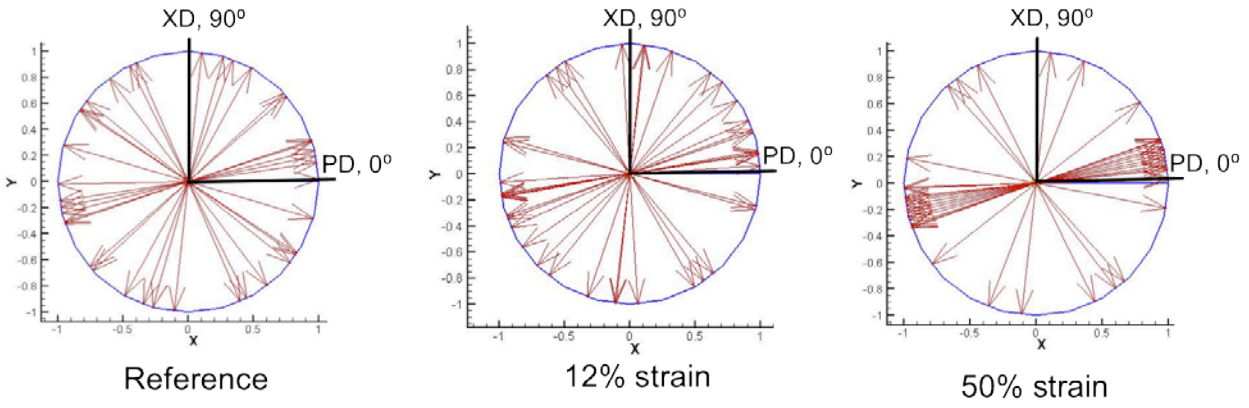

Figure 3-6. Micro-integrated cell rotations during deformation.

Next, we examined the interrelationship between the micro-integrated cellular deformations and the changes in scaffolds fibrous structure. This was facilitated by simplifying imaging and analysis to use single section imaging sets to allow for multiple states of deformation to be obtained with same specimen while maintaining cellular viability, which did not result in measureable information loss. No dependency was observed in the NAR-strain relationship for changes in the sequence of deformation, indicating that the cellular-scaffold deformations were largely elastic in nature. We noted in particular that, under strip biaxial

stretch, cells micro-integrated into electrospun PEUU scaffolds exhibited a rapid increase in NAR until approximately 60% strain (Figure 3-7a). At strain levels higher than 60%, a plateau in NAR was observed (Figure 3-7a). Moreover, this behavior did not depend upon the direction of strip biaxial stretch (PD vs. XD stretch). Interestingly, the cessation in NAR change with strain corresponded closely with complete straightening of the local fibrous structure (Figure 3-3). *This result suggested local fiber straightening, as opposed to macro-tissue level deformations, was the dominant mechanism for inducing cellular deformations.* It should be also noted that this behavior is in stark contrast to that observed in the native tissues, wherein aortic VIC nuclear deformations undergo relatively little change at low transvalvular pressures (i.e. low tissue stresses), while high transvalvular pressures (i.e. high tissue stresses) are dominated by fiber compaction effects (Figure 3-7b).

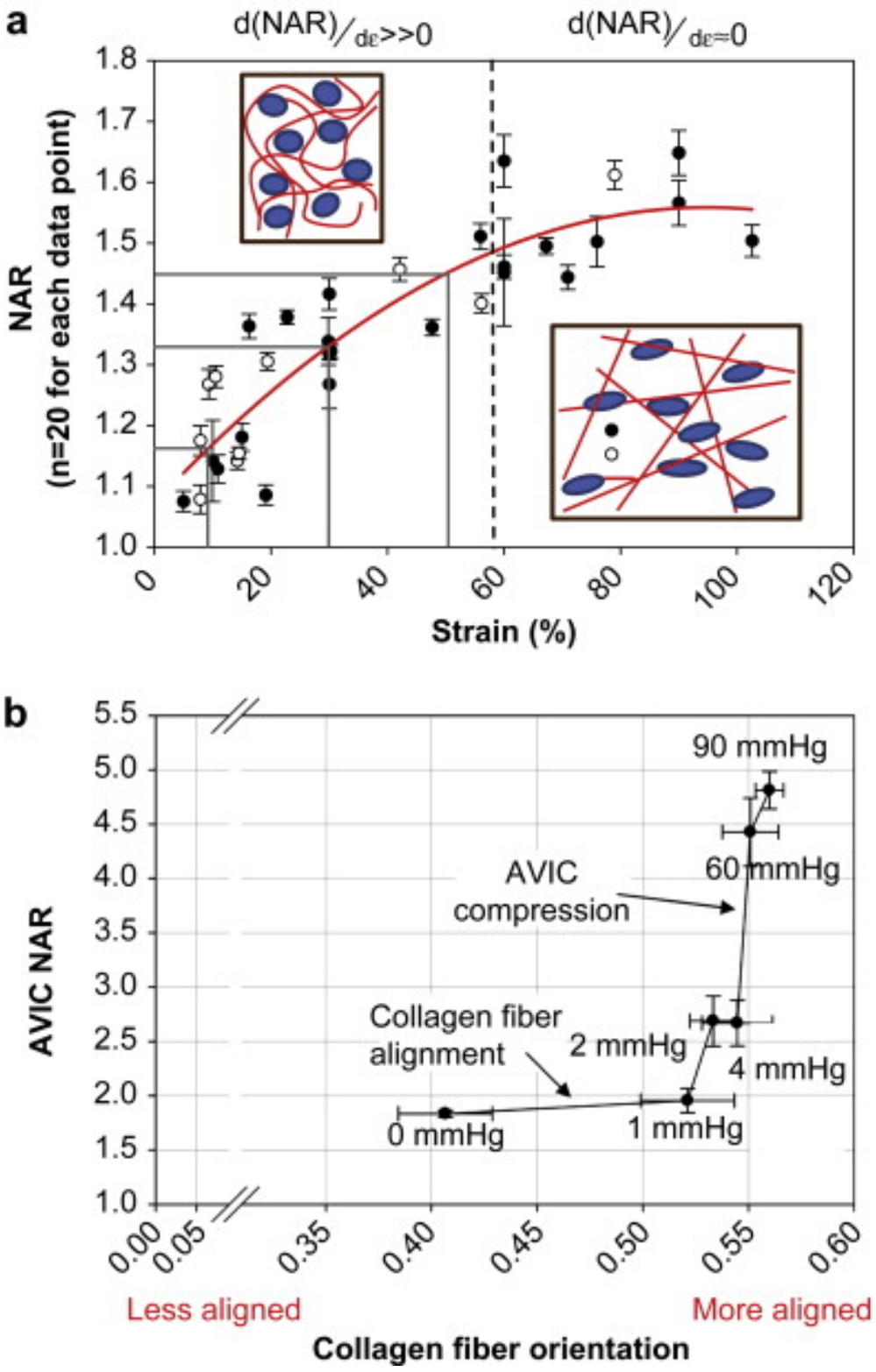

Figure 3-7. NAR change with deformation is closely related to local fiber microarchitecture.

3.3 DISCUSSION

3.3.1 Choice of scaffold in the study of cellular deformations in engineered tissues

Electrospinning produces continuous fiber scaffolds exhibiting a wide range of mechanical properties, while also providing suitable surfaces for cell proliferation and growth [62, 63, 73, 145-147]. The electrospinning process produces scaffold sheets of PEUU fibers (0.8 μm in diameter) approximately 300-400 μm thick to approximate the scale and mechanical behavior of native extracellular matrix, including the ability to undergo large deformations and fully recover when unloaded (i.e. nearly elastic behavior). While electrospinning can fabricate scaffolds that possess ECM-like structures, this morphology also results in pore sizes that are generally smaller (<5 μm) and more tortuous than those produced by other scaffold fabrication methods such as salt leaching [150] and thermally induced phase separation [151]. While it may be possible that cells seeded on the surfaces of electrospun matrices can migrate into the interior by displacing or enzymatically degrading individual fibers, an extended culture period and appropriate signals for cell migration into thick construct interiors might also be required. Thus, while electrospinning permits fabrication of biodegradable elastomeric matrices that resemble the scale, architecture, and mechanical behavior of the native ECM [65], achieving high cellular density and infiltration remains challenging.

To overcome this limitation, we utilized a technique to electrospray cells concurrently while electrospinning PEUU in a manner that allows the control of the degree of fiber alignment and mechanical anisotropy [61, 189]. This technique represents a reproducible and relatively rapid method to produce elastomeric fiber reinforced cellularized scaffolds which can mimic the biomechanical properties of native tissues [61] while providing an environment conducive to cell

viability. The current approach centered on our ability to simultaneously quantify cellular deformations and changes in scaffold fiber architecture under biaxial deformation in-situ.

3.3.2 Use of nuclear aspect ratio

In the present study, cell nuclear aspect ratio was chosen as the metric for cellular deformation. It is known that cell morphology profoundly affects a range of cellular functions, and that changes in the cell cytoskeleton lead to altered stress levels imparted on the nucleus, ultimately affecting cell function. For example, Thomas et al. [198] showed that gene expression and protein synthesis of primary osteogenic cells were altered by changing nuclear shape. Specifically, collagen Type I synthesis correlated directly with nuclear shape, where certain values promoted maximum synthesis, supporting the concept of gene expression and protein synthesis based on optimal distortion of the nucleus. Guilak et al. investigated chondrocyte nuclear deformations under compressive loads in articular cartilage in an attempt to explore how cell deformation may be a stimulus to cell metabolic activity [172]. They observed a reduction in chondrocyte volume with compressive loading, linked to mechanical transduction and signaling through mechano-sensitive channels [60]. We have shown that little AVIC deformation occurs with the large amount of fiber straightening for pressures below ~1 mmHg, followed by substantial increases in AVIC NAR from 4 to 90 mmHg [183] (Figure 3-7b). Taken as a whole, cell responses to tissue level stresses are modulated through complex micromechanical and fiber-compaction effects that occur under physiological stress levels.

3.3.3 Role of fiber micro-mechanics in cell deformations

The cell micro-integrated electrospun PEUU scaffolds exhibited micro-fiber morphologies and kinematics that were shown to directly influence local cellular deformations. For instance, in the unstrained configuration the electrospun PEUU fibers exhibited a tortuous architecture, which transitioned to a web-like network of straight, interconnected fibers at high levels of strain. The deformations of the micro-integrated VSMC were found to be primarily mediated by this phenomenon. The VSMC integrated electrospun PEUU constructs underwent fully recoverable large deformations akin to many native tissues. Moreover, while a non-linear relation between the tissue strain and NAR was observed for both the aortic valve and cell integrated electrospun PEUU (Figure 3-7), the underlying micro-mechanical mechanisms were clearly different. Initially, the integrated VSMC's exhibited a rapid increase in NAR as fibers straightened and tortuosity was reduced. Once the PEUU fibers became straightened and the architecture transitioned to an interconnected web like structure, changes in NAR were observed to plateau. In contrast to the compression mediated deformations observed in the AVIC (Figure 3-7b), the microintegrated VSMC deformation was mediated by the local reduction of tortuosity or straightening of the PEUU fibers (Figure 3-7a). Thus, cell-scaffold interactions can be subtle and can bring about significantly different deformation behaviors.

3.3.4 Broad considerations

Despite its early successes, tissue engineering continues to face challenges in repairing or replacing tissues that serve a predominantly biomechanical function. An evolving discipline called ‘‘functional tissue engineering’’ seeks to address the development of load-bearing

structures in several ways [199]. In particular, a critical subset of native tissue mechanical properties must be selected and prioritized as design objectives. This subset is important, given that the mechanical properties of the designs are not expected to completely duplicate the properties of the native tissues. Increasing evidence suggests that mechanical stress, as well as other physical factors, may significantly increase the biosynthetic activity of cells in bioartificial matrices. Clearly, the effects of physical factors on cellular activity must be determined in engineered tissues. Knowledge of these signals may shorten the iterations required to replace a tissue successfully and direct cellular activity and phenotype toward a desired end goal. Ultimately, incorporating each of these principles of functional tissue engineering should result in safer and more efficacious repairs and replacements.

Substantial difficulties are imposed in functional tissue engineering since there are multiple length scales with complex architectures, modes of deformation, and biochemical stimuli which work synergistically to determine physiologic responses. It is generally accepted that both chemical and mechanical factors modulate cell biosynthesis when producing extracellular matrix [58-60, 200]. Yet, the exact microstructural characteristics of the scaffolds will have a profound influence on cellular function. For example, collagen and fibrin gels are a popular choice in engineered scaffolds [116, 118-120, 201]. Yet, while possessing desirable characteristics such as cyto-compatibility and anisotropic mechanical properties, their tensile properties have not yet achieved that of native tissues. Moreover, native fibrous protein based gels are largely composed of short-range fibers, whereas native connective tissues are primarily composed of long fibers, which can span multi-mm scales and simultaneously facilitate flexibility and high tensile strength.

As an alternative, biodegradable synthetic polymers as scaffolds to support and encourage tissue regeneration have also proven successful. For example, Freed et al. employed non-woven meshes of polyglycolic acid as a scaffold for seeded chondrocytes and successfully showed the ability to regenerate cartilaginous tissues composed of glycosaminoglycans and collagen [137]. As mentioned previously, electrospinning is a versatile process and slight alterations in the manufacturing process enable the production of scaffolds with a wide array of fiber morphologies (i.e. fiber diameter, porosity, packing density, orientation, etc), which directly influence bulk mechanical properties [143, 144]. Controlled mechanical anisotropy, for example, is attained by using a rotating collection surface which induces a preferred fiber direction as the rotational speed of the collector increases [61]. This ability is extremely beneficial in mimicking native tissue architecture and has even been shown to approximate the highly nonlinear biaxial mechanical response of collagenous soft tissues, such as the native porcine pulmonary valve leaflet [61].

In light of these studies, the importance of scaffold-cell mechanical coupling becomes readily apparent in the rational design of engineered tissues. Moreover, the unique micromechanics of various scaffolds induce different cell deformation responses, which could correlate to substantial changes in cell proliferation and function. This phenomenon is illustrated by three grey bars placed at intervals of 20% strain which each correspond to unique NAR values. Instead, the change in cell deformation (or NAR)-strain relationship explored here can be used to guide future engineered tissue applications for these integrated electrospun PEUU scaffold.

3.3.5 Limitations

It should be noted that we investigated the response cell integrated electrospun PEUU scaffolds cultured for 48 hours, which contain minimal functional ECM. The forming ECM within the scaffold and its subsequent micromechanical effects will likely have a substantial effect on cellular deformation, and could prove critical in defining the long term behavior of cell function within integrated electrospun scaffolds. In addition, much of the complex interactions between VSMC and polymeric scaffolds remain unknown, including the nature of cellular focal adhesions to the PEUU matrix. It is likely that the nature and extent of adhesion sites between a cell and its surrounding matrix will directly impact manifestations of biosynthetic activity.

3.3.6 Summary

It remains a critical goal to understand how organ-level deformations, such as cyclic stretch, bending, and shear [202, 203], translate to microstructural deformations and ultimately as cellular mechanical stimuli. A great deal can be learned about the mechanical modulation of functional tissue from electrospun PEUU scaffolds, since they capture some aspects of native tissue microstructure and exhibit the ability to endure large deformations while recovering completely. Moreover, these issues become more challenging in the formation of actively contracting tissues, where cellular contraction must be coordinated at higher scales in order to provide large stresses required for organ contraction. The emergence of new materials and processing methods will clearly be required to meet these functional needs.

In the previous two chapters, we have quantified the following:

1. Gross fibrous structure, including fiber orientation distributions, tortuosity, and diameter
2. How these metrics translate to functional performance of the scaffold across multiple scales
3. The impact these characteristics have on cells residing within the scaffold

With this understanding, we can begin to explore interesting mechano-biological questions in a systematic fashion. Namely, we are interested how these cell integrated materials might evolve into a functional tissue to perform as a load bearing structure. To better inform our studies of the effects of finite mechanical cues on cell biosynthetic activity and matrix mechanical contribution to overall function, it is first necessary to determine how electrospun PEUU performs when exposed to right side hemodynamic conditions. Not only will this serve as valuable comparisons between native tissue and these elastomeric engineered materials at the organ level, it helps to guide tissue level mechanical conditioning protocols that best replicate the deformation magnitudes potentially observed in vivo.

4.0 ELECTROSPUN PEUU PERFORMANCE IN SIMULATED NATIVE HEMODYNAMIC CONDITIONS

Quantification of heart valve leaflet dynamics and deformation during the cardiac cycle is essential in understanding normal and pathological valvular function, as well as in the design of replacement heart valves. E arly efforts to quantify in vivo leaflet dynamic function have employed techniques such as fluoroscopic imaging, computed tomography and bi-plane x-ray imaging, magnetic resonance imaging and ultrasound. All of these techniques suffer from significant drawbacks such as the need for physical markers attached to the leaflet surface, patient radiation exposure, and limited temporal or spatial resolution. While ultrasound, which is non-invasive and inexpensive, is readily used as a diagnostic tool in clinical settings, it has limited three-dimensional abilities and lacks the fidelity necessary for research purposes. Optical techniques, which necessitate unobstructed view of the structure of interest, are much better suited to in vitro settings and can provide the spatial and temporal resolutions needed to accurately quantify details of leaflet dynamic function. After a brief introduction of native leaflet dynamic behavior, the following chapter presents an in vitro system, which was employed in tandem with a high speed imaging system to optically quantify electrospun PEUU function as a tri-leaflet valve. F urthermore, the effect material anisotropy has on leaflet function was investigated.

4.1 NATIVE DYNAMIC TRI-LEAFLET BEHAVIOR

The mechanisms ensuring the proper function of the heart valves are essentially controlled by the surrounding hemodynamic environment. Understanding the interactions between the heart valves and their dynamic fluid environment is thus critical to better understand normal valve function and disease progression. Accurate diagnosis and treatment of valve disease, along with the development of improved surgical strategies/techniques, requires a complete understanding of normal valve dynamics. As an example, investigators have undertaken the task of studying mitral valve (MV) dynamics and left ventricular fluid mechanics [15, 204-209]. However, due to the complexity of valve anatomy, it is difficult to theoretically [210] or computationally [211-213] determine the functional role and importance of each individual component. Moreover, these simulations are currently difficult to fully validate in vivo with available imaging technologies. As a result, experimental techniques to quantitatively characterize valve dynamics are deemed to be the gold standard.

Many approaches have been taken in attempt to quantify valvular dynamics. Early work by Thubrikar et al used biplane fluoroscopy to determine dynamic valve function. [214-216]. These experiments involved lead markers sutured onto the valve leaflets. Thubrikar reported that leaflet radial length does not change significantly during maximum flow. Instead he observed when the leaflet closes and coapt under increasing pressure, the radial length increases during diastole [217]. Thubrikar used two markers at the basal and belly region of the leaflet, which did not cover the free edge. Further, two markers only allowed straight distance measurements, and did not follow leaflet surface. More recently high resolution approaches, such as biplane x-ray imaging, demonstrated significant regional complexities in valve motion and strain [218]. However, in these studies the number of markers used was small so that the spatial resolution

was insufficient for detailed surface strain studies. A study by Iyengar et al. demonstrated the ability to accurately quantify the 3D leaflet surface of a pericardial valve throughout the full cardiac cycle via constructed laser light [219]. Unfortunately, this study was limited in that true material points were not tracked making strain calculation impossible. This is considered critical as the high degree of structural and mechanical heterogeneity in heart valve leaflets [16, 220, 221] suggests an equally complex regional strain response over the cardiac cycle.

4.2 OPTICAL IMAGING SYSTEM AND VALVE HOLDER DESIGN

4.2.1 Design parameters

Recently, our lab has developed a novel pulsatile duplicator (Figure 4-1) for biologically active semilunar heart valves materials for long-term studies. The system is capable of delivering physiologic hemodynamic conditions (right or left heart) to single semilunar valves for extended times with precise hemodynamic control. In order to accommodate a cell integrated PEUU tri-leaflet engineered valve, modifications were made to the present system. This was accomplished by adapting the outflow track of the flow loop from the left ventricle (II) to the compliance chamber (III).

This modification includes the development of a rigid, modular valve holding apparatus (Figure 4-1 bottom pane). The modular design was implemented as a result of the need to quickly assemble the valve in a reproducible manner. To this end, a leaflet assembly device (Figure 4-1 and 4-2), comprised of a central mandrel mating with a congruent member was devised to form and hold flat constructs for mounting within the valve mounting apparatus. The

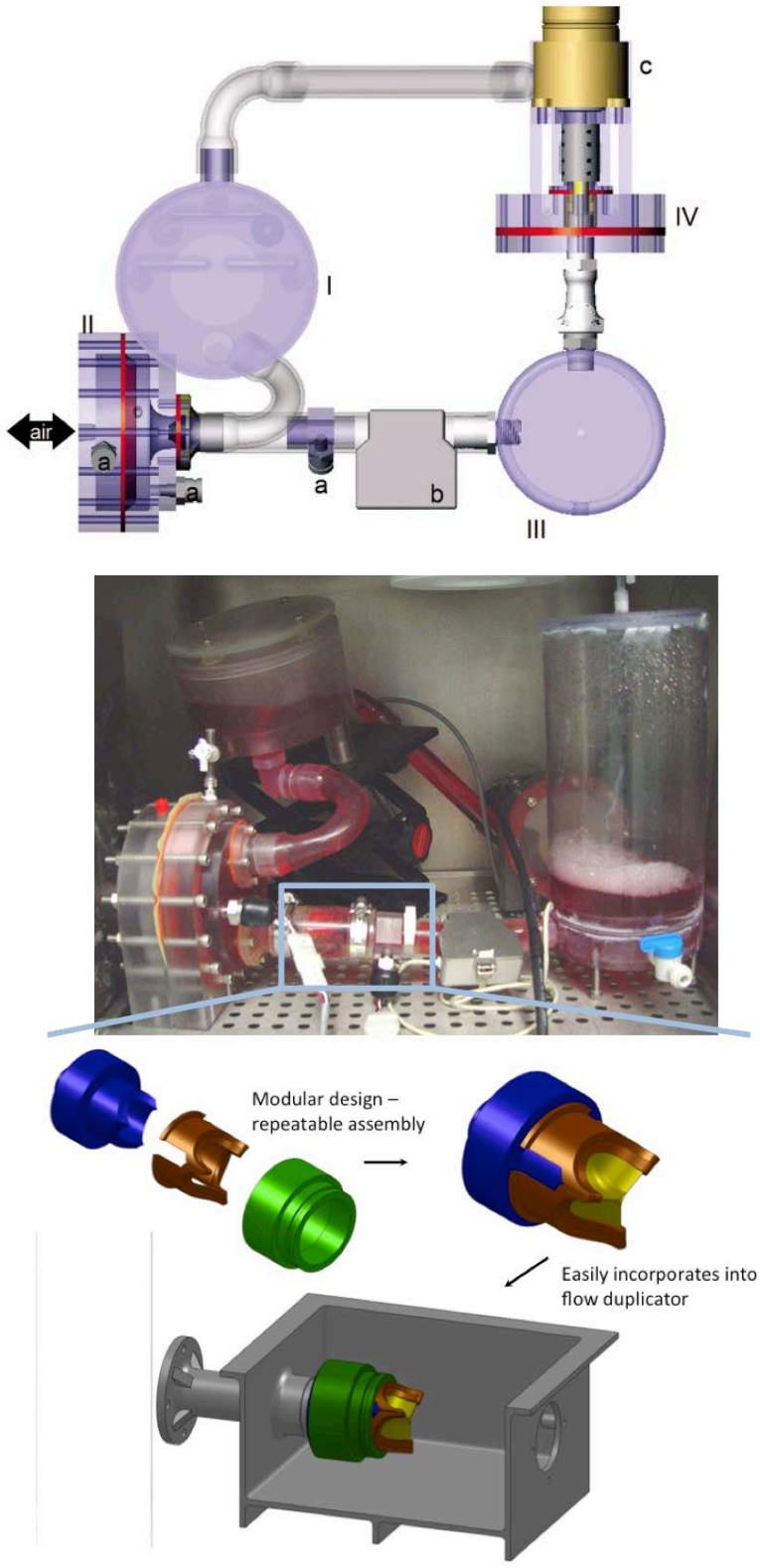

Figure 4-1. Pulse duplicator design and modifications necessary to create tri-leaflet PEUU valves.

upper and lower portions of the rigid assembly (Figure 4-2) can then be placed over the assembly mandrel, encasing the engineered leaflets, and fixed together. Lastly, the assembly mandrel can be withdrawn leaving behind a tri-leaflet valve. The apparatus proper is primarily tasked with the critical function of securely holding electrospun PEUU material in a physiologically relevant geometry. The overall geometry of the constructed valve was modeled after right RVOT dimensional measurements obtained via echocardiogram from 5 sheep ranging in weight from 28.5-43 kg. The diameter of the root measured 22.5 mm with leaflet height and thickness measuring 16.5 mm and 75 μm respectively.

In addition to emulating the gross RVOT dimensions of young sheep, the valve apparatus was designed to be low profile to maximize the leaflet-imaging pathway throughout the cardiac cycle. For imaging, the entire valve holder is housed within an imaging chamber (Figure 4-1 bottom) that can be filled with a 70:30 water-glycerin mix. This solution was chosen as it is optically clear but matches the index of refraction of the Pyrex valve sinus. The Pyrex sinus was manufactured to mate with the holding apparatus and extend out of the imaging box to connect to the rest of the pulsatile flow loop.

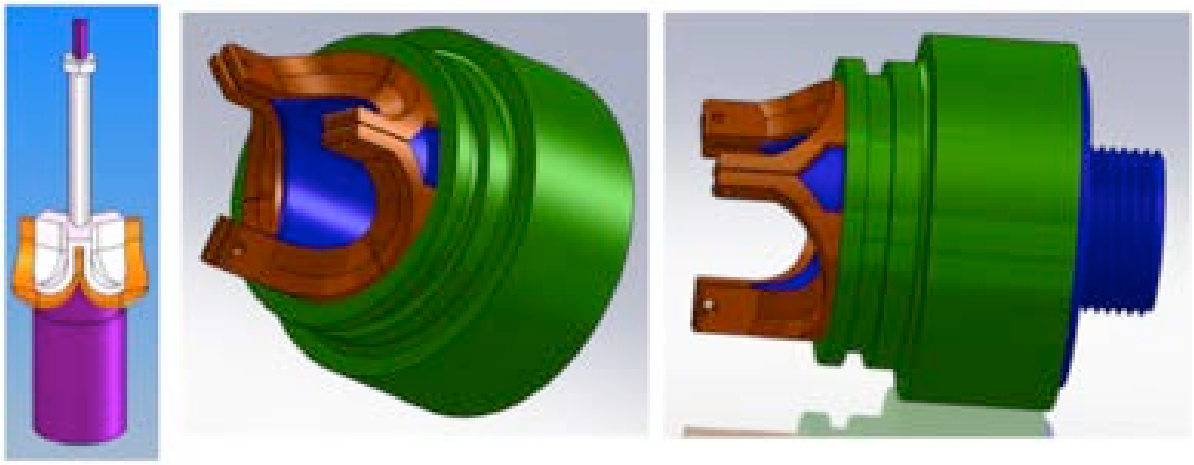

Figure 4-2. Modular valve holding apparatus.

4.3 PEUU LEAFLET PERFORMANCE

4.3.1 Valve preparation

Dry PEUU sheets were electrospun as described in chapter 2. T wo mandrel velocities were chosen, 1.5 m/s and 13.8 m/s, to produce isotropic and highly aligned materials to investigate the effects of structural anisotropy on leaflet dynamics and deformation. From the sheet of material, 3 interconnected semilunar leaflets were cut with the aid of a template to ensure consistent leaflet size (Figure 4-3). On the middle leaflet, fiducial markers were applied manually with tissue marking dye with an approximate spacing of 2 mm across the entire leaflet surface. A tri-leaflet valve was then formed with the valve holding apparatus and then mated to the Pyrex sinus and placed into the imaging box and submersed in the index matching glycerin-water solution.

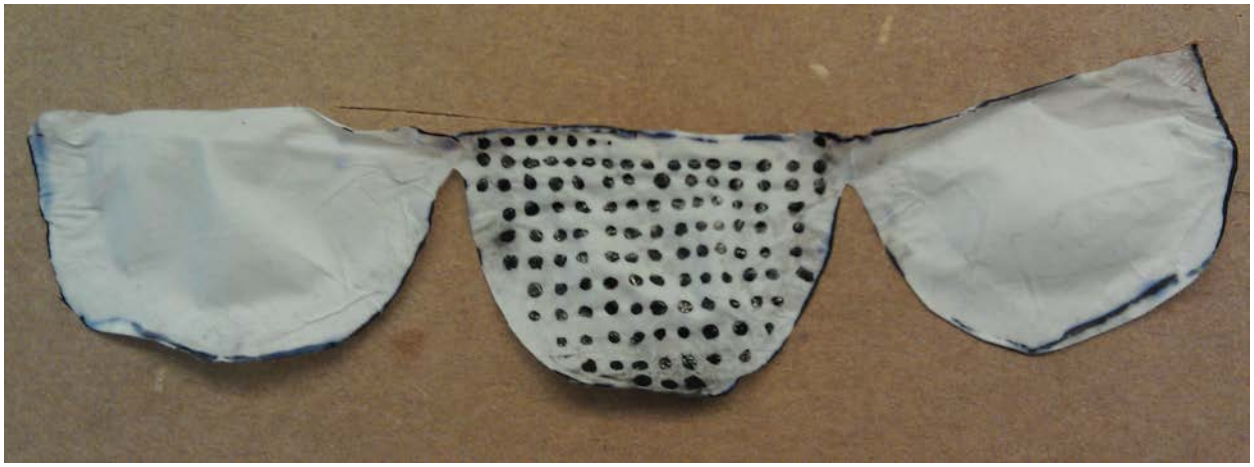

Figure 4-3. Preparation of PEUU material to quantify material performance as a tri-leaflet valve.

4.3.2 Camera calibration

Proper calibration of the imaging system is critical for accurate 3D reconstruction. This can be accomplished in many ways, but it is important to produce a phantom with points of known spatial locations that encompasses the entire imaging volume. To do this, a leaflet shaped piece was rapid prototyped with raised circular projections of known distance (2 x 2 mm spacing) that mates with the holding apparatus (Figure 4-4). Immediately prior to or following image acquisition, the full pulse duplicator system was set up to capture a static image of the phantom for calibration.

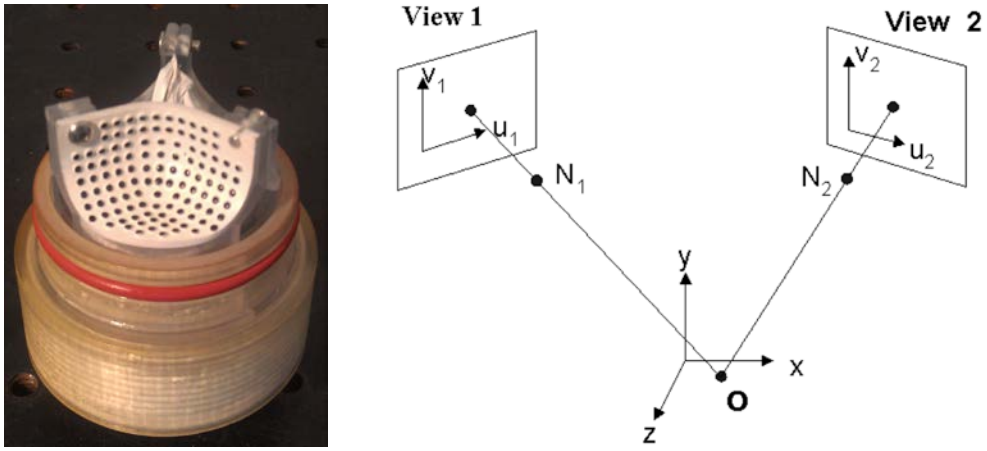

Figure 4-4. Installed calibration phantom and schematic of the DLT calibration setup showing a pair of camera coordinates (u_1 ,v_1) and (u_2 ,v_2) of the point O corresponding to the two views.

4.3.3 Quasi-static and high speed image acquisition

Two high-speed cameras (A504k Basler Inc., Germany) of 1280 x 1024 pixel resolution were placed at approximately 30 degrees from one another, focused on one entire engineered leaflet.

The motion of the leaflet outflow surface was recorded under both quasi-static and dynamic conditions while the valve annulus was filled with deionized water. For the quasi-static imaging, a static transvalvular pressure was achieved with compressed air, applied to the outflow side of the flow loop while leaving the ventricular side open to atmospheric pressure. In this manner, the transvalvular pressure was incrementally increased with a pressure regulator accurate to 0.26 mmHg for imaging at 0, 5, 10, 15, 20, 25, 30, 35, and 40 mmHg. For dynamic imaging, the entire cardiac cycle was recorded as a series of TIFF® images at a speed of 200 frames per second. The two cameras and hemodynamic data acquisition were triggered simultaneously to synchronize the images with the transvalvular pressure. The valves were imaged under normal ovine pulmonary valve hemodynamics. Systolic and diastolic pressures where 25/15 mmHg with a frequency of 1 Hz.

Following the image acquisition protocol described above, the acquired images required post-processing to segment the fiducial points in each imaging plane and track their displacement throughout the loading cycle. Briefly, custom MATLAB® software was used to digitize the markers and obtain the [x, y] pixel coordinates of each marker in the acquired image planes. Direct linear transformation was used to reconstruct the array of 3D spatial coordinates, using a calibration phantom of known dimensions.

4.3.4 Direct linear transform

It can be shown that the pair of camera coordinates (u_1,v_1) and (u_2,v_2) of the point O corresponding to the two views (Figure 4-4) can be related to the real coordinates (x,y,z) of O in the object space through a standard direct linear transformation by the expressions

$$u = \frac{Ax + By + Cz + D}{Ix + Jy + Kz + 1}, \qquad v = \frac{Ex + Fy + Gz + H}{Ix + Jy + Kz + 1} \tag{EQ. 4-1}$$

where the coefficients *A*–*K* are constants, which are dependent on the camera specific parameters as well as the camera configurations relative to the point *O*. Values of the constants can be determined via calibration using a set of six or more noncoplanar points whose object space coordinates are known *a priori* and using the above equations. Once the constants are determined the same expressions can be used to transfer the camera coordinates of any object in the two views back to its coordinates in the object space. While the main advantage of using two or more views is that the camera specific parameters need not be computed explicitly, it has to be noted that any change in camera configuration or position changes the values of the constants and requires recalibration.

4.3.5 Surface strain calculation

Once 3D displacements of fiducial points are obtained, leaflet strain can be determined. For this analysis, the leaflet is characterized as a thin membrane and its strain state is quantified exclusively in terms of its membrane or in plane strains. From the 3D points cloud, a mesh was formed of marker coordinates with Delaunay triangulation. Constraints on triangular element side length and vertex angles were implemented to eliminate the formation of unwanted elements.

The marker coordinates were then parameterized such that for each marker *i* the computational coordinates are defined as follows:

$$\xi_i = -1 + 2\left(\frac{x - x_{\min}}{x_{\max} - x_{\min}}\right)$$
$$\eta_i = -1 + 2\left(\frac{y - y_{\min}}{y_{\max} - y_{\min}}\right) \qquad \text{(EQ. 4-2)}$$

To calculate loft of each point on the leaflet surface ($z(\xi,\eta)$) a bi-linear triangular finite element representation was employed.

$$z(\xi,\eta) = \sum_{j=1}^{9} \hat{z}_j \phi_j(\xi,\eta) \qquad \text{(EQ. 4-3)}$$

Where $\hat{z}_j$ was the nodal value and $\phi_j(\xi,\eta)$ was the corresponding basis function. To calculate the nodal positions, we used the marker positions to minimize the error:

$$\varepsilon = \sum_{i=1}^{m} \left\| z^i - \sum_{j=1}^{9} \hat{z}_j \phi_j\left(\xi^i,\eta^i\right) \right\|^2$$
$$[\mathbf{h}]\{\hat{z}\} = \{\mathbf{z}\} \qquad \text{(EQ. 4-4)}$$

$$[\mathbf{h}] = \begin{bmatrix} \phi_1\left(\xi^1,\eta^1\right) & \phi_2\left(\xi^1,\eta^1\right) & \cdots & \phi_9\left(\xi^1,\eta^1\right) \\ \phi_1\left(\xi^2,\eta^2\right) & \phi_2\left(\xi^2,\eta^2\right) & \cdots & \phi_9\left(\xi^2,\eta^2\right) \\ \vdots & & & \vdots \\ \phi_1\left(\xi^m,\eta^m\right) & \phi_2\left(\xi^m,\eta^m\right) & \cdots & \phi_9\left(\xi^m,\eta^m\right) \end{bmatrix}. \qquad \text{(EQ. 4-5)}$$

Next, the fitted surfaces in the deformed and reference configurations were used to calculate the components of the metric tensors. The components of the strain tensor, ($\gamma_{\alpha\beta}$), were then calculated using metric tensors on the deformed ($g_{\alpha\beta}$) and reference ($G_{\alpha\beta}$) configurations

$$\gamma_{\alpha\beta} = \frac{1}{2}\left(g_{\alpha\beta} - G_{\alpha\beta}\right). \qquad \text{(EQ. 4-6)}$$

Both $G_{\alpha\beta}$ and $g_{\alpha\beta}$ were defined with respect to the reference curvilinear coordinate system. The physical components of the Euler-Almansi strain tensor ($\hat{e}_{\alpha\beta}$) were obtained from

$$\hat{e}_{\alpha\beta} = \frac{\gamma_{\alpha\beta}}{\sqrt{g_{(\alpha\alpha)} g_{(\beta\beta)}}}. \qquad \text{(EQ. 4-7)}$$

The Euler-Almansi strain tensor **e** was expressed in the form of dyads of contravariant unit vector $\mathbf{e}^{\alpha}$. To determine the circumferential and radial strain components e^{cc} and e^{rr}, the Euler-Almansi strains (**e**) were mapped onto the circumferential and radial directions n^{c} and n^{r} in the current configuration

$$\mathbf{e} = \hat{e}_{\alpha\beta}\mathbf{e}^{\alpha} \otimes \mathbf{e}^{\beta} \,. \qquad \text{(EQ. 4-8)}$$

The circumferential and radial components of the strain tensor were obtained from,

$$\begin{aligned} e_{cc} &= e_c \cdot e \cdot e_c \\ e_{rr} &= e_r \cdot e \cdot e_r \end{aligned} \,. \qquad \text{(EQ. 4-9)}$$

Where the circumferential unit vector ($\mathbf{e}_c$) was defined roughly parallel to the edge of the valve and the radial unit vector ($\mathbf{e}_r$), was pointing from the edge to the valve annulus. The principle values and directions of the strain tensor were obtained from solving the eigen value problem for the Euler-Almansi strain tensor $\mathbf{e}$ expressed in the mixed notation,

$$\det\left(\gamma^{\alpha}_{.\beta} - e_{(\mathbf{n})}\delta^{\alpha}_{.\beta}\right) = 0 \,. \qquad \text{(EQ. 4-10)}$$

Two eigen values $e_{(\mathbf{n}_1)}$ and $e_{(\mathbf{n}_2)}$ and their corresponding eigen vectors $\mathbf{n}_1$ and $\mathbf{n}_2$ were then calculated. Further, the principle stretch values $\lambda_{(\mathbf{n}_i)}$ were obtained using $e_{(\mathbf{n}_i)}$, as follows:

$$\lambda_{(\mathbf{n}_i)} = \frac{1}{\sqrt{1 - 2e_{(\mathbf{n}_i)}}} \,. \qquad \text{(EQ. 4-11)}$$

4.4 RESULTS

4.4.1 Static valve behavior

In addition to the coupled cell-scaffold deformation behavior observed in Chapter 3, quantifying electrospun PEUU leaflet deformation in response to a static pressure head will help to inform mechanical training studies. Specifically, quantifying leaflet in plane PEUU deformation will provide physiologically relevant constraints on the magnitudes of strain to investigate during mechanical training. Moreover, it provides a first glimpse of how this material might perform in vivo when exposed to complex loading regimes. As described above, both isotropic and highly anisotropic valves were constructed and exposed to increasing transvalvular pressure. The transvalvular pressures applied surpassed normal ovine pulmonary pressures of approximately 20 mmHg. Results show that the deformations experienced for both materials exhibited little change beyond 20 mmHg. This negated the need to conduct additional analyses at pressures beyond physiologic conditions.

For both material types, the tri-leaflet structure was visually observed to coapt well in response to transvalvular pressure. The anisotropic leaflet deformed more readily at low pressures and exhibited larger peak deformations at 20 mm Hg. When exposed to increasing transvalvular pressure, the strain field of the lower belly region increased in a fairly homogenous manner. While peak stretch values on the order of 1.3-1.4 were measured in the belly region for the isotropic and anisotropic materials, the average deformation across the full leaflet surface was 1.11 ± 0.03 for the isotropic (Figure 4-5) and 1.14 ± 0.06 for the anisotropic (Figure 4-6).

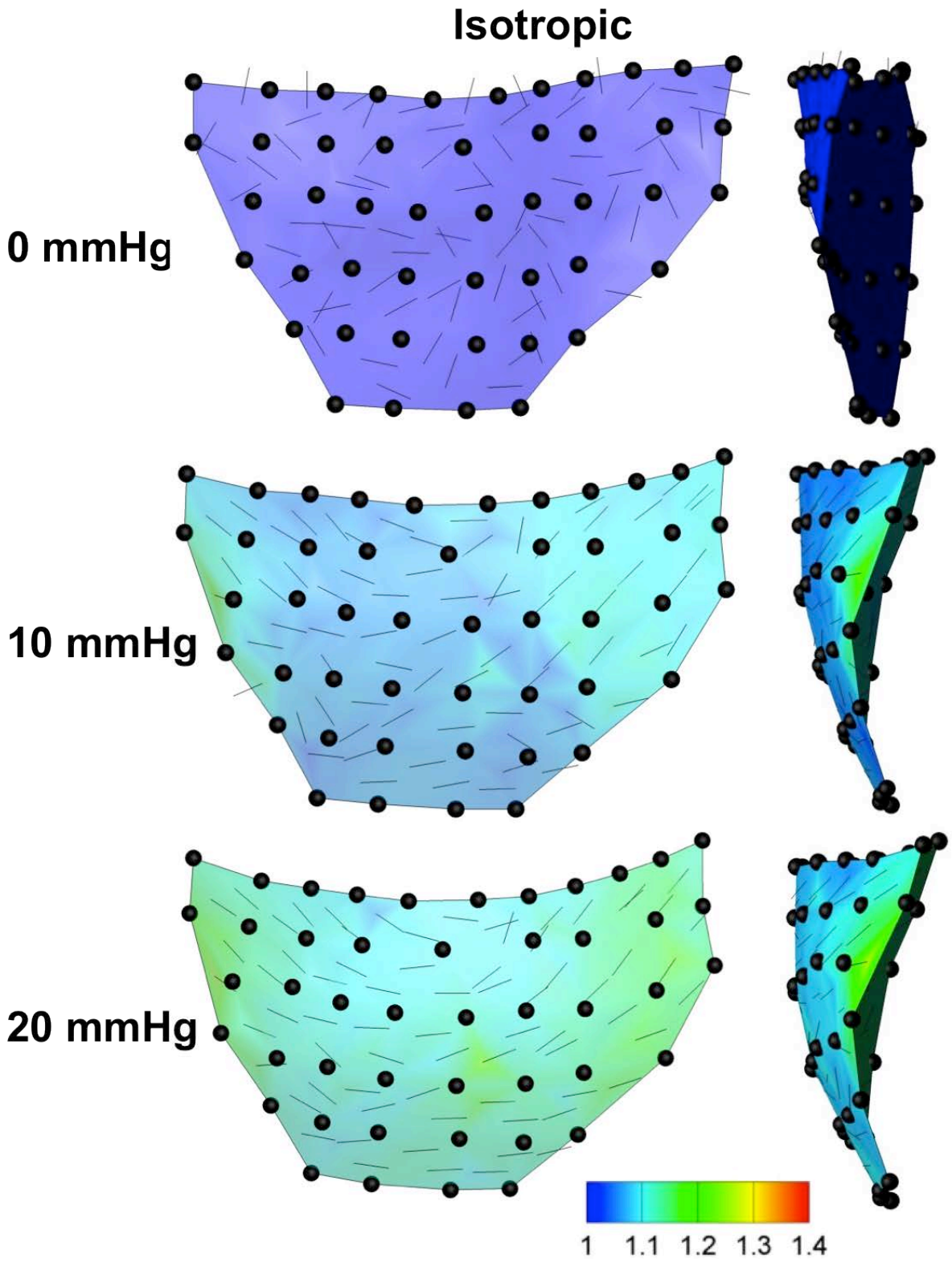

Figure 4-5. Isotropic material maximum principle strain contour (vector lines) across the imaged leaflet surface.

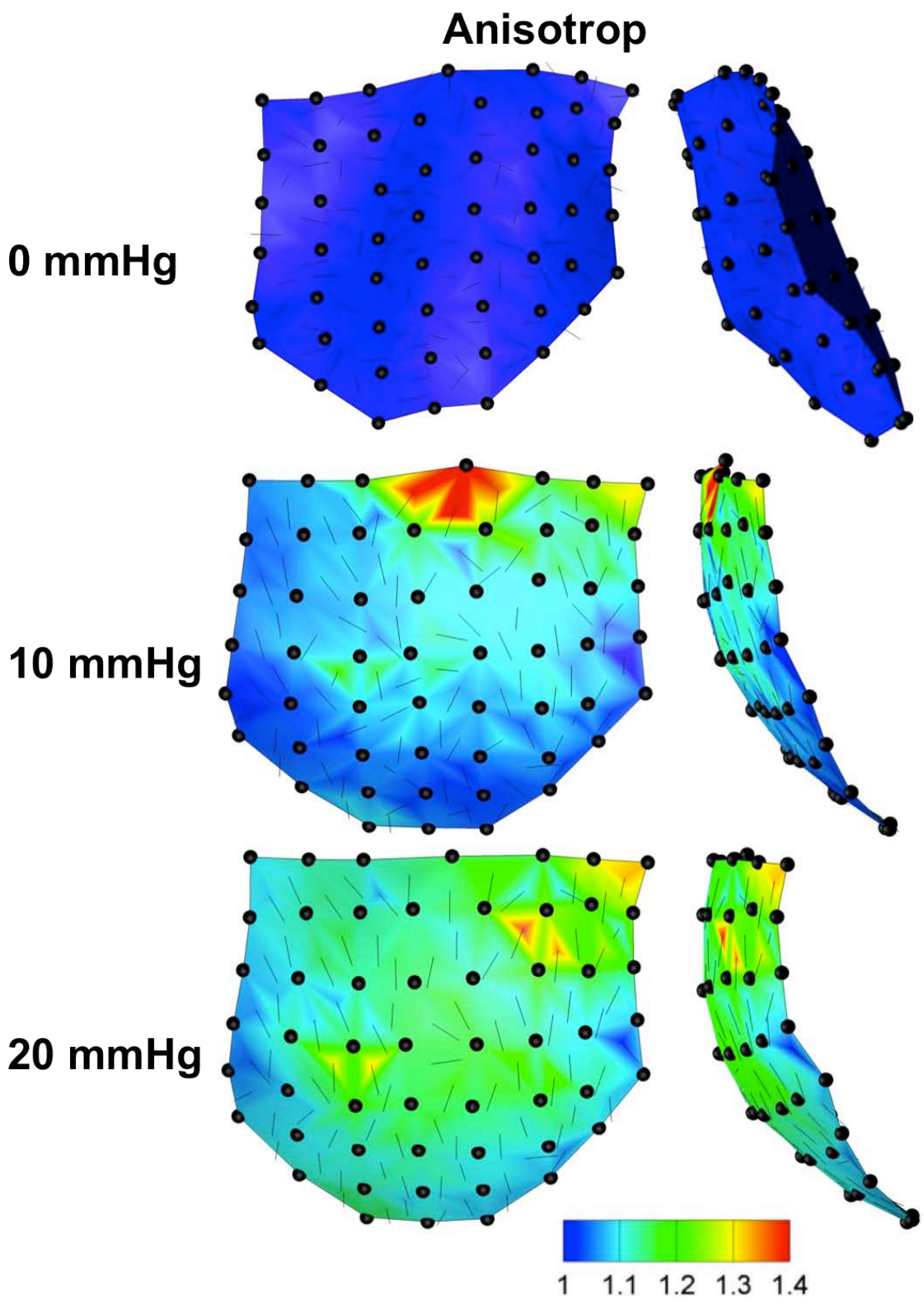

Figure 4-6. Anisotrpoic material maximum principle strain contour (vector lines) across the imaged leaflet surface.

The direction of principle stretch was observed to be drastically different for each material (Figure 4-7). For the isotropic material, the principle stretch occurred in a curvilinear fashion running from one commissure insertion down towards the belly region and back up to the opposite commissure. Conversely, the principle deformation direction aligns almost exclusively in the radial direction. The anisotropic deformation response showcases the effects of structural anisotropy with principle deformation occurring orthogonal to the principle fiber direction.

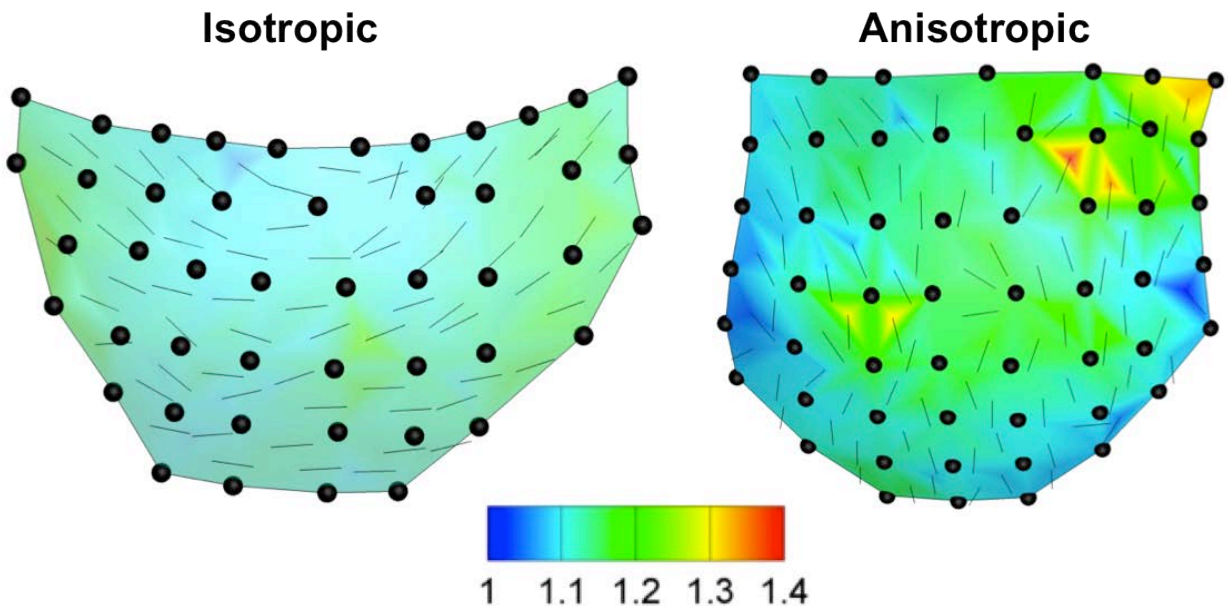

Figure 4-7. Major principle strain direction (vector lines) observed at peak physiologic pressure.

Areal stretch, which gives a sense of the total deformation experienced throughout the leaflet surface, exhibited trends quite similar to principle stretch. Peak values were again higher in the anisotropic leaflet with mean values of 1.11 ± 0.04 and 1.15 ± 0.08 for the isotropic and anisotropic materials respectively. Also, the belly region of the anisotropic leaflet appears to

deform more homogenously with increasing transvalvular pressure (Figure 4-8). Large shear strain was generally localized to the commissure regions and was likely a result of the boundary conditions imposed when clamping the material in a rigid frame. The shear strains observed throughout the rest of the leaflet were fairly minimal as seen in Figure 4-9.

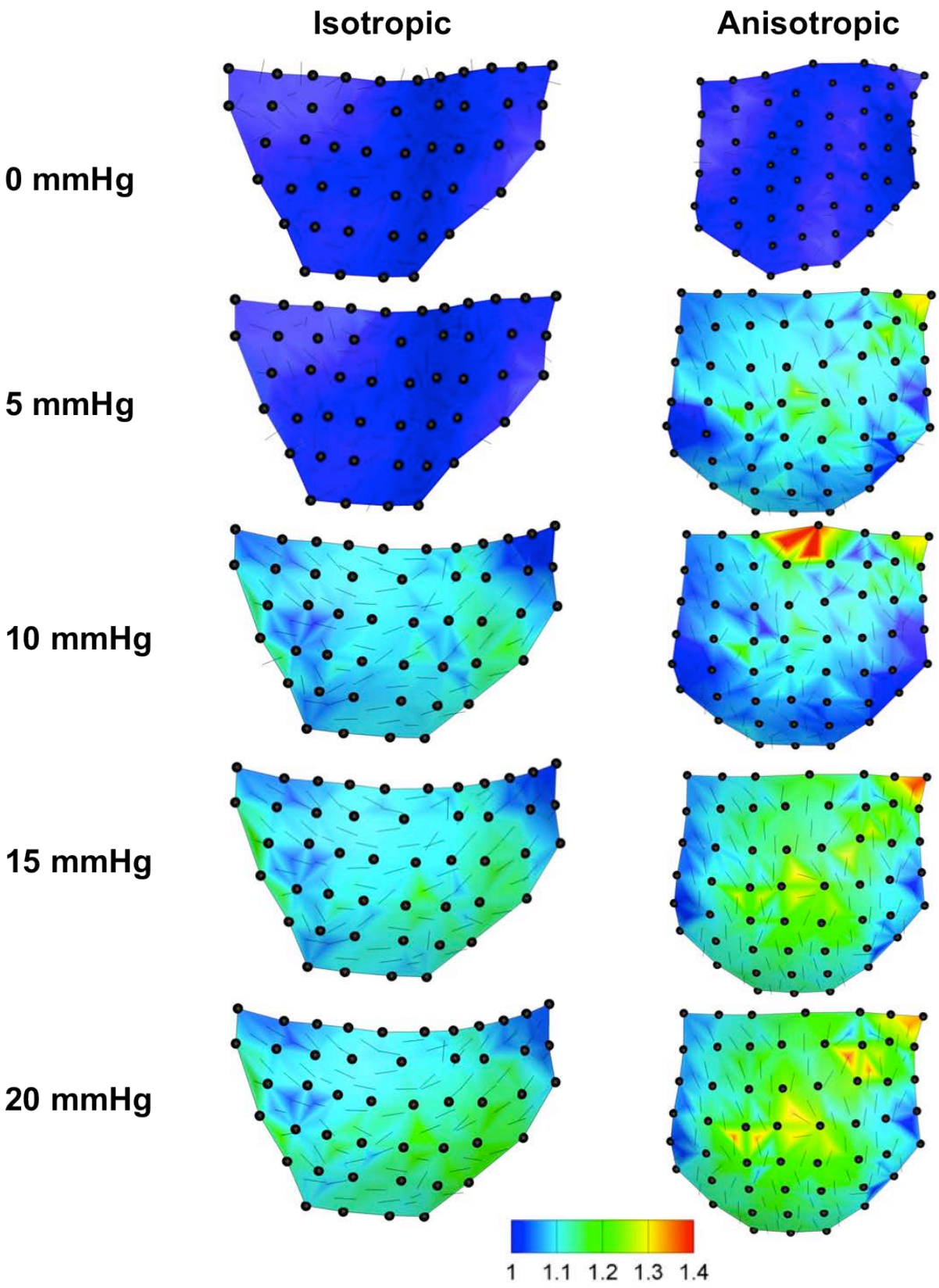

Figure 4-8. Areal strain contour across the imaged leaflet surface.

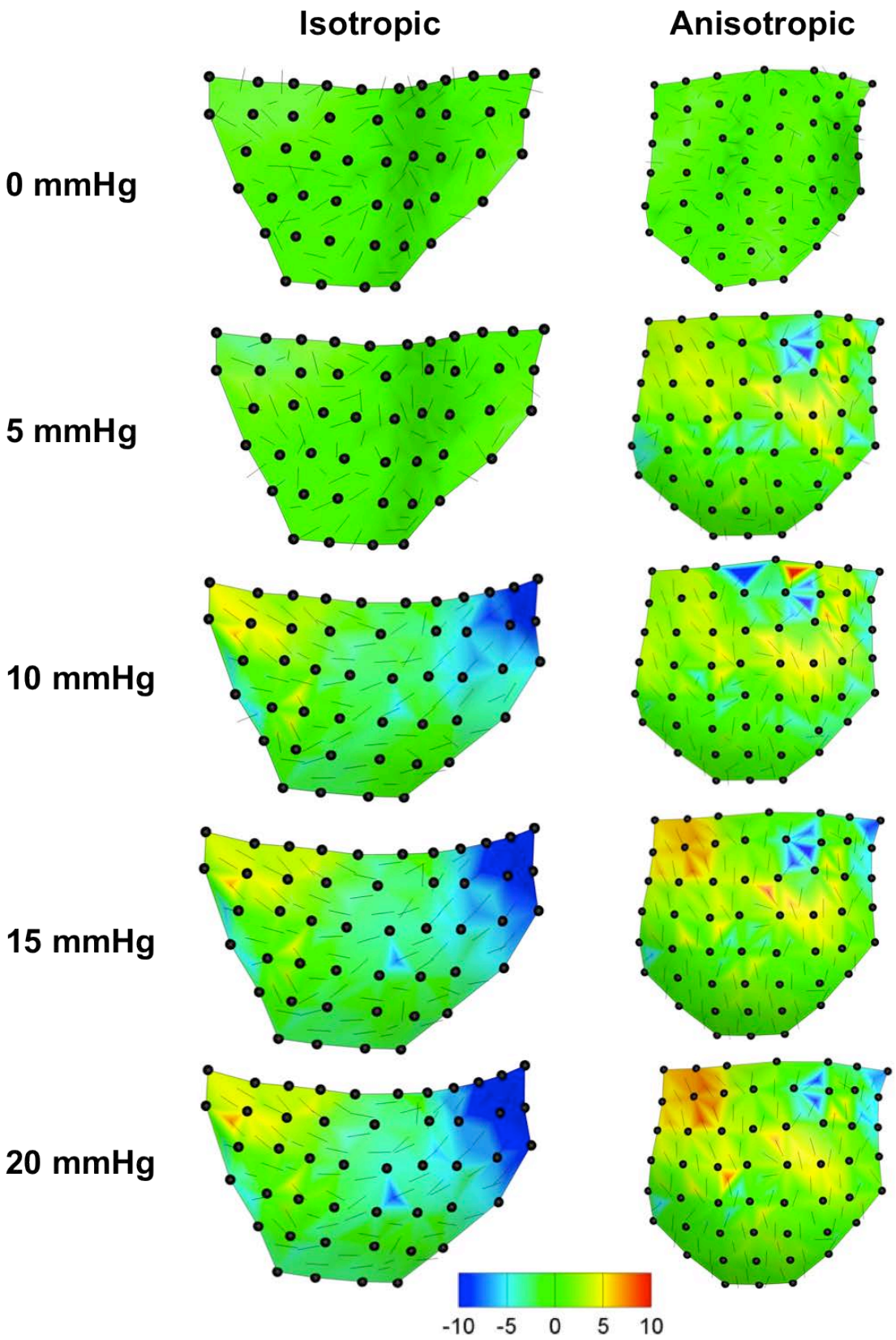

Figure 4-9. Local shear strain across the imaged leaflet surface.

4.4.2 Dynamic valve behavior

When exposed to ovine physiologic pressure and flow conditions, both material types performed well without major structural failure. During the course of capturing dynamic images of PEUU leaflet motion, the material was repeatedly capable of withstanding native hemodynamic conditions without measurable complications. In native tissues, the combined valve opening and closing phases only represent approximately 10 percent of the entire cardiac cycle. This trait is largely a function of hemodynamic characteristics, which are recapitulated by the computer controlled pulse duplicator.

Due to the short duration of the opening and closing phases in addition to the substantial motion that occurs during this period (Figure 4-10), it was not possible to reconstruct valve motion through the entire cardiac cycle. During the later portions of systole, when blood is ejected past the, leaflet surface, a large amount of "fluttering" is observed. This is quite pronounced along the leaflet free edge as highlighted by the white tracings in Figure 4-10. As a result, direct comparisons of leaflet deformation during the cardiac cycle cannot be directly compared with quasi-static measurements. However, despite the practical limitations of capturing leaflet deformation, structural alterations of the material do appear to qualitatively alter leaflet dynamics. First, the isotropic material consistently exhibited a larger opening orifice area compared to the anisotropic material. There also appears to be substantial changes in the duration between the onset of valve closure and complete leaflet coaptation.

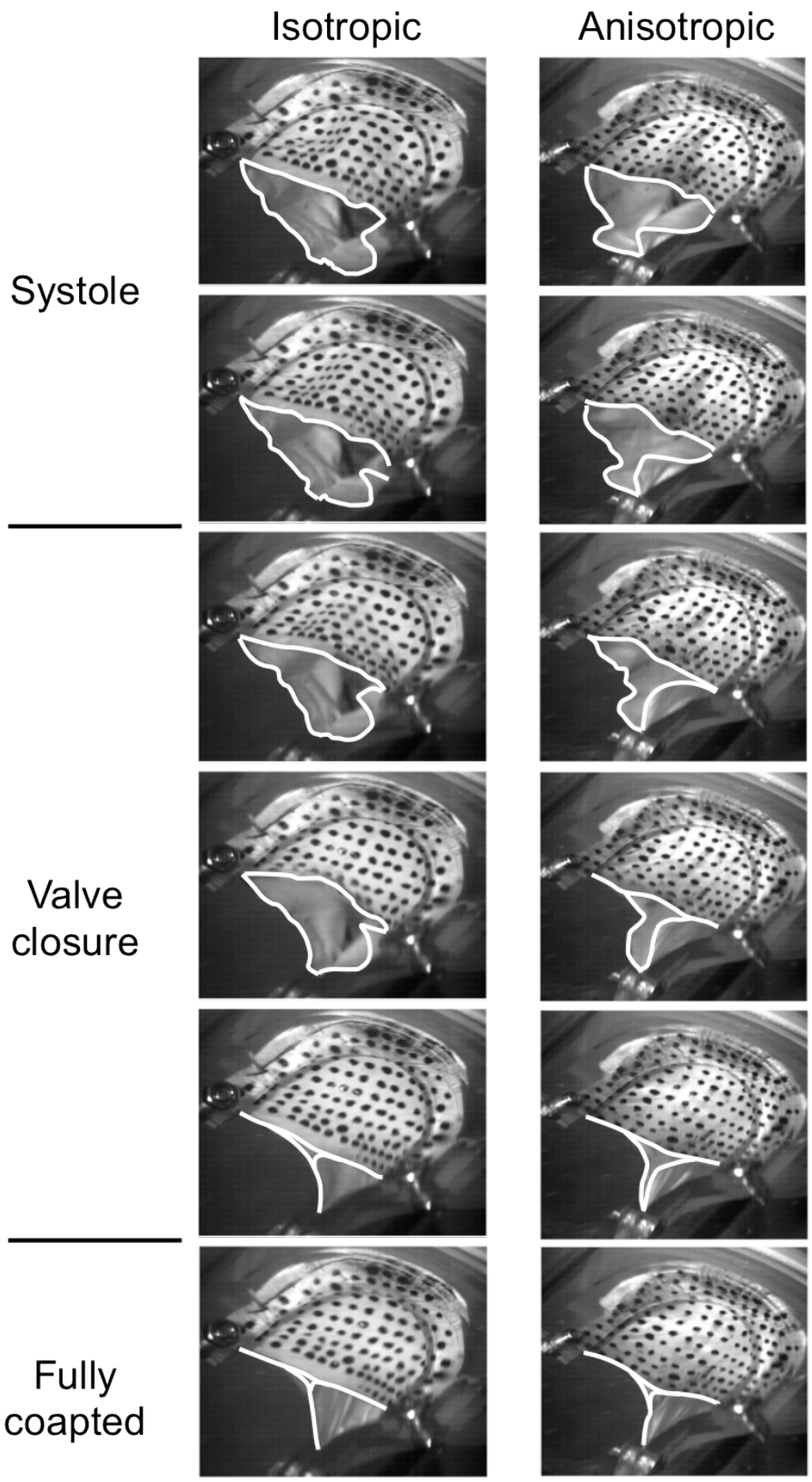

Figure 4-10. Valve closure dynamics.

4.5 DISCUSSION

This is the first study to employ electrospun elastomeric materials to investigate their gross mechanical performance as a tri-leaflet valve in vitro as a function of material microstructure. In this chapter, a pneumatic flow loop developed by Hildebrand et al [222, 223] was augmented to incorporate a custom valve holding frame that approximates native ovine valve geometry. From a general perspective, this study serves as a proof of principle that electrospun PEUU is indeed capable of withstanding the complex mechanical demands imposed by hemodynamic conditions experienced in the pulmonary outflow track. However, the principle thrust for this study was to experimentally quantify physiologically relevant strain fields exhibited by electrospun materials to logically guide further investigations of how mechanical cues at the tissue or organ level alter cell biosynthetic activity.

This experimental setup also enabled the systematic investigation of material structural characteristics on valve function. Leaflet area and geometry in the unloaded configuration remained consistent through the use of a custom valve holding device permitting the effect of fiber orientation on l eaflet deformation and dynamics to be investigated. Results show that structural anisotropy does alter the deformation and dynamic behavior of PEUU leaflets subjected to native pulmonary hemodynamic conditions in a measurable way. Specifically, the magnitude and direction of maximum principle strain were directly attributed to material microstructure. In isotropic materials, the maximum principle stretch direction was observed to follow a curvilinear pattern extending from one commissure region down towards the belly region and back up to the opposing commissure. In contrast, the highly anisotropic material maximum principle stretch direction was consistently in the radial direction.

Peak stretch magnitudes on the order of 1.3-1.4 were measured in the belly region for the isotropic and anisotropic materials. The average deformation across the full leaflet surface was 1.11 ± 0.03 for the isotropic and 1.14 ± 0.06 for the anisotropic materials. While still in the finite deformation range, these values are significantly smaller then those exhibited by native leaflet tissues. For example, in the belly region of native pulmonary leaflet tissues, radial stains upwards of 60% are commonplace. This disparity is largely due to electrospun PEUU materials exhibiting unique low load compliance behavior that does not completely recapitulate the toe-region response of the native leaflet stress-strain response. As a consequence, it was necessary to design the PEUU tri-leaflet valve to be nearly closed in the unloaded configuration. Otherwise, the leaflet was observed to function poorly, allowing regurgitate flow due to inadequate coaptation of the leaflets.

While some experimental observations could not be systematically investigated, they do implicate the critical role material microstructure has on leaflet function. For instance, the isotropic material consistently exhibited a shorter closing duration. The closing duration of the anisotropic material was approximately 40% longer lasting about 30-34 milliseconds. This may be a functional result of difference in bending rigidity of the two materials. The anisotropic material, which exhibits a reduced bending rigidity in the radial direction, may enable a more gradual closing in response when compared to the isotropic material. Interestingly, the opening orifice area appears to be affected by material structure during systole. The isotropic material exhibited an increase orifice area and may be attributed to its ability to more readily deform in the circumferential direction enabling the flowing fluid to force open the structure to a greater extent.

Building on the coupled cell-scaffold deformation results from Chapter 3 and the observed organ level deformations, these findings facilitate the rational design of experimental protocols aimed at quantifying the biosynthetic response of cells exposed to organ level appropriate deformations. More specifically, it is now possible to impose comparable levels of gross mechanical strain but in a simplified and controllable manner, approximating the physiologically relevant magnitudes observed in this Chapter. In this way, it is possible to logically impose gross strain magnitudes spanning sub-physiologic to super-physiologic states to assess the effects on cells populating the construct interstitium.

4.6 LIMITATIONS

While the construction of a tri-leaflet vale using electrospun PEUU resulting in remarkably lifelike leaflet function, this chapter does expose some limitations. Major difficulties were encountered in efforts to capture leaflet motion throughout the cardiac cycle. Due to the extent of leaflet motion and the buckling phenomena observed throughout the systolic phase of the cardiac cycle, it was not possible to adequately capture leaflet motion for reconstruction with the current system. Additional cameras or a more sophisticated reconstruction methodology may prove useful in extending the finding of the current study to encompass a greater portion of the cardiac cycle. Due to the extensive experimental effort necessary, the current study was limited to the assessment of one leaflet for each material structure. This limitation was deemed acceptable, as our primary focus was to approximate physiologically relevant leaflet deformations to inform additional in vitro studies aimed to explore the biosynthetic activity of cell within these scaffolds when exposed to finite defromations.

5.0 EFFECTS OF MECHANICAL STIMULATION ON MATRIX SYNTHESIS OF MICROINTEGRATED CELLS IN FIBROUS ELASTOMERIC SCAFFOLDS

In the case of a tissue engineered pulmonary valve (TEPV), the scaffold must have mechanical characteristics that help to promote tissue formation during both in-vitro conditioning, allow subsequent PV function upon implantation [224]. There is thus a need for anisotropic mechanical properties to facilitate valve function, as well as large strains to promote an aligned network of collagen fibers and overall tissue growth. The basic properties necessary for a bio-absorbable scaffolding material are non-toxicity (including degradation products), biocompatibility, resorbability, strength and processability. Besides the proper material properties, a TEPV scaffold needs to be engineered to possess the proper geometry for tissue formation. Proper engineering and construction techniques are expected to meet many of the other necessary design properties such as geometry, density, compliance, hemodynamics etc. while most of the biological activity of the TEPV should be fulfilled by the growing cells. The polymer scaffold temporarily provides the biomechanical structural characteristics for the replacement "tissue" until the cells produce their own extracellular matrix that will ultimately provide the structural integrity and biomechanical profile for the surrogate "tissue." During this process of tissue development, the scaffold will be gradually degraded eventually leaving no foreign materials within the replaced tissues. To date, TEPV scaffolds used by the Mayer group have been fabricated with non-woven fabrics that are very stiff compared to the native tissue [225].

Additionally, the formation of appropriate tissue prior to implantation requires appropriate mechanical stimulation and scaffold structure to help organize and improve the structure of the tissue formed. For instance, TEPV cultured under static conditions were much less organized and lacked the mechanical integrity of TEPV cultured under pulsatile conditions that mimicked the stresses and strains of the native tissue [181, 226]. Moreover, besides trying to duplicate the gross geometry of the heart valve no attempt has yet been made to design into the scaffold anisotropic properties to duplicate native PV leaflet properties and stimulate tissue formation. Thus, a combination of appropriate scaffold and mechanical stimulation could improve the quality of the tissue formed. To achieve these goals, a systematic study directed towards an understanding of key biomechanical factors in TEPV tissue development is clearly required. This is especially important when working with novel cell sources and scaffolds where the number of experimental variables is very large, as well as avoiding empirical "trial and error" approaches. However, within both the functioning native PV and TEPV, leaflets experience highly complex, time-varying external loading patterns resulting from local hemodynamic forces (including both high shear stresses during ejections and large trans-valvular pressures during diastole). Leaflet tissues respond to these forces by undergoing large anisotropic in-plane stretching and flexure. Mechanistic studies of tissue formation using intact leaflets can thus confounded by highly complex, time-varying physical conditions. Thus, alternative experimental approaches must first be undertaken before translation to the complex functioning valve can be performed.

Development of a functional TEPV will ultimately require that the microstructure, mechanical properties, and cell biology match as closely as possible to the native valve. While the polymer scaffold is meant to provide many of these features during the initial period of tissue

formation, the developing tissue must take over these functions progressively as the scaffold is absorbed. Ideally, the scaffold/tissue construct is seeded and grown in-vitro to achieve sufficient functionality at the time of implantation followed by continued growth and remodeling in-vivo. While progress has been made in cell sources and scaffolds, comparatively little work has been performed on the biomechanical aspects of TEPV biomaterials and the relation to scaffold characteristics. This is in part due to a lack of methods to assess and model the degrading polymer/ECM biocomposite tissue equivalent. Successful mathematical models can also greatly aid in optimizing the incubation process by minimizing the current costly and inefficient trial-and-error approach, and in understanding the in-vivo remodeling process and ultimately the long-term fate of the TEPV. While TEPV offers the potential to overcome limitations of current heart valve prosthesis (especially the very limited options for the pediatric population), the bioengineering challenge is determining how to optimize biological, structural, and mechanical factors of ECM formation for in-vivo success. A major step in this long-term goal is developing a thorough understanding of the underlying structural and mechanical factors responsible for the initial formation of functionally optimal TEPV ECM structures. To this end, the following chapter outlines recent efforts to attain a better understanding of how controlled mechanical cues alter VSMC biosynthetic activity.

5.1 PROTOCOLS

5.1.1 Cell culture and construct production

Microintegrated PEUU constructs were manufactured as described above (see Chapter 3). Immediately following the manufacturing process, the collection mandrel and microintegrated PEUU was moved to a biological safety cabinet maintaining sterile working conditions. The mandrel was then removed leaving a fully intact tube of microintegrated PEUU. For clarification, the following specimen coordinate convention will be used to reference the reader. The longitudinal direction of the construct will be referred to as the principle fiber direction (PD) while the orthogonal or circumferential direction is the cross preferred direction (XD). The tube was then cut in the XD such that approximately four individual ring specimens measuring 10 mm in width were obtained from a given batch. The specimen length and thickness was carefully measured with calipers and recorded. After microintegration VSMC, constructs were placed into static culture media (DMEM, 10% fetal bovine serum, 2% anti-anti, 1% HEPES) for 24-48 hours at 37 C prior to mechanical conditioning. These construct rings were then inserted into the tension bioreactor by sliding the pins of the actuating and stationary pins through the ring annulus (Figure 5-1). To each well, 7mL of complete media was added (DMEM, 10% FBS, 1% penicillin-streptomycin, and 0.5% fungizone, Gibco) and changed every 24 hours.

5.1.2 Mechanical training

The tension bioreactor used in this study is similar to that previously presented by Merryman et al. (Figure 5-1) [200]. Slight modifications were made to update the system enabling improved deformation control via. Motion control was conducted through custom Labview software (National Instruments Corporation, Austin, TX, U.S.A) through an individual stepper motor controller (NI PCI-7334, National Instruments Corporation, Austin, TX, U.S.A)

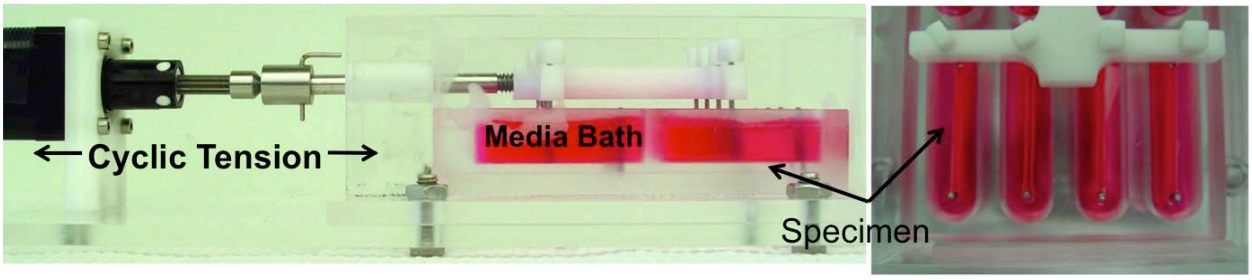

Figure 5-1. Specimen rings under uniaxial tension.

and integrated stepper driver and power unit (NI MID-7604, National Instruments Corporation, Austin, TX, U.S.A). The computer controlled stepper motor (Haydon Kerk Motion Solutions, Waterbury, CT, U.S.A.) drives a linear actuator passing through the chamber wall. The actuating arm has two orthogonal crossbars with exiting holes into which stainless steel pins are inserted. These pins align directly across from the stationary pins to apply uni-directional tension to up to 8 specimens simultaneously. The 8 separate well arrangement was chosen to limited the risk of cross contamination. The entire device, including lids, pins, and screws can be cold gas sterilized with ethylene oxide.

The biosynthetic response of microintegrated VSMC's was investigated for 3 s train levels as dictated by both the cell-construct deformation relationship defined in Chapter 3 and the

observed leaflet deformation magnitudes presented in Chapter 4. The strain level groups were comprised of low (15%), intermediate (30%), and high (50%) strain groups. These magnitudes were chosen as they correspond to a wide range of NAR deformations (Figure 3-7) and physiologically relevant deformations PEUU constructs might experience in vivo. A constant, quasi-static strain rate will be applied sufficient to obtain a 1 Hz cycle duration. Two culture durations of 7 and 14 day time points will be used for each strain level to quantify the ECM synthesis capacity of VSMC microintegrated in electrospun PEUU. For comparison purposes, 0 day and static groups were also carried out as well as control groups comprised of acellular electrospun PEUU. Upon completion of the mechanical training protocol, specimen rings were removed from the bioreactor, and specimen length, width, and thickness were measure and recorded for comparison with specimen dimensions prior to training.

5.1.3 Quantifying ECM biosynthesis – biochemical assays and histology

After dimensional changes were recorded, the construct rings were dissected into segments for biochemical analysis. Full width cuts were carried out at both locations that came in contact with the loading pins resulting in two segments. Due to the compressive forces experienced at the loading pin regions, the specimen consistently exhibited a compressed morphology. Since this segment was exposed to a combined loading modality, and not simply tensile loading, it was trimmed and discarded from further use. One segment was dedicated to collagen assays while the other segment was again bisected in the PD such that a small, 2 mm, segment was obtained and immediately placed immediately placed in 10% buffered formalin for histological analysis. The remaining segments were then bisected in the XD with a portion of each being used in GAG and DNA quantification assays respectively.

DNA was quantified by a technique adapted from Kim et al [227]. For each assay, samples were lightly patted dry with paper towel to remove excess fluid and weighed prior to extraction. Each sample was placed in a microcentrifuge tube and extracted in 1 ml of 0.125 mg/ml papain solution for 10 hours in a 60°C water bath. The 0.125 mg/ml papain solution was made immediately prior to use by adding L-cysteine dihydrochloride (Sigma) to a phosphate buffered EDTA solution (PBE) to a concentration of 10 mM, clarifying the solution using a syringe-driven filter (0.2 μm Millex®-LG PTFE membrane; Millipore, Bedford, MA), and adding papain (minimum 10 units/mg (P4762); Sigma) to a concentration of 0.125 mg/ml. The PBE solution was made beforehand by adding sodium phosphate dibasic (Sigma) and ethylenediaminetetraacetic acid (EDTA; Sigma) to deionized water at concentrations of 100 mM and 10 mM, respectively. The PBE solution was balanced to pH 6.5 with 0.5 N hydrochloric acid (Sigma) and sterile filtered using a vacuum filtration unit (0.2 μm PES membrane; Nalgene Labware). The extracts were assayed using the PicoGreen dsDNA quantitation kit (Molecular Probes, Eugene, OR) per the manufacturer's instructions and using the blue channel of a TBS-380 Mini-Fluorometer (Turner Biosystems, Sunnyvale, CA).

Collagen and sulfated glycosaminoglycans (S-GAG) were assayed by techniques adapted from Brown et al [228]. For each assay, samples were lightly patted dry with paper towel to remove excess fluid and weighed prior to extraction. Total collagen was extracted from samples using a solution of 0.5 M acetic acid (Sigma) and pepsin (1 mg/ml Pepsin A (P-7000); Sigma). Each sample was placed in a microcentrifuge tube and incubated in 1 ml of extraction solution overnight (~ 16 hours) on a rocker (Orbitron Rotator I™; Boekel Scientific, Feasterville, PA) in a refrigerator at 2-8°C.

Proteoglycans and S-GAG were extracted using a solution of 4 M guanidine-HCl (Sigma) and 0.5 M sodium acetate (Sigma). To minimize proteolysis during the extraction, 100 µl of protease inhibitor cocktail stock solution was added to each extraction solution. The stock solution was prepared according to the manufacturer's recommendations by dissolving one Complete Mini Protease Inhibitor Tablet™ (Roche Diagnostics, Basel, Switzerland) in 1.5 ml of deionized water. Each sample was incubated in 1 ml of extraction solution overnight on a rocker table (Boekel Scientific) in a refrigerator at 2-8°C. Following the extraction steps, the collagen and S-GAG extracts were assayed according to the guidelines provided with the Sircol™ and Blyscan™ assay kits, respectively (Biocolor Ltd., Newtownabbey, N. Ireland) using a Genesys 20 spectrophotometer (Thermo Spectronic, Rochester, NY).

Histological evaluations were carried out on dedicated specimen segments via paraffin embedding. Serial sections (6 µm) were stained with hematoxylin and eosin (H&E) for morphology, and with picrosirius red, a collagen protein specific stain.

5.1.4 Cellular response to global deformation

Preliminary results consistently indicated that 30% strain induced the highest biosynthetic response of the three strain levels investigated. As such, an additional group of specimens were mechanically conditioned for 21 days in an effort to ensure significant ECM accretion and organization. These specimens were used to investigate cellular deformations in response to macroscopic deformations similar to that previously described in Chapter 3. Unfortunately, direct comparison could not be made via confocal imaging modalities on specimens after mechanical conditioning. After the extended dynamic culture durations, it was not uncommon for cells on the specimen surface to undergo extensive proliferation. This translated to a

thickening at the specimen surface, prohibited appropriate imaging depth via confocal imaging. Instead, specimens were dissected immediately following dynamic culture by cutting segments 10 mm in length from the specimen midway between the post contact points. Two small custom wire coils were passed through the specimen four times at opposite ends [229] . The wire coils were used to carefully mount and hold the specimen on a custom mounting frame. The wire coils were rigid and so opposed displacements in the direction orthogonal to the applied deformation. The frame was employed to constrain the specimen in its deformed configuration of 15%, 30%, and 50% strain. Two specimens prepared in this manner for each strain level. All specimens were deformed in the same direction of stretch during dynamic culture (i.e. XP). Once placed on the mounting frame, the specimen was placed in 10% buffered formalin for 24 hours.

One practical issue when working with polymeric biomaterials is that traditional histological fixatives do not stabilize the entire structure in its given conformation. This can result in residual stresses being relieved upon being placed in embedding media or when sectioned. As a result, it was necessary to rely on the characteristics of the mounting media, glycomethacrylate (GMA) resin, to constrain a deformed specimen. After fixation was complete, the specimens were cast, along with the mounting frame, in GMA. Once the GMA was fully polymerized, the mointing frame and springs could be trimmed away maintaining the specimen in its deformed configuration for sectioning. Sections (5 μm) were cut, processed, and stained with H&E for further inspection via brightfield microscopy.

To quantify cellular deformations within these specimens, the particle analysis tools of ImageJ (National Institutes of Health) were employed to carry out measurements in a systematic manner. Processing involved the color segmentation of cells and their nuclei and fitting an ellipse to the segmented particles resulting in major and minor axis length measurements. Unlike

the analysis carried out in Chapter 3, this analysis included all detected cells for the quantification of changes in aspect ratio. This analysis was carried out on 3 digitized images from each specimen and compiled. Results are presented as mean ± standard deviation.

5.2 RESULTS

5.2.1 Conformational effects of mechanical training

From dimensional measurements obtained prior to and immediately following cyclic tensile loading, is was possible to quantify the effects of mechanical training in terms of conformational changes of the construct. The constructs did not exhibit a significant change in width but they did exhibit measurable elongation. Results indicate that both the duration of mechanical training and magnitude of the imposed cyclic deformation were significant contributors to specimen elongation (Figure 5-2a). While this finding is not unexpected, it could have interesting implications on polymer and ECM organization within the construct. Interestingly, acellular scaffolds exposed to cyclic tension for 21 days exhibited significantly more elongation than those that were microintegrated (Figure 5-2b). In regards to dimensional changes due to mechanical training, it was determined that matrix deposition has a profound effect on construct thickness accounting for an average thickening of 18.8 ± 3.1 percent while acellular specimens exhibited a decrease in thickness of 25.0 ± 7.6 percent for specimens exposed to 30% cyclic strain for 21 days.

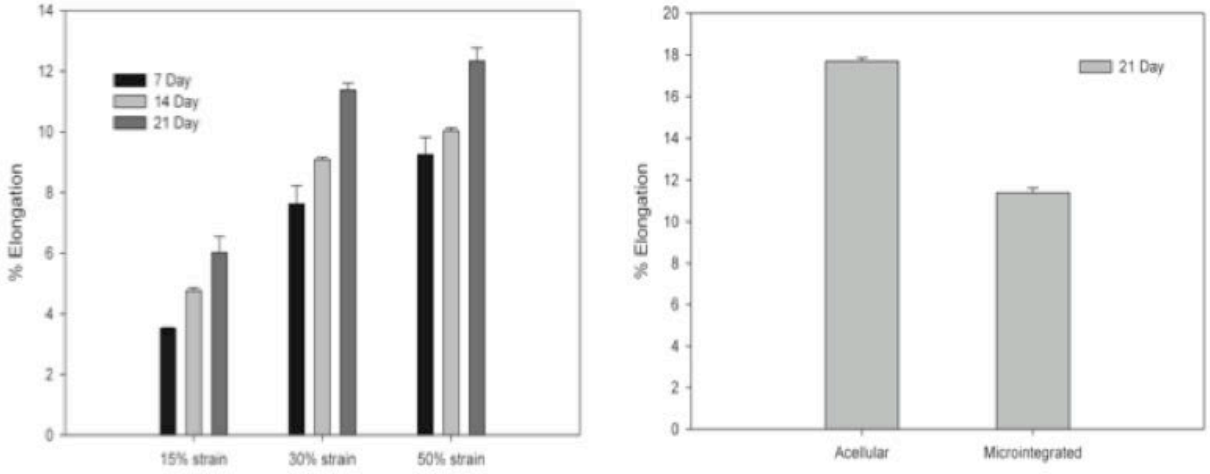

Figure 5-2. Specimen elongation as a function of strain magnitude and duration.

In terms of specimen volumetric changes resulting from mechanical training, no measurable change was observed for any specimens after 7 days (Figure 5-3). At 14 days, 30% and 50% strain groups exhibited a marginal increase in total volume but were not significantly different from one another. Specimens subjected to 30% strain for 21 days exhibited statistically significant increases in volume. Similarly, the acellular group subjected to 30% strain for 21 day exhibited a slight increase of thickness of approximately 3.0 ± 0.5 percent.

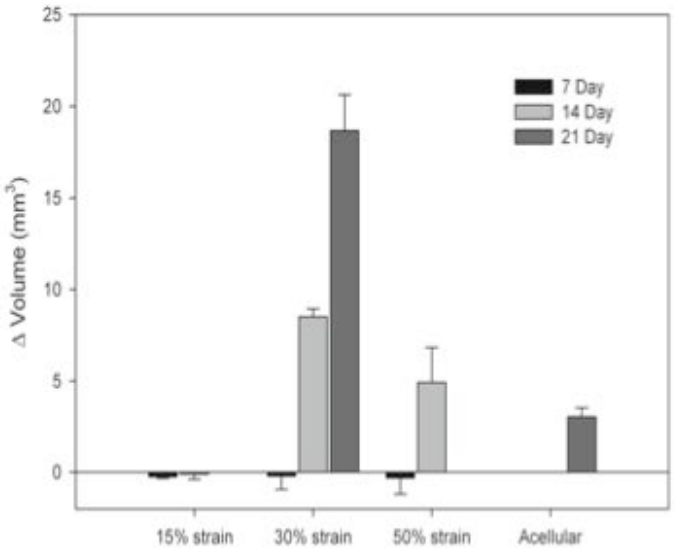

Figure 5-3. Volumetric changes observed during mechanical training.

5.2.2 Assessing tissue accretion

Due to inherent variability in the manufacturing process, large variations in cell densities were encountered. As a result, direct comparisons of ECM protein quantity could not be obtained. Instead, matrix protein quantities we normalized by DNA content on a wet weight basis. Results indicate that VSMC biosynthetic behavior is indeed a function of global strain with markedly improved soluble collagen synthesis in specimens exposed to 30% strain, while specimens subjected to 15 or 50% strain showed minimal increase over static and day 0 specimens (Figure 5-4). It is interesting to note that proteoglycan deposition was not sensitive to cyclic tension duration. Instead, sulfated GAG (sGAG) production appears to be driven primarily by the application of cyclic deformation as seen by a steady accretion response for all dynamically conditioned specimens.

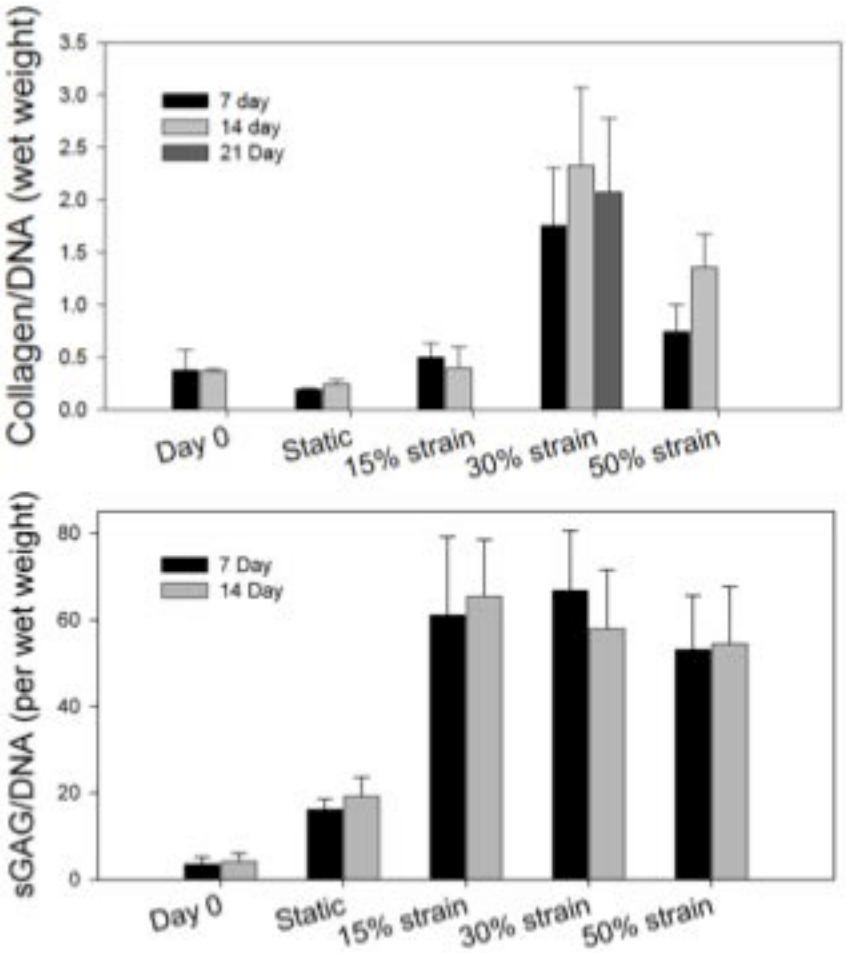

Figure 5-4. Matrix accretion quantification.

Biochemical assay results were corroborated by traditional histological preparations stained with H&E for general morphological assessment (Figure 5-5) and picrosirius red that binds specifically to collagen (Figure 5-6). From histology, we can see that cells are distributed reasonably well throughout the construct thickness at the time of manufacturing. Furthermore, after the application of 30% cyclic strain for 14 days cell and ECM rich regions, denoted by dark bands through the construct, can be seen to form.

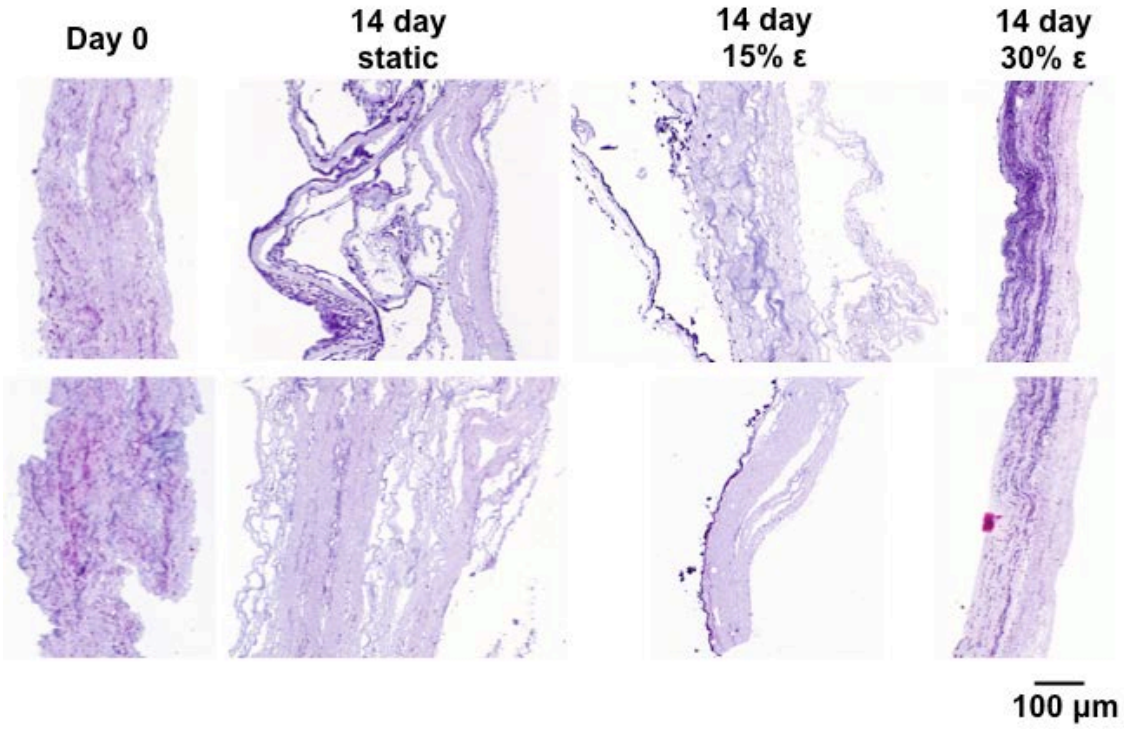

Figure 5-5. Representative H&E histology from dynamic cultured constructs.

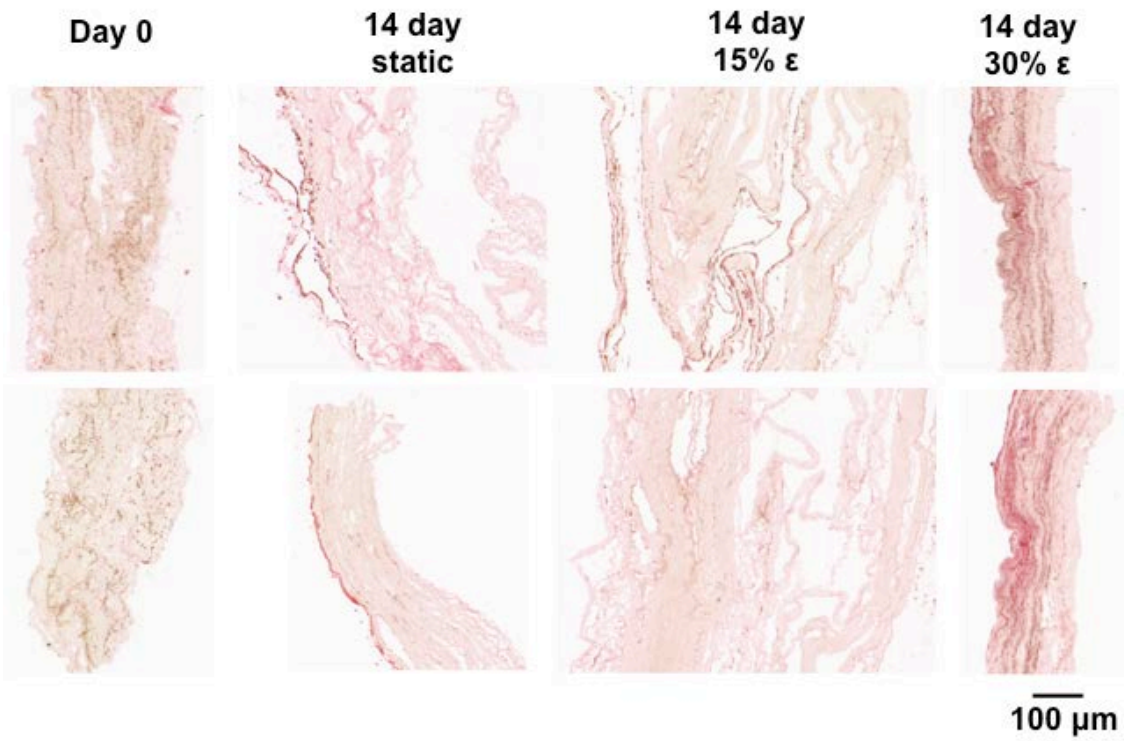

Figure 5-6. Representative picroserius histology from dynamic cultured constructs.

Static and 15% strain groups showed little discernable difference from Day 0. If we focus on a comparison between the day 0 and 30% strain groups (greatest matrix accretion response), we can see that cell viability is well preserved at the 14 day time point and cell and the matrix proteins they create tend to form a lamellar arrangement. Also, the additional matrix content appears to reduce delamination effects from handling and processing for histology.

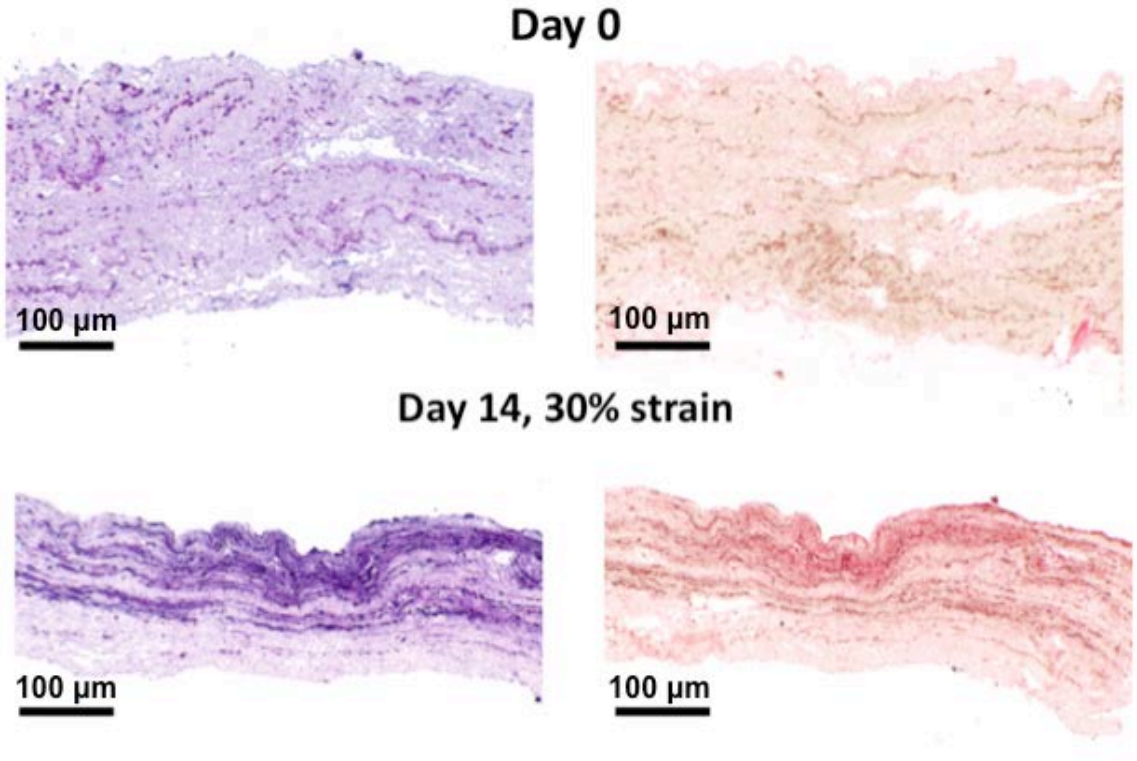

Figure 5-7. Representative tissue accretion response resulting from dynamic culture.

5.2.3 Cellular response to global deformation

It is anticipated that with de novo matrix deposition, there will be a concomitant change in the way global deformation is transmitted to the cell; hence, altering the cells deformation behavior to be more like that observed in native valve leaflets. After mechanical training, microintegrated

PEUU provides us with an ideal platform to test this hypothesis. In an effort to ensure significant ECM production and organization, mechanical training of 6 additional specimens was carried out for 21 days. Unfortunately, in our efforts to build upon what we learned in Chapter 3, it was determined that confocal imaging modalities were too limited in penetration depth to faithfully compare real time in situ deformation behavior with and without the presence of ECM. As a result, 3 discrete levels of construct deformation (15%, 30%, and 50%) were investigated by constraining the construct during fixation and embedding in GMA. After sectioning, there was no visible warping or deformation of the section that might indicate the release of internal stresses.

Unlike the analysis carried out in Chapter 3, all visible cells were included in the quantification of cellular deformation with construct strain. A straightforward image analysis approach was implemented to segment the cell bodies from their surrounding environment. Next, an ellipse was fit to the segmented geometry to measure the major and minor axis length enabling the calculation of a cell aspect ratio (CAR). When this analysis was carried out on newly produced constructs (Day 0), the change in cell aspect ratio followed a very similar plateau trend as was observed with confocal imaging modalities as described in Section 3.2 (Figure 5-8). However, after dynamic culture for 21 days and subsequent matrix production, the change in cell deformation with construct strain follows an affine trend. Furthermore, a statistically significant difference in cell aspect ratio change was observed at peak deformation between the Day 0 and dynamically cultured groups.

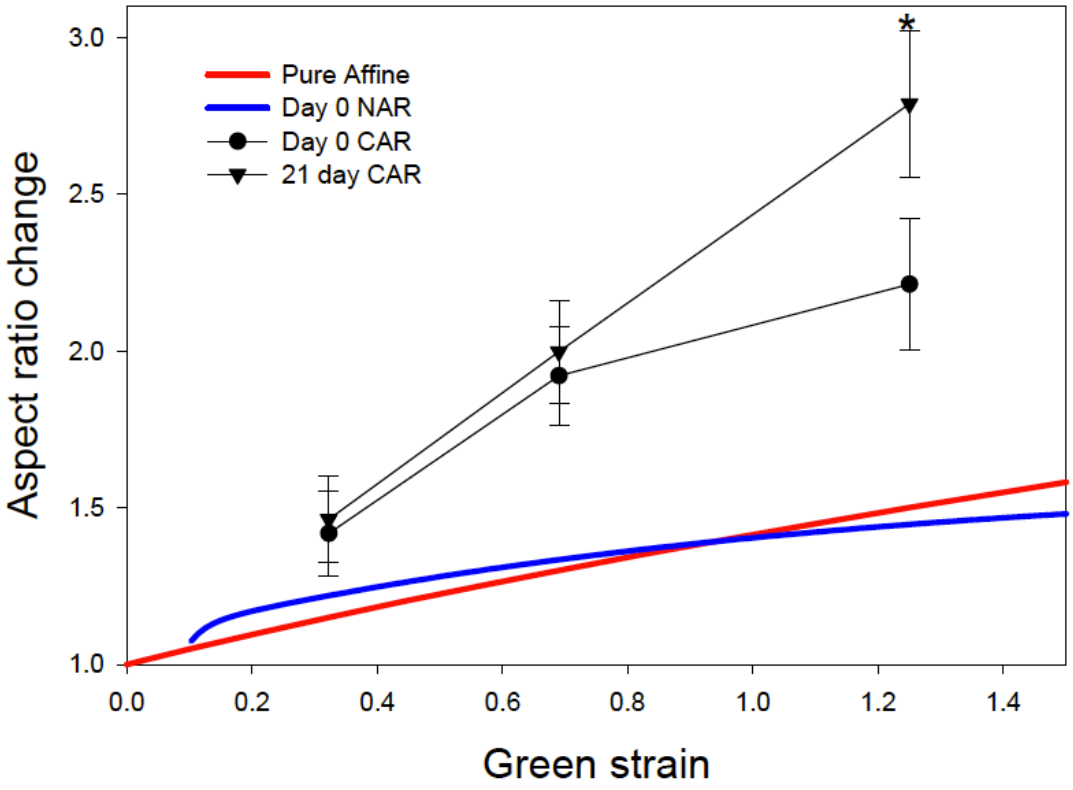

Figure 5-8. Initial and dynamic cultured cell deformation response to construct strain.

5.3 DISCUSSION AND IMPLICATIONS

Electrospinning permits fabrication of biodegradable elastomers into matrices that can resemble the scale and mechanical behavior of the native extracellular matrix. Traditionally, achieving high-cellular density and infiltration through cell seeding methods with the electrospinning technique remains challenging and time consuming. This obstacle has been overcome by electrospraying VSMC concurrently with electrospinning biodegradable,

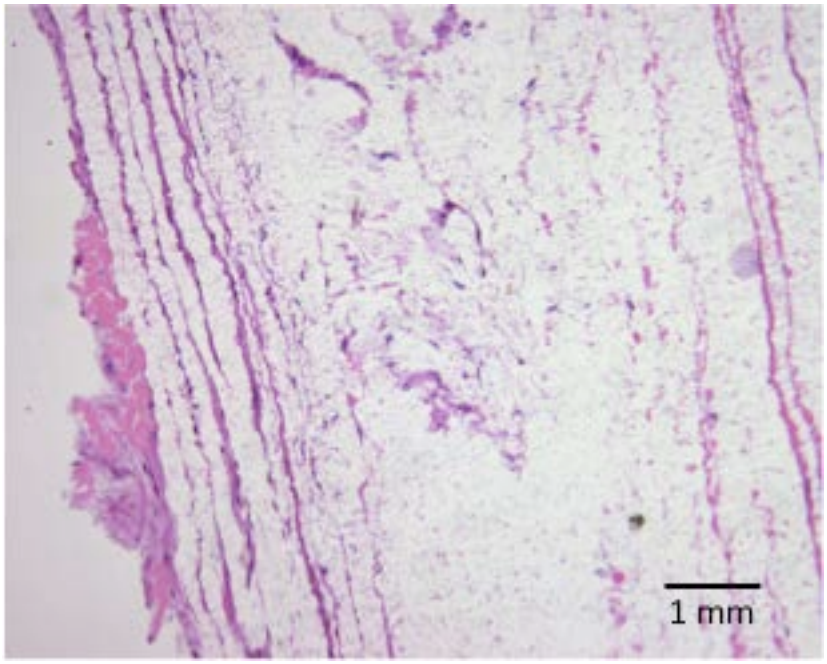

Figure 5-9. Lamellar cell and polymer arrangement produce by concurrent electrospinning and electrospraying after 21 days of culture.

elastomeric PEUU. While we have the capability to deliver cells throughout the specimen, the porous structure created, appears to restrict cell motility. A lamellar structure tends to be created during the concurrent electrospinning and electrospraying process with cell dense regions and polymer rich regions dispersed throughout (Figure 5-9). This arrangement persists through dynamic mechanical conditioning, where the cells do ha ve the ability to proliferate but are restricted to their respective, localized cell dense pockets. As the de novo matrix phase evolves, it tends to cause an overall thickening of the construct as seen by measurements taken prior to and following culture as well as histological sections. Acellular specimens, who undergo mechanical conditioning, also exhibited a slight increase in thickness. While it doesn account for the magnitude of thickening in the cell integrated specimens, it is likely attributed to polymer

fiber swelling. In other words, construct growth due to matrix accretion is predominantly observed in the transmural direction.

Another interesting finding is that cell inclusion through electrospraying mitigated construct elongation due to cyclic loading. This may be attributed to matrix protein production effectively reinforcing or stabilizing the overall structure. While not quantified, the handling characteristic of these constructs improves dramatically after dynamic culture. After production, the constructs typically exhibit the tendency to delaminate. However, after mechanical conditioning for 21 days, the constructs are much more resilient to handling and are less likely to delaminate.

This study is the first to quantify the effects of controlled mechanical cues on matrix synthesis in microintegrated elastomeric electrospun scaffolds. Results indicate that VSMC biosynthetic behavior is indeed a function of global strain with markedly improved matrix (soluble collagen) synthesis in specimens exposed to 30% strain. Static culture appears to have a deleterious effect on cell health, visual evidence of which can been seen in H&E stained sections where cells and their nuclei often appear fragmented or exhibiting a round cell morphology. This translated to minimal ECM synthesis during culture. Specimens subjected to 15% cyclic strains were not significantly different from static or day 0 specimens from a matrix synthesis or gross morphological perspective.

When specimens were subjected to the largest strain level, an intermediate biosynthetic response was observed. The mechanism for this behavior is not known but it may indicate that such large strains for newly integrated cells has undesirable effects. For instance, large tractions such as this may be deleterious for integrated cells initially, resulting in a lag period of matrix production where cells are reorienting or altering their interaction with surrounding PEUU fibers

to a more favorable stress state. Another plausible explanation could involve up regulation and production of matrix metalloproteinases (MMP) resulting in a competing effect, limiting new matrix deposition. Cyclic strain has been observed to induce MMP up regulation and release and is typically associated with active remodeling responses [230-232]. While a highly non-linear collagen synthesis behavior was observed, proteoglycan production was steady for all dynamic strain levels and time points studied. Cyclic strain appears to induce sGAG production but is not dependent on strain magnitude.

Building on previous work [75], the relationship between cell deformation and macroscopic construct strain was observed to shift from a nonlinear response, which plateaus at high strain to a linear cell deformation behavior with global deformation after mechanical conditioning (Figure 5-8). This supports our hypothesis that the evolution of biological constituents within engineered tissues plays a pivotal role in the mechanical traction experienced by the cell in response to global mechanical cues. It would be interesting to see if the coupled cell-construct deformation response would continue to transition towards that observed in native tissues (Figure 5-10). Furthermore, this phenomenon could represent a possible metric to evaluate the ability of an engineered tissue to recapitulate healthy native function or be utilized in modeling efforts to better understand and predict matrix accretion behaviors.

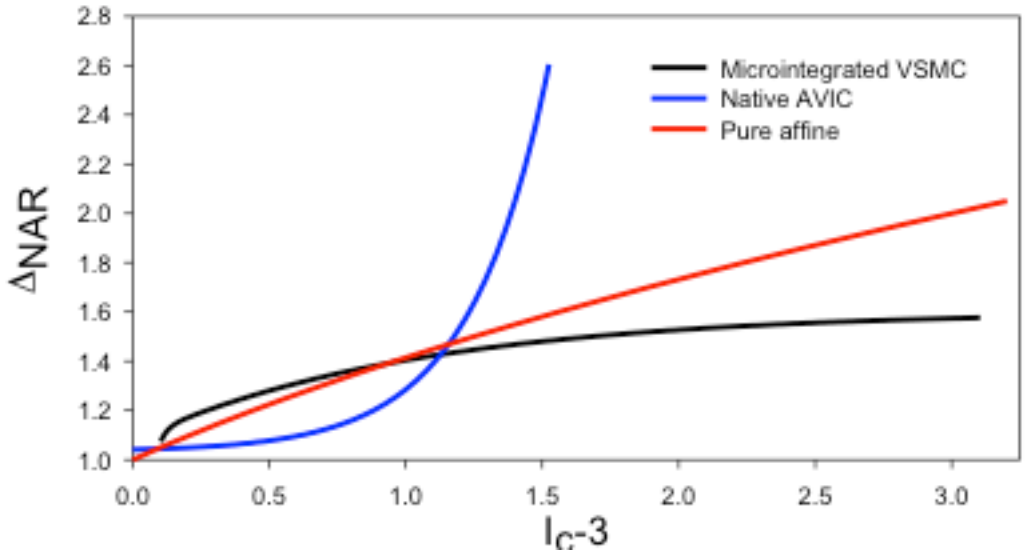

Figure 5-10. Cellular deformation comparison between microintegrated constructs and native VIC.

5.4 LIMITATIONS

Due to practical concerns in the current study, it was not possible to obtain real time in situ measurement of cellular deformation. Instead, a histology-based method was developed that required significant processing steps which could alter or distort the morphology of biological components within the engineered construct. Furthermore, the examination presented in Chapter 3 could not be compared to directly; both in terms of methods and the magnitude of construct deformation. After dynamic culture, the constructs were observed to be less distensible without inducing damage. As a result, 3 discrete levels of deformation were investigated (15%, 30%, and 50%) reflecting the strain magnitudes imposed during in vitro dynamic culture. The complex interactions between microintegrated VSMC and electrospun polymer scaffolds remain largely

unknown. While it was possible to quantify the relationship between cells and construct deformation, a mechanistic understanding of this phenomenon could not be readily obtained.

6.0 QUANTIFYING THE MECHANICAL CONTRIBUTION OF DE NOVO EXTRACELLULAR MATRIX

6.1 CONSTITUTIVE MODELS OF SOFT TISSUES

Constitutive models are theoretical descriptions of the mechanical behavior of a material. The functional form of which is determined by mechanical testing experiments wherein the resulting stress-strain behavior of a material offer modeling parameters. Soft tissues are characteristically complex (i.e. complex geometry, highly non-linear, highly anisotropic, undergo large deformations) which confounds accurate and unique constitutive relation determination. Soft biological tissue constitutive model development has been an active area of research for several decades. Stemming from the pioneering work introduced by Fung [233] in 1979, researchers have introduced a broad spectrum of soft tissue constitutive models. In general, these models have been application specific and can be classified as either phenomenological or structural. The term "structural" has been used to label models which characterize material response in terms of underlying tissue constituents. Researchers have successfully demonstrated the reliable and robust nature of these models in applications involving cardiac tissue, skin, blood vessels and the tissue of eye lens capsule [234-238]. Although varied approaches have been employed, the primary model goal has focused on accurate representations of the tissue fibrillar network. Independent of application, the collagen fiber network is considered to be the dominant

mechanism contributing to mechanical response. Therefore, many of the soft tissue constitutive models presented in the literature outside of heart valve mechanics involve features that can be applied to heart valve specific models.

Lanir and Fung established the biaxial mechanical response of soft tissues in 1974 through a series of tests involving rabbit skin [236]. Based on observations of these stress-strain relationships, Fung and co-workers later proposed a strain energy function to describe the highly nonlinear anisotropic material response exhibited in the artery wall [239]. Termed as "Fung-type" models, researches have used variations of the phenomenologically-motivated Fung strain energy form to address a broad spectrum of soft tissue applications [63, 65, 145, 235, 238, 240, 241]. The success and acceptance of the Fung model can be attributed to its robust ability to capture highly nonlinear experimentally derived data over a wide strain range. However, convexity and material stability issues limit the reliability of Fung-type models in a generalized computational framework.

While phenomenological models have been successfully applied to a broad spectrum of soft tissue applications, they lack the ability to capture the underlying mechanisms contributing to tissue behavior. Understanding the link between these underlying physiological functions is central to the development of meaningful constitutive models. Examination of pathological states and engineered tissue through computational simulation require a model foundation based on microstructural architecture. A class of models, referred to as "structural", attempt to characterize organ level tissue response in terms of fibrillar scale properties. These models are based on physiological microstructural features quantified through experiential means. Key tissue features such as fiber orientation and crimp period are directly incorporated into the

model. Researchers have used structural-based models to describe heart valve mechanical response [235-238].

In their work related to arterial wall mechanics, Holzapfel et al. proposed a constitutive model, which can be considered as "hybrid" in the structural sense [242]. This model considers a family of fibers embedded in an isotropic ground-matrix. A concept common to other structural-based approaches where the influence of non-fiber ECM components is characterized by a incompressible isotropic hyperelastic strain energy function [243]. Contributions to the strain energy from decoupled fiber families are described by an assumed exponential function. In the context of scale relevant modeling, the Holzapfel model addresses microstructural concerns by establishing discrete fiber families. However, the fiber response is characterized by a phenomenological-like function; a feature that is attractive in the sense that issues of convexity are supported by the assumed form.

6.1.1 Fundamentals of hyperelasticity

The two important measures in a material's mechanical behavior are stress, defined in its simplest form as force divided by the area it is acting on, and stretch or strain, measures of a change in length upon loading. An important aspect of defining a tissue's stress-strain behavior is the definition of zero stress state or reference state. In this state no loading is applied and the material is assumed to be completely stress free. In the case of finite deformations, several different definitions of stress and strain are used. Let the vector **X** represent the position of a point P in the reference configuration, and **x** the position of that same material point in a deformed configuration. Then, the deformation gradient tensor **F** describes the transformation of the line segment d**X** to d**x** as $\mathbf{F} = \partial\mathbf{x}/\partial\mathbf{X}$. A change in an infiitesimal volume element (dV) from

the reference to the deformed configuration is defined as $J = dV/dV_o = \det\mathbf{F}$, which is equivalent to $J = \rho/\rho_o = \det\mathbf{F}$ due to conservation of mass. In here, ρ is the tissue density in the current configuration and $\det\mathbf{F}$ is the determinant of $\mathbf{F}$.

Because $\mathbf{F}$ contains rigid body motions, alternative measure of strains are defined that purely represent deformations giving rise to strain energy. The Right Cauchy-Green tensor $\mathbf{C}$, the Left Cauchy--Green tensor $\mathbf{B}$, and the Green--Lagrange or Green's strain tensor $\mathbf{E}$ are defined in below, where $\mathbf{I}$ is the identity tensor.

$$\begin{aligned}\mathbf{C} &= \mathbf{F}^T\mathbf{F} \\ \mathbf{B} &= \mathbf{F}\mathbf{F}^T \\ \mathbf{E} &= \frac{1}{2}(\mathbf{C}-\mathbf{I})\end{aligned} \qquad \text{EQ. 6-1}$$

The Cauchy stress tensor $\mathbf{t}$ is derived from the traction vectors acting on a body's surfaces and is defined in the deformed configuration; in a uniaxial sense it is defined as force divided by deformed area. The Lagrangian or 1st Piola Kirchhoff stress tensor $\mathbf{P}$ is defined in the referential configuration and in a uniaxial sense is defined as force dived by initial area. The 1st Piola Kirchhoff stress tensor is related to the Cauchy stress tensor as $\mathbf{P} = J\mathbf{F}^{-1}\mathbf{t}$. The 2nd Piola Kirchhoff stress tensor $\mathbf{S}$, which has no direct physical meaning and represents a very useful stress measure in computational mechanics because it is a symmetric tensor, is in turn related to $\mathbf{t}$ as follows: $\mathbf{S} = J\mathbf{F}^{-1}\mathbf{t}\mathbf{F}^{-1}$. EQ. 6-2 gives an overview of all relations, including those between $\mathbf{P}$ and $\mathbf{S}$.

$$\begin{aligned}\mathbf{P} &= J\mathbf{F}^{-1}\mathbf{t} = J\mathbf{t}\mathbf{F}^{-T} \\ \mathbf{S} &= J\mathbf{F}^{-1}\mathbf{t}\mathbf{F}^{-T} \\ \mathbf{P} &= \mathbf{F}\mathbf{S} = \mathbf{S}\mathbf{F}^T \\ \mathbf{S} &= \mathbf{F}^{-1}\mathbf{P} = \mathbf{P}\mathbf{F}^{-T}\end{aligned} \qquad \text{EQ. 6-2}$$

Thermodynamic considerations place important restrictions on the functional form of constitutive equations [244] and are based on the first and second laws of thermodynamics for a thermo-mechanical continuum. Thermal and mechanical effects dominate the material's behavior, and electrical, chemical and other effects are ignored. The following provides a summary of the relevant concepts as previously presented in "Nonlinear theory of elasticity. Applications in biomechanics", Chapter 5 by Taber [244], "Nonlinear solid mechanics. A continuum approach for engineering" by Holzapfel [245], and "The nonlinear field theories of mechanics" by Truesdell and Noll [246]. The first law of thermodynamics deals with conservation of energy. For an arbitrary material region of a thermomechanical continuum, the principle of conservation of energy can be written in the form

$$\dot{K} + \dot{U} = \dot{P} + \dot{Q} \qquad \text{EQ. 6-3}$$

where K is the kinetic energy, U the internal energy (consists of thermal energy and strain energy), P the mechanical power input (the rate of work done on a body by applied loads) and Q the rate of heat input. The left side represents rate of change in internal energy, the right side the rate of change in energy that is added externally. For an arbitrary volume element that deforms from dV into dv, EQ. 6-3, written in the local form, and in terms of the Cauchy stress tensor **t**, or the first Piola Kirchhoff stress tensor **P**, respectively, results in:

$$\begin{aligned} \rho \dot{u} - \mathbf{t} : \mathbf{D} - \rho r + \overline{\nabla} \cdot \mathbf{q} = 0 \\ \rho_0 \dot{u} - \mathbf{P} : \dot{\mathbf{F}}^T - \rho_0 r + \nabla \cdot \mathbf{q}_0 = 0 \end{aligned} \qquad \text{EQ. 6-4}$$

where ρ_0 is the mass density in the reference configuration; ρ is the mass density in the deformed state; u the internal energy per unit mass; **D** the rate of deformation tensor; **F** the deformation gradient tensor; r the rate of heat production per unit mass due to internal sources; q and q_0 the outward--directed heat flux vectors per unit deformed and undeformed surface area,

respectively; $\nabla$is the gradient operator, and $\overline{\nabla}$ is the gradient operator with respect to the deformed state. The resulting form of the first law of thermodynamics (EQ. 6-4)) states that the rate of increase in internal energy of a volume element ($\rho\dot{u}$ or $\rho_0\dot{u}$) is equal to the sum of the rate of work done by the stresses on the element, i.e. the stress power (**t**:**D** or $\mathbf{P}:\dot{\mathbf{F}}^T$), the rate of internal heat production (ρr or $\rho_0 r$), and the rate of heat flow into the element ($-\overline{\nabla}\cdot\mathbf{q}$ or $-\overline{\nabla}\cdot\mathbf{q}_0$).

The first law of thermodynamics basically states that work can be converted into heat and vice versa, so that the total energy remains constant, but it does not consider dissipated energy. The second law of thermodynamics restricts the direction of energy conversion processes and is based on the concept of entropy (Σ). For a solid body, the second law of thermodynamics states that the time rate of change of the total entropy in a body is greater than or equal to the sum of the influx of entropy through the surface of the body and the entropy generated by internal heat sources. The Lagrangian local forms of this relation, which is also called the Clausius-Duhem inequality, is given by

$$\dot{\Sigma} - \frac{r}{T} + \frac{1}{\rho_0}\nabla\cdot\left(\frac{\mathbf{q}_0}{T}\right) \geq 0 \qquad \text{EQ. 6-5}$$

The possible forms for constitutive equations are restricted by thermodynamic considerations based on EQ. 6-4 and 6-5. The relevant constitutive principles for a thermomechanical material include coordinate invariance, determinism, local action, equipresence, material objectivity, physical admissibility, and material symmetry. The first six are described below;; the principle of material symmetry is used when specific forms of constitutive equations for elastic materials are derived, taking into account symmetries in the material.

The principle of coordinate invariance states that constitutive equations must be independent of the coordinate system that is used to describe the motion of a body, and hence should be developed in tensor form. The principle of determinism states that the stress distribution in a body at a given time is depended on the history of deformation and temperature. For an elastic material however, no energy is dissipated and temperature effects are neglected, so the stress at time t depends only on the instantaneous deformation. The principle of local action indicates that the motion and temperature at a point in a thermoelastic body can be determined from the values and the spatial derivatives of the dependent constitutive variables at a nearby point. For simple materials, this suggests, together with the principle of determinism, that the constitutive equations for a thermoelastic material can be written in the form

$$\begin{aligned} \mathbf{t} &= \mathbf{t}(\mathbf{R},\mathbf{F},T,\nabla T) \\ \mathbf{q} &= \mathbf{q}(\mathbf{R},\mathbf{F},T,\nabla T) \\ u &= u(\mathbf{R},\mathbf{F},T,\nabla T) \\ \Sigma &= \Sigma(\mathbf{R},\mathbf{F},T,\nabla T) \end{aligned} \qquad \text{EQ. 6-6)}$$

where **R** defines the spatial dependency. The principle of equipresence states that an independent variable that appears in one constitutive equation for a material, must be present in all constitutive equations for that material. This is useful if other effects are to be included.

The principle of material objectivity or material frame indifference states that constitutive equations must be invariant under rigid motions of the spatial reference frame. In other words, the events occurring at a point in a body must be independent of the motion of the observer. The deformation gradient tensor **F** is per definition an objective quantity, since it describes changes relative to a given reference configuration. Under a change of reference frame, a general second order tensor **T** transforms through the rotation tensor **Q** as $\mathbf{T}^{*} = \mathbf{Q}\cdot\mathbf{T}\cdot\mathbf{Q}^{T}$. Since deformation and temperature are objective, the constitutive relations for a thermoelastic material (EQ. 6-6)) are

frame indifferent. Using the conversion definitions of stress measures (EQ. 6-2), this eventually states

$$\begin{aligned}\mathbf{S} &= g(\mathbf{U}) \\ &= f(\mathbf{C}) \\ &= h(\mathbf{E})\end{aligned} \qquad \text{EQ. 6-7}$$

where *g*, *f* and *h* are called response functions, and **U** is the right stretch tensor which is obtained through polar decomposition of $\mathbf{F}$ ($\mathbf{F} = \mathbf{Q} \cdot \mathbf{U}$). For small rotations, this also holds for the other stress tensors **t** and **P**.

The principle of physical admissibility states that constitutive equations must be consistent with any of the basic laws of continuum mechanics, including the first and second laws of thermodynamics (EQ. 6-4 and 6-5). Stating these equations in terms of the 2nd Piola Kirchhoff stress **S** and eliminating *r* between these two equations yields

$$\rho_0\left(T\dot{\Sigma} - \dot{u}\right) + \mathbf{S} : \dot{\mathbf{E}} = 0. \qquad \text{EQ. 6-8}$$

EQ. 6-8 can now be combined with the general constitutive equations in EQ. 6-6) and the case is considered for which temperature is considered to be the independent variable. It is convenient to introduce the Helmholtz free energy function per unit undeformed volume as

$$\psi = u - T\Sigma \qquad \text{EQ. 6-9}$$

as a replacement for the internal energy u. Then, EQ. 6-6 is replaced by

$$\psi = \psi\left(\mathbf{R}, \mathbf{E}, T, \nabla T\right) \qquad \text{EQ. 6-10}$$

and EQ. 6-8 is transformed to

$$-\rho_0\left(\dot{\psi} + \Sigma\dot{T}\right) + \mathbf{S} : \dot{\mathbf{E}} = 0 \qquad \text{EQ. 6-11}$$

Combining EQ. 6-10 and 6-11, and using the chain rule yields

$$\left(\mathbf{S} - \rho_0 \frac{\partial \psi}{\partial \mathbf{E}}\right) : \dot{\mathbf{E}} - \rho_0\left(\Sigma + \frac{\partial \psi}{\partial T}\right)\dot{T} - \rho_0 \frac{\partial \psi}{\partial \nabla T} \cdot \nabla \dot{T} = 0 \qquad \text{EQ. 6-12}$$

For independent strain and temperature distributions, each of the three terms equals zero. And since **E** and T (and hence $\dot{\mathbf{E}}$ and $\dot{T}$) can be chosen arbitrarily, the expressions in parentheses must be zero. This results in the relations:

$$\mathbf{S} = \rho_0 \frac{\partial \psi}{\partial \mathbf{E}}$$
$$\Sigma = -\frac{\partial \psi}{\partial T} \qquad \text{EQ. 6-13}$$
$$\frac{\partial \psi}{\partial \nabla T} = 0$$

If the deformation is isothermal ($\dot{T}$ = 0) which is usually considered to be the case for biological tissues, then $\psi = \psi(\mathbf{R}, \mathbf{E})$ and the material behaves elastically. In this case, a strain energy

$$\Psi(\mathbf{R}, \mathbf{E}) = \rho_0 \psi(\mathbf{R}, \mathbf{E}) \qquad \text{EQ. 6-14}$$

per unit undeformed volume. Since the density ρ_0 of the undeformed body is independent of deformation, EQ. 6-13 gives the constitutive equation

$$S = \frac{\partial \Psi}{\partial \mathbf{E}} \qquad \text{EQ. 6-15}$$

where the 2nd Piola Kirchhoff stress tensor is derived from the scalar strain energy density function Ψ.

6.1.2 Phenomenological hyperelastic constitutive models

A material with a constitutive relation of the form described by EQ. 6-15) is called a hyperelastic material. In other words, the mechanical properties of a hyperelastic material are characterized completely by a scalar strain energy density function. During an isothermal deformation, the strain energy is associated with the free energy per unit undeformed (reference) volume, and the

strain energy is zero in the reference state. Materials that keep the volume constant throughout a deformation are characterized by the incompressibility constraint

$$J = \det \mathbf{F} = 1 \qquad \text{EQ. 6-16}$$

For incompressible materials with $J = 1$, Eq. (1.15) is expressed as

$$\mathbf{S} = 2\frac{\partial \Psi}{\partial \mathbf{C}} - p\mathbf{C}^{-1} = \frac{\partial \Psi}{\partial \mathbf{E}} - p\mathbf{C}^{-1} \qquad \text{EQ. 6-17}$$

where p is a Lagrange multiplier that is determined from the equations of motion and boundary conditions (kinematic constraints) and is usually associated with the hydrostatic pressure in a tissue. The Lagrange multiplier generally does not have a direct physical interpretation, but is needed to enforce the incompressibility constraint (Eq. (1.16)) [244]. Note that in the measures for stress as defined in EQ. 6-2, J = 1 for incompressible materials. A strain energy function exists for a perfectly elastic material; hyperelasticity is a subclass of (non--linear) elasticity, where the stress state of a material is independent of its loading history. The actual work done by the stress field on a hyperelastic material during a certain time interval depends only on the initial and final configurations, i.e., it is path independent [245]. Under the assumption of pseudoelasticity, the strain energy function should technically be referred to as a pseudo--strain energy function. In the rest of this dissertation, the general term strain energy is used. Under the condition of plane stress (with $S_{13} = S_{23} = S_{33} = 0$) for planar biaxial deformation, the strain energy is dependent on the strain components E_{11}, E_{22}, E_{12}, E_{33}. Because of the incompressibility constraint (EQ. 6-16), E_{33} can be calculated from the other components and only three of the four components are independent [247]. A reduced strain energy function can be defined as

$$S_{11} = \frac{\partial \hat{\Psi}}{\partial E_{11}}$$
$$S_{22} = \frac{\partial \hat{\Psi}}{\partial E_{22}} \quad . \qquad \text{EQ. 6-18}$$
$$S_{12} = \frac{\partial \hat{\Psi}}{\partial E_{12}} - C_{12}C_{33}^2 \frac{\partial \Psi}{\partial E_{33}}$$

Originally introduced to describe the behavior of skin tissue, the strain energy function proposed by Tong and Fung [248] has provided a reliable foundation for soft tissue mechanics [234, 249]. Researchers have successfully used variations of this model to describe a number of soft tissue applications including skin, blood vessels, myocardium, and heart valvular tissue. Fung-Type models couple quadratic and exponential forms to describe the energy potential form. While this form is attractive in the sense that it p rovides latitude related to the parameter estimation from experimental data, the model does not directly ensure a convexity of the resulting strain energy function. In a two dimensional framework, a common form of Fung-type strain energy function is given by

$$\Psi(\mathbf{E}) = \frac{1}{2} c\left[\exp(Q) - 1\right] \qquad \text{EQ. 6-19}$$

where c is the material parameter and Q is given by $a_{ijkl}E_{ij}E_{kl}$.

$$Q = a_1 E_{11}^2 + a_2 E_{22}^2 + 2a_3 E_{11}E_{22} + a_4 E_{12}^2 + a_5 E_{11}E_{12} + a_5 E_{22}E_{12} \qquad \text{EQ. 6-20}$$

In the form given above, the seven non-dimensional material parameters (c, $a1$,…, $a6$) are determined by fitting the constitutive equations to experimental data and do not directly provide physiologic insight. Three dimensional forms of the model have been presented by expanding the form of Q [250].

Most biological tissues are characterized as anisotropic and cannot be adequately described by isotropic constitutive equations. A material is considered anisotropic when its

material properties are directionally dependent. These materials can be viewed as being composed of an isotropic matrix material, or ground substance, and one or more families of fibers responsible for the anisotropy. As proposed by Spencer [178], the derivation of the constitutive relation is based on the principle of material symmetry. This approach can be viewed as a "hybrid" approach, between pure phenomenological and fully structural. The simplest representation of this is transverse isotropy, with one family of fibers. The fiber direction in the reference configuration is defined by a unit vector **a**(**X**), and its structural tensor is defined as $a \otimes a$. The so called pseudo invariants of **C** and **a**, related to the fibers, are now introduced as

$$\begin{aligned} I_4 &= \mathbf{a}^T \mathbf{C}\mathbf{a} = \lambda_A^2 \\ I_5 &= \mathbf{a}^T \mathbf{C}^2 \mathbf{a} \end{aligned} \qquad \text{EQ. 6-21}$$

where λ_A is the stretch in fiber family A. For a transversely isotropic material, the strain energy is written in terms of the five invariants as $\Psi = \Psi(I_1,I_2,I_3,I_4,I_5)$. When a material consists of two families of fibers, where the second fiber family is defined by the unit vector **b**, additional strain invariants are defined associated with this additional fiber family and the interaction between the two families. The invariants I_6-I_8 are defined as

$$\begin{aligned} I_6 &= \mathbf{b}^T \mathbf{C}\mathbf{b} = \lambda_B^2 \\ I_7 &= \mathbf{b}^T \mathbf{C}^2 \mathbf{b} \\ I_8 &= a^T \mathbf{C}\mathbf{b} \end{aligned} \qquad \text{EQ. 6-22}$$

In soft tissues, the strain energy function is often divided into an isotropic and an anisotropic part representing the isotropic matrix and the fibers, respectively, resulting in

$$\Psi = \Psi_{iso}(I_1,I_2) + \Psi_{aniso}(I_4,I_5) \qquad \text{EQ. 6-23}$$

when assuming incompressibility,

$$\Psi = \Psi_{iso}(I_1) + \Psi_{aniso}(I_4,I_6) \qquad \text{EQ. 6-24}$$

Various functional forms of Ψ_{iso} and Ψ_{aniso} have been proposed. Ψ_{iso} often takes a neo-Hookean formulation as follows

$$\Psi_{iso} = \frac{c}{2}(I_1 - 3) \qquad \text{EQ. 6-25}$$

while Ψ_{aniso} is typically described by more complex phenomenological expressions similar to those outlined above [242, 251-256].

6.1.3 Structural constitutive models

Based on concepts introduced by Lanir [134, 257, 258], a class of soft tissue constitutive models based fiber scale properties has evolved. These models are classified as "structural" as they characterize the material response in terms of the micro-structural tissue constituents. Structural models integrate information related to tissue composition and structure directly into the constitutive relationship. However, the description of fiber scale properties such as orientation and crimp are cast in terms of statistical distributions due to a microstructure complexity that prohibits individual representation. This stochastic description is based on data homogenized at a representative element scale of approximately 100 μm. At this scale, characterization of the fiber microstructure is relative to the fiber ensemble. For example, the fiber angular distribution function, R(θ), describes the dominant fiber alignment direction in an ensemble framework. In this sense, structural models have a meso-scale focus as they characterize an organ scale response in terms of fiber structure attributes at a scale in between cellular and organ. The framework established by the early work of Lanir attained practical relevance to soft tissue modeling with the introduction of an experimentally derived form for fibrillar orientation by Sacks [135]. This work used data collected using SALS techniques to develop analytical

functions suitable for direct implementation into the context of a structural model. Additionally, Sacks presented a distribution for fiber recruitment stemming from crimp periods observed in bovine pericardium.

6.1.4 Structural model formulation

Structural models treat the contributions of fibrillar and non-fibrillar constituents to the strain energy independently. The fiber network and ground-matrix are described in terms of finite strain fiber-reinforced continuum mechanics [259]. A tissue strain energy function is characterized by the uncoupled sum of isotropic and anisotropic contributors.

$$\psi = \psi_{iso}^{M}(\mathbf{E}) + \psi_{aniso}^{F}(\mathbf{E}) \qquad \text{EQ. 6-26}$$

ψ_M and ψ_F are strain energy functions representing ground-matrix and fiber contributions respectively. The ground-matrix function describes low-strain behavior and provides stiffness in an unloaded state. Tissue response to large strains is accommodated by the anisotropic strain energy function characterizing the fibrillar microstructure. Common choices for the isotropic contribution, ψ^F, include neo-Hookean and Mooney-Rivlin material assumptions [243, 260]. The use of a neo-Hookean form has shown sufficient fidelity with respect to prediction of low strain behavior [260]. The material parameter μ describing the shear modulus can be estimated through experimental means.

$$\psi_{iso}^{M} = \frac{\mu}{2}(tr\mathbf{C} - 3) \qquad \text{EQ. 6-27}$$

For the fiber response, structural models seek to form a homogenized strain energy function based on an assumed fiber ensemble behavior. Lanir proposed a form based on the uniaxial strain energy of a given fiber ensemble [134, 257]. This form ignores shear, bending and

fiber-to-fiber interactions. Relative to the reference configuration, tissue level strain energy, ψ_F, is developed by summing the contribution of fiber ensembles acting at independent orientations based on a measured fiber orientation distribution.

$$\psi^F(\mathbf{E}) = \int_\theta R(\theta)\psi^f(\theta,\mathbf{E})d\theta = \int_\theta R(\theta)\psi^f(\varepsilon)d\theta \qquad \text{EQ. 6-28}$$

where ψ_f is the uniaxial fiber ensemble strain energy and ε is a uniaxial Lagrangian strain defined as

$$\varepsilon = N\cdot \mathbf{E}N \qquad \text{EQ. 6-29}$$

The second Piola-Kirchhoff stress tensor is obtained by

$$S(\mathbf{E}) = \frac{\partial\psi(\mathbf{E})}{\partial\mathbf{E}} \qquad \text{EQ. 6-30}$$

which leads to a fiber stress contribution of

$$S^F(\mathbf{E}) = \int_\theta R(\theta)s^f(\varepsilon)\left[N\otimes N(\theta)\right]d\theta \qquad \text{EQ. 6-31}$$

gives the fiber ensemble orientation and s_f defines the ensemble uniaxial stress response. The homogenization considers the θ domain ($-\pi/2$, $\pi/2$).

Investigators [135, 261] have successfully used an exponential form for the ensemble stress based on the behavior observed by Fung [262] in his early work examining tissue response in “simple elongation”. Many models based on exponential strain energy forms have been presented in the literature. With respect to heart valve mechanics, Billiar and Sacks [16, 263] proposed a two-parameter model in their work related to the aortic valve.

$$s^f(\varepsilon) = \mathrm{A}\left[\exp(\mathrm{B}\varepsilon) - 1\right] \qquad \text{EQ. 6-32}$$

This effective fiber stress-strain law has also been extended to capture the transition from an exponential behavior to linear elastic, as is often exhibited by highly collagenous tissues. This model states that the effective fiber stress follows and exponential form for strains less than the

$$s^f(\varepsilon)=\begin{cases} A\left[\exp(B\varepsilon)-1\right] & for\ \ \varepsilon_{ens}<\varepsilon_{ub} \\ \left.\frac{\partial s}{\partial \varepsilon}\right|_{\varepsilon_{ens}=\varepsilon_{ub}}\cdot\left(\varepsilon_{ens}-\varepsilon_{ub}\right)+A\left[\exp(B\varepsilon_{ub})-1\right] & for\ \ \varepsilon_{ens}\geq\varepsilon_{ub} \end{cases} \quad \text{EQ. 3-33}$$

upper bound strain, ε_{ub}, which is the strain at which all collagen fibers become straight. However, once the ε_{ub} is attained, the collagen fibers were assumed to behave linear elastically, and the response is linear.

The material parameters A and B are derived from fitting the assumed stress response to experimental equibiaxial planar strain data. Using this exponential form, the resulting model can be considered hybrid in the sense that the fiber homogenization is accomplished from direct fibrillar orientation measurements and the fiber stress response is essentially phenomenological. Alternate choices for fiber strain energy functions have been developed and are generally tailored to the mode of deformation exhibited by the tissue involved.

For negative strain values the ensemble stress, s_f, is set to zero as fibers are assumed to be incapable of carrying the load in compression. This is an assumption common to all structural based models as they do not consider the fiber load-bearing until fully straightened [135]. The basis for this choice is rooted in the aggregate behavior of the tissue as illustrated in Figure 2-1. In both radial and circumferential direction, the tissue exhibits negligible stiffness; a property that is attributed to the crimped nature of the fiber network at an unloaded state. The expression used to characterize the ensemble stress (EQ. 6-36) is parameterized using data dominated by high strain effects and therefore effectively neglects any low strain mechanisms. At these strain regimes, loads are assumed to be resisted by ECM background matrix (Eq. 6-28). Based on SALS measurements, forms for the fiber angular distribution function, *R*, based on Gaussian and Beta functions have been presented [17, 135, 220]. A Gaussian distribution form is given by

$$R(\theta) = \frac{1}{\sigma\sqrt{2\pi}} \exp\left[\frac{-(\theta-\mu)^2}{2\sigma^2} \right] \qquad \text{EQ. 6-34}$$

where σ is the standard deviation and μ is the distribution mean. Appropriately normalized, the function describes the fraction of fibers acting over and increment $d\theta$ and obeys the framework of a probability density function.

Alternatively, Beta functions have been used by investigators as they exhibit attractive properties related to enforcing physically realistic bounds [135]. For instance, a stochastic approach can be taken where a recruitment distribution is used to describe the fraction of fibers realizing a fully straightened state at a given stretch, defined over lower stretch bounds (E_{lb}, strain where recruitment begins) and upper stretch bounds (E_{ub}, strain where all fibers are uncrimped). With this, the combined ensemble S-E relationship can be expressed as

$$S^{ens} = \phi \int_0^{E^{ens}} D(x)\left[1 - \frac{\sqrt{1+2x}}{\sqrt{1+2E^{ens}}} \right] dx \qquad \text{EQ. 6-35}$$

where D(x) is defined as a beta distribution function, β(y), mapped to the interval [E_{lb}, E_{ub}] and with a mean and standard deviation as

$$D(E,\mu,\sigma) = \begin{cases} \dfrac{\beta(y, s_1, s_2}{E_{ub} - E_{lb}} & E_{lb} \le E \le E_{ub} \\ 0 & otherwise \end{cases} \qquad \text{EQ. 6-36}$$

with s_1 and s_2 as

$$s_1 = \frac{\mu^2 - \mu^3 - \mu\sigma^2}{\sigma^2} \qquad s_2 = \frac{\mu^2}{\sigma^2} s_1 \qquad \text{EQ 6-37}$$

6.2 DETERMINING DE NOVO MATRIX MECHANICAL BEHAVIOR

6.2.1 Engineered PEUU-ECM construct production and testing

Microintegrated electrospun constructs were again produced as prescribed in Chapter 3 and mechanical conditioned under 30% cyclic uniaxial strain for 21 days as previously presented. The specimens were conditioned for a total of 21 days in an attempt to ensure the greatest matrix synthesis and organization. The intent of the following testing protocol is to specifically probe the mechanical contribution of the ECM phase to overall mechanical behavior. In the present study 10 x 10mm specimens were used, with the specimen edges aligned to the longitudinal (x_1) and circumferential (x_2) axes of the mandrel. Thin sections of polypropylene mono-filament suture were cut to form four small markers in the central 3 x 3mm region of the specimen used to compute local strains using the method presented in Chapter 2. The resulting deformation gradient tensor **F** was computed from the displacement of these fiducial markers. Axial stretches $\lambda_{PD} = F_{11}$ and $\lambda_{XD} = F_{22}$ were determined, where PD and XD refer to the preferred and cross-preferred fiber directions, respectively. All testing was performed in water at room temperature. The components of the Cauchy stress tensor **t** were calculated from the axial loads and the individual specimen dimensions at each time t, which were calculated from the initial measured specimen dimensions and the relevant deformation gradient tensor, assuming tissue incompressibility. The components of the Second Piola Kirchhoff stress and Lagrangian or first Piola Kirchhoff stress tensors (**S** and **P** respectively) were calculated from t using EQ. 6-2.

Engineered constructs (n = 5) were prepared for planar biaxial mechanical testing under stress control, and the four sides of each specimen were tethered using nylon suture and small stainless steel hooks (Section 2.1.3), as described in detail in [16, 264]. The test specimen was

then mounted onto a custom made planar biaxial testing device. Each side of the square test specimen was connected to the motor carriages via sutures to apply four point loads. The load on each axis was constantly monitored using force transducers (with a signal conditioner) and the applied load was controlled by adjusting the stepper motors using custom software and a data acquisition board installed on a PC. Testing was performed at room temperature, in deionized water, under stress control, and starting from a preload of 0.5g. Throughout testing, in plane axial stretches were determined from the two dimensional deformation gradient tensor **F**, determined from displacements of four markers affixed to the surface of the specimen, as described above.

Constructs were preconditioned for 10 cycles under equibiaxial stress, up to the determined maximum testing stress of 300 kPa. The testing protocol consisted of axial stress ratio controlled protocols (t_{11}:t_{22} = 30:300, 150:300, 225:300, 300:300, 300:225, 300:150, 300:30) using a half cycle time of 15 s to quantify the quasistatic response. These ratios were chosen to cover a wide range of stress states. Total testing time was approximately 2 h per specimen.

6.2.2 ECM degradation protocol and subsequent biaxial testing

Probing the mechanical contribution of each phase of the construct (i.e. polymer or matrix) necessitated the ability to isolate an individual phase for mechanical characterization. Since the polymer phase comprised the majority of the construct in terms of volume fraction and stress generation, it was most practical to isolate this phase by removing the biological portion of the construct. This was accomplished by placing the specimen in 0.25% Trypsin EDTA (Invitrogen™, USA) for 24 hours at 37 °C. Validation of the degradation protocol was carried out by staining sections before and after degradation with H&E for visual comparison. The same

biaxial testing protocol outlined above was again used after degradation to quantify the PEUU scaffold mechanical behavior. After matrix degradation, construct compliance was observed to increase significantly, requiring a subsequent reduction of the peak stress at run time to 200 kPa. This approach enables the direct comparison of the biaxial mechanical response of the total construct with its subsequent degraded mechanical behavior.

6.2.3 Tissue analog development

In order to investigate any coupled effects of individual phases in the scaffold-tissue composites, it was necessary to employ a tissue analog with tunable mechanical properties within the range of native tissue. This approach permitted quantifying interaction (coupling) between both phases by first gaining insight into the contributions from decoupled constituents. As such, we utilized polyacrylamide gel (PAM gel) as described in previous work in our lab [139]. With this system, we were able to adjust the concentration of acrylamide/bis prior to polymerization to control the modulus. Previous studies showed the system capable of producing phantoms with elastic moduli within the range of 30 to 800 kPa. To make 10 ml of 20.7% PAM gel, 6900 µl of a 30% solution of 37:5 acrylamide/bis (Bio-Rad Laboratories, Hercules, CA) and 450 µl of deionized water were combined along with with 2500 µL of 1.5M Tris/HCl buffer (Bio-Rad) and 100 µL of 10% sodium dodecyl sulfate (SDS) (Bio-Rad) as per the manufacturer's instructions. Fresh 10% ammonium persulfate (APS) (SIGMA, Sigma- Aldrich Co., St. Louis, MO) was mixed, and 50 µL was added to the solution along with 5 µL of tetramethyleethylenediamine (TEMED) (Bio-Rad). The solution was gently mixed and cast between a 0.5 mm glass spacer plate and a cover plate in a Bio-Rad SDS-PAGE gel assembly system. In these ECM phantoms, 1 ml of 1-butanol (SIGMA) was mixed with 4.5 ml of deionized water, and approximately 100-200 µL was

carefully pipetted on top of the cast PAM gel liquid to provide an anaerobic seal. After forty minutes, the plates were removed from the gel assembly system and separated. Specimens were cut from the gel sheet and stored in cold deionized water until tested.

To fabricate the continuous scaffold-ECM composites, squares of electrospun PEUU scaffold were cut to 10x10 mm. These scaffold segments were coated with liquid PAM gel to fully absorb into the scaffold. PAM gel-infused scaffold was then slid between the glass plates and surrounded by additional liquid PAM gel. As in the ECM phantoms, approximately 100-200 μL of saturated 1-butanol was carefully pipetted on top of the cast PAM gel liquid to provide an anaerobic seal. After forty minutes, the plates were removed from the gel assembly system and separated. Specimens were cut from the gel sheet and stored in cold deionized water until tested.

6.2.4 Tissue analog biaxial testing

Biaxial tensile mechanical testing was performed on segments of PEUU scaffold-embedded PAM gel. A total of 3 specimens were evaluated. Following previously published methods for biaxial mechanical testing [16], specimens were cut to 10 mm per side, and thickness measurements were taken using a micrometer at six locations and averaged. Stainless steel 0.016-inch diameter hooks tied to both ends of 10 cm long nylon suture line were attached to specimens with four hooks per side forming two loops of suture. A total of sixteen hooks were placed creating four pairs of sutures. Four small cut portions of polypropylene suture were attached to the middle region of the specimen in a square pattern using cyanoacrylate glue to serve as fiducial markers for strain tracking. The specimen was then placed in the biaxial testing device chamber filled with deionized water, and the suture loops were attached to stainless steel

dowels on actuator arms. The preferred direction of the scaffold was aligned with the device X1 axis.

Using custom-written control software, stress control biaxial mechanical testing was performed. Free-floating (no-load) reference states were taken before preconditioning, after preconditioning, and after full protocol testing. A 0.5g gram tare load was applied to the specimen to enable proper device operation. Tare reference states before preconditioning, after preconditioning, and after full protocol testing were also recorded. Preconditioning was performed for ten cycles with a fifteen second half cycle time. In all specimens, it was found that ten cycles of preconditioning was adequate to ensure consistent loading results from subsequent tests. A seven protocol testing regime was used with peak X_1:X_2 stress ratios of 30:300, 150:300, 225:300, 300:300, 300:225, 300:150, and 300:30 kPa. Tests were performed for ten cycles with a fifteen second half cycle time. As in the analysis described in Section 2.1.3, t he post-preconditioned 0.5g tare configuration was used as the reference state.

6.2.5 Matrix area fraction

In addition to quantifying the mechanical behavior of the engineered construct, matrix area fraction measurements are necessary to appropriately quantify the contribution of each phase to the gross construct planar behavior. To do so, an image analysis based protocol was implemented to analyze digitized histological sections for matrix content (Figure 6-1). First, representative full thickness images stained with picrosirius red (PSR) or H&E were chosen from the 14 and 21-day time points respectively. The color images were then converted to greyscale in for each channel (i.e. red, green, blue). For both stain types, the biological phase was most apparent in the green channel. A threshold was then applied to the green channel to: a) segment the entire area

encompassed by the construct and b) segment only the matrix portion of the section. Both measurements were necessary to accurately calculate the matrix area fraction while accounting for regions of the image that did not contain matrix or polymer (i.e. voids within the specimen and areas beyond the specimen itself). The collagen area fraction was then determined as the ratio of the collagen are to total area and multiplied by 100 to obtain a percentage value. This analysis was carried out for images of 5 pi crosirius stained specimens and 6 H &E strained specimens.

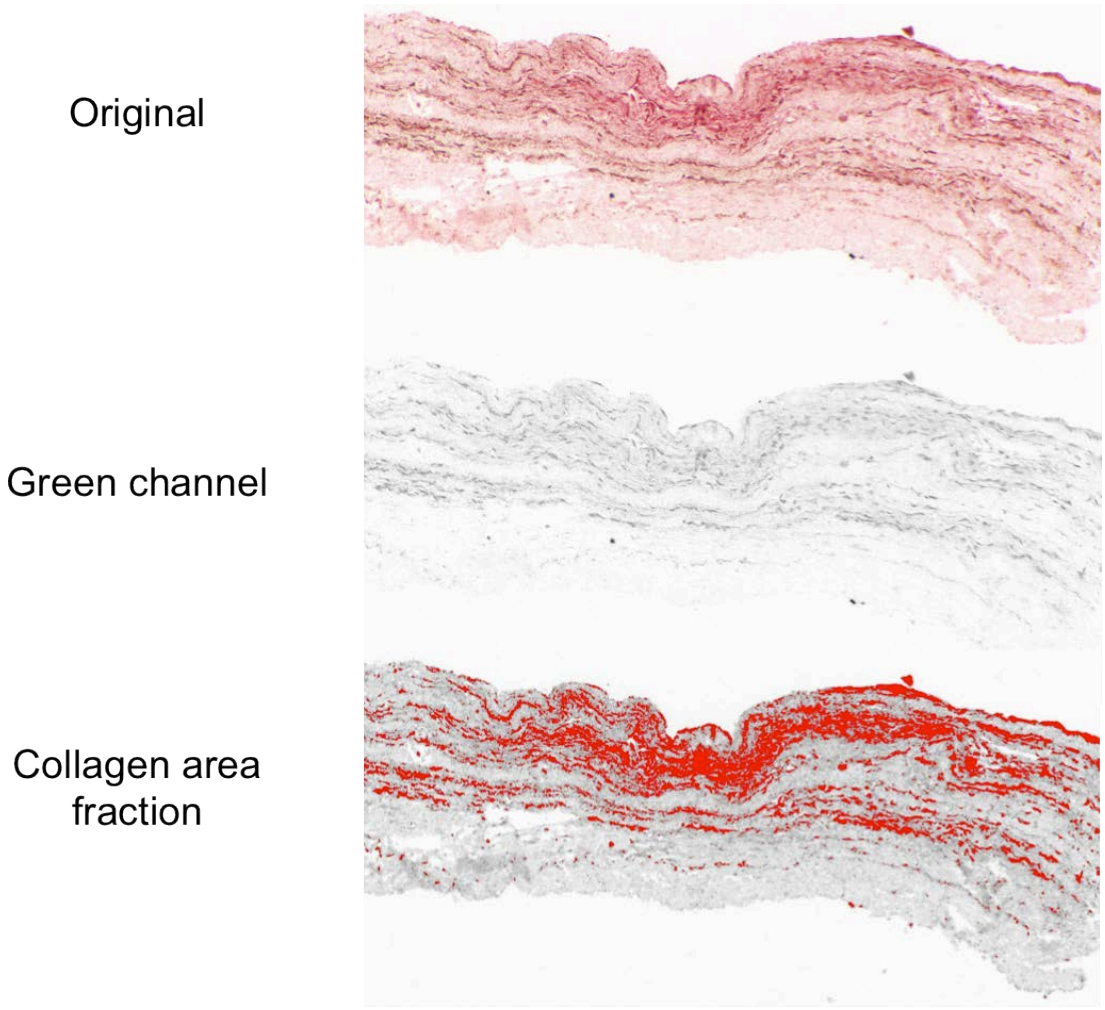

Figure 6-1. Representative matrix area fraction quantification protocol for picrosirius red sections.

6.2.6 Estimating de novo matrix mechanical behavior

The primary goal of this chapter is to elucidate mechanical behavior characteristics of the engineered constructs' biological phase (Figure 6-2). Due to practical reasons, it is not possible to isolate and directly test the mechanical behavior of the evolving matrix phase. However, it is possible to determine the matrix mechanical contribution if we assume that the total mechanical response is simply the summation of the individual phases and any potential interactions that might arise between them.

$$\Psi = \phi_{PEUU}\Psi_{PEUU} + \phi_{Matrix}\Psi_{Matrix} + \Psi_{PEUU-Matrix} \qquad \text{EQ. 6-36}$$

In this formulation, the total construct strain energy is comprised of the individual phase strain energies multiplied by their respective volume fractions (ϕ) along with any coupling (or interaction) response as denoted by, $\Psi_{PEUU-Matrix}$. It is important to note, the only unknown variable in EQ. 6-36 that cannot be quantified by experimental means is Ψ_{Matrix}. From the relations presented in EQ. 6-22, it is possible to calculate strain energy by multiplication of the observed Green strain (**E**) and corresponding 2nd Piola Kirchhoff stress (**S**). In our experimental system, the total strain energy (Ψ) is determined from the construct biaxial response while the PEUU contribution is determined from the degraded mechanical response. Rearranging equation 6-36 for the unknown quantity (Ψ_{Matrix}) gives us the following relation,

$$\Psi_{Matrix} = \frac{\Psi - \left(\phi_{PEUU}\Psi_{PEUU} + \Psi_{PEUU-Matrix}\right)}{\phi_{Matrix}}. \qquad \text{EQ. 6-37}$$

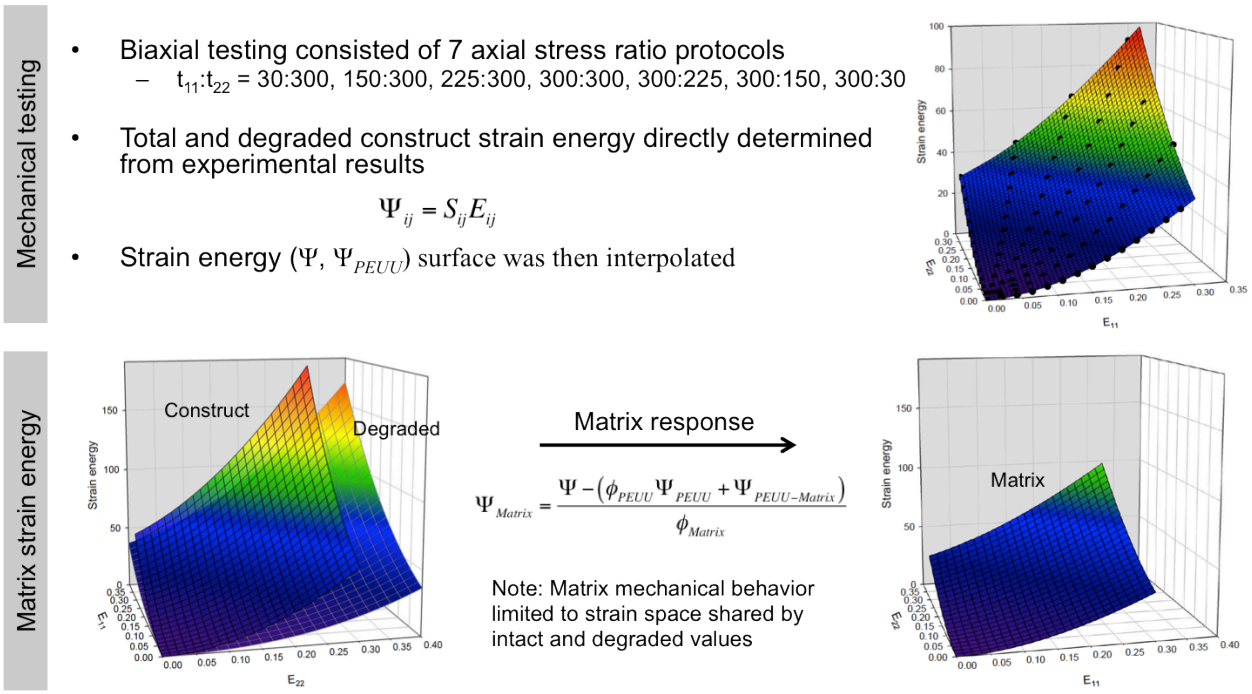

Figure 6-2. Overview of the process to assess de novo matrix mechanical behavior.

In addition to direct experimental comparisons, it is possible to further estimate the resultant matrix strain energy. This was accomplished by applying a Yeoh type hyperelastic material model [265] to the strain energy surface formed as described by EQ. 6-37 assuming incompressibility. It should be noted that this analysis is only carried out where the intact and degraded constructs share a common strain space (Figure 6-3, highlighted region). The constraint was imposed to avoid ambiguities that might arise from interpolating values beyond the experimental data sets. The highly nonlinear experimental results necessitated the use of a reduced polynomial form as follows:

$$\Psi_{\text{model}} = C_1(I_1 - 3) + C_2(I_1 - 3)^2. \qquad \text{EQ. 6-38}$$

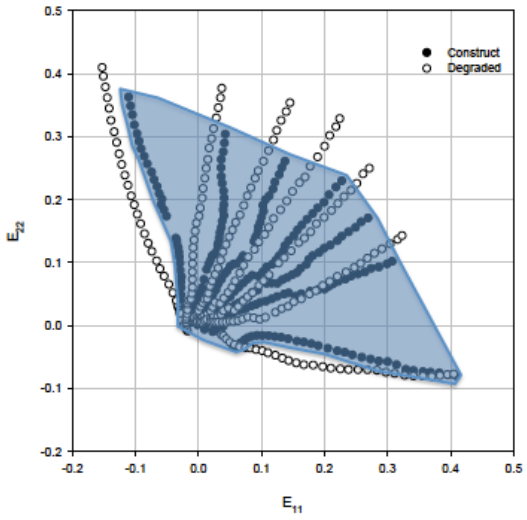

Figure 6-3. Assessing matrix mechanical behavior was limited to the strain space shared by the intact and degraded values observed at run time.

Minimization of the error between the above analytical solution and experimental strain energy data results in 2 parameters which can then be used to estimate the materials shear modulus. The relation between the model parameters and shear modulus (μ) is defined as,

$$\mu = 2\left(C_1 + C_2\right) \qquad \text{EQ. 6-39}$$

which can then be used to approximate the material tensile modulus.

6.3 RESULTS

6.3.1 ECM degradation

Prior to degradation, newly formed matrix proteins are typically observed throughout the construct (Figure 6-4a). The Trypsin degradation protocol proved successful in removing the vast majority of biological components after 24 hours. This was visually confirmed via

histological evaluation of adjacent specimen segments from the 21 day 30% strain conditioning group. Adjacent segments were excised from the specimen, one portion was placed in 10% buffered formalin solution for 24 hours while the other was degraded with trypsin and then fixed with the same formalin solution. Comparison of intact and degraded H&E stained construct segments clearly shows matrix removal (Figure 6-4). It should be noted, PEUU remains unstained throughout H&E staining protocols and provides very little contrast under bright field microscopy. As such, the images have been inverted for improved visualization. Bright green represents ECM while PEUU appears grey.

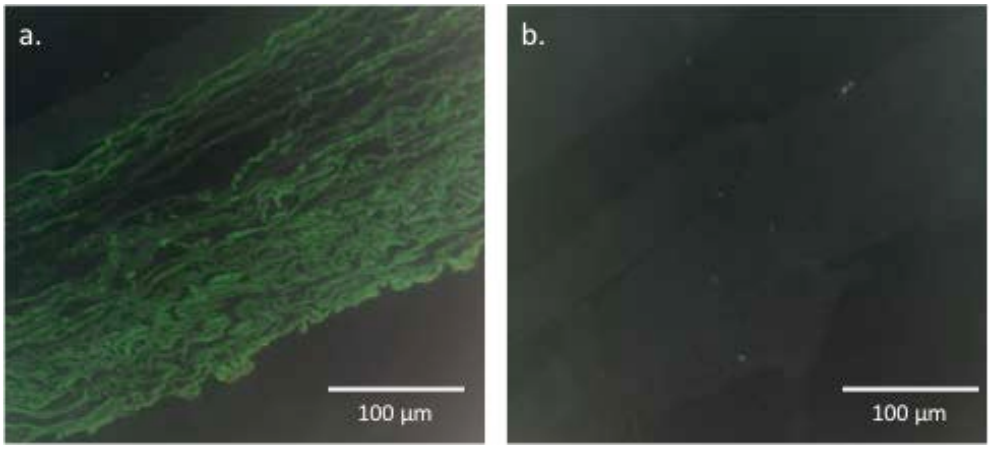

Figure 6-4. ECM degradation protocol validation.

To ensure that the degradation protocol did not adversely affect polymer structure and mechanical behavior, mechanical validation was carried out on 6 a cellular specimens. Experimental results show that there was no significant change in the biaxial response due to the enzymatic degradation protocol. The mechanical responses before and after the degradation protocols were remarkably consistent indicating a high level of repeatability (Figure 6-5). Typically, little variation was observed in the strain space enveloped by the multi-protocol

biaxial testing. Furthermore, interpolated values at equal states of biaxial strain exhibit similar responses.

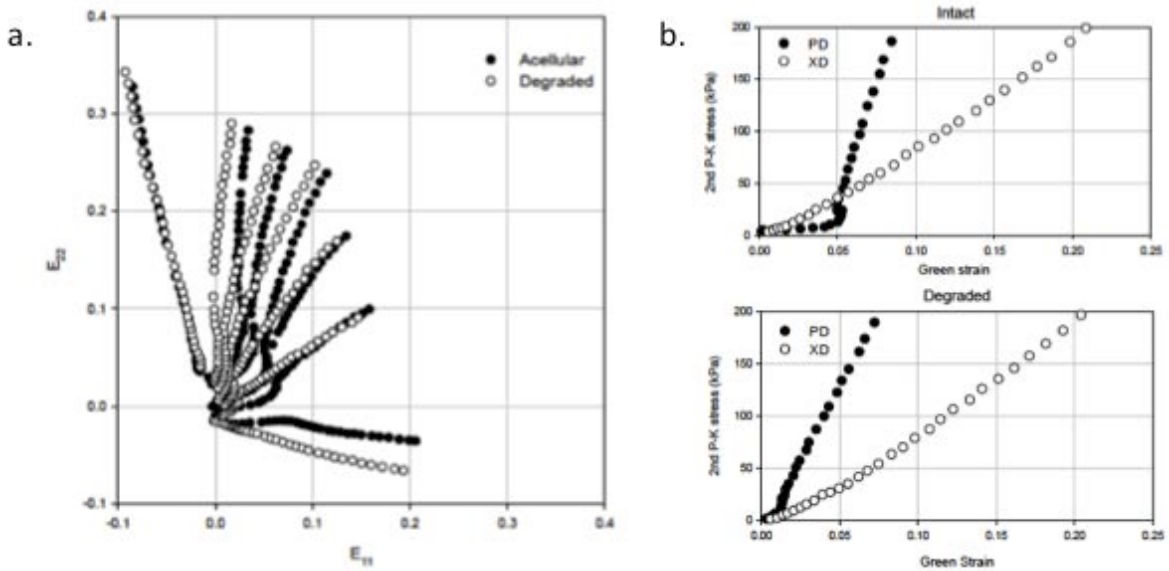

Figure 6-5. Trypsin degradation has no measureable effect on PEUU tensile behavior.

6.3.2 Assessing constituent volume fraction

Identifying the ratio of each constituent to the full volume of the construct is critical to accurately assess the mechanical contribution of each when deformed. The analysis performed acceptably well on both PSR and H&E stain histological sections. Results suggest that 14 day, PSR stained sections exhibit a 5:1 ratio of PEU U to matrix while the 21 day specimens stained with H&E suggest a 4.2:1 ratio (Table 3). The method was consistent between both staining protocols, despite PSR specifically binding to collagen where H&E stains more generally for all biological material.

Table 3. Matrix area quantification.

Specimen	Treatment	Stain	% area fraction			Area fraction (sq. µm)		
			PEUU	ECM	Void	PEUU	ECM	Void
1			75.7	15.4	8.9	204.4	41.6	24.0
2			69.2	18.2	12.6	214.5	56.4	39.1
3	14 day 30% strain	PSR	77.8	15.9	6.3	241.2	49.3	19.5
4			78.2	9.3	12.5	242.4	28.8	38.8
5			74.3	16.4	9.3	230.3	50.8	28.8
		Mean	75.0	15.0	9.9	226.6	45.4	30.0
		SEM	1.6	1.5	1.2	7.5	4.8	3.9

Specimen	Treatment	Stain	% area fraction			Area fraction (sq. µm)		
			PEUU	ECM	Void	PEUU	ECM	Void
1			57.0	13.9	29.1	245.1	59.8	125.1
2			63.2	10.4	26.4	177.0	29.1	73.9
3	21 day 30% strain	H&E	58.9	14.4	26.7	164.9	40.3	74.8
4			55.2	18.9	25.9	154.6	52.9	72.5
5			60.2	12.5	27.3	168.6	35.0	76.4
		Mean	58.9	14.0	27.1	182.0	43.4	84.5
		SEM	1.4	1.4	0.6	16.2	5.7	10.2

6.3.3 Tensile mechanical response of PAM integrated PEUU

The biaxial testing protocol to mechanically evaluate electrospun PEUU before and after impregnation with PAM gel was accomplished without incident. The repeated measures experimental design allowed direct comparison of the tensile behavior of PEUU with and without the addition of an isotropic phase of known mechanical properties. For instance, the 20.7% PAM gel selected for impregnation has a known shear modulus of 51 kPa. These tissue analog specimens represent an ideal platform to validate the analysis presented in Section 6.2.6. The only caveat is that an appropriate model form must be used to reasonably estimate material modulus values. In this case, PAM gel is well documented to exhibit tensile behaviors consistent with Mooney-Rivlin hyperelastic solids. The following model form can describe these materials,

$$\Psi_{Mooney-Rivlin} = C_1\left(I_1 - 3\right) + C_2\left(I_2 - 3\right). \qquad \text{EQ. 6-40}$$

Results of this analysis are presented for 3 tissue analog specimens in Table 4. From the mean predicted shear modulus it is clear that our analysis is capable of accurately predicting gross material mechanical characteristics. Furthermore, it allows insight into any coupling phenomena integration of an isotropic phase might induce. Specifically, there appears to be no measureable coupling effect by the incorporation of an isotropic phase.

Table 4. Shear modulus estimates from mechanical evaluation of PAM impregnated PEUU.

Predicted shear modulus (kPa)	
Specimen 1	57.1
Specimen 2	51.2
Specimen 3	53.2
Mean	53.83
Error	1.73

6.3.4 De novo matrix strain energy response

From thorough planar biaxial mechanical assessment of engineered constructs it is possible to deduce the mechanical behavior of newly formed matrix proteins. Specifically, from repeated testing of constructs before and after enzymatic degradation it is possible to quantify mechanical contribution of the newly formed biological phase on a per specimen basis. This approach is advantageous as it circumvents specimen variability to a large extent. Subsequent analysis directly from experimental results indicates that the matrix phase exhibits a highly nonlinear mechanical response (Figure 6-6).

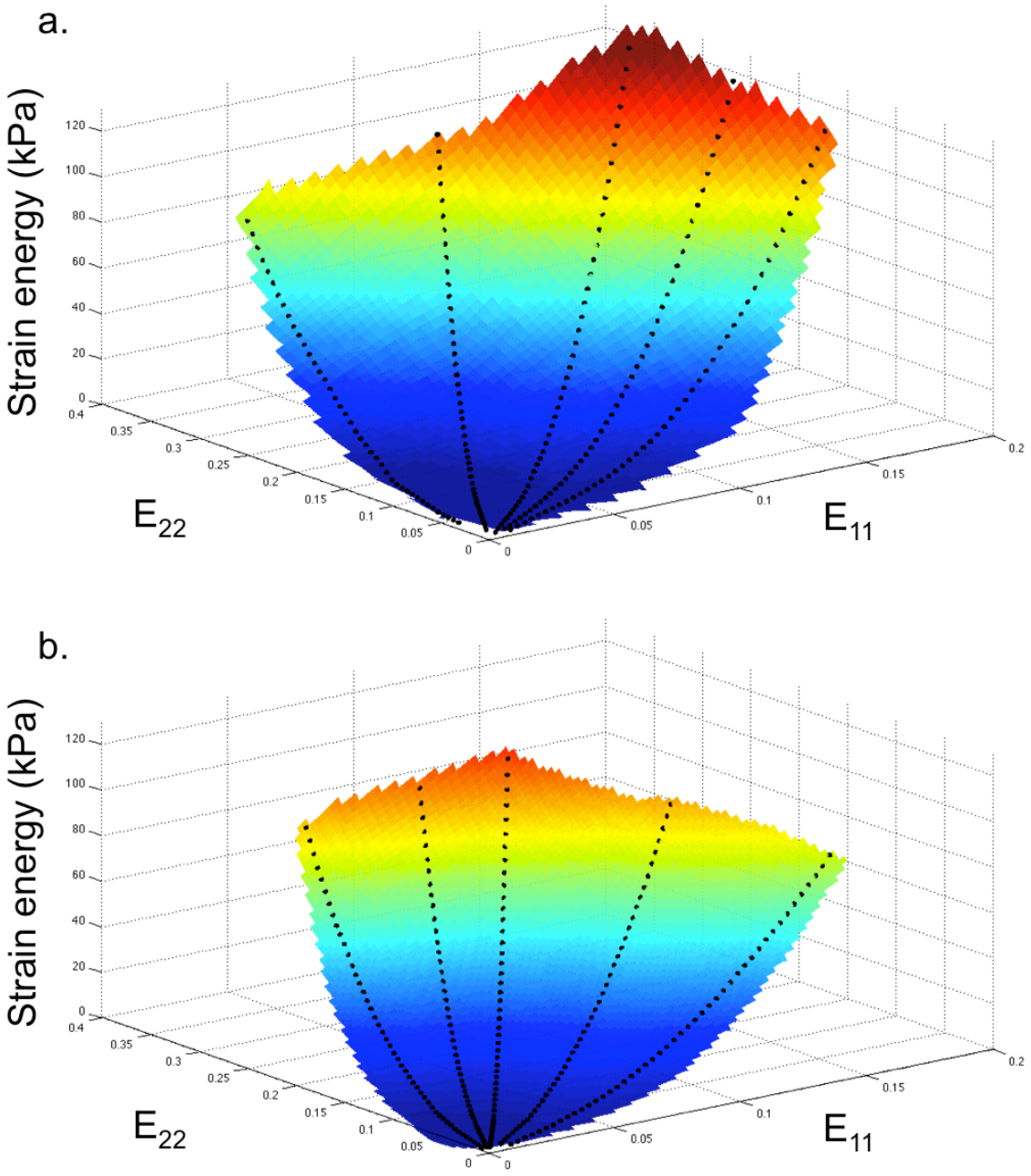

Figure 6-6. Matrix strain energy responses of representative specimens during biaxial testing.

Furthermore, it is possible to estimate the biaxial stress-strain response of each specimen from the newly obtained strain energy surfaces. This is accomplished first by interpolating strain energy values for states of equi-strain. From there, taking the partial derivatives (i.e. with respect to E_{11} and E_{22}) of a polynomial curve fit though the equi-strain response, results in evaluations of the matrix biaxial stress-strain response (Figure 6-7). These estimates indicate that the newly formed matrix phase exhibit a highly anisotropic biaxial response. It should be noted that stresses in the specimen orthogonal to the PEUU principle fiber direction were one order of magnitude larger then the cross preferred direction. The engineered specimens consistently exhibited ratios of peak stress in each orthogonal direction ranging from 5-10 fold.

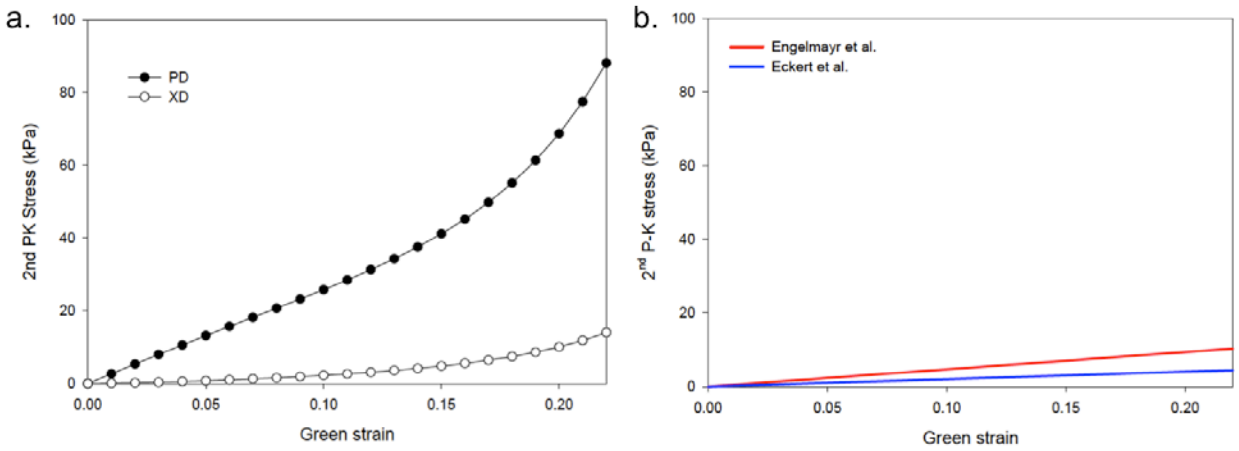

Figure 6-7. Tensile behavior comparison of de novo matrix in (a) electrospun PEUU and (b) PGA:PLLA nonwoven constructs.

In an effort to further estimate the material behavior of the newly formed matrix phase, the analysis presented in Section 6.2.6 w as employed to quantify the material's shear modulus. While it is unable to capture the inherent anisotropy exhibited by the matrix phase, application of EQ. 6-38 does produce a reasonable assessment of the small strain matrix mechanical properties suitable for comparison with other engineered tissue behaviors in recent literature. The results of this analysis with a 2 parameter Yeoh model are presented in the following (Table5).

Table 5. Estimated shear modulus values for the newly formed matrix phase.

Specimen #	Predicted shear modulus (kPa)
1	1204.1
2	1580.8
3	2758.7
4	1420.3
5	1331.0
Mean	1659.0
SEM	281.7

Treatment	Predicted shear modulus (kPa)
PGA:PLLA - flex	15.7
PGA:PLLA - In vivo	6.8 - 14.8
PEUU - finite strain	**1659.0 ± 281.7**

6.4 DISCUSSION

Improved means of understanding tissue formation and remodeling in engineered tissues is necessary to further the tissue engineering field and ultimately develop functionally-equivalent tissues. Unfortunately, variation exists among cell types, scaffold materials, culturing techniques, and subsequent analysis, making efforts to understand the overall functional equivalency of engineered constructs and the factors that prominently influence their efficacy less clear. Often,

little mechanical testing is performed with only bulk assays (collagen, calcium), geometric measurements, and histology used to evaluate the engineered tissue performance. Though some long-term results have been encouraging, most work in this field is empirically based, limited in scope, and has yet to elucidate time course changes in structure and mechanical behavior necessary to properly evaluate tissue formation and function.

To our knowledge, this is the first reported study to consider the effects of large deformation and the corresponding outcomes in terms of ECM mechanical integrity. The current chapter affirmed the assertion that finite deformation plays a critical role in matrix production as well as the mechanical robustness of the newly formed matrix constituents (Figure 6-7). Furthermore, the results reveal interesting insights into the functional role of the matrix accretion process in engineered tissues. While it is difficult to discern changes in material properties directly from biaxial test results alone, additional analysis proved extremely beneficial in characterizing the mechanical contribution of newly formed matrix elements.

6.4.1 Use of PAM gel as a tunable tissue analog

The use of an isotropic phase of known mechanical properties enables validation of our mechanical testing a theoretical analysis protocol. From the tensile response of plain electrospun PEUU and PAM integrated PEUU it was possible to deduce the mechanical contribution of each constituent to the combined stress-strain behavior. After impregnation with PAM, PEUU constructs had a much more robust feel with significantly increase bending rigidity. In tension, at low levels of strain, the PAM gel dominated the mechanical behavior. As larger strains were experienced, the PEUU phase was recruited. When a Mooney-Rivlin type hyperelastic model was fit to the strain energy response specific to the PAM gel, the estimated shear modulus value

was determined to be 53.8 ± 1.7 kPa. This is in very close agreement with the known material shear modulus value of 51 kPa.

Furthermore, these results indicate that incorporation of an isotropic phase such as PAM gel results in no measurable coupling between each constituent. This is in sharp contrast to the high degree of coupling observed by Engelmayr et al. for nonwoven PGA:PLLA blends (Figure 6-8, [138]). In this study, it was determined that newly formed ECM elements primarily served a reinforcing role increase fiber-fiber interactions as depicted in the following schematic.

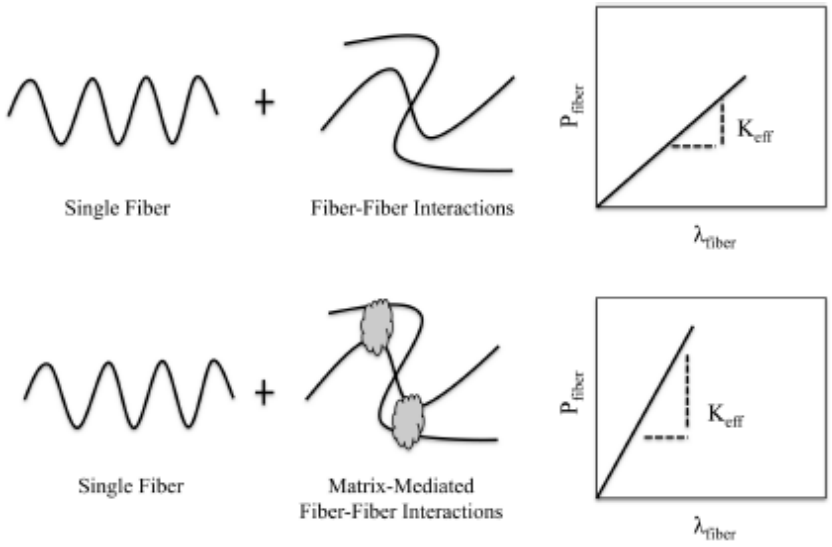

Figure 6-8. Proposed mechanism for matrix reinforcement of PGA:PLLA constructs.

6.4.2 De novo matrix mechanical assessment

Estimation of biaxial material properties from matrix strain energy data suggests that the formed matrix elements create a strongly anisotropic phase. Interestingly, the observed anisotropy was orthogonal to the applied direction of deformation. This indicates that the fibrous PEUU microstructure likely dictates matrix organization as new proteins are assimilated into the

construct. This phenomenon has recently been reported in other electrospun fibrous constructs aimed at recapitulating intervertebral disk engineered tissues [266]. In this study, PCL electrospun scaffolds were seeded with mesenchymal stem cells and maintained in static culture up to 10 weeks. We have also observed this behavior in our lab with the use of cell seeded needled non-woven PGA:PLLA scaffold blends. Both in vitro culture [267] and in vivo implantation (Eckert doctoral thesis) exhibited similar findings where the gross fiber orientation induced a micropatterning effect on matrix elaboration within the construct.

In addition to the development of a highly oriented matrix phase, results suggest that the mechanical integrity improves dramatically with finite construct strain. In fact, the newly formed matrix phase exhibits stress-strain behaviors approaching the response of glutaraldehyde bovine pericardial tissue (Figure 6-9). The mechanical response of glutaraldehyde fixed pericardial tissues has been well documented, as it is a clinically relevant material used for cardiovascular reconstruction and valve bioprostheses (Figure 1-7) [263, 268-273]. From the experimental and theoretical investigation of Sacks et al. [274], it is possible to directly compare the mechanical response of pericardial tissues, over relevant deformation magnitudes, with results of the current study. It can be seen that the mechanical response of the matrix principle direction is very similar up to a Green strain of approximately 0.09. Beyond this range, the de novo matrix response is more compliant with peak stresses obtained by both materials being comparable.

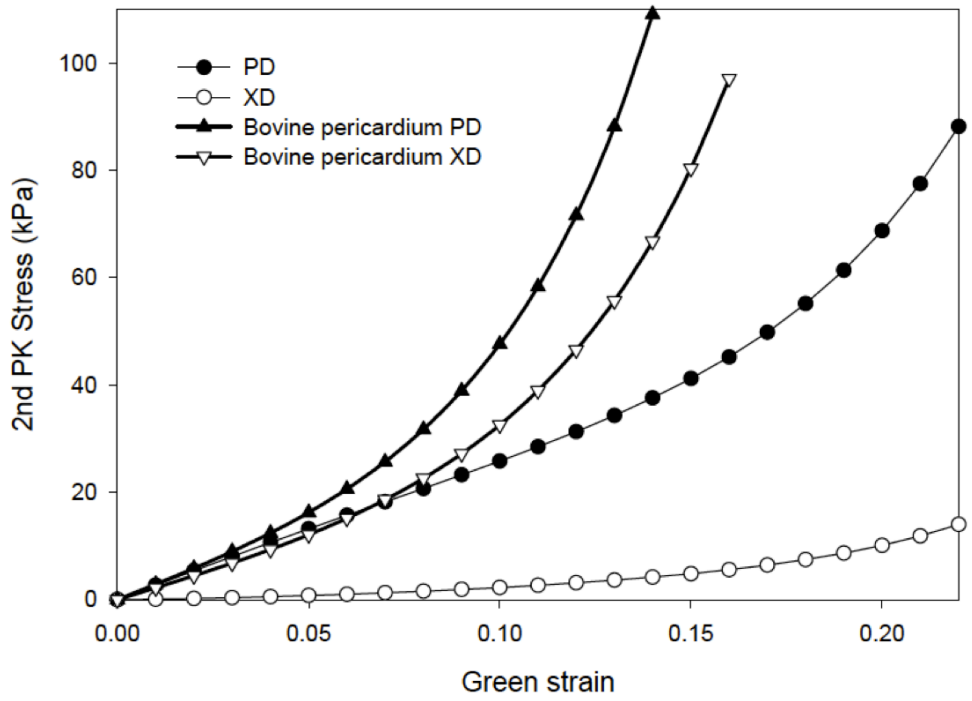

Figure 6-9. Biaxial mechanical comparison of representative de novo matrix behavior with documented glutaraldehyde treated bovine pericardium.

Also, from small strain theory predictions, the mean shear modulus for all 5 specimens was 1659 ± 281.7 kPa. Direct comparison of these results with other investigations is difficult. Specifically, findings are typically reported as gross changes from the original material behavior and little effort is made to delineate the respective constituent contributions. However, comparing our recent laboratory findings at comparable culture durations of cell seeded PGA:PLLA blends in vitro and in vivo exhibited shear modulus values approximately 2 orders of magnitude lower. For VSMC seeded needled non-woven constructs exposed to cyclic bending, the resultant effective matrix shear modulus was 46 kPa [138]. When the same PGA:PLLA scaffold is implanted in the right pulmonary outflow track of an ovine model for 7 days, the matrix phase of the explant only exhibited a shear modulus of 6.77 ± 1.43 kPa.

6.4.3 Challenges posed by the use of microintegrated PEUU

While the use of cell integrated electrospun polymers as a platform to investigate mechanically mediated matrix synthesis and material behavior was overall positive, it was not without mentionable difficulty. In its current state, electrospinning is a relatively immature technology in its application to engineered materials. While a benefit with its ability to produce materials of wide ranging mechanical behaviors, the electrospinning process is inherently chaotic with a multitude of manufacturing parameters that can drastically alter morphological or material characteristics. In the current study, manufacturing difficulties limited total throughput to about 30%. Some critical issues that limited the use of microintegrated PEUU were thickness variations across the specimen, specimen delamination, and inconsistent deposition of cells.

When specimen are produced, the process calls for a spinning collection mandrel to control fiber orientation while it is translated on a horizontal stage in an effort to deliver fibers evenly across a larger swatch of the mandrel. This method does increase the amount of usable material produced but discarding significant portions at the boundaries is necessary. The primary method to regulate thickness is to empirically control the duration of polymer deposition. This is not a significant issue for dry electrospun materials (i.e. without concurrent cellular integration) but cell culture is costly and reducing the amount of material discarded significant portions would be beneficial.

The lamellar arrangement of cells and polymer previously mentioned in Chapter 5 can be a concern as it can lead to delamination of the structure. Often, delamination related failure of the specimen is readily apparent immediately following production. While careful inspection can limit the use of material likely to fail via delamination, it is again a matter of discarding large numbers of cells, which are costly to produce. Despite efforts made to reduce the amount of

media used to deliver cells via electrospraying in hopes of resolving delamination, the issue still persists.

In addition to the delamination challenges created by spraying cell culture media on the specimen, inconsistent deposition of cells throughout the specimen was encountered. Unfortunately, the occurrence of this characteristic was more difficult to diagnose at the time of specimen production. Inconsistencies in the special deposition of cells are evident even after extended tissue culture and mechanical training (Figure 6-9). The prevalence of this difficulty

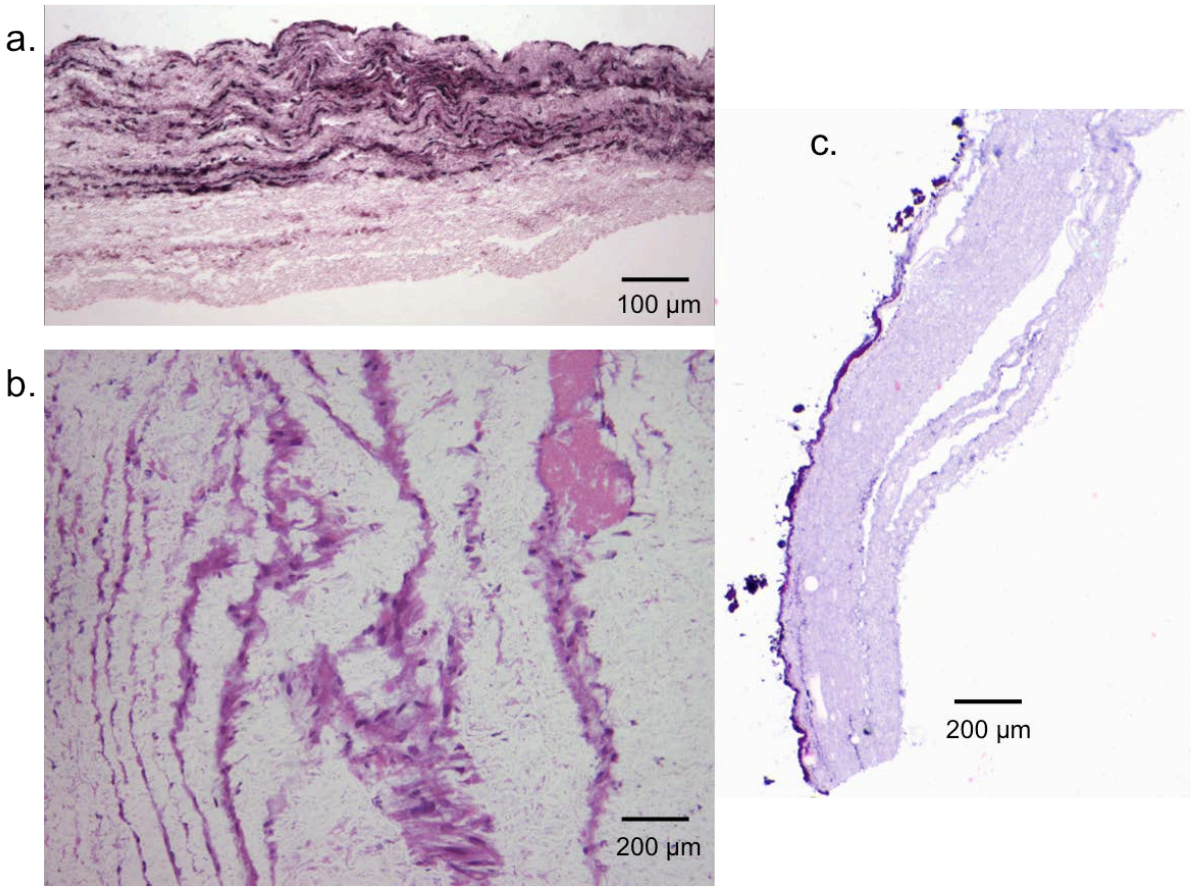

Figure 6-10. ECM elaboration can be limited by manufacturing variability.

varied significantly between specimens and ranged from partial microintegration of the specimen to the occasional acellular construct.

It should be noted, despite the encountered challenges, this novel manufacturing technique did enable the detailed investigation of deformation dependent cell biosynthetic activity and the subsequent quantification of de novo matrix mechanical behavior. Furthermore, it is likely that there does not exist a more suitable material for such specific investigations of fundamental phenomena related to tissue engineering. Continued advancement of material production and processing is critical for future tissue engineering efforts from fundamental scientific endeavors to clinical applications.

6.4.4 Limitations

While there is strong mechanical evidence that the newly formed ECM phase is highly anisotropic, we were unable to verify the structure visually. This is largely a result of practical limitations of preparing specimens for histological evaluation or limitations in imaging technology. While GMA and paraffin embedded specimens enabled reliable transverse sections, en face sectioning was found to be unsuccessful. Extensive cutting artifacts making imaging impossible confounded all efforts. In a similar light, it was assumed that matrix area fractions from transverse sections through the specimen are representative of overall volume fraction. Furthermore, confocal based imaging techniques were also unsuccessful. Two main characteristics prohibited detailed imaging of the matrix phase in situ. First, extensive cell proliferation at the specimen surface limited our ability to image deep enough into the specimen to investigate cell morphologies and matrix structure embedded in PEUU. Also, the strong

autofluorescent nature of PEUU resulted in substantial scattering of the signal effectively drowning out matrix specific signals.

7.0 SUMMARY AND CONCLUSIONS

Tissue engineering is a fast moving, interdisciplinary field with promise to transform acute and chronic medical care. Rather than replacing a diseased or defective native valve with a mechanical or animal tissue derived artificial valve, a tissue-engineered valve would be a living organ, able to respond to growth and physiological forces in the same way that the native aortic valve does. While a great deal of progress has been made, hallmark technical issues (appropriate selection of cell source, material selection, use of biochemical factors) still persist. Moreover, the success of many engineered tissue therapies rests on their ability to perform critical mechanical functions and exhibit structural features akin to healthy native tissue.

To date, our understanding of newly formed ECM physical properties and how they contribute to gross mechanical function remains limited. In the current study, we have employed cell integrated electrospun scaffolds as a platform to investigate the effects of mechanical conditioning that utilizes finite deformations of cells seeded within an elastomeric, fibrous scaffold that closely recapitulates native pulmonary valve structure and mechanical behavior. It is our hypothesis that optimal levels of finite deformation exist that can be exploited to manage ECM production and improve matrix mechanical behavior. It is through this hypothesis driven, systematic investigation that we hope to inform the rational design of future engineered tissue therapies.

7.1 PRINCIPLE FINDINGS

7.1.1 Scale dependent structure-function characterization of PEUU

A review of recent literature shows, elastomeric scaffolds fabricated by electrospinning natural polymers, synthetic polymers or polymer blends have received widespread attention. This is largely due to the ability to produce biocompatible polymer constructs that exhibit many soft tissue-like mechanical behaviors [61-63]. However, beyond basic characterization of the mechanical behavior of electrospun scaffolds, little has been done to gain a full understanding of how these scaffolds deform across multiple length scales. Though they may be able to recapitulate the mechanical behavior of native collagenous tissues at the tissue level, it is unclear how their microstructure deforms at the cellular level. Moreover, this lack of knowledge underscores the need for an experimental and mathematical framework beyond phenomenological modeling approaches to elucidate the functional performance of these scaffolds.

In the current work, electrospun PEUU was found to exhibit complex, hierarchical structures spanning multiple length scales which combine in a coordinated manner to form a scaffold with tunable tissue level mechanical behaviors. The micromechanical behavior, which differs from native valvular tissues, is characterized by short interconnected fibers that function in a uniquely organized fashion that is functionally similar to the long fiber structure induced behavior of native collagenous tissues. The detailed experimental investigations of electrospun PEUU described above enabled the characterization and quantification of scaffold gross fibrous structure; including fiber orientation distributions, tortuosity, and diameter. Moreover, with this information it is possible to gain insight about how these metrics translate to functional

performance of the scaffold. With a developed understanding of how these scaffolds perform across multiple length scales, it is possible to address further reaching implications when cells are introduced into the scaffold and how they would respond to their local environment when exposed to dynamic deformation.

7.1.2 Evolving coupled cell-scaffold deformation relationship

Static and cyclic modes of mechanical stimulation have been shown to alter protein synthesis and the amount and integrity of ECM proteins. Engelmayr et al. [139] demonstrated that cyclic flexural deformation not only increased ECM mass in nonwoven scaffold-ECM composites, but also the effective ECM stiffness. Yet, despite our growing understanding of the cause-effect relationship of mechanical stimulation on cellular processes, the specific mechanisms responsible for these phenomenona continue to be poorly understood, especially for cells embedded within three dimensional synthetic scaffolds [75, 171]. Ultimately, development of engineered tissue or organ replacements must rest on a strong fundamental knowledge of cellular interactions with the local environment and how these interactions span multiple length scales to contribute to the overall function [172-174]. Much can be learned about the mechanical modulation of functional tissue from electrospun PEUU scaffolds, since they capture some aspects of native tissue microstructure and exhibit the ability to endure large deformations while recovering completely.

Cells perceive and respond to their environment in a complex mechano-chemical fashion. A critical goal of the current work is to develop a more complete understanding of how organ-level deformations, such as cyclic stretch [202, 203], translate to microstructural deformations and ultimately as cellular mechanical stimuli. It has been shown that there is a concomitant

change in cell deformation with matrix accretion. Specifically, a transition in coupled cell-scaffold deformation behavior was quantified, where newly formed constructs exhibited a highly non-linear cell deformation response while dynamically conditioned specimens exhibited an affine cell-scaffold deformation relationship. This finding supports the assertion that the evolution of biological constituents within engineered tissues plays a pivotal role in the mechanical traction experienced by the cell in response to global mechanical cues.

While our experimental findings suggest that there is little or no coupling between the PEUU structure and subsequent phases, it would be interesting to further investigate how the newly formed biological components convect with the gross structure during deformation. In the current study, all analyses effectively homogenized the structure and did not directly consider the lamellar arrangement that was shown to develop. It is likely that this unique structure would translate to a more complex function at the tissue or organ level. Qualitatively, the development of a newly formed matrix phase positively impacted construct integrity in terms of improved handling characteristics and mitigated delamination characteristics often seen in acellular electrospun PEUU scaffolds. Similarly, the lamellar structure created during dynamic culture likely possesses unique characteristics that directly influence how mechanical tractions are imposed on cells immobilized within the construct. Additional investigations could prove useful in further testing the hypothesis that the evolving matrix component within engineered tissues plays a critical role on cellular deformations. Moreover, the cell deformation response may prove useful as a metric to quantify how well a biologically active engineered material recapitulates native function after extended culture, inclusion of humoral factors, or more complex dynamic loading regimes.

7.1.3 Electrospun PEUU performance as a tri-leaflet valve

This was the first known study to employ electrospun elastomeric materials to investigate gross mechanical performance as a tri-leaflet valve in vitro as a function of material microstructure. Both the isotropic and highly anisotropic materials investigated in this study exhibited the ability to perform the basic function of a tri-leaflet valve. For both materials, full coaptation was observed preventing retrograde flow. With the development of a valve holding apparatus, leaflet size and geometry were maintained to specifically test leaflet performance as a function a material microstructure. Unfortunately, due to substantial leaflet motion and buckling phenomena (or fluttering) of the leaflet during the ejection phase, quantification of the entire cardiac cycle was not obtainable. However, quantification of the closing phase of the valve cycle was accomplished in both quasi-static and dynamic testing modalities.

From the quasi-static application of increasing transvalvular pressure, it was possible to characterize leaflet deformation across a majority of the leaflet surface. Roughly 85-90% of the unstrained leaflet surface could be imaged. The remaining surface was typically obstructed from view by the clamping mechanism constraining the leaflet. From these experiments, peak stretch magnitudes on the order of 1.3-1.4 were measured in the belly region for the isotropic and anisotropic materials. The average deformation across the full leaflet surface was 1.11 ± 0.03 for the isotropic and 1.14 ± 0.06 for the anisotropic materials. While still in the finite deformation range, these values are significantly smaller then those exhibited by native leaflet tissues.

From the dynamic imaging data sets, qualitative observations were made implicating the critical role material microstructure during leaflet motion. For example, the isotropic material consistently exhibited a shorter closing duration with the closing duration of the anisotropic material being approximately 40% longer, lasting about 30-34 milliseconds. This may be a

functional result of difference in bending rigidity of the two materials. The anisotropic material, which exhibits a reduced bending rigidity in the radial direction, may enable a more gradual closing in response when compared to the isotropic material. Interestingly, the opening orifice area appears to be affected by material structure during systole. The isotropic material exhibited an increase orifice area and may be attributed to its ability to more readily deform in the circumferential direction enabling the flowing fluid to force open the structure to a g reater extent.

The major goal of quantifying the organ level function of electrospun PEUU as a tri-leaflet valve, was to systematically inform in vitro experiments aimed at understanding the relationship between global construct strain and mechano-dependent cell biosynthetic activity. Gaining insight about physiologically relevant deformations experienced by electrospun PEUU leaflet when exposed to native ovine RVOT hemodynamic conditions made it possible to develop experimentally guided mechanical conditioning protocols. In this way, it is possible to logically impose gross strain magnitudes spanning sub-physiologic to super-physiologic states to assess the effects on cells populating the construct interstitium.

7.1.4 Matrix accretion response to finite cyclic deformation

Electrospinning permits fabrication of biodegradable elastomers into matrices that can resemble the scale and mechanical behavior of the native extracellular matrix. High cell densities can be obtained throughout the specimen via concurrent cell electrospraying and polymer electrospinning. This study is the first to quantify the effects of controlled finite mechanical cues on matrix synthesis and mechanical properties in microintegrated elastomeric electrospun

scaffolds. Results indicate that VSMC biosynthetic behavior is indeed a function of global strain with markedly improved soluble collagen synthesis in specimens exposed to 30% strain. Collagen production as a function of cyclic strain magnitude was observed to be nonlinear for microintegrated VSMC with no significant difference in collagen production being observed between static and 15% strain specimens. For specimens exposed to the largest uniaxial cyclic deformation of 50%, an intermediate biosynthetic response was observed. From this it can be concluded that the elastomeric nature of electrospun PEUU is conducive to the synthesis of critical structural matrix proteins.

Interestingly, peak biosynthetic activity correlates well with in vitro principle strain levels observed for both isotropic and anisotropic PEUU tri-leaflet valves exposed to native ovine right side pressure and flow conditions. This suggests that physiologic hemodynamic conditions are optimal for the development of robust ECM accretion for VSMC microintegrated electrospun PEUU constructs. While collagen biosynthesis was directly influence by cyclic strain magnitude, proteoglycan production was consistent for all strain levels investigated in the current study. Sulfated GAG production was observed to significantly increase in specimens exposed to cyclic deformations but strain magnitude was not a determining factor.

Our results also indicate that cellular integration mitigates construct elongation resulting from the applied cyclic deformation. When compared to acellular specimens subjected to comparable cyclic strain magnitude and duration, the microintegrated specimens elongated approximately 40% less. While the mechanism for this behavior is unknown, it could have important performance implications for in vivo implantations where leaflet distention could result in catastrophic leaflet failure.

7.1.5 Quantifying de novo matrix mechanical contribution

Healthy native valvular tissues are known to undergo complex modes of deformation (i.e. cyclic stretch, flexure, and flow). The first hypothesis presented in Section 1.9 stated that these mechanical cues unique to heart valves could be exploited to optimize ECM synthesis within electrospun scaffolds in-vitro. While combined modes of deformation have been investigated in the development of engineered tissues [229, 267, 275, 276], the current body of work specifically investigated the effects of planar deformation modes as they represent the largest deformation magnitudes encountered by heart valves. Moreover, secondary modes of deformation (i.e. flexure or flow) typically occur on much smaller scales usually less than 10% strain. The novel results showed that cyclic finite deformations induced:

1. Measurable increases in biosynthetic activity
2. Production of collagenous matrix exhibiting strong mechanical anisotropy and stress levels comparable to bioprosthetic valve tissues

From PAM impregnation of electrospun PEUU, it was determined that the addition of an isotropic phase of known material behavior has no measurable coupling behavior. As a result, the gross tensile response of PEUU constructs was simply evaluated as the summation of the respective constituents. This is not to say that there is no coupling behavior but it is likely a secondary effect that could not be measured by tensile mechanical testing alone. For other modes of deformation, such as flexure or shear, it would not be beyond reason to anticipate more prominent coupling effects. For example, an added isotropic phase could effectively reduce fiber mobility or reorganization leading to an altered recruitment behavior that would translate to a unique stress-strain behavior.

Using PAM gel as a tissue analog could also create limitations in the study as it may not fully mimic forming tissue and accurately recapitulate potential mechanisms of interaction. For instance, PAM gel readily infiltrated the PEUU structure during polymerization where the microintegrated constructs exhibit a definite lamellar structure. This difference in structural organization alone could translate to altered mechanical behaviors at the tissue level. Furthermore, the developing matrix phase investigated in the current study (and soft tissues in general), are nonlinear and anisotropic, while PAM gel is known to be linear and highly isotropic. The PEUU scaffold embedded PAM gel studies presented above relied heavily on the assumption that PAM gel interacted with the scaffold in the same manner as tissue. Although differences may exist, the specific requirements for the tissue analog (able to be cast, tunable shear modulus, safe to create, no harsh solvents that could degrade scaffold, etc.) limited possible choices. Future studies could be aimed at investigating possible differences between scaffold interactions with PAM gel and tissue.

Recent literature shows that there is a wide array of scaffold materials and cell sources being actively investigated in efforts to produce functional engineered tissues (Table 6). Electrospun PEUU, being elastomeric, provides a significant advantage over recently investigated engineered materials, such as non-woven blends, as a platform to investigate the complex processes that characterize the evolution of engineered constructs. As presented in Chapter 6, matrix accretion in PGA:PLLA blend materials mediates fiber interconnectivity, owing to a strong coupling effect between the polymer and ECM phases. However, the effective stiffness of the newly formed phase is on the order of 6.8-14.8 kPa. Related efforts with rapidly degrading scaffolds, such as non-woven PGA or fibrin gels, have shown the ability to produce

Table 6. Modulus comparison of engineered and native cardiovascular tissues.

Material	Processing	Cell source	Culture period	Culture stimuli	Strain magnitude during culture	Mechanical testing conditions	Material evaluated	Collagen* (% weight)	Tensile modulus (MPa, mean ± SEM)		Strain (%)	
									PD	XD	PD	XD
Fibrin[1]	Gel	Human dermal fibroblast	3 weeks	Transvalvular pressure	--	Uniaxial	Composite	--	1.12 ± 0.4	0.58 ± 0.4	--	
P4HB coated PGA[2]	Nonwoven	Human saphenous myofibroblast	3 weeks	Transvalvular pressure	--	Uniaxial	Composite	78.9 ± 7.4 (w)	5.6 ± 0.7	3.8 ± 1.5	--	
PGA[3]	Nonwoven	Rat VSMC	10 weeks	Uniaxial strain	7%	Unixial	Composite	--	~ 0.70 ± 0.1#		--	
PGA[4]		Porcine VSMC	7-8 weeks	Inflation	1.5%	Unixial	Composite	43.9 ± 1.6 (d)	11.8 ± 2.7#		--	
PEUU	Electrospun	Rat VSMC	3 weeks	Uniaxial strain	30%	Biaxial	Formed tissue	2.4 ± 0.5 (d)	2.3 ± 1.8	0.2 ± 0.1	13-16 ± 3.0	
							Construct		3.3 ± 0.5	2.9 ± 0.5		
P4HB coated PGA[5]	Nonwoven	Human saphenous myofibroblast	4 weeks	Static w/ insulin and hypoxia	NA	Unixial	Composite	26.3 ± 2.2 (d)	21.5 ± 5.3#		10 - 20	
PLLA[6]	Braided	Rabbit chondrocyte	4 weeks	Static	NA	Unixial	Composite	--	108.4 ± 27.7#		~ 8	
Collagen[7]	Extruded	Rat dermal fibroblast	25 days	Static	NA	Unixial	Composite	--	83.4 ± 10.8#		5 - 10	
PCL[8]	Electrospun	Bovine MSC	4 weeks	Static	NA	Unixial	Composite	2.6 ± 0.4 (d)	5.9 - 8.5#		--	
Porcine aortic valve[9]	NA	NA	NA	NA	NA	Biaxial	Matrix only	~ 55 (d)[11]	9.1 ± 0.2	1.8 ± 0.1	3 ± 0.01	53 ± 0.1
Bovine pericardium[10]	NA	NA	NA	NA	NA	Biaxial	Matrix only	~ 90 (d)[12]	14.9 ± 2.8	2.8 ± 0.4	15	

* Weights reported as percent dry (d) or wet (w)
# Directional mechanical properties were not evaluated
-- Values not reported

[1]Robinson et al. [123], [2]Mol et al. [277], [3]Kim et al. [278], [4]Dahl et al. [279] [5]Balguid et al. [280], [6]Cooper et al. [281], [7]Gentleman et al. [282], [8]Nerurkar et al. [283], [9]Liao et al. [87], [10]Sacks et al. [274], [11]Bashey et al. [284], [12]Schoen et al. [285]

anisotropic materials when combined with dynamic mechanical training (Table 6, [123, 286]). While encouraging, these approaches generally lack sufficient mechanical integrity and the ability to undergo finite deformations for extended periods, characteristic of heart valve tissues. Moreover, when mechanical testing is performed on composite engineered tissues, it is difficult to deduce the mechanical contribution of the newly formed and evolving matrix phase. This is particularly apparent in the use of relatively stiff polymers that are processed to create three-dimensional structures or materials that are know to degrade slowly. Conversely, the present indicates, for the first time, that finite deformations promote the production of a robust matrix phase that exhibits material properties approaching that of both the PEUU scaffold and clinically relevant tissues for heart valve replacement. For example the tensile modulus exhibited by the matrix phase in the preferred direction (2.3 ± 1.8 MPa) is on the order of that exhibited by the PEUU polymer (2.9 – 3.3 MPa), native porcine aortic valve leaflets (1.8 – 9.1 MPa), and the cross preferred direction of glutaraldehyde fixed bovine pericardium (2.8 ± 0.4 MPa).

The current work represents a first step in the systematic development of electrospun constructs for in vivo use. Biologically active constructs are critical to facilitate host acceptance and integration [287]. However, fully recapitulating all biological and mechanical characteristics of healthy native tissues is well beyond our current understanding. Instead, in vitro studies, as presented above, offer valuable insight into the early development of a newly formed, evolving matrix phase. Practical experimental constraints limit our ability to develop engineered constructs with newly formed matrix phases that dominate the mechanical response of the engineered tissue. In fact, the amount of de novo matrix proteins that can reasonably be attained in electrospun constructs at relatively short time periods represents a fairly small fraction of the total construct. In related studies by Nerurkar et al., the percent dry weight of collagen at 3-10

weeks for mesenchymal stem cells seeded in an electrospun PCL scaffolds was approximately 2-8% [266, 288]. Moreover, despite the developing matrix phase, the uniaxial tensile moduli reported in these studies showed no significant change between newly manufactured specimens and those after 4 weeks of culture.

As a result, it is necessary to develop sensible means to assess the mechanical behavior of these newly formed matrix phases. To this end, simply matching mechanical properties of a tissue at the time of implant does not ensure the appropriate remodeling response necessary for long-term efficacy. Most tissue engineered approaches involve a scaffold that is intended to degrade over time and is to be replaced by host cell infiltration, tissue growth, and remodeling phenomena. Without insight into the evolution of these engineered materials, it prohibits the development of next generation materials that seek to attain functional equivalence. The current investigation shows that it is possible to regulate biosynthetic activity and assess the production of a collagenous matrix exhibiting robust mechanical properties via exogenous mechanical cues even at relatively short experimental time points. It is hoped that this improved understanding of the matrix elaboration process in these elastomeric, fibrous constructs will lead to the rational design of materials and manufacturing methods for future tissue engineered efforts.

7.2 FUTURE DIRECTIONS

As a whole, the presented work forms the basis for a number of prospective investigates aimed at gaining detailed insight into the function of cell integrated electrospun elastomeric scaffolds as load bearing engineered tissues. Many of the results presented will be used to inform or test more sophisticated theoretical approaches geared towards probing functional characteristics of

electrospun PEUU materials. These efforts will explore PEUU electrospun materials both as a way to understand the evolution and maturation of engineered tissues and their applicability to clinically relevant issues such as a tissue engineered substitute for pulmonary valve repair.

One area of interest is improving the mechanical performance from the microstructural level to improve tissue engineering scaffold design. In spite of electrospinning's flexibility and ability to form complex fiber assemblies, additional studies are required to elucidate how the fibrous microstructure translates into specific tissue (or meso-scale) level mechanical behavior. Deterministic structural models can quantify how key structures contribute to the mechanical response as a function of bulk deformation across multiple scales, as well as provide a better understanding of cellular mechanical response to local microstructural deformations. To develop this structural model analysis work is currently underway to produce a full description of the real fiber network geometry, including connectivity information, fiber diameter and orientation. From there, a multi-scale finite element model can be used to investigate and optimize micro-architectural features, which then direct macroscopic function. A mechanistic understanding of how the material micro structure translates into a specific mechanical response would lead to a better performing generation of tissue engineered constructs.

Other ongoing modeling efforts seek to improve the efficacy of valve replacement surgeries by optimizing the geometry of a leaflet formed from electrospun PEUU. An empirically determined unloaded leaflet shape may result in abnormal valve function due to incomplete coaptation of the leaflets and asymmetric stress distributions. To determine the final deformed shape of an engineered PV replacement under transvalvular pressure, the following key factors must be determined: the scaffold anisotropic mechanical properties, optimal thickness, and the exact initial leaflet shape. With this information, it is possible to develop a

design framework to determine optimal leaflet shape. A generalized Fung-type hyperelastic constitutive model is currently being implemented into a commercial FE software package to simulate the mechanical behavior of electrospun PEUU scaffolds. By perturbing the initial shape of leaflet and simulating its quasi-static deformation under PV diastolic loading, the optimal shape of the unloaded leaflet can be determined by comparing the deformed shape of leaflet obtained from FE simulation of the tissue engineered PV with the one from microCT scan of a native ovine PV. Validation of this methodology can be directly obtained from the results of Chapter 4 since the PEUU mechanical behavior and leaflet boundary conditions are well defined.

Another logical extension of the current work is to inform the development of a tissue accretion model describing the matrix elaboration behavior within a fibrous elastomeric structure. From the current work, a detailed understanding of material microstructure has been obtained. Furthermore, the coupled cell-construct deformation behavior has been experimentally quantified initially after cell microintegration and following 21 day of mechanical training. This provides unique results for which the model can be tuned. The overarching goal of this work would be to evaluate and optimize microstructural features that are critical to the formation of robust ECM. This modeling framework could also prove useful in predictive simulations effectively guiding future experimental investigations.

Important to any tissue engineering work, understanding the native properties one desires to replicate is crucial to assessing the success of the work. The experimental evaluation of native leaflet mechanical properties initially introduced in Section 1.2.2 and described in detail in Appendix A, are readily conducive to the development of a structural constitutive bi-layer material model. Not only would such a theoretical framework improve our understanding of

native leaflet functions, it could inform tissue engineering efforts of critical structure-function relationships necessary for healthy native function.

APPENDIX A

ON THE BIAXIAL MECHANICAL PROPERTIES OF THE LAYERS OF THE AORTIC VALVE LEAFLET

Comprised of three leaflets (right coronary, left coronary, and non-coronary) and situated between the left ventricle and the aorta, the aortic valve (AV) functions to prevent retrograde blood flow back into the left ventricle. The normal functioning AV experiences at least three billion cycles in a single lifetime, and as a result the AV leaflet has evolved into a highly specialized structure. The AV can become diseased due to tissue degeneration and mineralization. It is estimated that more than 75,000 prosthetic heart valves are implanted annually domestically and ~250,000 worldwide [289]. Although current heart valve replacements have extended the life of many patients, there is to date still no ideal alternative. Moreover, the knowledge of the etiology of valve disease is still very limited. Improvements to our understanding of heart valve disease and the development of novel heart valve therapies must rest on a strong fundamental knowledge of native AV function.

AV leaflets are composed of three morphologically distinct layers: the fibrosa, spongiosa, and ventricularis (Figure 7-1) [290]. The fibrosa is situated on the aortic surface of the leaflet and exhibits multiple corrugations oriented along the circumferential direction. The ventricularis

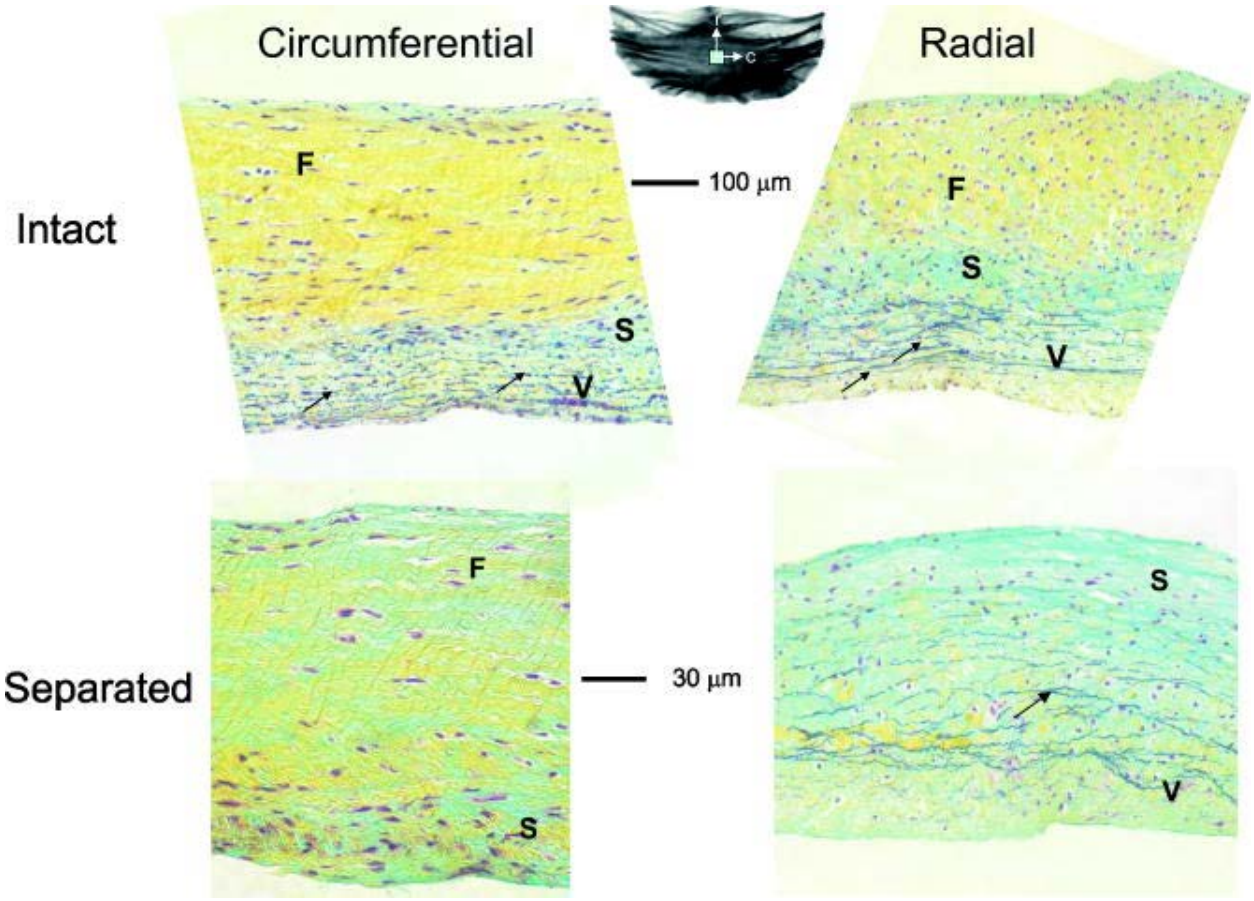

Figure A-1. Highly specialized structures and a distinct tri-layer arrangement of the AV.

faces the left ventricle, and the spongiosa is located between the fibrosa and ventricularis layers. These layers are composed of varying amounts of the connective tissue proteins collagen and elastin, as well as glycosaminoglycans (GAG's) and valve interstitial cells. The interstitial cells exhibit phenotypic characteristics of both fibroblast and smooth muscle cells enabling them to facilitate cell-cell communication, tissue remodeling, wound healing, and contraction [6, 194, 291, 292].

The fibrosa is composed predominantly of a dense network of Type I collagen fibers (Figure 7-1). The collagen fibers of the fibrosa form larger structures of well aligned bundles

oriented in the circumferential direction. When the leaflet is unloaded, the collagen bundles exhibit a highly undulated arrangement. The ventricularis is composed of a dense network of elastin and collagen fibers. Due to its relatively high elastin content and its attachment via the spongiosa to the fibrosa, the ventricularis has been reported to exert compressive forces that keep the fibrosa in the undulated conformation found in unloaded intact leaflets [79, 221, 293, 294]. The ventricularis is also responsible for the elastic recoil seen when the leaflet is unloaded [221]. The spongiosa is primarily comprised of GAG's and fibrous structures coupling the outer layers. Currently, the structure-function relationship of the spongiosa is not well understood. One hypothesis suggests that due to its loose organization, the spongiosa enables local movement and shearing between the fibrosa and ventricularis layers during dynamic loading [295-297]. However, substantial experimental evidence to support this hypothesis is currently lacking.

Due to the predominance of Type I fibrillar collagen, the fibrosa and ventricularis layers are the major tensile load bearing layers. Moreover, the ventricularis is thought to contribute to the low strain (stress) behavior and the fibrosa is primarily responsible for the high strain (stress) response of the leaflet tissue. Yet, to date detailed knowledge of the function and mechanical interactions of the AV layers remains limited. Vesely et al. [79] separated the layers of the leaflet and employed uniaxial tensile testing techniques to investigate the function and interaction of the fibrosa and ventricularis. These studies were the first to show that the intact AV leaflet exhibits a preloaded configuration [79]; the fibrosa was observed to elongate while the ventricularis contract after separation. They were also able to show that the extensibility of the separated layers is markedly different than the intact tissue.

In a related study, we explored the effects of transvalvular pressure on the intact and separated AV collage structure using small angle light scattering (SALS) [220]. This study

quantitatively determined that the collagen fiber alignment of the fibrosa and ventricularis are quite different at low transvalvular pressures. When the intact leaflet was separated and the fibrosa and ventricularis layers of the leaflet were analyzed separately, the fibrosa exhibited a high degree of orientation while the ventricularis exhibited a more random orientation. Interestingly, the fiber alignment of both layers became increasingly similar with increased transvalvular pressure and became indistinguishable at pressures above 60 mm Hg (note that 80 mmHg is the normal transvalvular pressure level). It was also found that the rate and amount of reorientation of the fibrous microstructure are both regionally and layer variant. The comparable degree of collagen fiber alignment in the ventricularis and fibrosa layers at high transvalvular pressures indicates the possibility that the ventricularis can make significant mechanical contributions to the leaflet stiffness.

Yet, despite available biaxial mechanical experimental studies on the mechanical behavior of the intact AV leaflet [16-19], there have been no studies that characterize the multi-axial mechanical properties of the individual leaflet layers. Knowledge of these subtle but important layer properties and interactions is vital to our understanding native valve function, and will lay the basis for rational replacement heart valves. In addition, all previous heart valve tissue constitutive models either assume uniform transmural wall stress or utilize a membrane tension formulation [17, 20-22]. Development of true 3D stress-based constitutive models requires knowledge of the individual layer responses.

The current study was thus undertaken to further our understanding of the role of each leaflet layer in the mechanical function of the native aortic valve leaflet. In order to obtain layer specific mechanical properties, a micro-dissection protocol was developed so that the leaflet could be separated into two distinct layers without damage. The intact leaflet and separated

layers were then subjected to mechanical testing, histological evaluations, and detailed thickness measurements to determine how the layers interact and contribute to the function of the intact leaflet.

A.1 PROTOCOLS

A.1.1 Tissue preparation

Fresh porcine aortic valves were obtained at a local abattoir and placed into phosphate buffered saline (PBS) and kept on ice for transport to the laboratory. At the laboratory, leaflets were removed from the aortic root. The right coronary leaflet only was chosen for study due to its large size in comparison to the left and non-coronary leaflets. The right coronary leaflet was then placed back into PBS and snap frozen at -80 °C. This storage technique was selected to avoid tissue degradation prior to testing, and was based on previous studies that demonstrated the minimal effects on connective tissue mechanical behavior following short term low-temperature storage [298].

Prior to testing, leaflets were removed from the freezer and thawed in a 37°C water bath. A rectangular test specimen was cut from the central lower belly region (below the Nodulus of Arantii) of the leaflet measuring approximately 9 mm in the circumferential direction and 6 mm in the radial direction (Figure 7-2). The region from the Nodulus of Arantii to the free edge (coaptation region) was discarded due to the fibrous nature of the nodulus and the inherent lack of a distinct tri-layered structure in the coaptation region. Although small in size, this specimen could be reproducibly separated and tested without subsequent damage. The specimen was then

placed into PBS with 1 mM phenylmethylsulfonyl fluoride (PMSF) to prevent proteolytic degradation of the specimen during the course of testing.

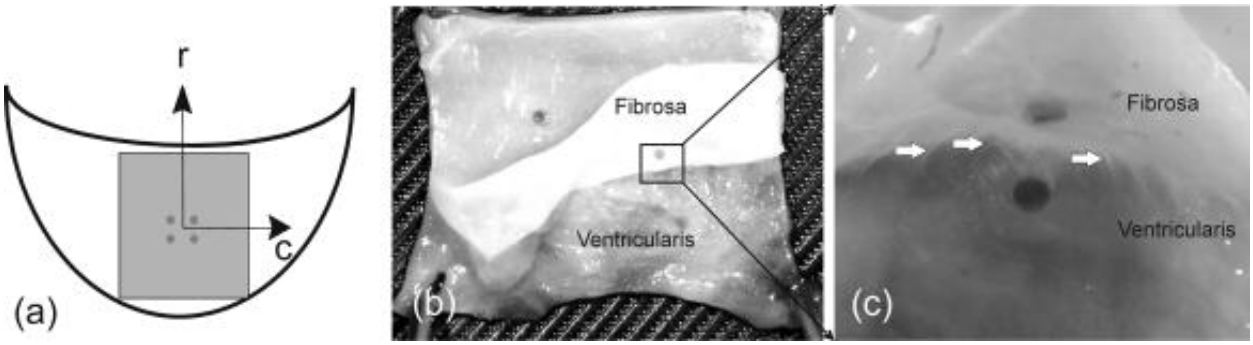

Figure A-2. Microdissection of an aortic leaflet specimen.

A.1.2 Microdissection

The dissection technique of the leaflet layers was developed based on previous methods [220, 294] and modified to work with the biaxial test specimens rather than the intact leaflet. For testing, the previously tested intact specimen was placed on a cork dissection board with the fibrosa surface facing down. Four 25 gauge needles were passed through only the fibrosa to keep it secured to the board. While keeping the specimen moist with PBS at all times, the ventricularis layer was gently lifted upwards with delicate forceps to expose the spongiosa layer. In preliminary studies, it was found that the spongiosa contained numerous interconnecting fibrous structures that couple the fibrosa and ventricularis (Figure 7-2). In order to separate the outer fibrous layers, it was necessary to manually sever each interconnection. This was accomplished through the use of a low power dissection microscope and ophthalmic micro-scissors.

A.1.3 Time course effects of layer separation

To quantify the potential for time-dependent effects of layer separation, it was first necessary to investigate the tissue response following dissection as the layers were allowed to fully attain their stress free configurations (Figure 7-3a). For a total of 8 leaflets, the displacements of four fiducial markers placed on each of the outer layers of the leaflet prior to separation were used to optically quantify deformations resulting from dissection. To produce the array of securely adhered markers, polypropylene disks 50-70 μm thick and ~400 μm in diameter were glued to the specimen center with cyanoacrylate adhesive (Permabond, Somerset, NJ) in a 2 x 2 array with dimensions of approximately 2.5 mm x 4 mm in the circumferential and radial directions respectively. The polypropylene disks were obtained by cutting cross sections from a length of 2-0 nonabsorbable surgical suture (Ethicon Inc., Somerville, NJ). This marker material was chosen because of its ability to securely adhere to the specimen surface through various modes of testing, the handling involved in microdissection, and to reduce the amount of adhesive required.

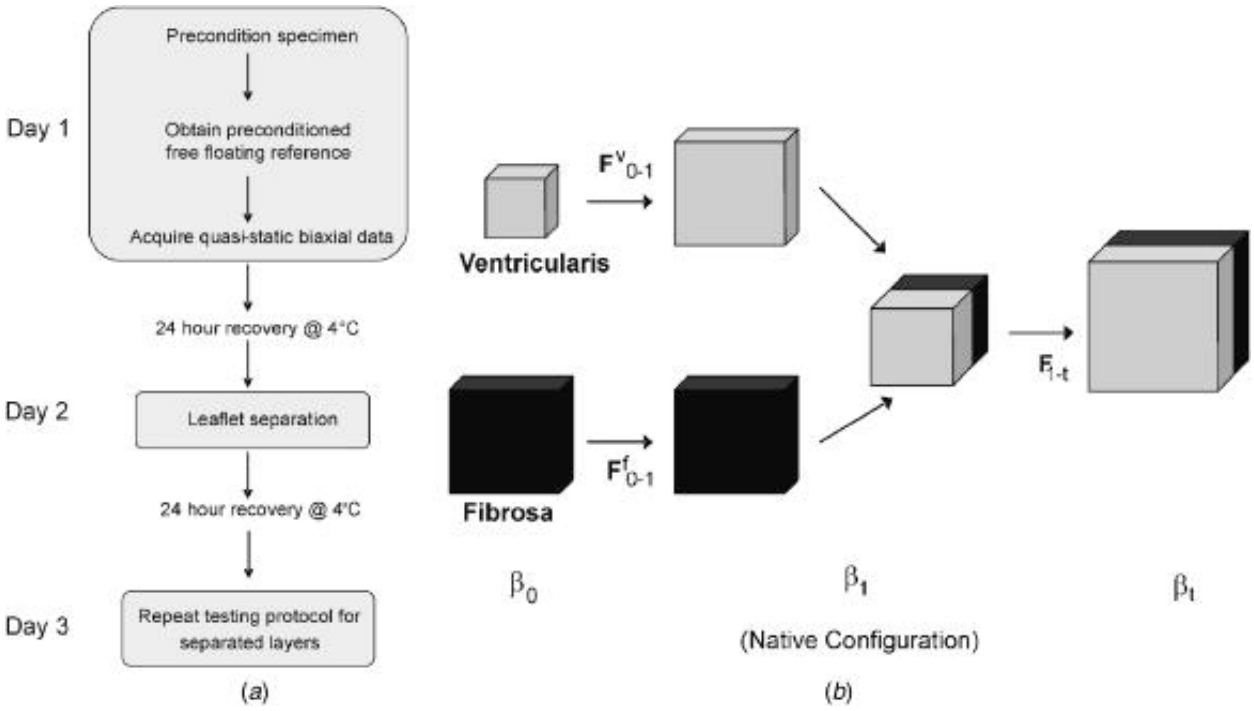

Figure A-3. Depiction of the full three day testing protocol and kinematic reconstruction of a bilayer material.

The resulting displacements of the markers were used to compute the components of the 2-D deformation gradient tensor **F** [178]. The components **F** are $\lambda_C=\mathbf{F}_{11}$, $\lambda_R=\mathbf{F}_{22}$, and $\kappa_1=\mathbf{F}_{12}$, $\kappa_2=\mathbf{F}_{21}$ where λ_C, λ_R, κ_1, and κ_2 are the circumferential and radial stretches, and shear strains, respectively.

A.1.4 Kinematic reconstruction

For a bilayer tissue configuration, one would normally start with the individual layers in their separated, stress free reference configuration. Sequential deformations would then arise from coupling the layers in the intact configuration (accounting for any pre-strains) and the application of external loads. We define states as

β_0 - the separated, unconstrained configuration,

β_1 - the intact configuration,

β_t - the current configuration of the intact tissue in response to external loads.

We thus notate the deformation gradient tensor associated with the transition from β_0 to β_1 as $\mathbf{F}^{L}_{0\text{-}1}$. Similarly, the deformation gradient tensor associated with the transition from β_1 to β_t is defined as $\mathbf{F}^{L}_{1\text{-}t}$. The total deformation gradient is then

$$\mathbf{F}^{L}_{t} = \mathbf{F}^{L}_{0\text{-}1}\mathbf{F}^{L}_{1\text{-}t} \qquad \text{EQ. A-1}$$

where $\mathbf{F}^{L}_{i}$ is the deformation gradient tensor for state i = 0,1,t and layer L represents the fibrosa or ventricularis respectively (Figure 7-3b). However, for valve leaflet tissues the native state is the intact configuration, which is not the stress free state. As a result, it is necessary to work in reverse from the native configuration to the stress free state and the biaxial deformation of the intact tissue due to testing is actually computed in reverse order.

A.1.5 Biaxial mechanical testing

A detailed description of the biaxial testing device and methods used for planar biological tissues has been presented previously [16]. Briefly, for the current study 250g load cells (Model 31, Honeywell Sensotec, Columbus, OH) were used to acquire load values. Leaflet deformations were measured optically by tracking a four marker array with a 1Kx1K pixel imaging system. The biaxial testing system was automated allowing the marker locations and axial forces to be continuously recorded with custom marker tracking and data acquisition software.

The biaxial testing protocol involved the testing of intact tissue, dissection of the leaflet, and then the testing of the separated layers (n=7). The complete protocol to test the intact and separated layers spanned three days (Figure 7-3a). On the first day, the intact specimen was

subjected to systematic thickness measurements and seven biaxial testing protocols to fully describe the specimen's quasi-static mechanical behavior. Thickness measurements were obtained by averaging six thickness measurements which were taken across the entire specimen using a Sterret® (Model 1010, The L.S. Starrett Co., Athol, Massachusetts) dial caliper which was accurate to 24.5 μm. Biaxial testing was conducted with the circumferential and radial specimen axis aligned with the device axis and submerged in a bath of PBS held at room temperature. Specimens were first preconditioned by cyclically loading the specimens to the desired maximum membrane tension of 60 N/m for intact and separated fibrosa specimens and 20 N/m for separated ventricularis specimens. Immediately following the preconditioning cycles, the specimen was completely unloaded and imaged in its preconditioned free-floating configuration. This reference state was chosen because it most closely represented the unloaded leaflet physiologic state.

Mechanical testing consisted of axial tension ratio controlled protocols (T_{11}:T_{22}=0.1:1.0, 0.5:1.0, 0.75:1.0, 1.0:1.0, 1.0:0.75, 1.0:0.5, 1.0:0.1) using a half cycle time of 15 seconds to quantify the quasi-static response. Following biaxial testing the specimen was removed from the device and placed back into the PBS/PMSF holding media and stored at 4°C for 24 hours. It should be noted that the tension-stretch plots reported in this study start from the 0.5 gram preload, which was used to ensure test response repeatability. Afterwards, the specimen was removed from refrigeration and was manually separated as described above. After dissection the specimen was again allowed to recover in the holding media at 4°C for 24 hours. Thickness measurements of the individual layers were recorded as previously described and the separated layers were tested individually.

A.1.6 Dual intact strain imaging

Despite the tri-layered architecture, previous modeling attempts for planar tissues such as heart valves generally assume the transmural strain field to be homogeneous. To provide experimental data to support or refute this assumption, the following study was conducted. Simultaneous images were acquired during equi-biaxial loading from the fibrosa and ventricularis surfaces by adding an additional camera to the biaxial testing apparatus. A total of eight specimens were tested in this manor.

A.1.7 Strip biaxial testing of the ventricularis layer

From pilot studies it was apparent that membrane stresses as small as 1 N/m induced substantial deformation of the ventricularis. Due to the extremely compliant nature of the separated ventricularis layer and the limits of the current biaxial testing device, it was not possible to accurately investigate its mechanical response at tension levels less than ~1 N/m. As a result, a custom device for strip biaxial testing was used due to its greater precision and sensitivity in measuring loads as a function of stretch. The testing apparatus consisted of a small bath secured to a computer controlled translation stage to which one end of the specimen could be mounted via a fixed bar. The opposite end of the specimen was attached to a flexible bending bar (316V stainless steel, 0.009 in. diameter) that extended out of the bath and was secured to a stationary mount. Through horizontal translation of the bath the distance between the fixed and flexible bar was increased, subjecting the specimen to prescribed elongations. The stainless steel bending bar, which had a known stiffness, was capable of achieving a load resolution of 2.91 mN/mm. During loading the specimen was viewed with a CCD camera to track the motion of markers

placed at both ends of the specimen. The video resolution of the testing apparatus was approximately 57 pixels/mm with a corresponding strain resolution of 0.27 percent. Tracking these markers and measuring the deformation of the bending bar enabled both strain measurements and the force applied to the specimen to be calculated in real time. The net run time load resolution was 0.33 mN and the net strain resolution was 0.32 percent.

To perform these tests seven right coronary leaflets were subjected to the microdissection protocol outlined above. The separated ventricularis specimens measured approximately 9.0 mm x 6.5 mm in the circumferential and radial directions respectively. Instead of the typical suture tethers used during biaxial testing, two small custom wire coils were passed through the specimen four times at opposite ends [229] . The wire coils were used to carefully mount and hold the specimen in the testing device. The wire coils were rigid and so opposed displacements in the direction orthogonal to the applied load. In pilot studies, we observed no significant specimen narrowing during elongations of approximately 15 percent.

For preconditioning, the specimen was stretched so that the tension-stretch curve was seen to make the transition from the toe region to the high modulus region of the curve. The specimen was stretched in a cyclic manor until the tension-stretch curves became repeatable. Once the specimen was preconditioned, data was acquired while the specimen was slowly stretched until a complete stress-stretch curve was obtained. After testing, the specimen was removed from the device so that the wire coils could be carefully removed. The specimen was then rotated 90 degrees, the wire coils were passed through the untested side of the specimen, and the specimen was remounted in the testing device. The full testing protocol of preconditioning and acquiring data was repeated.

A.1.8 Tissue preparation

Representative tissue specimens from the central belly region of intact and dissected right coronary leaflets were fixed in 10% buffered formalin, embedded in paraffin wax, and sectioned (5μm) for light microscope examination. Movat's Pentachrome staining, where nuclei and elastin stain black, collagen stains yellow, and ground substance stains blue, was performed to evaluate tissue content and layer thickness. S tained sections were digitized via bright field microscopy and evaluated with image analysis software to quantify layer thicknesses. Layer boundaries were visually defined and the average distance of at least five locations between boundaries determined.

A.1.9 Statistical analysis

Results are expressed as mean ± standard error of the mean (SEM). Statistical significance of the simultaneous imaging results were determined by the Mann-Whitney Rank Sum test. Statistical significance of the time course effects of dissection were determined by two-sided student's t-test. Differences were considered statistically significant when $p<0.05$.

A.2 RESULTS

A.2.1 Layer separation

Histological evaluation of the separated leaflet tissues indicated that the microdissection protocol developed did not induce observable damage to the outer fibrous layers (Figure 7-1). Histological results further indicated that all dissections occurred entirely within the spongiosa layer as desired. During separation the spongiosa was bisected and the remaining GAG-rich tissues were observed in both the fibrosa and ventricularis to remain intact.

Transient deformations resulting from layer separation occurred differently for each respective layer (Figure 7-3a). After dissection, it was observed that the fibrosa initially elongated to 28.2% and 4.8% in the radial and circumferential directions respectively. This elongation was observed to occur immediately after dissection with no observable additional deformations occurring afterwards. The ventricularis, on the other hand, exhibited a gradual contraction as it attained a stress free configuration. It contracted 10.9% and 8.2% in the radial and circumferential directions, respectively, with all deformations ceasing after one hour (Figure 7-7). Both layers demonstrated statistically significant directional layer dimensional changes. The total thickness of the separated layers was larger than the intact thickness and was observed to increase in thickness after separation. We see that the total thickness after separation was slightly but not significantly larger than the intact thickness while the total thickness 24 hours post separation was significantly larger ($p = 0.041$).

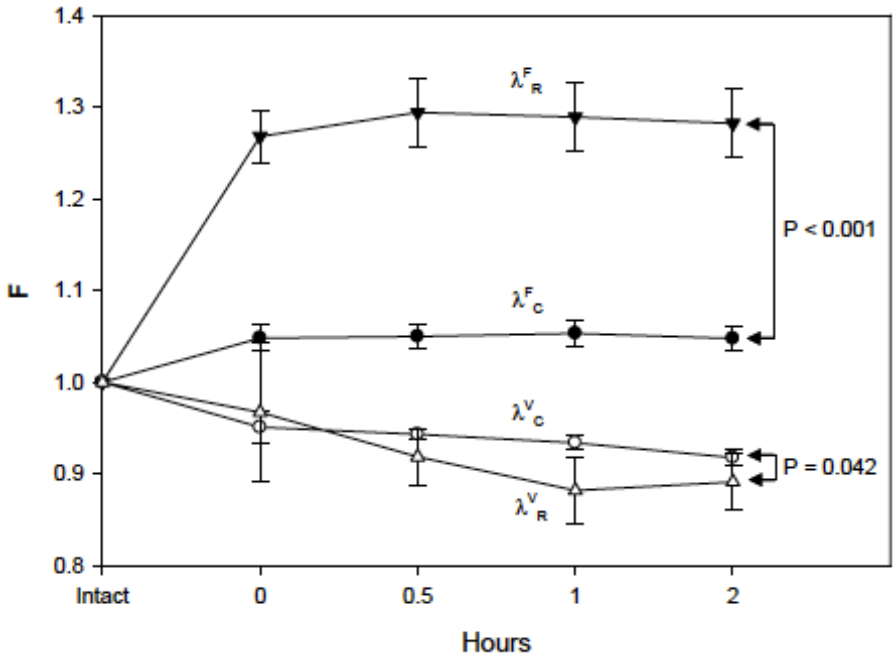

Figure A-4. The time course effects of leaflet separation.

A.2.2 Biaxial mechanical properties

Several interesting results were observed from biaxial mechanical behavior of the intact and separated tissues (n = 7, Figure 7-5). The intact AV leaflet and its separated layers were very compliant initially, manifested in the substantial elongations exhibited at loads of only 0.5 g. The results also indicate that the intact and separated layers exhibited significant anisotropic responses along with differences in the extensibility between the intact and separated specimens.

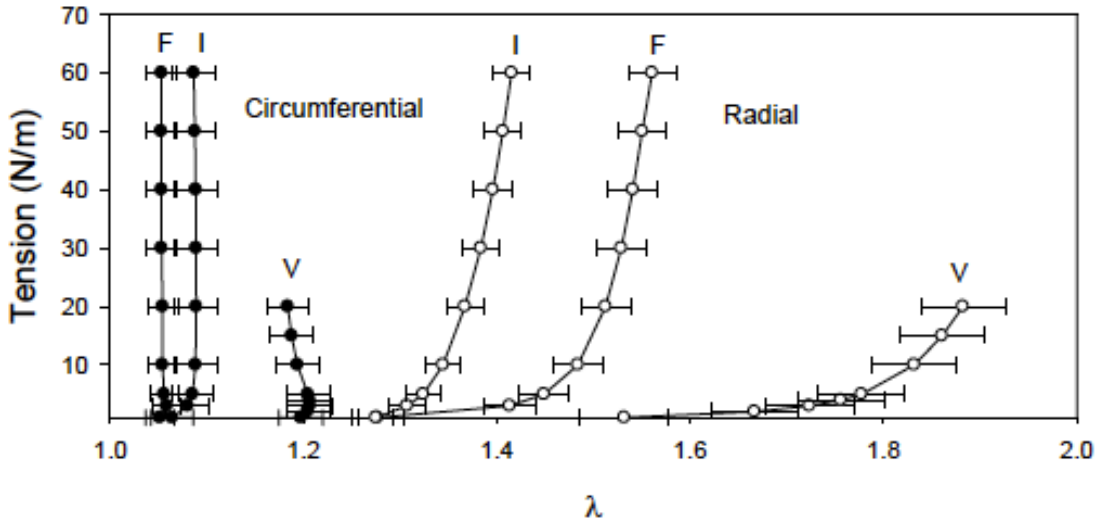

Figure A-5. Mean equibiaxial tissue behavior of the intact, separated fibrosa, and ventricularis layers each with respect to their own preconditioned, free floating reference state (β_0).

The intact tissue response was in agreement with previously reported equibiaxial tension data [16] and lies between the separated tissue responses. The separated fibrosa behavior was quite similar to the intact response with the exception that it was slightly less extensible in the radial direction. It should also be noted that the transition from the low to high modulus region was much more abrupt for the separated fibrosa when compared to the intact response. In contrast, the ventricularis exhibited an extremely compliant equibiaxial behavior that is made apparent by the long toe region. The behavior of the ventricularis at extreme stretch levels indicates that it is capable of making significant contributions to the stress handling ability of the intact tissue.

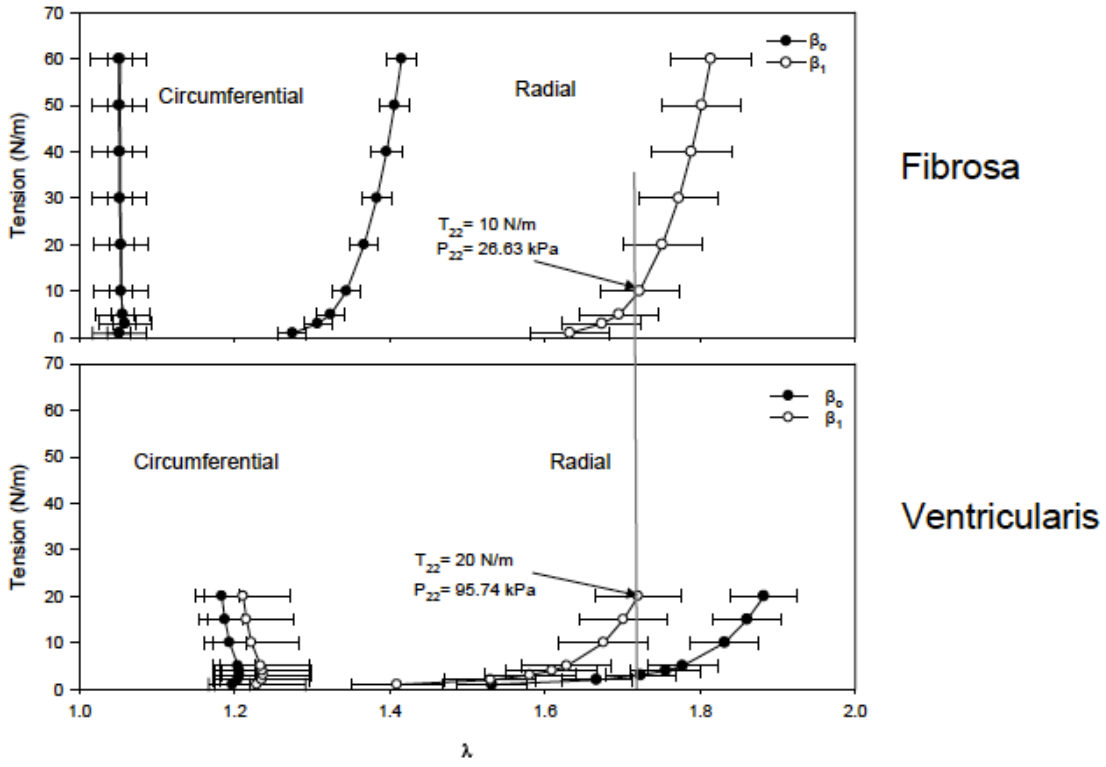

Figure A-6. The equibiaxial responses of the fibrosa and ventricularis computed with respect to both β_0 and β_1.

Our results also highlight the subtle but important effects of reference state (Figure 7-6). Due to the anisotropic nature of AV tissues this phenomenon was most apparent in the radial direction. If the separated, free floating reference (β_0) is chosen the fibrosa appears to be less extensible in the radial direction than when referenced to the intact state (β_1). The ventricularis on the other hand, exhibits the opposite relationship where it appears to be more extensible when β_0 is chosen as opposed to the reference state. These large changes are induced by the preloaded nature of leaflet tissues and the resulting deformations that occur upon separation. When referenced to the intact conformation (β_o) substantial differences were seen between the radial contributions of each layer. Thickness measurements (Table 7) enabled us to calculate corresponding first Piola-Kirchoff stresses: $P_{22}^{v} = 95.74$ kPa while $P_{22}^{f} = 26.63$ kPa at equivalent

levels of stretch. These results suggest that the ventricularis layer makes profound contributions to the intact leaflet response in the radial direction.

A.2.3 Dual intact tissue strain imaging

The accuracy of the simultaneous imaging system was verified by testing a latex rubber specimen with dimensions similar to the AV specimens (Figure 7-7a). The equibiaxial tension-stretch behavior of intact tissue during simultaneous imaging indicates that the strains experienced by each layer are nearly identical ($n = 8$, Figure 7-7b). Although the ventricularis tended to undergo slightly larger deformations, the measured strains were not significantly different, suggesting that the strain distribution through the thickness of the specimen is homogeneous.

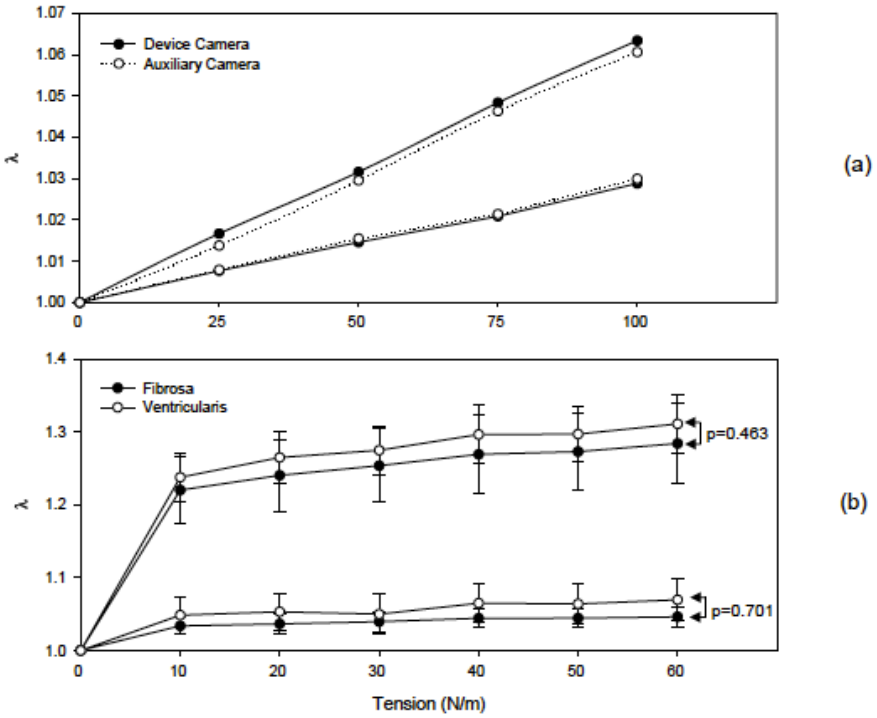

Figure A-7. Simultaneous imagining system verification by testing of a latex rubber specimen.

A.2.4 Intact leaflet and layer thickness

The observed changes in layer dimensions post-dissection (Figure 7-4a) suggested layer thickness change may also be time dependent. To better explore the changes in layer thickness changes with dissection and time, five additional specimens were prepared as above and caliper thickness measurements acquired in the intact, immediately following separation, and 24 hours after separation (while stored in PBS/PMSF holding media solution at 4°C). The mean caliper method thickness was 428.90 ± 17.45 μm for the intact leaflet tissue, and 317.14 ± 30.57 μm and 158.21 ± 21.24 μm for the separated fibrosa and ventricularis layers, respectively, measured immediately after dissection (Table 8). From these results it can be seen that the whole fibrosa layer (i.e. including the spongiosa remnant shown in Figure 7-1) is 2.07 ± 0.17 times the thickness of the ventricularis layer (also including the spongiosa remnant), which is in close

Table 7. Thickness measurements for intact and separated leaflet layers were obtained manually via caliper measurements and from histology sections.

	Caliper thickness measurments (μm)									
		Time=0						Time=24 h		
Specimen	Intact	Total F layer	Total V layer	Total F+total V	F adjusted	V adjusted	F adjusted+V adjusted	Total F layer	Total V layer	Total F layer +total V layer
1	489.86	410.03	228.60	638.63	500.03	182.88	682.91	442.69	272.14	714.83
2	442.69	264.89	166.91	431.80	323.03	133.53	456.56	286.66	206.83	493.49
3	417.29	243.11	108.86	351.97	296.48	87.09	383.57	308.43	127.00	435.43
4	391.89	308.43	119.74	428.17	376.13	95.79	471.93	370.11	170.54	540.66
5	402.77	359.23	166.91	526.14	438.08	133.53	571.62	391.89	174.17	566.06
Mean	428.90	317.14	158.21	475.34	386.75	126.56	513.32	359.95	190.14	550.09
SEM	17.45	30.57	21.24	49.29	37.28	16.99	51.93	28.28	24.11	46.82

agreement with results previously reported [79, 299]. Interestingly, the separated layer thicknesses were also observed to increase 42.82 ± 8.69 and 31.93 ± 8.23 μm in the fibrosa and ventricularis, respectively, 24 hours after separation (Table 7).

The comparison of dissected layer thickness to the intact state is affected by layer expansion/contraction after dissection (Figure 7-4). When conducting biomechanical tests on layers, accurate thickness values in the intact state are critical to compute the resulting stresses. In order to determine the corresponding true intact thicknesses of the separated layers, we use the following approach assuming tissue incompressibility. The transmural stretch λ_{TT} is computed using $\lambda_{TT} = \frac{1}{\lambda_{CC}\lambda_{RR}}$, where λ_{CC} and λ_{RR} correspond to the stretches induced by dissection for each layer in the circumferential and radial directions, respectively (Figure 7-4). Next, the layer thickness in the intact state t_{intact} can be determined from the measured separated layer thickness

Table 8. Thickness measurements for intact and individual leaflet layers obtained from histology.

	Intact AV histology thickness (μm)						
Specimen	Total	V proper	S proper	F proper	V proper/ total	S proper/ total	F proper/ total
1	420.62	100.10	157.02	161.53	0.24	0.37	0.38
2	389.75	121.79	91.27	178.03	0.31	0.23	0.46
3	373.36	119.96	106.04	148.22	0.32	0.28	0.40
4	372.20	109.74	112.07	149.42	0.29	0.30	0.40
Mean	388.98	112.90	116.60	159.30	0.29	0.30	0.41
SEM	11.28	5.02	14.16	6.93	0.02	0.03	0.02

$t_{separated}$ by $t_{intact}=\lambda_{TT}\, t_{separated}$. When applied to the thickness values immediately after dissection, the corrected total reconstructed thickness was 513.32 ± 51.93 μm (Table 7). This was, however, 84.42 μm greater than the measured intact state (Table 7).

In comparison, the histology based thickness measurements indicated that the fibrosa was 1.90 ± 0.17 times the thickness of the ventricularis layer (Table 8). It should be carefully noted that when using the histology based technique, we distinguish between the layer "proper" and the remnant spongiosa tissue (e.g. Figure 7-1). This is important when attempting to compute actual layer tissue stresses, where use of the fibrosa and ventricularis "proper" should be used, since high GAG content of the spongiosa suggests it has negligible load bearing capabilities. Using this designation, we observed that the fibrosa and ventricularis constitute 41% and 29% of the total layer thickness, respectively (Table 8).

A.2.5 Strip biaxial ventricularis testing

Extremely small tensions (~0.2 N/m) were generated from substantial elongations of approximately 12% and 19% in the circumferential and radial directions respectively (Figure 7-8).

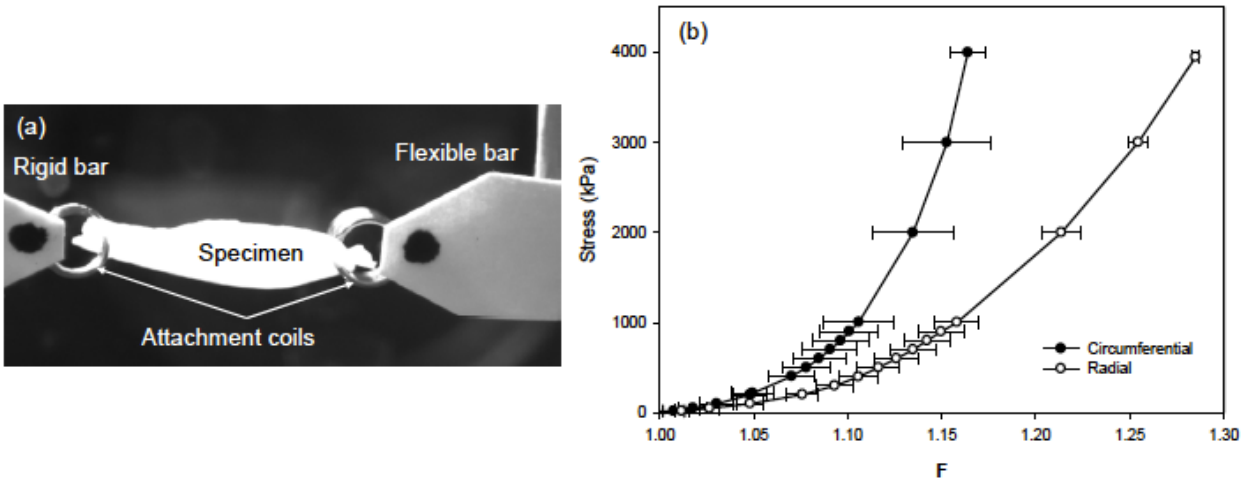

Figure A-8. Strip biaxial mechanical response of aortic ventricularis layer.

These results from the strip biaxial testing of the ventricularis layer in both the circumferential and radial directions showed that the mechanical response of the ventricularis was anisotropic from the onset of deformation (Figure 7-8). In addition, the material behavior was found to be independent of the axis first chosen for testing. As a result, comparable responses were seen whether the circumferential or radial axis was chosen to be tested first and the introduction of small perforations from the wire coil tethering method were of no measurable consequence.

A.3 DISCUSSION

The objective of the current study was to investigate, for the first time, the layer specific biaxial mechanical properties of the AV leaflet. Our goal was to assemble a novel, comprehensive dataset appropriate for developing a 3D stress based constitutive model. We feel that this is needed to move the field beyond "effective" membrane or membrane-like solid models. For example, in the present study experimental quantification of the extension or contraction of the layers resulting from separation made it possible to determine the appropriate stress-free reference configuration (Figure 7-4). In prior studies, the intact leaflet was assumed to be the stress free reference configuration even though the layers do exhibit a preloaded configuration [79]. Results of the present study clearly indicated a complex, layered behavior that will be needed for accurate modeling efforts of the AV leaflet.

A.3.1 Effects of dissection

Our histological preparations show that dissections clearly took place within the spongiosa layer and the remnants of the spongiosa remained well intact (Figure 7-1). Through the dissection process all interconnecting fibers in the spongiosa were severed, relieving internal forces. Post dissection, the fibrosa was seen to quickly elongate and then remain relatively constant while the ventricularis exhibited viscoelastic characteristics in its gradual contraction to a stress free state. The radially dominated expansion of the fibrosa immediately after dissection was likely facilitated by the flattening of the large corrugations in the intact state (Figure 7-4). It is also interesting to note that the ventricularis layer experienced a more uniform contraction (Figure 7-4), with measured deformations consistent with previously reported values [79]. It should be

noted that the elastin fibers in circumferential sections appears as short fiber ends that project out of the plane of the image, whereas the elastin in the radial sections appears as long continuous fibers (Figure 7-1). Thus, elastin in the ventricularis (at the light-microscope level) is radially oriented, consistent with previous studies [221, 290]. The radially orientation of the elastin fibers help to explain why we observed slightly larger radial contractile strains in this layer (Figure 7-4), and our observation that in unconstrained intact leaflets tendency to curl toward the ventricularis layer.

A.3.2 Separated tissue behavior

Both the fibrosa and ventricularis layers exhibited substantial mechanical anisotropy, as well as a non-linear behavior typical of soft tissues (Figure 7-5). The separated fibrosa response was quite similar to intact tissue, but less compliant. It can also be seen that the transition from the toe region was more gradual in the case of the intact tissue compared to the separated fibrosa.

One of the most interesting discoveries in the current study was that the ventricularis dominated the mechanical response of the intact leaflet tissue in the radial direction at the higher stress levels. Specifically, the ventricularis began to contribute to the intact response when λ_r ~1.4, whereas the fibrosa does not significantly contribute until a stretch of more than λ_r~1.6. On average, the ventricularis produces a tension of approximately 20 N/m at $\lambda_r = 1.72$ (the mean maximum found), while the fibrosa produces an average tension of about 10 N/m. From the thickness measurements (Table 7) we calculated the corresponding first Piola-Kirchoff stresses of $P_{22}^{v} = 95.74$ kPa and $P_{22}^{f} = 26.63$ kPa (Figure 7-6). These results suggest that the ventricularis layer indeed makes profound contributions to the intact leaflet response in the radial

direction. This response is in agreement with our earlier findings where the degree of orientation in the valve layers was comparable at high transvalvular pressure levels [220]. This behavior may indicate a possible safety mechanism to prevent overextension of the leaflet when exposed to high transvalvular pressures.

A.3.3 Dual surface strain measurements

By simultaneously imaging the specimen from the fibrosa and ventricularis sides it was possible to investigate leaflet surface strain distributions (Figure 7-7). Although the ventricularis tended to undergo slightly larger deformations, the measured strains were not statistically different from the fibrosa surface. Slight discrepancies between the surfaces may be attributed to stress concentrations at the suture attachments affecting each layer differently, as well as flattening of the corrugations of the fibrosa as the tissue is loaded. Our results suggest that the transmural strain field (but not the stress field) is homogenous, within experimental error.

A.3.4 Ventricularis layer mechanical behavior

Although informative, the strip biaxial tests used to evaluate the mechanical behavior of the ventricularis layer cannot be directly compared to planar biaxial testing. In order to assess the differences in the two loading methods, we applied our structural constitutive model and published values for the native aortic valve intact leaflet [17] to simulate the effects of the two strip biaxial loading conditions. The model enabled us to prescribe stretches required to obtain a maximum tension of 60 N /m in the direction of elongation while fixing the stretch in the orthogonal direction to a value of one. From the simulation results (Figure 7-9) larger stretches

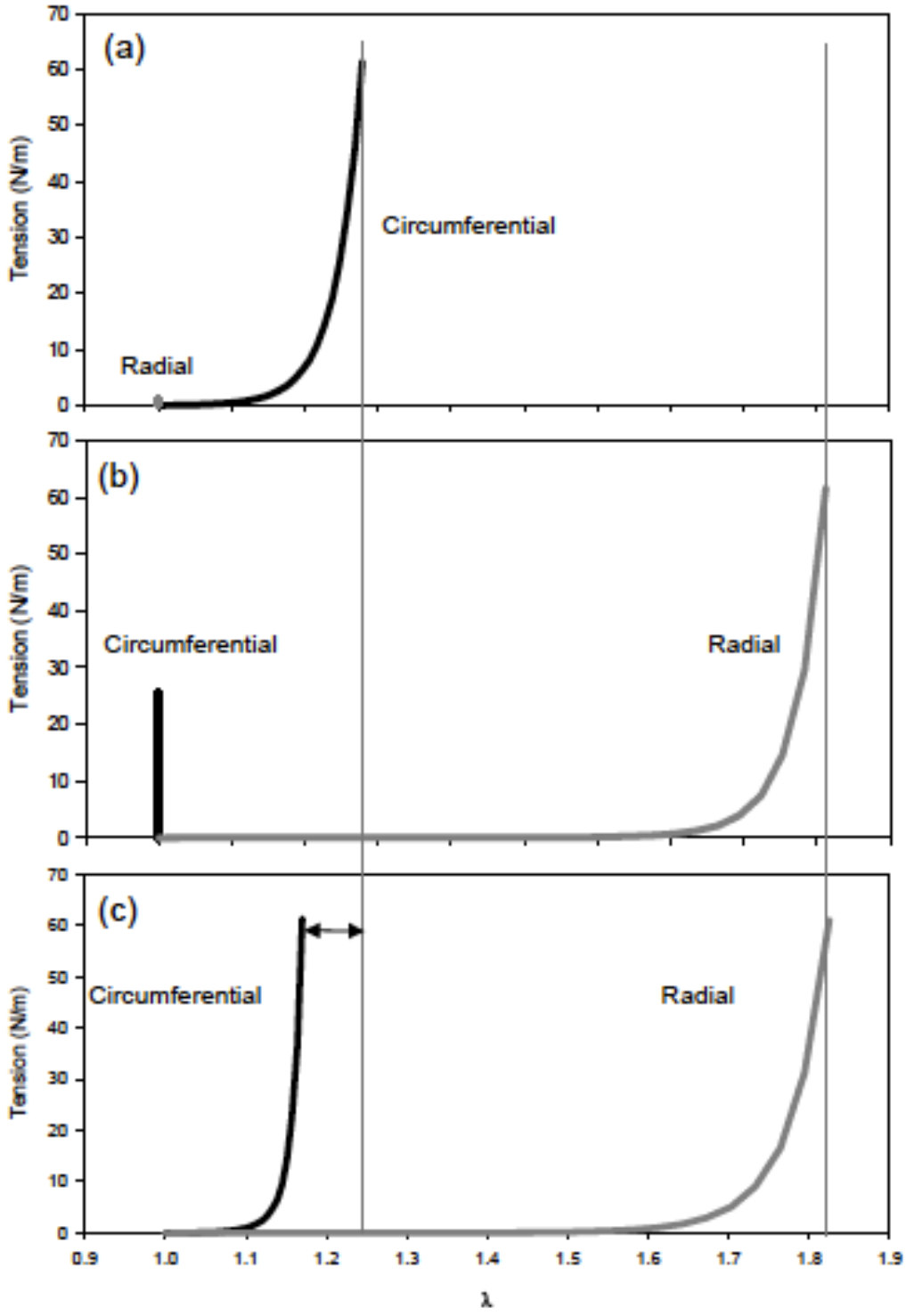

Figure A-9. Simulations for the intact native porcine AV leaflet exposed to strip biaxial and equi-biaxial loading conditions.

are required to attain the maximum tension of 60N/m in the circumferential direction compared to the planar biaxial tension results. The radial peak stretches were essentially unaffected (Figure 7-9). Thus, strip biaxial tests actually *underestimate* the degree of anisotropy.

Taken as a whole, our experimental observations indicate that the ventricularis layer is mechanically anisotropic for all strain ranges (Figure 7-5,7-8). These experimental findings indicated that while there is a radially preferred elastin fiber network (Figure 7-1), the circumferentially oriented collagen fibers clearly dominated the entire ventricularis stress-strain response. However, it should be noted that the elastin network probably contributes mechanically to loading by reducing the radial stretches in the low stress region (as well as aiding in contracting the leaflet in the radial direction). Although the stress generated is small in comparison to the complete working range of the valve, it may be indicative of subtle but important micromechanical behaviors in the AV leaflet. The exact function of the ventricularis preload in heart valve physiology remains unclear, but likely assists in regulating radial leaflet deformations during the cardiac cycle.

A.3.5 Thickness measurements

The difficulties in obtaining simple yet critical soft tissue dimensions are well known in the soft tissue biomechanics literature. Thus, in the present study we explored these questions of layer dimensions in-depth. The intact thickness measurements obtained from the caliper measurement method were found to be slightly larger than the histological evaluations (Tables 7 and 8). The discrepancies between measurement methods may be attributed to slight shrinkage due to the use of xylene and alcohols that dehydrate the tissue during histological preparations. However, both

methods were reasonably close given the inherent difficulties in soft tissue dimensional measurements.

More importantly, we observed that the total thickness of the separated tissues was greater than the initial intact thickness immediately following separation. The initial increase after separation could potentially indicate the presence of small compressive forces exerted by the fibrous structures connecting the fibrosa and ventricularis. During leaflet separation these structures are severed releasing the compressive forces and allowing the layer thicknesses to increase. The continued increase in thickness at 24 hour post separation time point is likely due to increased hydration of the exposed surface area of the spongiosa remnants on either layer is drastically increased exposing the hydrophilic proteoglycans which then swell in response. This explanation is further supported by the observation that *both* layers exhibited an increase in thickness from immediately afterward and 24 hours post-dissection (an increase of 42.82 ± 8.69 μm and 31.93 ± 8.23 μm in the fibrosa and ventricularis layers, respectively).

Thus, while it is straightforward to correct for changes in layer dimensions due to expansion/contraction post-dissection, the effects of swelling and stress-release of the spongiosa layer after dissection negate the use of separated tissue dimensions (using a caliper or any other method) for layer dimensions. As such, the histology based measurements are the most appropriate method since they enable us to measure accurately identify and measure layer boundaries in the intact state. In the present study, we observed that the fibrosa layer consists of 41% and the ventricularis layer 29% of the intact leaflet thickness (Table 7).

A.3.6 The mechanical role of the spongiosa

The functional role of the spongiosa remains unclear. T raditional thinking suggests that the spongiosa enables local movement and shearing between the fibrosa and ventricularis layers during dynamic loading due to its loose organization [295-297]. This observation is likely a result of histological preparations that can show a discrete, loosely organized spongiosa layer but does not make a distinction between morphologic and functional properties or characteristics. The numerous attachments observed between the outer layers of the leaflet during separation indicate a robust attachment as opposed to the idea of loosely attached layers. Instead, we view the spongiosa from a functional perspective: as an interior surface specialization of the fibrosa and ventricularis layers that strongly resists delamination through extensive collagen fiber inter-connections. Therefore, it we feel that it is reasonable to ignore the spongiosa for in-plane biaxial response simulations. Our results indicate that the intact tissue responds as a tightly bound fibrosa and ventricularis layers. This is somewhat in disagreement with prior convention where the spongiosa facilitates sliding between the fibrosa and ventricularis layer [2, 290]. This phenomenon could be a result of the quasi-static testing methods employed which are unable to investigate the complex dynamic behavior of the native leaflet.

A.3.7 Limitations

The results from this study should not be considered universal for the entire leaflet. Rather, it is only applicable to the lower belly region that lies between the Nodulus of Arantii and the basal attachment. Structures such as the fibrous nodulus and the commissural regions no doubt have vastly different mechanical properties [300] and cannot be accurately described by the results of

the current investigation. These regions may even make significant contributions that could potentially alter the mechanical behavior of the belly region in vivo. Also, biaxial testing experiments are only indicative of the leaflet properties when the valve is closed and cannot capture the complex bending properties encountered in dynamic situations.

This study was conducted solely with porcine right coronary leaflets which may result in discrepancies when applied to other tissues. It is well documented that there are subtle but important anatomical differences between various species [301]. For example, porcine right coronary leaflets which are generally large in size contain a muscular shelf that could alter the mechanical behavior of the tissue. In contrast, human aortic valves do not contain a muscular shelf and the right coronary is generally the smallest of the three leaflets [302].

A.4 SUMMARY AND CONCLUSIONS

The biaxial mechanical behavior of native intact and manually separated leaflet layers was measured. Due to differences in their respective morphologies, each leaflet layer exhibited distinct mechanical behaviors. We were able to show that stress varies through the thickness of the leaflet while the strain experienced is homogeneous. Our experimental results also indicate that the fibrous layers of the leaflet are inherently anisotropic from the onset of loading. We concluded that histology based thickness measurements are the most appropriate since they enable us to determine layer specific thicknesses. Accordingly, the ratio of the fibrosa and ventricularis thicknesses is critical in modeling the stress-strain behavior of each layer and their contribution to intact tissue function. Current studies now underway are developing a 3D constitutive model of the intact AV based on bilayer mechanical contributions for the AV leaflet.

APPENDIX B

TIME-DEPENDENT BIAXIAL MECHANICAL BEHAVIOR OF THE AORTIC HEART VALVE LEALFET

Recent technological advancements have enabled affordable high-speed imaging systems to be incorporated with a high speed mechanical testing device. Grashow et al. [32, 303] developed such a system using a planar biaxial configuration for the investigation of the mitral valve anterior leaflet (MVAL). It was found that the MVAL exhibited no strain rate sensitivity, did not creep, but did exhibit stress relaxation. In a related in-vivo study of the mitral valve chordae tendineae [304], it was found that the chordae exhibited a strain plateau during valve closure. This result indicated a constant strain along the uniaxially loaded chordae during closure, indicating a neglible creep response.

The structural basis for these unique findings were recently explored in a recent study by Liao et al. [305] which investigated the molecular behavior of collagen via small angle x-ray scattering. Results from this study indicated that:

1. Fibril straining did not occur until the end of the non-linear region of the tissue level stress-strain curve

2. At high tension levels the fibril D-period spacing (ε_d) increased linearly with increased tension
3. During creep tests no changes in tissue strain or ε_d were observed
4. During stress relaxation tests ε_d initially decayed rapidly and was then followed by a slower rate of decay as compared to the tissue-level stress decay rate for the remainder of the test.

These results suggested that valvular collagen fibrils are intrinsically elastic, were only loaded once the large fiber structures become fully straightened, and that valvular tissues are structured at the molecular level (and probably higher level structures as well) to achieve near-perfect elastic behaviors under physiological loading conditions.

However, we do not have similar information regarding the time dependent behavior of the AVL under dynamic loading conditions. Although both valve tissues exhibit similar compositions, the AVL is geometrically, structurally, and biomechanically quite different from the MV leaflet. Thus, the objective of the current study was to quantify the time dependent behaviors of the native AVL under dynamic physiological loading conditions, and compare the resulting responses with our previous findings for the MVAL.

B.1 METHODS

B.1.1 Tissue preparation

Fresh porcine AV were obtained at a local abattoir and placed into phosphate buffered saline (PBS) and kept on ice for transport to the laboratory. At the laboratory, leaflets were removed

from the aortic root and then placed back into PBS and snap frozen at -80 °C. Based on previous studies, short term low-temperature storage has been shown to induce minimal effects on connective tissue mechanical behavior [306]. As such this storage technique was selected to avoid tissue degradation prior to testing. Proceeding testing, leaflets were removed from the freezer and thawed in a 37°C water bath. A rectangular test specimen was cut from the central lower belly region of the leaflet measuring approximately 9 mm in the circumferential direction and 6 mm in the radial direction.

B.1.2 Mechanical testing

A complete description of the development and use of the biaxial testing device used throughout this study has been recently presented [30, 165]. A couple caveats from the experimental methods detailed previously include a maximum equibiaxial membrane tension of 60 N/m and the current study utilized a preconditioned, free floating configuration as the unloaded reference state. Both modifications were employed as they more closely replicate physiologic AV function (see Discussion). Evaluation of AV stretch rate sensitivity involved 8 specimens loaded to a maximum membrane tension of 60 N/m for quasi-static and high speed cycles in which preconditioned specimens were stretched and unstretched in half cycle times of 1, 0.5, 0.1, 0.05 s. The peak equibiaxial tension of 60 N/m was chosen as it corresponds to in-vivo diastolic pressures [2], as well as a physiologic stresses of ~240 kPa [307] for an assumed thickness of 500μm and a volume fraction of 0.5. Since tissue specimens were subjected to an equi-biaxial tension state with negligible shearing, we quantified the hysteresis by examining the tension–areal stretch response, so that the area under this curve represents the total tissue membrane strain energy in units of N/m. This definition of hysteresis is more general and represents the

total loss of mechanical energy. A detailed description of the testing methods employed can be found in Grashow et al. [165].

While we were able to consistently obtain excellent loading data, unavoidable water bath vibrations present at the end of the 0.05 s unloading phase prevented us from obtaining accurate load data for the low stress portion of the unloading curve. It should be noted that these were not due to device loading frame vibrations but from fluid currents in the bath caused by the motion of the suture attachment mechanism in the bath. Qualitatively, there were no observable differences from the other test groups. However, it was necessary to exclude the hysteresis measurements for the 0.05 s loading time group in the present study.

To assess planar biaxial relaxation and creep, preconditioned specimens were again loaded to the maximum membrane tension of 60 N/m but with a rise time of 100 ms. A total of six specimens were tested for each of the stress relaxation and creep protocols. Again, specifics of the testing methods and device control employed have been previously described [30]. For the current study, an equi-biaxial tension state was chosen as it best represents the multi-axial loading state experienced in-vivo.

B.1.3 Statistical analysis

Results were expressed as mean ± standard error of the mean (SEM), with differences considered statistically significant when $p<0.05$. To determine the effects of stretch rate on the observed peak stretch and hysteresis, comparisons between all loading times were performed using one-way repeated measures analysis of variance (ANOVA). For all tests, the circumferential and radial data groups were considered separately. One-way ANOVA tests were also used to assess any directional differences between specimen axes in both creep and relaxation experiments over

the length of the test (100 ms, 300 ms, 1s and 3 hrs). All statistics were performed with a commercial software package (SigmaStat; SPSS Inc.,Chicago, IL).

B.2 RESULTS

B.2.1 Effects of strain rate on AV tissue response

The biaxial testing device was capable of replicating physiologic stretch rates for the AV leaflet (Table 9) and the resulting shapes of the tension vs. stretch loading curves for all loading protocols (15 s, 1 s, 0.5 s, 0.1 s, 0.05 s) were very similar (Figure 7-10). Results indicate consistent tension-stretch responses for all protocols and no observable stretch rate sensitivity. n = 8. The stretch and strain rate values measured during testing, with biaxial strain rates ranging from quasi-static to physiologic, reported as the mean ± SEM. To quantify test repeatability, the initial 1.0 s half-cycle protocol was compared to an additional protocol performed after testing (Figure 7-10b). High levels of repeatability indicate that the biaxial device capable of accurately controlling high strain rate tests while not causing tissue damage. For comparison, previously reported in vivo stretch and strain rate data from Thubrikar [2], who utilized a canine model and high-speed imaging to measure in vivo leaflet uni-dimensional strain rates throughout the cardiac cycle. Note that the shortest loading time of 0.05 s produced peak stretches and strain rates comparable to those measured in vivo, suggesting that the current study was able to produce physiological strain rates.

Table 9. Stretch and strain rate values measured during testing.

Half cycle time	Stretch		Strain rate (%/s)	
	Circular	Radial	Circular	Radial
15 s	1.18 ± 0.02	1.57 ± 0.06	1.2 ± 0.14	3.8 ± 0.40
1 s	1.19 ± 0.02	1.64 ± 0.03	19.5 ± 1.85	63.96 ± 2.63
0.5 s	1.19 ± 0.02	1.63 ± 0.03	37.8 ± 3.61	126.83 ± 5.26
0.1 s	1.19 ± 0.02	1.63 ± 0.04	185.9 ± 20.1	630.9 ± 25.7
0.05 s	1.19 ± 0.02	1.59 ± 0.03	381.0 ± 47.2	1183.8 ± 51.3
In vivo (Thubrikar, 1990)	1.11 ± 0.02	1.31 ± 0.04	440 ± 80.0	1240 ± 160.0

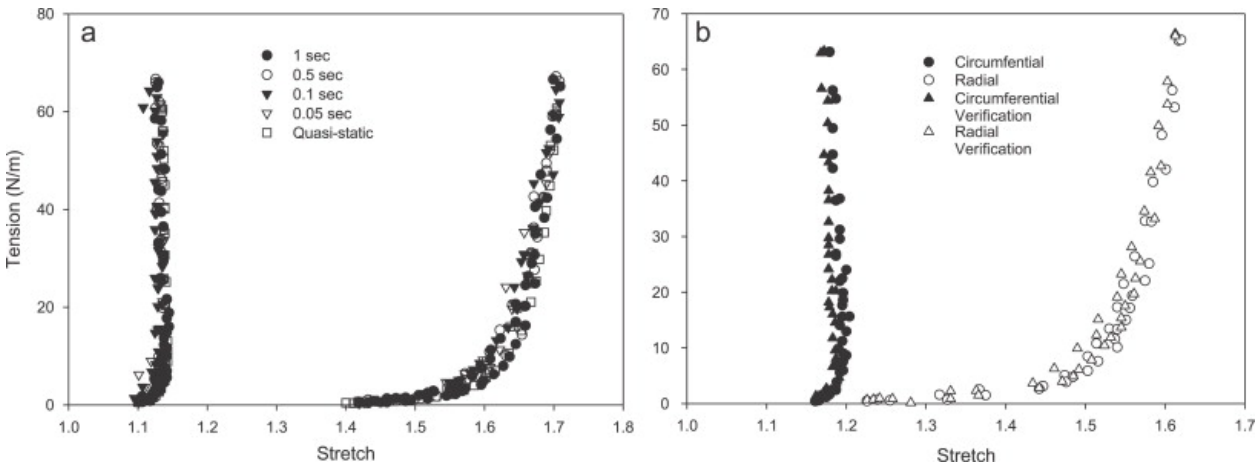

Figure B-1. Effects of strain rate on AV biaxial mechanical behavior.

Also, the mean peak stretches realized during testing are in agreement with previously reported values [16, 23]. Overall, the tension-stretch behaviors exhibited in the current study were in close agreement with previously reported biaxial behaviors for native AV tissues [16, 23]. As noted earlier, we used the preconditioned free-floating reference state since it best

approximated the physiologic unloaded configuration. In preliminary studies, we found that there were in fact subtle but measurable changes in the unloaded tissue due to preconditioning.

Also, the mean peak stretches realized during testing are in agreement with previously reported values [16, 23]. Overall, the tension-stretch behaviors exhibited in the current study were in close agreement with previously reported biaxial behaviors for native AV tissues [16, 23]. As noted earlier, we used the preconditioned free-floating reference state since it best approximated the physiologic unloaded configuration. In preliminary studies, we found that there were in fact subtle but measurable changes in the unloaded tissue due to preconditioning. In addition, no measurable strain rate effects were observed (Figure 7-10a) and the testing device exhibited high repeatability (Figure 7-10b). To better present the strain rate effects, mean λ^{c}_{peak} and λ^{r}_{peak} for each cycle period were pooled for all specimens (Figure 7-11). No significant differences were found between any of the loading time protocols in both the circumferential ($p = 0.821$) and radial ($p = 0.486$) directions. Although the MVAL exhibited a stiffer response in the radial direction than the AVL, peak stretches in the circumferential and radial directions were not dependent upon the rate of stretch (Figure 7-11b). Circumferential and radial peak stretch is significantly different while peak stretches at the 60 N/m equibiaxial tension state revealed no significant differences for any loading time ($p = 0.821$ and $p = 0.486$ for the circumferential and radial peak stretch respectively). These results support the observation that AVL tension is independent of the rate of stretch. Similarly, the mitral valve anterior leaflet exhibited peak stretch rate independence.

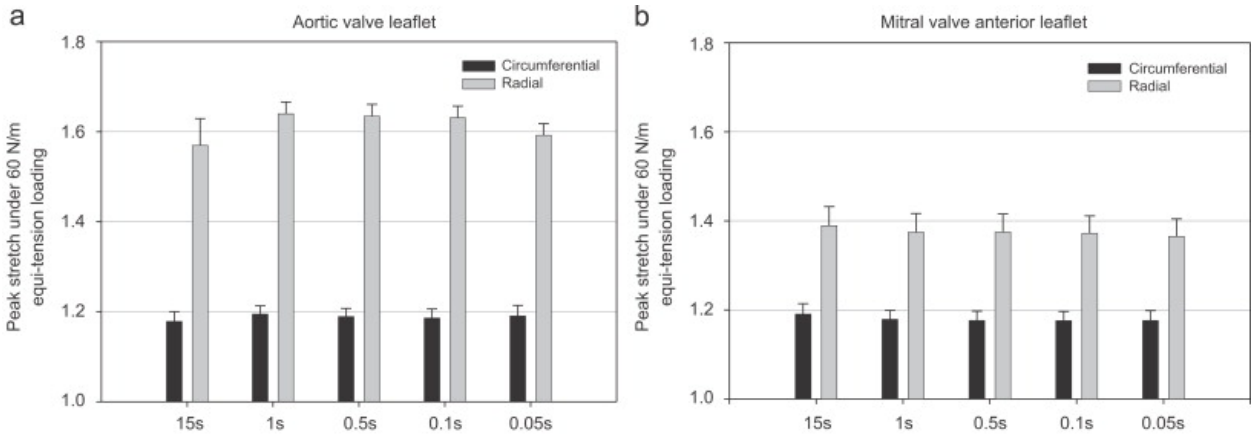

Figure B-2. Strain rate sensitivity on AV peak stretch.

B.2.2 Effects of strain rate on hysteresis

In addition to quantifying the loading response, we also explored the hysteresis responses, defined as the area under tension-areal stretch curve, along the circumferential and radial directions. We consistently observed no detectable hysteresis in the circumferential direction and a small amount in the radial direction for all strain rates. This definition was utilized as it represents the total tissue membrane strain energy in units of N/m. 0.05 s half cycle time is not presented due to unavoidable bath currents. AV hysteresis changes due to increased strain rate were not significantly different (Loading – p=0.342, Unloading – p=0.083, Change in energy – p=0.387). Examination of the tension-areal stretch response suggests no significant difference in membrane strain energy between the various strain rate groups (p = 0.342). Although levels of strain energy differed for the AVL compared to the MVAL, both tissues exhibited a strain rate independent hysteresis response (Figure 7-12c,d).

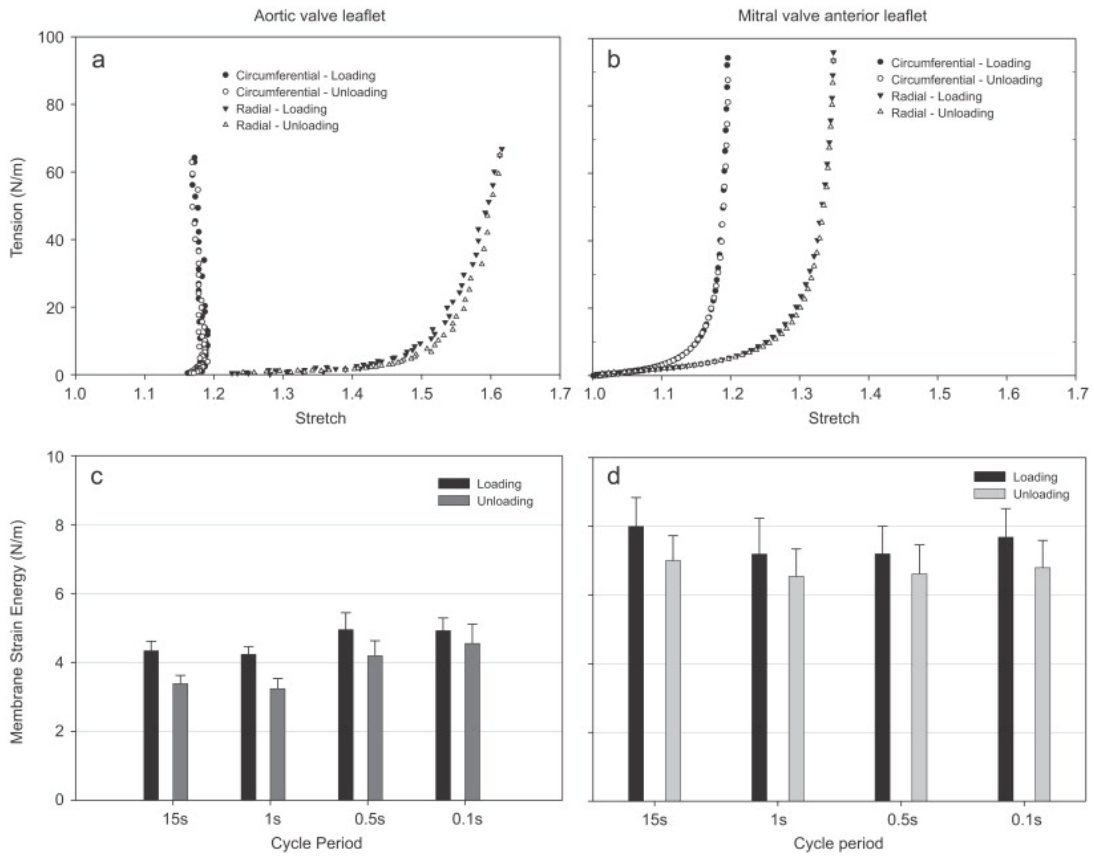

Figure B-3. AV and MVAL hysteresis and strain rate dependence.

B.2.3 Biaxial stress relaxation

For stress-relaxation, peak stretches were maintained to within 0.1% strain over the entire three hour test period. Substantial stress relaxation was observed in both the circumferential and radial directions. Rapid relaxation was observed during the initial 20 minutes of the test, but continued relaxation occurred very slowly up to and beyond the 3 hour time point (Figure 7-13a).

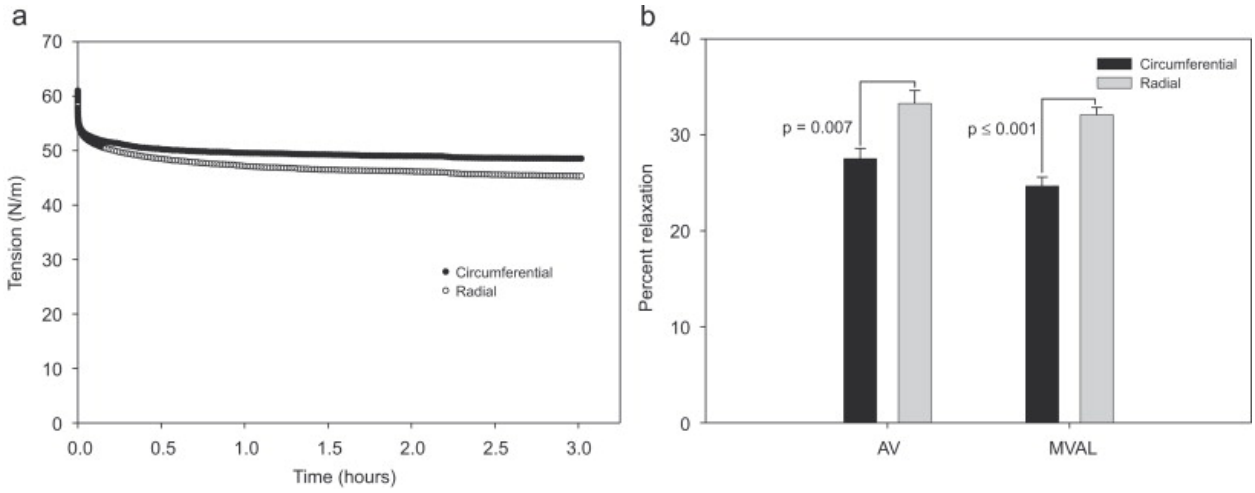

Figure B-4. AV and MVAL relaxation behavior.

Quantitatively, the relaxation percentage in the circumferential direction (27.51±1.07%) was statistically different (p=0.007) from the relaxation percentage in the radial direction (33.28±1.35%). Although the AV tended to exhibit more relaxation, it was not significantly different from the MVAL values of 24.67±0.93% and 32.09±0.77% in the circumferential and radial directions respectively (Figure 7-13b).

B.2.4 Biaixal creep response

The high degree of mechanical anisotropy in the leaflet as reported previously [2, 16, 294, 308-310] was observed in the creep experiments (Figure 7-14a). Specifically, peak stretches at the 100 ms time point were 1.04±0.026 in the circumferential direction and 1.43±0.067 in the radial direction (Figure 7-14b). In sharp contrast to the relaxation studies, the observed creep was negligible in both the circumferential and radial specimen axes (Figure 7-14b).

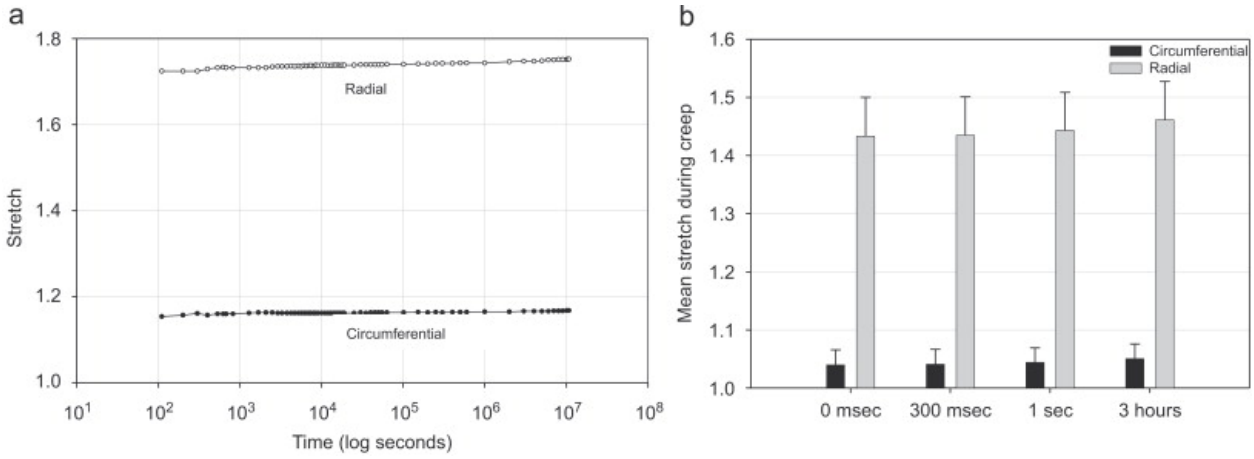

Figure B-5. AV planar biaxial creep behavior.

Mean stretches in the circumferential and radial directions indicated no significant differences between the creep stretch levels at different time points (100ms, 300ms, 1s and 3 hr) on either the circumferential ($p = 0.821$) or radial ($p = 0.486$) axes (Figure B-5b).

B.3 DISCUSSION

Traditionally, soft collagenous tissues such as the AVL have been characterized as anisotropic non-linear viscoelastic materials. Modeling and simulation of their time-dependent responses has most often utilized the quasi-linear viscoelastic (QLV) approach [24]. As with most classic viscoelastic theories, the QLV approach assumes that the tissues time dependent mechanical properties are all manifestations of the same mechanism, represented as a continuous spectrum. The underlying physical basis for the observed viscoelastic behavior may include collagen fibril-fibril interactions [25] or intrinsic collagen viscoelasticity. If these assumptions hold, then both creep and relaxation behaviors would be derivable from each other [26].

However, Thornton et al. [27, 311] observed a disparity between the rate of relaxation and creep at low stress level and further demonstrated that ligament creep could not be predicted from relaxation data utilizing QLV theory. Mechanistically, it was shown that collagen fiber crimp was reduced during ligament creep, indicating a fiber recruitment mediated behavior [27]. In a related study, Provenzano et al. [28] suggested a more general approach than QLV theory is required to describe the nonlinear viscoelastic behavior of rat medial collateral ligament. During this study the author's observed the rate of creep and relaxation to be dependent upon initial stress and strain levels respectively. It was also observed that the rate of relaxation proceeded faster than the rate of creep in contra-lateral ligaments.

However, our findings clearly indicate that the mechanisms responsible for creep and relaxation in the AVL are functionally independent and the fiber-recruitment model of Thornton cannot account for the observations of the current study. Thus, in agreement with recent MVAL studies [30-32] the AVL does not conform to viscoelastic material definitions when exposed to planar biaxial loading states. Instead, we feel that it is more appropriate to describe these tissues as quasi-elastic as they resemble elastic materials when subjected to physiological loading states. That is to say, AVL and MVAL both exhibit the following unique mechanical properties:

1. Are capable of undergoing large, rapid strains during valve closure in response to the trans-valvular pressure gradients and returning to their original configuration when unloaded.
2. Exhibit no measurable creep under physiologically relevant loading conditions (e.g. when the valve is closed and loaded).
3. Exhibit very small viscous dissipative effects (hysteresis)
4. Exhibit substantial, directionally dependent stress relaxation.

Taken as a whole, our results suggest that it is probably not necessary to develop models of valve tissue time dependent behavior since, under physiologic loading states the valvular tissues appear to exhibit elastic-like behavior. We feel that it is perhaps more relevant to focus on how the valvular tissue achieves this amazing feat and how it may be altered in diseased states.

B.3.1 Physiological loading, strain levels, and strain rates

The range of strain rates utilized in the present study was chosen such that they encompass strain rates from quasi-static to physiologic. More specifically, specimens were loaded to a maximum equibiaxial membrane tension of 60 N/m, which corresponds to in-vivo diastolic pressures; during varied time intervals resulting in the desired range of strain rates. These values were based on previous studies [2] of canine leaflet motion during the cardiac cycle and strains exhibited during normal transvalvular pressures. In this study, 3 radiopaque markers were place on the leaflet in the radial or circumferential direction. Using mid-diastole as the reference configuration, displacement of the circumferentially and radially oriented markers could be obtained throughout the cardiac cycle. In addition, radiopaque markers attached to the leaflet surface were used in a similar manor to quantify leaflet deformation in response to transvalvular pressure. The authors reported in-vivo strains of 10.1% and 30.8% in the circumferential and radial directions respectively during valve closure. Valve closure occurred in two phases involving both a slow and rapid closure phase. The duration of the closure phases was approximately 20-25 msec. From these in-vivo measurements the corresponding strain-rates are 440±80.0%/sec and 1240±160.0%/sec in the circumferential and radial directions respectively. In the current study, the maximum strain-rates obtained were 381.0±47.2%/sec and

1183.8±51.3%/sec in the circumferential and radial directions respectively. Although subtle variations between species are likely, it is reasonably to assume that comparable strain-rates would be observed. Based upon this limited experimental data, the high speed biaxial testing device employed for the current study was capable of replicating in-vivo strain rates.

When relating the current study to AV function, it is interesting to note that the stress–strain behavior of the AV was independent of stretch rate in both the circumferential and radial directions for all cycle periods (strain rates). The mitral valve anterior leaflet also exhibits the same stretch rate independence (Figure 7-11 and 7-12) [303]. Similarly, findings reported by Naimark et al. [312] showed no significant strain rate dependence in the stress–strain relationship of mammalian pericardia for strain rates between 1 and 100%/s. Naimark et al. speculated that the lack of strain rate dependence may be attributed to the stabilizing effects of the glycosaminoglycans that surround the pericardial collagen fibers. Despite these similarities some inconsistencies do arise throughout contemporary literature. For instance, Leeson-Deitrich et al. [313] found significant differences in the stress–strain response at different strain rates of both the AV and pulmonary valves. Unfortunately, the current study does not provide further insight into the cause of such irregularities. Potential explanations for these disparities could be attributed to subtle structural differences or arise from varied modes of deformation (biaxial vs. uniaxial).

B.3.2 Stress relaxation.

Qualitatively, the stress-relaxation exhibited in the AV was consistent with findings for other collagenous soft tissues [28, 314-318]. However, the relaxation was observed to be anisotropic with the radial direction exhibiting greater relaxation than the circumferential direction ($p =$

0.007). This discrepancy is likely a result of the structural anisotropy exhibited by the AV. Namely, circumferentially oriented collagen fibers are required to rotate towards the radial axis during equi-biaxial loading conditions. As a result, achieving the desired 60 N/m equi-tension state requires strains in the radial direction approximately 4 times greater than those in the circumferential direction. The relaxation behavior observed could also have some association with the different strain rates required to obtain the 60 N/m equibiaxial tension. Since both material axes are elongated over a 100ms duration the radial axis experiences rates of deformation much greater than the circumferential direction.

B.3.3 Creep and its relationship to stress relaxation.

Despite the observed relaxation behavior, the AVL did not exhibit any measurable degree of creep over the three hour test duration (Figure 7-14). This behavior was observed in the MVAL [30] but was inconsistent with findings for ligament [28, 311] and pericardium [315] both of which exhibit creep. It is important to note that the uniaxial testing methods employed in the mentioned studies for pericardium may account for disparities observed in creep behaviors and may not necessarily indicate material differences. For example, uniaxial loading conditions impart vastly different microstructural kinematics (i.e collagen fiber rotations) than those exhibited during multiaxial loading conditions owing to multiple apparent behaviors from the same material [76]. The discrepancy in microstructural kinematics arises as a result of the vastly different boundary conditions experienced between the uniaxial and biaxial testing configurations. In uniaxial creep testing, specimen edges orthogonal to the direction of deformation remain unconstrained allowing all fibers the potential to rotate in a time dependent manner in an attempt to achieve a state of reduced fiber stress. On the other hand, there are no

unconstrained segments of the specimen during biaxial creep testing owing to a lack of time dependent changes in fiber orientation.

B.3.4 Potential effects of regional variations in the AVL.

The interesting response exhibited by both the collagen fibril and tissue brings about interesting aspects pertaining to leaflet behavior. In the current study, the belly region was evaluated as the representative region of leaflet function. It has been well established in previous studies that the AVL exhibits significant regional variations in mechanical behavior with respect to strains measured in intact tissues in the belly region [319] and biaxial mechanical properties measured of the central coaptation region (near the nodulus of Arantii) under planar biaxial stretch [16]. Currently, the only experimental studies that we are aware of for the commissure region are the flexural properties recently performed by Mirnajafi et al. [320]. In this study it was noted that the commissure region is composed of a dense network of collagenous fibers, with no observable GAGs and is consistent with previous studies [2]. It is likely that the commissure region experiences much greater stresses in the circumferential direction, as evidenced by the highly oriented collagen fibers observed in this region [220, 320]. In comparison, the belly region is the only part of the AV leaflet rich in highly viscous GAGs [33], and is thus most likely to exhibit viscoelastic behavior. While we are aware of the profound regional variations in mechanical properties of the leaflet, the quasi-elastic behavior of the AVL belly region likely represents an upper bound to tensile viscoelastic behavior for the entire leaflet.

In a related in-vivo study of the mitral valve chordae tendineae [304], it was found that the chordae exhibit a strain plateau during valve closure. T his constant strain along the uniaxially loaded chordae during closure indicates a m inimal creep response. This result is

consistent with the recent small angle X-ray studies of Liao et al. [305] on the mitral valve leaflet indicating that the valvular collagen fibril is not intrinsically viscoelastic. Since the commissure region of the AV contains dense collagen fibers and low levels of proteoglycans, it would not be unreasonable to anticipate a similar response during physiologic function.

B.3.5 Insight into underlying structural mechanisms.

In an attempt to understand the underlying structural basis for the unique quasi-elastic mechanical behavior of valvular tissues, we have employed small angle x-ray scattering to determine the relation between collagen fibril kinematics and tissue level mechanical properties in the MVAL under biaxial loading [25]. During relaxation the D-period spacing of the collagen fibril was observed to decrease and correlates to tissue level relaxation behavior. However, the collagen fibril d-period remained constant while exposed to a constant stress. This D-period behavior when exposed to a constant stress was also exhibited in the rat tail tendon while tissue level creep was observed and attributed to fibrillar slippage [321]. Thus, this investigation suggested that the valvular collagen fibrils do not exhibit intrinsic viscoelastic behavior under tension.

Based on the findings that the response exhibited at both the fibril and tissue levels were similar, we are lead to believe that the unique valvular tissue behavior is a function of the interaction between the collagen fibrils and its surrounding matrix. We also feel that this response is greatly influenced by the difference in the loading state applied to the tissue during stress relaxation and creep experiments. It has been documented that collagen fibrils are discontinuous and adjacent fibrils are linked via orthogonally oriented proteoglycans [25, 322]. These proteoglycans tend to rotate in the direction of tissue deformation and could potentially

contribute mechanically at large strains [25]. These interactions may play a role during constant strain experiments whereby the energy stored in the extended stiff collagen fibers is transferred to the proteoglycan bridges or other ECM structures, enabling the collagen fibers to attain a lower energy state. However, during constant stress conditions the collagen fibers are unable to transfer energy to the surrounding matrix as they are responsible for balancing the externally applied tractions. In addition, the lack of valvular tissue level creep could also indicate that the strength and number of interaction between collagen fibril and other ECM (e.g. proteoglycan-collagen interactions) varies between tissues. If the number of interactions or strength of these interactions is increased they would prevent the sliding mechanism exhibited by rat tail tendon fibrils, and thus the tissue level creep, under constant stress conditions.

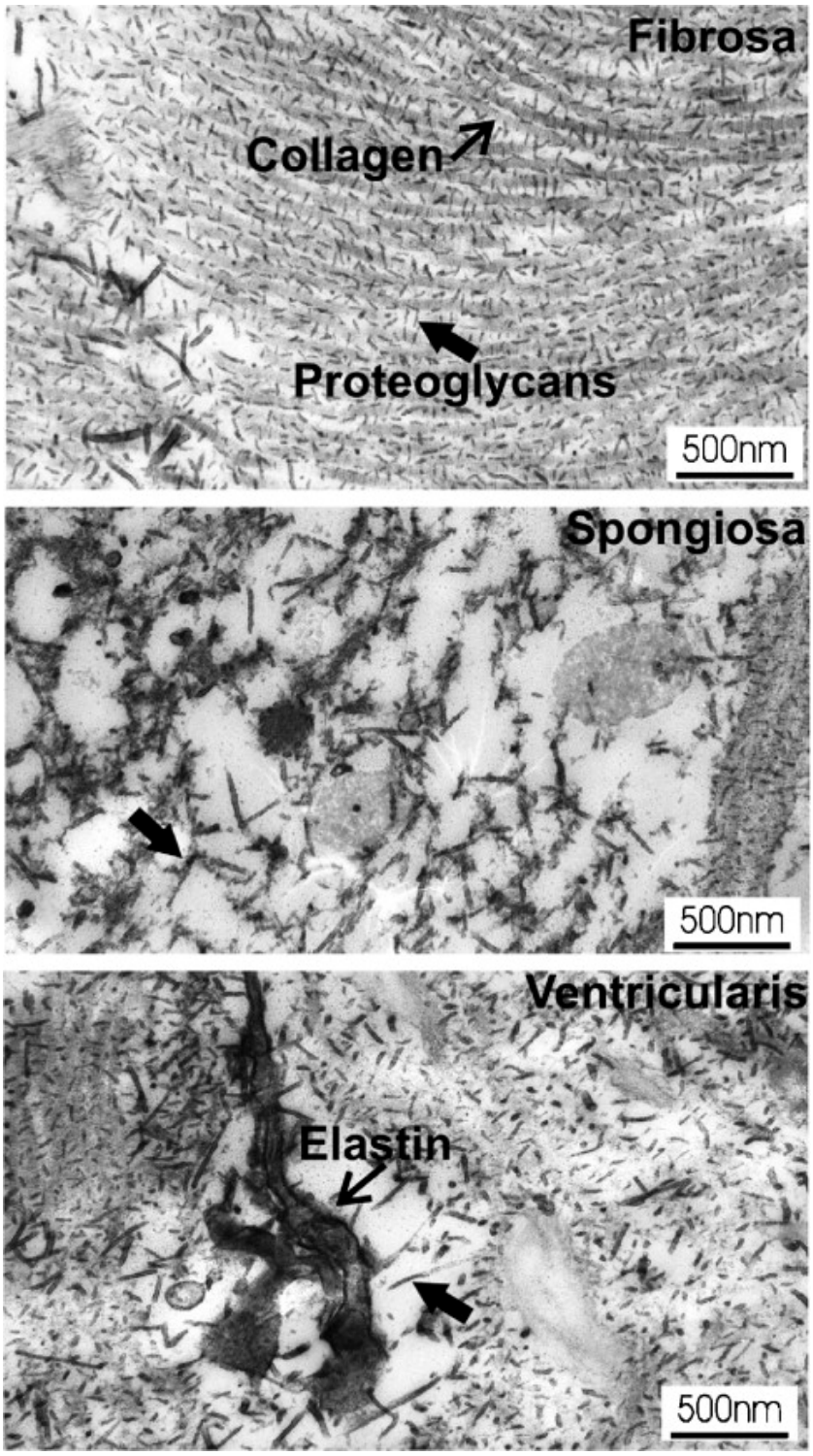

Figure B-6. Ultrastructural interaction in fibrosa, spongiosa, and ventricularis layers revealed with TEM and Cuperomeronic Blue staining.

To gain better insight into these mechanisms, we utilized a transmission electron microscopy (TEM) technique developed by Haigh and Scott [323] on the AV tissues. Briefly, this procedure involves the use of Cuperomeronic Blue and the critical electrolyte concentration technique to stain proteoglycans. We observed abundant proteoglycans, not only in spongiosa layer, but also in the fibrosa and ventricularis layers (Figure 7-15). In the fibrosa layer specifically, small proteoglycans (decorin) were found to mechanically interact with collagen fibrils via specific binding to the collagen D-period (Figure 7-15a). These abundant collagen-matrix interactions may lead to tissue-level viscoelastic behavior under non-physiological conditions, such as stress relaxation, while the collagen fibril itself is intrinsically elastic.

B.3.6 Relation to valvular function.

Although the structural mechanisms underlying the time dependent mechanical behavior of the AVL has been shown to be rather complex, its functional basis is straightforward and intuitive. Namely, the ability of the tissue to primarily exhibit an elastic behavior while exhibiting the capability to locking up at physiologic loading conditions is highly desirable. It is interesting to note that valvular tissues are comprised of typical soft tissue constituents but exhibit functionally unique behaviors. The exact structural mechanisms underlying this unique behavior remain uncertain and warrant further investigation as they may have important implications related to degenerative valve disease [33] as well as developing engineered valvular tissues in-vivo [34].

B.3.7 Limitations.

The current study experienced limitations similar to those previously reported by Grashow et al. for the MVAL leaflet [30, 165]. It is also important to note that the subtle disparities between leaflets such as stress and strain distribution [309, 324] or geometrical differences were not taken into consideration nor were potential differences between species [301]. Also, only the belly region of the AVL has been systematically evaluated in the current study. Taking into consideration the significant regional variation in structure and mechanical behavior throughout the AVL [16] we feel that it is reasonable to conclude that the quasi-elastic behavior of the AVL belly region (only region to contain significant quantities of viscous proteoglycans) likely represents an upper bound to tensile viscoelastic behaviors.

B.3.8 Conclusions

The results for both the AVL and MVAL support our observation that valvular tissues functionally behave as anisotropic quasi-elastic materials. These results appear to be unique to valvular tissues and indicate an ability to withstand loading without time-dependent effects under physiologic loading conditions. Based on the current results, we speculate that degenerated ECM components in diseased AV might induce changes in these quasi-elastic behaviors, leading to valvular deterioration. Moreover, these subtle tissue behaviors could prove critical to the development of tissue engineered alternatives for valve repair or replacement.

BIBLIOGRAPHY

1. Sutton, J.P., 3rd, S.Y. Ho, and R.H. Anderson, *The forgotten interleaflet triangles: a review of the surgical anatomy of the aortic valve.* Ann Thorac Surg, 1995. **59**(2): p. 419-27.

2. Thubrikar, M., *The Aortic Valve*1990, Boca Raton: CRC. 221.

3. Bashey, R.I. and S.A. Jimenez, *Collagen in heart valves*, in *Collagen*, M.E. Nimni, Editor 1988, CRC Press: Boca Raton. p. 258-274.

4. Rabkin, E., et al., *Evolution of cell phenotype and extracellular matrix in tissue-engineered heart valves during in-vitro maturation and in-vivo remodeling.* Journal of Heart Valve Disease, 2002. **11**(3): p. 308-14; discussion 314.

5. Filip, D.A., A. Radu, and M. Simionescu, *Interstitial cells of the heart valves possess characteristics similar to smooth muscle cells.* Circ Res, 1986. **59**(3): p. 310-20.

6. Messier, R.H., Jr., et al., *Dual structural and functional phenotypes of the porcine aortic valve interstitial population: characteristics of the leaflet myofibroblast.* Journal of Surgical Research, 1994. **57**(1): p. 1-21.

7. Rabkin-Aikawa, E., et al., *Dynamic and reversible changes of interstitial cell phenotype during remodeling of cardiac valves.* J Heart Valve Dis, 2004. **13**(5): p. 841-7.

8. Rabkin-Aikawa, E., et al., *Clinical pulmonary autograft valves: pathologic evidence of adaptive remodeling in the aortic site.* J Thorac Cardiovasc Surg, 2004. **128**(4): p. 552-61.

9. Merryman, W.D., et al., *Correlation between heart valve interstitial cell stiffness and transvalvular pressure: implications for collagen biosynthesis.* Am J Physiol Heart Circ Physiol, 2006. **290**(1): p. H224-31.

10. Merryman, W.D., et al., *The effects of cellular contraction on aortic valve leaflet flexural stiffness.* J Biomech, 2006. **39**(1): p. 88-96.

11. Dvorin, E.L., et al., *Quantitative evaluation of endothelial progenitors and cardiac valve endothelial cells: proliferation and differentiation on poly-glycolic acid/poly-4-*

hydroxybutyrate scaffold in response to vascular endothelial growth factor and transforming growth factor beta1. Tissue Eng, 2003. **9**(3): p. 487-93.

12. Paranya, G., et al., *Aortic valve endothelial cells undergo transforming growth factor-beta-mediated and non-transforming growth factor-beta-mediated transdifferentiation in vitro.* Am J Pathol, 2001. **159**(4): p. 1335-43.

13. Dahl, K.N., A.J. Ribeiro, and J. Lammerding, *Nuclear shape, mechanics, and mechanotransduction.* Circ Res, 2008. **102**(11): p. 1307-18.

14. Otto, C.M., *Clinical practice. Evaluation and management of chronic mitral regurgitation.* N Engl J Med, 2001. **345**(10): p. 740-6.

15. Reul, H. and N. Talukder, *Heart valve mechanics*, in *The Heart*1989, McGraw Hill.

16. Billiar, K.L. and M.S. Sacks, *Biaxial mechanical properties of the natural and glutaraldehyde treated aortic valve cusp--Part I: Experimental results.* Journal of Biomechanical Engineering, 2000a. **122**(1): p. 23-30.

17. Billiar, K.L. and M.S. Sacks, *Biaxial mechanical properties of the native and glutaraldehyde-treated aortic valve cusp: Part II--A structural constitutive model.* Journal of Biomechanical Engineering, 2000b. **122**(4): p. 327-35.

18. Christie, G.W. and B.G. Barratt-Boyes, *Age-Dependent Changes in the Radial Stretch of Human Aortic Valve Leaflets Determined by Biaxial Stretching.* Annals of Thoracic Surgery, 1995. **60**: p. S156-159.

19. Christie, G.W. and B.G. Barratt-Boyes, *Mechanical properties of porcine pulmonary valve leaflets: how do they differ from aortic leaflets?* Ann Thorac Surg, 1995. **60**(2 Suppl): p. S195-9.

20. Sacks, M.S., T.V. Lam, and J. Stella, *A structural constitutive model for the native pulmonary heart valve leaflet.* Journal of Biomechanial Engineering, submitted.

21. May-Newman, K. and F.C. Yin, *A constitutive law for mitral valve tissue.* J Biomech Eng, 1998. **120**(1): p. 38-47.

22. Driessen, N.J., C.V. Bouten, and F.P. Baaijens, *Improved prediction of the collagen fiber architecture in the aortic heart valve.* J Biomech Eng, 2005. **127**(2): p. 329-36.

23. Stella, J.A. and M.S. Sacks, *On the biaxial mechanical properties of the layers of the aortic valve leaflet.* J Biomech Eng, 2007. **129**(5): p. 757-66.

24. Fung, Y.C., *Biomechanics: Mechanical Properties of Living Tissues*. 2nd ed1993, New York: Springer Verlag. 568.

25. Liao, J. and I. Vesely, *Relationship between collagen fibrils, glycosaminoglycans, and stress relaxation in mitral valve chordae tendineae.* Ann Biomed Eng, 2004. **32**(7): p. 977-83.

26. Wineman, A.S. and K.R. Rajagopal, *Mechanical Response of Polymers* 2000, Cambridge, 2000: Cambridge University Press. 328.

27. Thornton, G.M., C.B. Frank, and N.G. Shrive, *Ligament creep behavior can be predicted from stress relaxation by incorporating fiber recruitment.* Journal of Rheology, 2001. **45**(2): p. 493-507.

28. Provenzano, P., et al., *Nonlinear ligament viscoelasticity.* Ann Biomed Eng, 2001. **29**(10): p. 908-14.

29. Stella, J.A., J. Liao, and M.S. Sacks, *Time-dependent biaxial mechanical behavior of the aortic heart valve leaflet.* J Biomech, 2007. **40**(14): p. 3169-77.

30. Grashow, J.S., et al., *Planar biaxial creep and stress relaxation of the mitral valve anterior leaflet.* Ann Biomed Eng, 2006a. **34**(10): p. 1509-18.

31. Liao, J., et al. *Collagen fibril kinematics in mitral valve leaflet under biaxial elongation, creep, and stress relaxation*. in *Society for Heart Valve Disease Third Biennial Meeting*. 2005. Vancouver: SHVD.

32. Grashow, J.S., et al., *Planar biaxial creep and stress relaxation of the mitral valve anterior leaflet.* Ann Biomed Eng, 2006. **34**(10): p. 1509-18.

33. Schoen, F.J., *Cardiac valves and valvular pathology: update on function, disease, repair, and replacement.* Cardiovasc Pathol, 2005. **14**(4): p. 189-94.

34. Sutherland, F.W., et al., *From stem cells to viable autologous semilunar heart valve.* Circulation, 2005. **111**(21): p. 2783-91.

35. Yacoub, M.H. and J.J. Takkenberg, *Will heart valve tissue engineering change the world?* Nature clinical practice. Cardiovascular medicine, 2005. **2**(2): p. 60-1.

36. Mendelson, K.a.S., F. J., *Heart Valve Tissue Engineering: Concepts, Approaches, Progress, and Challenges.* Annals of Biomedical Engineering, 2006. **34**(12): p. 1799 - 1819.

37. Hoffman, J.I. and S. Kaplan, *The incidence of congenital heart disease.* J Am Coll Cardiol, 2002. **39**(12): p. 1890-900.

38. Samanek, M., *Congenital heart malformations: prevalence, severity, survival, and quality of life.* Cardiology in the young, 2000. **10**(3): p. 179-85.

39. Stark, J., *The use of valved conduits in pediatric cardiac surgery.* Pediatr Cardiol, 1998. **19**(4): p. 282-8.

40. Mayer, J.E., Jr., *Uses of homograft conduits for right ventricle to pulmonary artery connections in the neonatal period.* Semin Thorac Cardiovasc Surg, 1995. **7**(3): p. 130-2.

41. Allen, B.S., et al., *Pericardial tissue valves and Gore-Tex conduits as an alternative for right ventricular outflow tract replacement in children.* Ann Thorac Surg, 2002. **74**(3): p. 771-7.

42. Cheitlin, M.D., *Pathophysiology of valvular aortic stenosis in the elderly.* Am J Geriatr Cardiol, 2003. **12**(3): p. 173-7.

43. Schoen, F. and R. Levy, *Tissue heart valves: Current challenges and future research perspectives.* Journal of Biomedical Materials Research, 1999. **47**: p. 439-465.

44. Cannegieter, S., F. Rosendaal, and E. Briet, *Thromboembolic and bleeding complications in patients with mechanical heart valve prostheses.* Circulation, 1994. **89**: p. 635-641.

45. Leyh, R.T., et al., *Anticoagulant therapy in pregnant women with mechanical heart valves.* Arch Gynecol Obstet, 2003. **268**(1): p. 1-4.

46. Chan, W.S., S. Anand, and J.S. Ginsberg, *Anticoagulation of pregnant women with mechanical heart valves: a systematic review of the literature.* Arch Intern Med, 2000. **160**(2): p. 191-6.

47. Schoen, F. and R. Levy, *Pathology of Substitute Heart Valves.* Journal of Cardiac Surgery, 1994. **9**: p. 222-227.

48. Sacks, M.S. and F.J. Schoen, *Collagen fiber disruption occurs independent of calcification in clinically explanted bioprosthetic heart valves.* J Biomed Mater Res, 2002. **62**(3): p. 359-71.

49. Rastelli, G.C., et al., *Surgical Repair for Pulmonary Valve Atresia with Coronary-Pulmonary Artery Fistula: Report of Case.* Mayo Clinic proceedings. Mayo Clinic, 1965. **40**: p. 521-7.

50. Ross, D.N. and J. Somerville, *Correction of pulmonary atresia with a homograft aortic valve.* Lancet, 1966. **2**(7479): p. 1446-7.

51. Perron, J., et al., *Valved homograft conduit repair of the right heart in early infancy.* The Annals of thoracic surgery, 1999. **68**(2): p. 542-8.

52. Urban, A.E., et al., *Truncus arteriosus: ten-year experience with homograft repair in neonates and infants.* The Annals of thoracic surgery, 1998. **66**(6 Suppl): p. S183-8.

53. Yuan, S.M., et al., *Right ventricular outflow tract reconstruction: valved conduit of choice and clinical outcomes.* Journal of cardiovascular medicine, 2008. **9**(4): p. 327-37.

54. Wells, W.J., et al., *Homograft conduit failure in infants is not due to somatic outgrowth.* The Journal of thoracic and cardiovascular surgery, 2002. **124**(1): p. 88-96.

55. Langer, R. and J.P. Vacanti, *Tissue engineering.* Science, 1993. **260**(5110): p. 920-6.

56. Gilbert, T.W., et al., *Degradation and remodeling of small intestinal submucosa in canine Achilles tendon repair.* J Bone Joint Surg Am, 2007. **89**(3): p. 621-30.

57. Fujimoto, K.L., et al., *An elastic, biodegradable cardiac patch induces contractile smooth muscle and improves cardiac remodeling and function in subacute myocardial infarction.* J Am Coll Cardiol, 2007. **49**(23): p. 2292-300.

58. Shelton, J.C., D.L. Bader, and D.A. Lee, *Mechanical conditioning influences the metabolic response of cell-seeded constructs.* Cells Tissues Organs, 2003. **175**(3): p. 140-50.

59. van der Meulen, M.C. and R. Huiskes, *Why mechanobiology? A survey article.* J Biomech, 2002. **35**(4): p. 401-14.

60. Sarkadi, B. and J.C. Parker, *Activation of ion transport pathways by changes in cell volume.* Biochim Biophys Acta, 1991. **1071**(4): p. 407-27.

61. Courtney, T., et al., *Design and analysis of tissue engineering scaffolds that mimic soft tissue mechanical anisotropy.* Biomaterials, 2006. **27**(19): p. 3631-8.

62. Nerurkar, N.L., D.M. Elliott, and R.L. Mauck, *Mechanics of oriented electrospun nanofibrous scaffolds for annulus fibrosus tissue engineering.* J Orthop Res, 2007. **25**(8): p. 1018-28.

63. Yoshimoto, H., et al., *A biodegradable nanofiber scaffold by electrospinning and its potential for bone tissue engineering.* Biomaterials, 2003. **24**(12): p. 2077-82.

64. Yarin, A.L. and E. Zussman, *Upward needleless electrospinning of multiple nanofibers.* Polymer, 2004. **45**(9): p. 2977-2980.

65. Stankus, J.J., J. Guan, and W.R. Wagner, *Fabrication of biodegradable elastomeric scaffolds with sub-micron morphologies.* J Biomed Mater Res, 2004. **70A**(4): p. 603-14.

66. Li, W.J., et al., *Fabrication and characterization of six electrospun poly(alpha-hydroxy ester)-based fibrous scaffolds for tissue engineering applications.* Acta Biomater, 2006. **2**(4): p. 377-85.

67. Li, W.J., et al., *Electrospun nanofibrous structure: a novel scaffold for tissue engineering.* J Biomed Mater Res, 2002. **60**(4): p. 613-21.

68. Matthews, J.A., et al., *Electrospinning of collagen nanofibers.* Biomacromolecules, 2002. **3**(2): p. 232-8.

69. Pedicini and Farris, *Mechanical behavior of electrospun polyurethane.* Polymer, 2003. **44**: p. 6857-6862.

70. Bibekananda, S., et al., *Electrospinning of continuous aligned polymer fibers.* Applied Physics Letters, 2004. **84**(7): p. 1222-1224.

71. Pham, Q.P., U. Sharma, and A.G. Mikos, *Electrospinning of polymeric nanofibers for tissue engineering applications: a review.* Tissue Eng, 2006. **12**(5): p. 1197-211.

72. Teo, W.E., W. He, and S. Ramakrishna, *Electrospun scaffold tailored for tissue-specific extracellular matrix.* Biotechnol J, 2006. **1**(9): p. 918-29.

73. Li, W.J., et al., *Engineering controllable anisotropy in electrospun biodegradable nanofibrous scaffolds for musculoskeletal tissue engineering.* J Biomech, 2007. **40**(8): p. 1686-93.

74. Mauck, R.L., et al., *Engineering on the Straight and Narrow: The Mechanics of Nanofibrous Assemblies for Fiber-Reinforced Tissue Regeneration.* Tissue Engineering Part B: Reviews, 2009. **15**(2): p. 171-193.

75. Stella, J.A., et al., *Tissue-to-cellular level deformation coupling in cell micro-integrated elastomeric scaffolds.* Biomaterials, 2008. **29**(22): p. 3228-36.

76. Gilbert, T.W., et al., *Fiber kinematics of small intestinal submucosa under biaxial and uniaxial stretch.* J Biomech Eng, 2006. **128**(6): p. 890-8.

77. Johnson, J., A. Ghosh, and J. Lannutti, *Microstructure-Property Relationships in a Tissue-Engineering Scaffold.* Journal of Applied Polymer Science, 2007. **104**: p. 2919-2927.

78. Sacks, M.S., *Biomechanics of native and engineered heart valve tissues*, in *Functional Tissue Engineering*, F. Guilak, et al., Editors. 2003, Spring-Verlag: New York.

79. Vesely, I. and A. Lozon, *Natural preload of aortic valve leaflet components during glutaraldehyde fixation: Effects on tissue mechanics.* Journal of Biomechanics, 1993. **26**(2): p. 121-131.

80. Sacks, M.S. *Biaxial mechanical behavior of bovine pericardium as a bioprosthetic material*. in *Proceedings of the 11th Conference Engineering, Engineering Mechanics Division/ASCE*. 1996. Fort Lauderdale, FL.

81. Smith, D.B., et al., *Fatigue-induced changes in bioprosthetic heart valve three-dimensional geometry and the relation to tissue damage.* J Heart Valve Dis, 1999. **8**(1): p. 25-33.

82. Vesely, I., J.E. Barber, and N.B. Ratliff, *Tissue damage and calcification may be independent mechanisms of bioprosthetic heart valve failure.* J Heart Valve Dis, 2001. **10**(4): p. 471-7.

83. Sung, H.W., et al., *In vitro evaluation of cytotoxicity of a naturally occurring cross-linking reagent for biological tissue fixation.* J Biomater Sci Polym Ed, 1999. **10**(1): p. 63-78.

84. Schoen, F.J., *Future directions in tissue heart valves: impact of recent insights from biology and pathology.* J Heart Valve Dis, 1999. **8**(4): p. 350-8.

85. Zheng, M.H., et al., *Porcine small intestine submucosa (SIS) is not an acellular collagenous matrix and contains porcine DNA: Possible implications in human implantation.* Journal of Biomedical Materials Research Part B: Applied Biomaterials, 2005. **73B**(1): p. 61-67.

86. Badylak, S., *The extracellular matrix as a biologic scaffold material.* Biomaterials, 2007. **28**: p. 3587-3593.

87. Liao, J., E.M. Joyce, and M.S. Sacks, *Effects of decellularization on the mechanical and structural properties of the porcine aortic valve leaflet.* Biomaterials, 2008. **29**(8): p. 1065-74.

88. Donald O. Freytes, R.M.S.S.F.B., *Uniaxial and biaxial properties of terminally sterilized porcine urinary bladder matrix scaffolds.* Journal of Biomedical Materials Research Part B: Applied Biomaterials, 2008. **84B**(2): p. 408-414.

89. Baker, B.M. and R.L. Mauck, *The effect of nanofiber alignment on the maturation of engineered meniscus constructs.* Biomaterials, 2007. **28**(11): p. 1967-1977.

90. Bidanda, B. and P. Bartolo, *Virtual prototyping & bio manufacturing in medical applications*2008, New York: Springer. xv, 299.

91. Freitas, S., H.P. Merkle, and B. Gander, *Microencapsulation by solvent extraction/evaporation: reviewing the state of the art of microsphere preparation process technology.* Journal of Controlled Release, 2005. **102**(2): p. 313-332.

92. Aubert, J.H. and R.L. Clough, *Low-density, microcellular polystyrene foams.* Polymer, 1985. **26**(13): p. 2047-2054.

93. Caneba, G.T. and D.S. Soong, *Polymer Membrane Formation through the Thermal-Inversion Process. 1. Experimental Study of Membrane Structure Formation.* Mucromolecules, 1985. **18**: p. 2538-2545.

94. Lloyd, D.R., K.E. Kinzer, and H.S. Tseng, *Microporous membrane formation via thermally induced phase separation. I. Solid-liquid phase separation.* Journal of Membrane Science, 1990. **52**(3): p. 239-261.

95. Lloyd, D.R., S.S. Kim, and K.E. Kinzer, *Microporous membrane formation via thermally-induced phase separation. II. Liquid--liquid phase separation.* Journal of Membrane Science, 1991. **64**(1-2): p. 1-11.

96. Liu, X. and P.X. Ma, *Phase separation, pore structure, and properties of nanofibrous gelatin scaffolds.* Biomaterials, 2009. **30**(25): p. 4094-4103.

97. van de Witte, P., et al., *Phase transitions during membrane formation of polylactides. I. A morphological study of membranes obtained from the system polylactide-chloroform-methanol.* Journal of Membrane Science, 1996. **113**(2): p. 223-236.

98. Nam, Y.S. and T.G. Park, *Biodegradable polymeric microcellular foams by modified thermally induced phase separation method.* Biomaterials, 1999. **20**(19): p. 1783-1790.

99. Ho, M.-H., et al., *Preparation of porous scaffolds by using freeze-extraction and freeze-gelation methods.* Biomaterials, 2004. **25**(1): p. 129-138.

100. Leatrese, D.H., K. Byung-Soo, and J.M. David, *Open pore biodegradable matrices formed with gas foaming.* Journal of Biomedical Materials Research, 1998. **42**(3): p. 396-402.

101. Lips, P., et al., *Gas foaming of segmented poly(ester amide) films* Polymer, 2005. **46**(22): p. 9396-9403.

102. Guan, J., K.L. Fujimoto, and W.R. Wagner, *Elastase-sensitive elastomeric scaffolds with variable anisotropy for soft tissue engineering.* Pharm Res, 2008. **25**(10): p. 2400-12.

103. Atkinson, P.M. and D.R. Lloyd, *Anisotropic flat sheet membrane formation via TIPS: atmospheric convection and polymer molecular weight effects.* Journal of Membrane Science, 2000. **175**(2): p. 225-238.

104. Barnes, C.P., et al., *Nanofiber technology: Designing the next generation of tissue engineering scaffolds.* Adv Drug Deliv Rev, 2007.

105. Zhang, S., *Fabrication of novel biomaterials though molecular self-assembly.* Nature Biotechnology, 2003. **21**(10): p. 1171-1178.

106. Niece, K.L., et al., *Self-Assembly Combining Two Bioactive Peptide-Amphiphile Molecules into Nanofibers by Electrostatic Attraction.* Journal of the American Chemical Society, 2003. **125**(24): p. 7146-7147.

107. Kisiday, J., et al., *Self-assembling peptide hydrogel fosters chondrocyte extracellular matrix production and cell division: Implications for cartilage tissue repair.* Proceedings of the National Academy of Sciences of the United States of America, 2002. **99**(15): p. 9996-10001.

108. Di Zio, K. and D.A. Tirrell, *Mechanical Properties of Artificial Protein Matrices Engineered for Control of Cell and Tissue Behavior.* Macromolecules, 2003. **36**(5): p. 1553-1558.

109. Caplan, M.R., et al., *Effects of systematic variation of amino acid sequence on the mechanical properties of a self-assembling, oligopeptide biomaterial.* Journal of Biomaterials Science, Polymer Edition, 2002. **13**: p. 225-236.

110. Ghanaati, S., et al., *Dynamic in vivo biocompatibility of angiogenic peptide amphiphile nanofibers.* Biomaterials, 2009. **30**(31): p. 6202-6212.

111. Rajangam, K., et al., *Peptide amphiphile nanostructure-heparin interactions and their relationship to bioactivity.* Biomaterials, 2008. **29**(23): p. 3298-3305.

112. Meyers, R.A., *Molecular biology and biotechnology : a comprehensive desk reference*1995, New York: VCH. xxxviii, 1034.

113. Nedoviâc, V. and R. Willaert, *Applications of cell immobilisation biotechnology*. Focus on biotechnology ; v. 8B2005, Dordrecht ; New York: Springer. vi, 573.

114. Jen, A.C., M.C. Wake, and A.G. Mikos, *Review: Hydrogels for cell immobilization.* Biotechnol Bioeng, 1996. **50**(4): p. 357-64.

115. Anseth, K., C. Bowman, and L. Brannon-Peppas, *Mechanical properties of hydrogels and their experimental determination* Biomaterials, 1996. **17**: p. 1647-1657.

116. Neidert, M.R. and R.T. Tranquillo, *Tissue-engineered valves with commissural alignment.* Tissue Eng, 2006. **12**(4): p. 891-903.

117. Thomopoulos, S., G.M. Fomovsky, and J.W. Holmes, *The development of structural and mechanical anisotropy in fibroblast populated collagen gels.* J Biomech Eng, 2005. **127**(5): p. 742-50.

118. Isenberg, B.C., C. Williams, and R.T. Tranquillo, *Endothelialization and flow conditioning of fibrin-based media-equivalents.* Ann Biomed Eng, 2006. **34**(6): p. 971-85.

119. Isenberg, B.C., C. Williams, and R.T. Tranquillo, *Small-diameter artificial arteries engineered in vitro.* Circ Res, 2006. **98**(1): p. 25-35.

120. Williams, C., et al., *Cell sourcing and culture conditions for fibrin-based valve constructs.* Tissue Eng, 2006. **12**(6): p. 1489-502.

121. Grassl, E.D., T.R. Oegema, and R.T. Tranquillo, *A fibrin-based arterial media equivalent.* J Biomed Mater Res A, 2003. **66**(3): p. 550-61.

122. Rosner, B.I., T. Hang, and R.T. Tranquillo, *Schwann cell behavior in three-dimensional collagen gels: evidence for differential mechano-transduction and the influence of TGF-beta 1 in morphological polarization and differentiation.* Exp Neurol, 2005. **195**(1): p. 81-91.

123. Robinson, P.S., et al., *Functional tissue-engineered valves from cell-remodeled fibrin with commissural alignment of cell-produced collagen.* Tissue Eng Part A, 2008. **14**(1): p. 83-95.

124. Karamichos, D., R.A. Brown, and V. Mudera, *Collagen stiffness regulates cellular contraction and matrix remodeling gene expression.* J Biomed Mater Res A, 2007. **83**(3): p. 887-94.

125. Francis Suh, J.K. and H.W.T. Matthew, *Application of chitosan-based polysaccharide biomaterials in cartilage tissue engineering: a review.* Biomaterials, 2000. **21**(24): p. 2589-2598.

126. Rachel, G., et al., *Hepatocyte behavior within three-dimensional porous alginate scaffolds.* Biotechnology and Bioengineering, 2000. **67**(3): p. 344-353.

127. Koichi, M., et al., *A novel two-step method for the formation of tissue-engineered cartilage by mature bovine chondrocytes: The alginate-recovered-chondrocyte (ARC) method.* Journal of Orthopaedic Research, 2003. **21**(1): p. 139-148.

128. Mosahebi, A., et al., *A Novel Use of Alginate Hydrogel as Schwann Cell Matrix.* Tissue Engineering., 2001. **7**(5): p. 525-534.

129. Dar, A., et al., *Optimization of cardiac cell seeding and distribution in 3D porous alginate scaffolds.* Biotechnol Bioeng, 2002. **80**(3): p. 305-12.

130. Murat, E., D. Vivek, and G. Gary, *Hepatocyte Attachment on Biodegradable Modified Chitosan Membranes: In Vitro Evaluation for the Development of Liver Organoids.* Artificial Organs, 1998. **22**(10): p. 837-846.

131. Madihally, S.V. and H.W.T. Matthew, *Porous chitosan scaffolds for tissue engineering.* Biomaterials, 1999. **20**(12): p. 1133-1142.

132. Chung, T.W., et al., *Preparation of alginate/galactosylated chitosan scaffold for hepatocyte attachment.* Biomaterials, 2002. **23**(14): p. 2827-2834.

133. Thomopoulos, S., Fomovsky, Gregory M., Chandran Preethi L., Holmes, Jeffry W. , *Collagen fiber alignment does not explain mechanical anisotropy in fibroblasr populated collagen gels.* JBME, 2007. **129**(5): p. 642-650.

134. Lanir, Y., *Constitutive Equations for Fibrous Connective Tissues.* journal of biomechanics, 1983. **16**: p. 1-12.

135. Sacks, M.S., *Incorporation of experimentally-derived fiber orientation into a structural constitutive model for planar collagenous tissues.* J Biomech Eng, 2003. **125**(2): p. 280-7.

136. Sacks, M.S., *A structural constitutive model for chemically treated planar tissues under biaxial loading.* Computational Mechanics, 2000. **26**: p. 243-249.

137. Freed, L.E., et al., *Biodegradable Polymer Scaffolds for Tissue Engineering.* Nature Biotechnology, 1994. **12**: p. 689-693.

138. Engelmayr, G.C. and M.S. Sacks, *A structural model for the flexural mechanics of nonwoven tissue engineering scaffolds.* J Biomech Eng, 2006. **128**: p. 610-622.

139. Engelmayr, G.C., Jr. and M.S. Sacks, *Prediction of extracellular matrix stiffness in engineered heart valve tissues based on nonwoven scaffolds.* Biomech Model Mechanobiol, 2008. **7**(4): p. 309-21.

140. Taylor, G., *Disintegration of Water Drops in an Electric Field.* Proceedings of the Royal Society of London. Series A. Mathematical and Physical Sciences, 1964. **280**(1382): p. 383-397.

141. Taylor, G., *The Force Exerted by an Electric Field on a Long Cylindrical Conductor.* Proceedings of the Royal Society of London. Series A. Mathematical and Physical Sciences, 1966. **291**(1425): p. 145-158.

142. Taylor, G., *Electrically Driven Jets.* Proceedings of the Royal Society of London. A. Mathematical and Physical Sciences, 1969. **313**(1515): p. 453-475.

143. Venugopal, J., et al., *Interaction of cells and nanofiber scaffolds in tissue engineering.* J Biomed Mater Res B Appl Biomater, 2007.

144. Chen, M., et al., *Role of fiber diameter in adhesion and proliferation of NIH 3T3 fibroblast on electrospun polycaprolactone scaffolds.* Tissue Eng, 2007. **13**(3): p. 579-87.

145. Stankus, J.J., et al., *Microintegrating smooth muscle cells into a biodegradable, elastomeric fiber matrix.* Biomaterials, 2006. **27**(5): p. 735-44.

146. Zhong, S., et al., *An aligned nanofibrous collagen scaffold by electrospinning and its effects on in vitro fibroblast culture.* J Biomed Mater Res A, 2006. **79**(3): p. 456-63.

147. Tian, F., et al., *Quantitative analysis of cell adhesion on aligned micro- and nanofibers.* J Biomed Mater Res A, 2007.

148. Riboldi, S.A., et al., *Electrospun degradable polyesterurethane membranes: potential scaffolds for skeletal muscle tissue engineering.* Biomaterials, 2005. **26**(22): p. 4606-15.

149. Rockwood, D.N., et al., *Characterization of biodegradable polyurethane microfibers for tissue engineering.* J Biomater Sci Polym Ed, 2007. **18**(6): p. 743-58.

150. Wake, M.C., P.K. Gupta, and A.G. Mikos, *Fabrication of pliable biodegradable polymer foams to engineer soft tissues.* Cell Transplant, 1996. **5**(4): p. 465-73.

151. Guan, J., et al., *Preparation and characterization of highly porous, biodegradable polyurethane scaffolds for soft tissue applications.* Biomaterials, 2005. **26**(18): p. 3961-71.

152. Balguid, A., et al., *Tailoring Fiber Diameter in Electrospun Poly(epsilon-Caprolactone) Scaffolds for Optimal Cellular Infiltration in Cardiovascular Tissue Engineering.* Tissue Eng Part A, 2008.

153. Pham, Q.P., U. Sharma, and A.G. Mikos, *Electrospun Poly(Îµ-caprolactone) Microfiber and Multilayer Nanofiber/Microfiber Scaffolds: Characterization of Scaffolds and Measurement of Cellular Infiltration.* Biomacromolecules, 2006. **7**(10): p. 2796-2805.

154. Telemeco, T.A., et al., *Regulation of cellular infiltration into tissue engineering scaffolds composed of submicron diameter fibrils produced by electrospinning.* Acta Biomaterialia, 2005. **1**(4): p. 377-385.

155. Nam, J., et al., *Improved cellular infiltration in electrospun fiber via engineered porosity.* Tissue Eng, 2007. **13**(9): p. 2249-57.

156. Marc, S., et al., *Ultraporous 3D polymer meshes by low-temperature electrospinning: Use of ice crystals as a removable void template.* Polymer Engineering & Science, 2007. **47**(12): p. 2020-2026.

157. Baker, B.M., et al., *The potential to improve cell infiltration in composite fiber-aligned electrospun scaffolds by the selective removal of sacrificial fibers.* Biomaterials, 2008. **29**(15): p. 2348-2358.

158. Frey, M.W. and L. Li, *Electrospinning and porosity measurements of nylon-6/poly(ethylene oxide) blended nonwovens.* Journal of Engineered Fibers and Fabrics, 2007. **2**(1): p. 31-37.

159. Yang, S., et al., *The Design of Scaffolds for Use in Tissue Engineering. Part II. Rapid Prototyping Techniques.* Tissue Eng, 2002. **8**(1): p. 1-11.

160. Yeong, W.-Y., et al., *Rapid prototyping in tissue engineering: challenges and potential.* Trends in Biotechnology, 2004. **22**(12): p. 643-652.

161. Wei, X., et al., *Rapid Prototyping of Polyurethane for the Creation of Vascular Systems.* Journal of Bioactive and Compatible Polymers, 2008. **23**(2): p. 103-114.

162. Thomas, B., et al., *Cell and organ printing 2: Fusion of cell aggregates in three-dimensional gels.* The Anatomical Record Part A: Discoveries in Molecular, Cellular, and Evolutionary Biology, 2003. **272A**(2): p. 497-502.

163. Ringeisen, B.R., et al., *Laser Printing of Pluripotent Embryonal Carcinoma Cells.* Tissue Eng, 2004. **10**(3-4): p. 483-491.

164. Liu, V.A. and S.N. Bhatia, *Three-Dimensional Photopatterning of Hydrogels Containing Living Cells.* Biomedical Microdevices, 2002. **4**(4): p. 257-266.

165. Grashow, J.S., A.P. Yoganathan, and M.S. Sacks, *Biaxial stress-stretch behavior of the mitral valve anterior leaflet at physiologic strain rates.* Ann Biomed Eng, 2006b. **34**(2): p. 315-25.

166. Wang, J.H. and B.P. Thampatty, *An introductory review of cell mechanobiology.* Biomech Model Mechanobiol, 2006. **5**(1): p. 1-16.

167. Merryman, W.D., et al. *Contractile abilities of the aortic valve leaflet interstitial cell*. in *Biomedical Engineering Society (BMES) Annual Fall Meeting*. 2004. Philadelphia, PA.

168. Yanagisawa, M., et al., *Effects of compressive force on the differentiation of pluripotent mesenchymal cells.* Life Sci, 2007. **81**(5): p. 405-12.

169. Terraciano, V., et al., *Differential response of adult and embryonic mesenchymal progenitor cells to mechanical compression in hydrogels.* Stem Cells, 2007. **25**(11): p. 2730-8.

170. Song, G., et al., *Mechanical stretch promotes proliferation of rat bone marrow mesenchymal stem cells.* Colloids Surf B Biointerfaces, 2007. **58**(2): p. 271-7.

171. Roeder, B.A., et al., *Local, Three-Dimensional Strain Measurements Within Largely Deformed Extracellular Matrix Constructs.* Journal of Biomechanical Engineering, 2004. **126**(6): p. 699-708.

172. Guilak, F., A. Ratcliffe, and V.C. Mow, *Chondrocyte deformation and local tissue strain in articular cartilage: a confocal microscopy study.* J Orthop Res, 1995. **13**(3): p. 410-21.

173. Ingber, D.E., *Mechanobiology and diseases of mechanotransduction.* Ann Med, 2003. **35**(8): p. 564-77.

174. Lee, D.A. and M.M. Knight, *Mechanical loading of chondrocytes embedded in 3D constructs: in vitro methods for assessment of morphological and metabolic response to compressive strain.* Methods Mol Med, 2004. **100**: p. 307-24.

175. Sacks, M.S., *Biaxial mechanical evaluation of planar biological materials.* Journal of Elasticity, 2000. **61**: p. 199-246.

176. Billiar, K.L. and M.S. Sacks, *A method to quantify the fiber kinematics of planar tissues under biaxial stretch.* J Biomech, 1997. **30**(7): p. 753-6.

177. Bathe, K.J., *Finite Elements Proceedures in Engineering Analysis*1982, Englewood Cliffs,NJ: Prentice-Hall.

178. Spencer, A.J.M., *Continuum Mechanics*1980, New York: Longman Scientific & Technical. 183.

179. Venugopal, J., et al., *Interaction of cells and nanofiber scaffolds in tissue engineering.* J Biomed Mater Res B Appl Biomater, 2008. **84**(1): p. 34-48.

180. Tian, F., et al., *Quantitative analysis of cell adhesion on aligned micro- and nanofibers.* J Biomed Mater Res A, 2008. **84**(2): p. 291-9.

181. Engelmayr, G.C., Jr., et al., *The independent role of cyclic flexure in the early in vitro development of an engineered heart valve tissue.* Biomaterials, 2005. **26**(2): p. 175-87.

182. Lanir, Y., *Rheological behavior of skin.* The rheology of blood, blood vessels and associated tissues, 1980: p. 276-294.

183. Huang, H.Y., J. Liao, and M.S. Sacks, *In-situ deformation of the aortic valve interstitial cell nucleus under diastolic loading.* J Biomech Eng, 2007. **129**(6): p. 880-89.

184. Stylianopoulos, A., et al., *Computational predictions of the tensile properties of electrospun fibre meshes: Effect of fibre diameter and fibre orientation.* Journal of Mechanical Behavior of Biomedical Materials, 2008. **1**: p. 326-335.

185. Kidoaki, S., I.K. Kwon, and T. Matsuda, *Structural features and mechanical properties of in situ-bonded meshes of segmented polyurethane electrospun from mixed solvents.* J Biomed Mater Res B Appl Biomater, 2006. **76**(1): p. 219-29.

186. Shin YM, et al., *Experimental characterization of electrospinning: the electrically forced jet and instabilities.* Polymer, 2001. **42**: p. 9955-9967.

187. Shin YM, et al., *Electrospinning: A whipping jet generates submicron polymer fibers.* Applied Physics Journal, 2001. **78**(8): p. 1149-1151.

188. Hohman MM, et al., *Electrospinning and electrically forced jets. I. Stability theory.* Physics of Fluids, 2001. **13**(8): p. 2201-2220.

189. Stankus, J.J., Soletti, L., Fujimoto, K., Hong, Y., Vorp, D.A., Wagner, W.R., *Fabrication of cell microintegrated blood vessel constructs through electrohydrodynamic atomization.* Biomaterials, 2007. **28**(17): p. 2738-46.

190. Martin, R.M., H. Leonhardt, and M.C. Cardoso, *DNA labeling in living cells.* Cytometry A, 2005. **67**(1): p. 45-52.

191. Screen, H.R., et al., *Development of a technique to determine strains in tendons using the cell nuclei.* Biorheology, 2003. **40**(1-3): p. 361-8.

192. Guilak, F., A. Ratcliffe, and V.C. Mow, *Chondrocyte deformation and local tissue strain in articular cartilage: a confocal microscopy study.PG - 410-21.* J Orthop Res, 1995. **13**(3).

193. Arnoczky, S.P., et al., *In situ cell nucleus deformation in tendons under tensile load; a morphological analysis using confocal laser microscopy.* J Orthop Res, 2002. **20**(1): p. 29-35.

194. Taylor, P.M., et al., *The cardiac valve interstitial cell.* International Journal of Biochemistry and Cell Biology, 2003. **35**(2): p. 113-8.

195. Chaudhuri, B.B., P. Kundu, and N. Sarkar, *Detection and Gradation of Oriented Texture.* Pattern Recognition Letters, 1993. **14**(2): p. 147-153.

196. Karlon, W.J., et al., *Automated measurement of myofiber disarray in transgenic mice with ventricular expression of ras.* Anat Rec, 1998. **252**(4): p. 612-25.

197. Dafalias, Y.F., *Orientation distribution function in non-affine rotations.* Journal of the Mechanics and Physics of Solids, 2001. **49**: p. 2493-2516.

198. Thomas, C.H., et al., *Engineering gene expression and protein synthesis by modulation of nuclear shape.* Proc Natl Acad Sci U S A, 2002. **99**(4): p. 1972-7.

199. Butler, D.L., S.A. Goldstein, and F. Guilak, *Functional tissue engineering: the role of biomechanics.* J Biomech Eng, 2000. **122**(6): p. 570-5.

200. Merryman, W.D., et al., *Synergistic effects of cyclic tension and transforming growth factor-beta1 on the aortic valve myofibroblast.* Cardiovasc Pathol, 2007. **16**(5): p. 268-76.

201. Robinson, P.S., et al., *Functional Tissue-Engineered Valves from Cell-Remodeled Fibrin with Commissural Alignment of Cell-Produced Collagen.* Tissue Eng, 2007.

202. Engelmayr, G.C., et al., *The flexure-stretch-flow bioreactor: A novel tool for studying heart valve tissue mechanobiology.* Annals of Biomedical Engineering, in-press.

203. Engelmayr, G.C., Jr. and M.S. Sacks, *Prediction of extracellular matrix stiffness in engineered heart valve tissues based on nonwoven scaffolds.* Biomech Model Mechanobiol, 2007.

204. Ormiston, J.A., et al., *Size and motion of the mitral valve annulus in man. I. A two-dimensional echocardiographic method and findings in normal subjects.* Circulation, 1981. **64**(1): p. 113-20.

205. Bellhouse, B.J. and F.H. Bellhouse, *Fluid mechanics of the mitral valve.* Nature, 1969. **224**: p. 615-618.

206. Otsuji, Y., et al., *Insights from three-dimensional echocardiography into the mechanism of functional mitral regurgitation: direct in vivo demonstration of altered leaflet tethering geometry.* Circulation, 1997. **96**(6): p. 1999-2008.

207. Schwammenthal, E., et al., *Dynamics of mitral regurgitant flow and orifice area. Physiologic application of the proximal flow convergence method: clinical data and experimental testing.* Circulation, 1994. **90**(1): p. 307-22.

208. Ming, L. and H.K. Zhen, *Study of the closing mechanism of natural heart valves.* Applied Mathematics and Mechanics, 1986. **17**(10).

209. Hartiala, J.J., et al., *Velocity-encoded cine MRI in the evaluation of left ventricular diastolic function: measurement of mitral valve and pulmonary vein flow velocities and flow volume across the mitral valve.* Am Heart J, 1993. **125**(4): p. 1054-66.

210. Arts, T., et al., *Stresses in the closed mitral valve: a model study.* J Biomech, 1983. **16**(7): p. 539-47.

211. Kunzelman, K.S., M.S. Reimink, and R.P. Cochran, *Flexible versus rigid ring annuloplasty for mitral valve annular dilatation: a finite element model.* J Heart Valve Dis, 1998. **7**(1): p. 108-16.

212. Kunzelman, K.S., et al., *Finite element analysis of the mitral valve.* J Heart Valve Dis, 1993. **2**(3): p. 326-40.

213. Kunzelman, K.S., et al., *Anatomic basis for mitral valve modelling.* J Heart Valve Dis, 1994. **3**(5): p. 491-6.

214. Thubrikar, M., et al., *Analysis of the design and dynamics of aortic bioprostheses in vivo.* J Thorac Cardiovasc Surg, 1982. **84**(2): p. 282-90.

215. Thubrikar, M., et al., *Stress analysis of porcine bioprosthetic heart valves in vivo.* Journal of Biomedical Materials Research, 1982. **16**: p. 811.

216. Thubrikar, M., et al., *Interpretation of aortic root angiography in dogs and in humans.* Cardiovasc Res, 1982. **16**(1): p. 16-21.

217. Thubrikar, M.J., J. Aouad, and S.P. Nolan, *Comparison of the in vivo and in vitro mechanical properties of aortic valve leaflets.* J Thorac Cardiovasc Surg, 1986. **92**(1): p. 29-36.

218. Smith, D.B., et al., *Surface geometric analysis of anatomic structures using biquintic finite element interpolation.* Ann Biomed Eng, 2000. **28**(6): p. 598-611.

219. Iyengar, A.K.S., et al., *Dynamic in vitro quantification of bioprosthetic heart valve leaflet motion using structured light projection.* Ann Biomed Eng, 2001. **29**(11): p. 963-73.

220. Sacks, M.S., D.B. Smith, and E.D. Hiester, *The aortic valve microstructure: effects of transvalvular pressure.* Journal of Biomedical Materials Research, 1998. **41**(1): p. 131-41.

221. Vesely, I., *The role of elastin in aortic valve mechanics.* Journal of Biomechanics, 1998. **31**(2): p. 115-123.

222. Hildebrand, D.K., *Design and Evaluation of a Novel Pulsatile Bioreactor for Biologically Active Heart Valves*, in *Bioengineering*2003, University of Pittsburgh: Master's Thesis.

223. Hildebrand, D.K., et al., *Design and hydrodynamic evaluation of a novel pulsatile bioreactor for biologically active heart valves.* Ann Biomed Eng, 2004. **32**(8): p. 1039-49.

224. Merryman, W.D., et al., *Defining biomechanical endpoints for tissue engineered heart valve leaflets from native leaflet properties.* Progress in Pediatric Cardiology, 2006. **21**(2): p. 153-60.

225. Hoerstrup, S.P., et al., *Functional living trileaflet heart valves grown In vitro.* Circulation, 2000. **102**(19 Suppl 3): p. III44-9.

226. Hoerstrup, S.P., et al., *New pulsatile bioreactor for in vitro formation of tissue engineered heart valves.* Tissue Eng, 2000. **6**(1): p. 75-9.

227. Kim, Y.J., et al., *Fluorometric assay of DNA in cartilage explants using Hoechst 33258.* Anal Biochem, 1988. **174**(1): p. 168-76.

228. Brown, A.N., et al., *Combining chondrocytes and smooth muscle cells to engineer hybrid soft tissue constructs.* Tissue Eng, 2000. **6**(4): p. 297-305.

229. Engelmayr, G.C., Jr., et al., *Cyclic flexure and laminar flow synergistically accelerate mesenchymal stem cell-mediated engineered tissue formation: Implications for engineered heart valve tissues.* Biomaterials, 2006. **27**(36): p. 6083-95.

230. von Offenberg Sweeney, N., et al., *Cyclic strain-mediated regulation of endothelial matrix metalloproteinase-2 expression and activity.* Cardiovascular Research, 2004. **63**(4): p. 625-34.

231. Hasaneen, N.A., et al., *Cyclic mechanical strain-induced proliferation and migration of human airway smooth muscle cells: role of EMMPRIN and MMPs.* The FASEB journal : official publication of the Federation of American Societies for Experimental Biology, 2005. **19**(11): p. 1507-9.

232. Haseneen, N.A., et al., *Mechanical stretch induces MMP-2 release and activation in lung endothelium: role of EMMPRIN.* Am J Physiol Lung Cell Mol Physiol, 2003. **284**(3): p. L541-7.

233. Fung, Y.C., K. Fronek, and P. Patitucci, *Pseudoelasticity of arteries and the choice of its mathematical expression.* Am J Physiol, 1979. **237**(5): p. H620-31.

234. Sacks, M.S., D.B. Smith, and E.D. Hiester, *A small angle light scattering device for planar connective tissue microstructural analysis.* Ann Biomed Eng, 1997. **25**(4): p. 678-89.

235. Lanir, Y. and Y.C. Fung, *Two-dimensional mechanical properties of rabbit skin. I. Experimental system.* J Biomech, 1974. **7**(1): p. 29-34.

236. Lanir, Y. and Y.C. Fung, *Two-dimensional mechanical properties of rabbit skin. II. Experimental results.* J Biomech, 1974. **7**(2): p. 171-82.

237. Lanir, Y., *Constitutive Equation for the Lung Tissue.* Journal of Biomechanical Engineering, 1983. **105**: p. 374-380.

238. Hutmacher, D.W., J.C. Goh, and S.H. Teoh, *An introduction to biodegradable materials for tissue engineering applications.* Ann Acad Med Singapore, 2001. **30**(2): p. 183-91.

239. Chuong, C.J. and Y.C. Fung, *Three-dimensional stress distribution in arteries.* J Biomech Eng, 1983. **105**(3): p. 268-74.

240. Hutmacher, D.W., *Scaffolds in tissue engineering bone and cartilage.* Biomaterials, 2000. **21**(24): p. 2529-43.

241. Hutmacher, D.W., *Scaffold design and fabrication technologies for engineering tissues--state of the art and future perspectives.* J Biomater Sci Polym Ed, 2001. **12**(1): p. 107-24.

242. Holzapfel, G.A. and T.C. Gasser, *A new constitutive framework for arterial wall mechanics and a comparative study of material models.* Journal of Elasticity, 2000. **61**: p. 1-48.

243. Einstein, D.R., et al., *Dynamic finite element implementation of nonlinear, anisotropic hyperelastic biological membranes.* Comput Methods Biomech Biomed Engin, 2003. **6**(1): p. 33-44.

244. Taber, L.A., *Nonlinear Theory of Elasticity, Applications in Biomechanics*2004, Danvers, MA: World Scientific Publishing.

245. Holzapfel, G.A., *Nonlinear solid mechanics : a continuum approach for engineering*2000, Chichester ; New York: Wiley. xiv, 455.

246. Truesdell, C. and W. Noll, *The Nonlinear Field Theories of Mechanics*. 3rd ed, ed. S.S. Antman2004, Berlin: Springer-Verlag.

247. Holzapfel, G.A. and R.W. Ogden, *On planar biaxial tests for anisotropic nonlinearly elastic solids. A continuum mechanical framework.* Mathematics and Mechanics of Solids, 2009. **14**(5): p. 474-489.

248. Tong, P. and Y.C. Fung, *The stress-strain relationship for the skin.* J Biomech, 1976. **9**(10): p. 649-57.

249. Joyce, E.M., et al., *Functional collagen fiber architecture of the pulmonary heart valve cusp.* Ann Thorac Surg, 2009. **87**(4): p. 1240-9.

250. Humphrey, J.D., *Mechanics of the arterial wall: review and directions.* Crit Rev Biomed Eng, 1995. **23**(1-2): p. 1-162.

251. Holzapfel, G.A., *Determination of material models for arterial walls from uniaxial extension tests and histological structure.* J Theor Biol, 2006. **238**(2): p. 290-302.

252. Holzapfel, G.A., T.C. Gasser, and R.W. Ogden, *Comparison of a multi-layer structural model for arterial walls with a fung-type model, and issues of material stability.* J Biomech Eng, 2004. **126**(2): p. 264-75.

253. Humphrey, J.D., R.K. Strumpf, and F.C. Yin, *Determination of a constitutive relation for passive myocardium: I. A new functional form.* J Biomech Eng, 1990. **112**(3): p. 333-9.

254. Humphrey, J.D. and F.C. Yin, *On constitutive relations and finite deformations of passive cardiac tissue: I. A pseudostrain-energy function.* J Biomech Eng, 1987. **109**(4): p. 298-304.

255. Natali, A.N., E.L. Carniel, and H. Gregersen, *Biomechanical behaviour of oesophageal tissues: material and structural configuration, experimental data and constitutive analysis.* Med Eng Phys, 2009. **31**(9): p. 1056-62.

256. Yang, W., et al., *Directional, regional, and layer variations of mechanical properties of esophageal tissue and its interpretation using a structure-based constitutive model.* J Biomech Eng, 2006. **128**(3): p. 409-18.

257. Lanir, Y., *Plausibility of structural constitutive equations for swelling tissues--implications of the C-N and S-E conditions.* J Biomech Eng, 1996. **118**(1): p. 10-6.

258. Lanir, Y., *Plausibility of Structural Constitutive-Equations for Isotropic Soft-Tissues in Finite Static Deformations.* Journal of Applied Mechanics-Transactions of the Asme, 1994. **61**(3): p. 695-702.

259. Spencer, A., *Deformations of fibre-reinforced materials*. Oxford science research papers1972, Glasgow: Oxford university press. 128.

260. Holzapfel, G.A. and H.W. Weizsacker, *Biomechanical behavior of the arterial wall and its numerical characterization.* Comput Biol Med, 1998. **28**(4): p. 377-92.

261. Lanir, Y., O. Lichtenstein, and O. Imanuel, *Optimal design of biaxial tests for structural material characterization of flat tissues.* J Biomech Eng, 1996. **118**(1): p. 41-7.

262. Fung, Y.C., *Stress-strain-history relations of soft tissue in simple elongation*, in *Biomechanics: Its Foundations and Objective*, Y.C. Fung, P. N., and M. Anliker, Editors. 1972, pretice-Hall: New Jersey. p. 181-208.

263. Billiar, K.L. and M.S. Sacks, *Biaxial mechanical properties of the native and glutaraldehyde-treated aortic valve cusp: Part II--A structural constitutive model.* J Biomech Eng, 2000. **122**(4): p. 327-35.

264. Gloeckner, D.C., et al., *Passive biaxial mechanical properties of the rat bladder wall after spinal cord injury.* J Urol, 2002. **167**(5): p. 2247-52.

265. Yeoh, O.H., *Some Forms of the Strain Energy function for Rubber*. Vol. 66. 1993: RUBDIV. 754-771.

266. Nerurkar, N.L., et al., *Engineered disc-like angle-ply structures for intervertebral disc replacement.* Spine, 2010. **35**(8): p. 867-73.

267. Engelmayr, G.C., Jr., et al., *A novel flex-stretch-flow bioreactor for the study of engineered heart valve tissue mechanobiology.* Ann Biomed Eng, 2008. **36**(5): p. 700-12.

268. Sacks, M.S., *Biaxial mechanical behavior of fixed bovine pericardium*, in *Proceedings of the 5th World Biomaterials Congress*1996.

269. Billiar, K.L. and M.S. Sacks, *Biaxial mechanical properties of the natural and glutaraldehyde treated aortic valve cusp--Part I: Experimental results.* J Biomech Eng, 2000. **122**(1): p. 23-30.

270. Barbenel, J.C., P. Zioupos, and J. Fisher, *The mechanical properties of bovine pericardium*, in *Biomaterials and Clinical Application*, A. Pizzoferrato, et al., Editors. 1987, Elsevier: Amsterdam. p. 421.

271. Crofts, C.E. and E.A. Trowbridge, *The tensile strength of natural and chemically modified bovine pericardium.* Journal of Biomedical Materials Research, 1988. **22**: p. 89-98.

272. Langdon, S.E., et al., *Biaxial mechanical/structural effects of equibiaxial strain during crosslinking of bovine pericardial xenograft materials.* Biomaterials, 1999. **20**(2): p. 137-53.

273. Liao, K., et al., *Bovine pericardium versus porcine aortic valve: comparison of tissue biological properties as prosthetic valves.* Artif Organs, 1992. **16**(4): p. 361-5.

274. Sacks, M.S. and C.J. Chuong, *Orthotropic mechanical properties of chemically treated bovine pericardium.* Ann Biomed Eng, 1998. **26**(5): p. 892-902.

275. Klouda, L., et al., *Effect of biomimetic conditions on mechanical and structural integrity of PGA/P4HB and electrospun PCL scaffolds.* J Mater Sci Mater Med, 2008. **19**(3): p. 1137-44.

276. Boerboom, R.A., et al., *Effect of strain magnitude on the tissue properties of engineered cardiovascular constructs.* Ann Biomed Eng, 2008. **36**(2): p. 244-53.

277. Mol, A., et al., *Autologous human tissue-engineered heart valves: prospects for systemic application.* Circulation, 2006. **114**(1 Suppl): p. I152-8.

278. Kim, B.S., et al., *Cyclic mechanical strain regulates the development of engineered smooth muscle tissue.* Nat Biotechnol, 1999. **17**(10): p. 979-83.

279. Dahl, S.L., et al., *Mechanical properties and compositions of tissue engineered and native arteries.* Annals of Biomedical Engineering, 2007. **35**(3): p. 348-55.

280. Balguid, A., et al., *Hypoxia induces near-native mechanical properties in engineered heart valve tissue.* Circulation, 2009. **119**(2): p. 290-7.

281. Cooper, J.A., Jr., et al., *Biomimetic tissue-engineered anterior cruciate ligament replacement.* Proceedings of the National Academy of Sciences of the United States of America, 2007. **104**(9): p. 3049-54.

282. Gentleman, E., et al., *Mechanical characterization of collagen fibers and scaffolds for tissue engineering.* Biomaterials, 2003. **24**(21): p. 3805-13.

283. Nerurkar, N.L., et al., *Nanofibrous biologic laminates replicate the form and function of the annulus fibrosus.* Nature Materials, 2009. **8**(12): p. 986-92.

284. Bashey, R., T. Torii, and A. Angrist, *Age-related collagen and elastin content of human heart valves.* J Gerontol, 1967. **22**: p. 203-8.

285. Schoen, F.J. and R.J. Levy, *Calcification of bioprosthetic heart valves*, in *Replacement Cardiac Valves*, E. Bodnar and R.W.M. Frater, Editors. 1991, Pergamon Press, Inc.: New York. p. 125-148.

286. Kortsmit, J., et al., *Nondestructive and noninvasive assessment of mechanical properties in heart valve tissue engineering.* Tissue engineering. Part A, 2009. **15**(4): p. 797-806.

287. Badylak, S.F., *The extracellular matrix as a biologic scaffold material.* Biomaterials, 2007. **28**(25): p. 3587-93.

288. Nerurkar, N.L., et al., *Dynamic culture enhances stem cell infiltration and modulates extracellular matrix production on aligned electrospun nanofibrous scaffolds.* Acta Biomaterialia, 2011. **7**(2): p. 485-91.

289. AHA, *Heart Disease and Stroke Statistics - 2003 Update*, 2002, A merican Heart Association: Dallas, Tx.

290. Schoen, F., *Aortic valve structure-function correlations: Role of elastic fibers no longer a stretch of the imagination.* Journal of Heart Valve Disease, 1997. **6**: p. 1-6.

291. Filip, D.A., A. Radu, and M. Simionescu, *Interstitial cells of the heart valve possess characteristics similar to smooth muscle cells.* Circulation Research, 1986. **59**(3): p. 310-320.

292. Mulholland, D.L. and A.I. Gotlieb, *Cell biology of valvular interstitial cells.* Canadian Journal of Cardiology, 1996. **12**(3): p. 231-6.

293. Vesely, I., *Reconstruction of loads in the fibrosa and ventricularis of porcine aortic valves.* Asaio J, 1996. **42**(5): p. M739-46.

294. Vesely, I. and R. Noseworthy, *Micromechanics of the fibrosa and the ventricularis in aortic valve leaflets.* Journal of Biomechanics, 1992. **25**(1): p. 101-113.

295. Talman, E.A. and D.R. Boughner, *Effect of altered hydration on the internal shear properties of porcine aortic valve cusps.* Ann Thorac Surg, 2001. **71**(5 Suppl): p. S375-8.

296. Talman, E.A. and D.R. Boughner, *Glutaraldehyde fixation alters the internal shear properties of porcine aortic heart valve tissue.* Annals of Thoracic Surgery, 1995. **60**: p. S369-S373.

297. Talman, E., Boughner, DR., *Internal shear properties of fresh porcine aortic valve cusps: implications for normal valve function.* Journal of Heart Valve Disease, 1996. **5**(2): p. 152-9.

298. Woo, S., Orland, CA, Camp, JF, Akeson, WH, *Effects of postmortem storage by freezinf on ligament tensile behavior.* Journal of Biomechanics, 1994. **19**: p. 399-404.

299. Sauren, A.A., et al., *Aortic valve histology and its relation with mechanics-preliminary report.* J Biomech, 1980. **13**(2): p. 97-104.

300. Mirnajafi, A., et al., *The flexural rigidity of the aortic valve leaflet in the commissural region.* Journal of Biomechanics, in-press.

301. Mohri, H., D. Reichenback, and K. Merendino, *Biology of homologous and heterologous aortic valves*, in *Biological Tissue in Heart Valve Replacement*, M. Ionescu, D. Ross, and G. Wooler, Editors. 1972, Butterworths: London. p. 137.

302. Mohri H, R.D., Merendino KA, *Biological tissue in heart valve replacement*1972, Butterworths, London. 137-194.

303. Grashow, J.S., A.P. Yoganathan, and M.S. Sacks, *Biaixal stress-stretch behavior of the mitral valve anterior leaflet at physiologic strain rates.* Ann Biomed Eng, 2006. **34**(2): p. 315-25.

304. Ritchie, J., et al., *The material properties of the native porcine mitral valve chordae tendineae: An in vitro investigation.* J Biomech, 2006. **39**(6): p. 1129-35.

305. Liao, J., et al., *The relation between collagen fibril kinematics and mechanical properties in the mitral valve anterior leaflet.* J Biomech Eng, 2007. **129**(1): p. 78-87.

306. Woo, S.L.Y., et al., *Effects of Postmortem Storage by Freezing on Ligament Tensile Behavior.* Journal of Biomechanics, 1994. **19**: p. 399-404.

307. Cataloglu, A., R.E. Clark, and P.L. Gould, *Stress analysis of aortic valve leaflets with smoothed geometrical data.* Journal of Biomechanics, 1977. **10**: p. 153-158.

308. Sauren, A.A., et al., *The mechanical properties of porcine aortic valve tissues.* J Biomech, 1983. **16**(5): p. 327-37.

309. Lo, D. and I. Vesely, *Biaxial Strain Analysis of the Porcine Aortic Valve.* Annals of Thoracic Surgery, 1995. **60**: p. S374-378.

310. Missirlis, Y. and M. Chong, *Aortic Valve Mechanics - Part I: Material Properties of Natural Porcine Aortic Vavles.* Journal of Bioengineering, 1978. **2**: p. 287-300.

311. Thornton, G.M., et al., *Ligament creep cannot be predicted from stress relaxation at low stress: a biomechanical study of the rabbit medial collateral ligament.* J Orthop Res, 1997. **15**(5): p. 652-6.

312. Naimark, W.A., et al., *Correlation of structure and viscoelastic properties in the pericardia of four mammalian species.* American Journal of Physiology, 1992. **263**(32): p. H1095-H1106.

313. Leeson-Dietrich, J., D. Boughner, and I. Vesely, *Porcine Pulmonary and Aortic Valves: A Comparison of Their Tensile Viscoelastic Properties at Physiological Strain Rates.* The Journal of Heart Valve Disease, 1995. **4**: p. 88-94.

314. Dunn, M.G. and F.H. Silver, *Viscoelastic behavior of human connective tissues: relative contribution of viscous and elastic components.* Connect Tissue Res, 1983. **12**(1): p. 59-70.

315. Lee, J.M. and D.R. Boughner, *Mechanical properties of human pericardium. Differences in viscoelastic response when compared with canine pericardium.* Circ Res, 1985. **57**(3): p. 475-81.

316. Lee, J.M., D.W. Courtman, and D.R. Boughner, *The glutaraldehyde-stablized porcine aortic valve xenograft. I. Tensile viscoelastic properties of the fresh leaflet material.* Journal of Biomedical Materials Research, 1984. **18**: p. 61-77.

317. Rigby, R., et al., *The mechanical properties of rat tail tendon.* The Journal of General Physiology, 1959. **43**: p. 265-282.

318. Vesely, I., D.R. Boughner, and J. Leeson-Dietrich, *Bioprosthetic Valve Tissue Viscoelasticity: Implications on Accelerated Pulse Duplicator Testing.* Annals of Thoracic Surgery, 1995. **60**: p. S379-383.

319. Adamczyk, M.M. and I. Vesely, *Characteristics of compressive strains in porcine aortic valves cusps.* J Heart Valve Dis, 2002. **11**(1): p. 75-83.

320. Mirnajafi, A., et al., *The flexural rigidity of the aortic valve leaflet in the commissural region.* J Biomech, 2006. **39**(16): p. 2966-73.

321. Folkhard, W., et al., *Structural dynamic of native tendon collagen.* J Mol Biol, 1987. **193**(2): p. 405-7.

322. Redalli, A., Vesentini, S., Soncini, M., Vena, P., Mantero, S., Montevecchi, F.M. , *Possible role of decorin glycosaminoglycans in fibril to fibril force tranfer in relative*

mature tendons - a computational study from molecular to microstructural level. Journal of Biomechanics, 2003. **36**: p. 1555-69.

323. Haigh, M. and J.E. Scott, *A method of processing tissue sections for staining with cu-promeronic blue and other dyes, using CEC techniques, for light and electron microscopy.* Basic Appl Histochem, 1986. **30**(4): p. 479-86.

324. Adamczyk, M.M. and I. Vesely, *Biaxial strain distributions in explanted porcine bioprosthetic valves.* J Heart Valve Dis, 2002. **11**(5): p. 688-95.